Optical confirmation and weak lensing mass constraints for distant Sunyaev-Zel’dovich-detected galaxy clusters

DISSERTATION
zur
Erlangung des Doktorgrades (Dr. rer. nat.)
der
Mathematisch-Naturwissenschaftlichen Fakultät
der
Rheinischen Friedrich-Wilhelms-Universität Bonn

vorgelegt von
Hannah Zohren
aus
Bonn – Bad Godesberg

Bonn, September 2021

Angefertigt mit Genehmigung der Mathematisch-Naturwissenschaftlichen Fakultät
der Rheinischen Friedrich-Wilhelms-Universität Bonn

1. Gutachter:	Prof. Dr. Peter Schneider
2. Gutachter:	Prof. Dr. Thomas Reiprich

Tag der Promotion:	31.01.2022
Erscheinungsjahr:	2022

Abstract

Galaxy clusters reside in the densest regions of the large-scale matter distribution of the Universe. Therefore, their number density as a function of mass and redshift is a powerful tool for cosmological studies aiming, for example, to uncover the nature of dark matter and dark energy. A detection of galaxy clusters through the Sunyaev-Zel'dovich (SZ) effect, a spectral distortion of the cosmic microwave background (CMB) due to inverse Compton scattering of CMB photons with free electrons in the hot intracluster medium, has proven to be very useful to assemble nearly mass-limited samples of clusters. Two ingredients are essential to make full use of these samples for cosmological studies: firstly, the selection function of the cluster sample needs to be well-understood, and secondly, the scaling relation between the observable mass proxy and the true underlying cluster mass has to be accurately calibrated over a wide redshift range. The research in this thesis addresses both of these prerequisites.

The first part of this thesis contributes to an understanding of the selection function of the second *Planck* catalogue of Sunyaev-Zeldovich sources (PSZ2). We conduct an optical follow-up of a sample of 32 PSZ2 cluster candidates preselected at low SZ detection significance $3 \lesssim S/N \lesssim 6$ and approximately at redshifts $z \gtrsim 0.7$ with ACAM on the 4.2-m William Herschel Telescope. A red-sequence analysis based on observations in the r, i, and z band provides photometric redshift and richness estimates. We obtain spectroscopic redshifts from additional long-slit observations for a subset of clusters. Comparing the measurements to a scaling relation calibrated at low redshifts reveals that the optical richness is in many cases smaller than expected from the SZ-based mass. Likely reasons include Eddington bias, projection effects, or noise-induced detections, which are more frequent at low signal-to-noise ratios. Still, for 18 (7) of the cluster candidates at redshift $z > 0.5$ ($z > 0.8$), we measured a richness that is at least half of the average value expected from the scaling relation, marking the threshold we regard for the confirmation of massive clusters.

The complex selection function of the investigated cluster sample based on SZ and optical data inhibits its use for cosmological studies. However, the validation of massive cluster candidates provides a basis for further astrophysical investigations of individual targets.

The second part of this thesis aims to calibrate the cluster mass scale of the SZ–mass scaling relation of galaxy clusters in the high-redshift regime. For this purpose, weak lensing masses of nine massive clusters from the South Pole Telescope SZ (SPT-SZ) Survey are obtained from galaxy shape measurements based on *Hubble Space Telescope* (*HST*) Advanced Camera for Surveys (ACS) imaging in the bands F606W and F814W. This sample comprises clusters with high SZ-detection significances $\xi > 6.0$ and high redshifts of $z \gtrsim 1.0$ in the SPT-SZ Survey. The *HST*/ACS data are supplemented with observations from the Wide Field Camera 3 (WFC3) onboard the *HST* and the FORS2 imager at the Very Large Telescope (VLT) to enable a robust removal of cluster members while preferentially selecting background source galaxies at $z \gtrsim 1.8$, carrying most of the weak lensing signal. We estimate the source redshift distribution and average geometric lensing efficiency with the help of photometric redshift catalogues from the CANDELS/3D-HST fields with a revised calibration. Fitting the tangential reduced shear profiles with spherical NFW models assuming a fixed concentration–mass relation provides weak lensing mass measurements. Combining these with results at lower redshifts from earlier studies, we constrain the redshift evolution of the SZ–mass scaling relation of clusters in the SPT-SZ Survey for the first time out to the highest redshift $z \sim 1.7$ for a sample with a well-defined selection function. We find that the refined constraints are consistent with previous results. That is, a lower mass scale is preferred in the analysis including a weak lensing mass calibration than in an analysis based on a flat *Planck* $\nu\Lambda$CDM cosmology combined with the SPT-SZ cluster counts.

Contents

CHAPTER 1

Introduction

Cosmologists seek to understand the Universe as a whole including its origin, composition, and past and future evolution. Despite the manifold challenges arising from the enormous scales of masses, energies, and distances involved in this endeavour, scientists have come up with an impressive amount of methods to investigate arguably one of humankind's most important unanswered questions: What is the Universe made of?

Over the past decades, joint theoretical, numerical, and observational efforts have led to the so-called standard model of cosmology, which describes the properties of the Universe regarding its expansion and the formation of structures in it with only six parameters using the physical laws known today. So far, this model agrees remarkably well with various observations from the early to the recent times of the Universe. Some of the key observations the cosmological model can explain include, for instance, the isotropic cosmic microwave background (CMB), which was emitted around 380,000 years after the Big Bang, with small fluctuations of the intensity, a mass fraction of helium of about 25 per cent in nearly all cosmic objects, the web-like distribution of matter on large scales, and the expansion of the Universe as measured from galaxies receding from us. According to the standard model of cosmology, the Universe consists approximately of 5 percent ordinary (or baryonic as cosmologists like to call it) matter, 26 per cent dark matter, and 69 per cent dark energy (Planck Collaboration et al., 2020b). Choosing to label the latter two components as 'dark' is a clear indicator of our remaining ignorance about their nature.

Dark matter does not interact electromagnetically, and the postulated particles it could consist of have not been directly detected so far. Instead, its presence can be traced through its gravitational interaction with luminous matter or through gravitational lensing. The latter denotes a systematic distortion and deflection of light

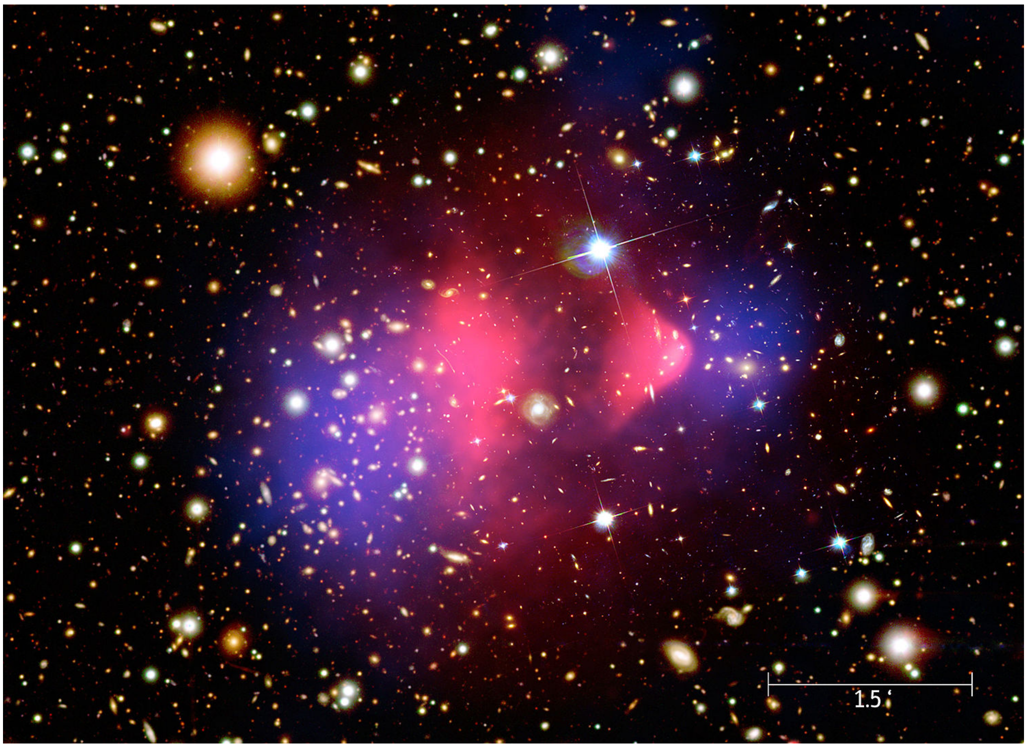

Figure 1.1 – This is a composite image of the 'Bullet' cluster 1E 0657 − 56. The optical image from Magellan and *HST* shows the galaxies (in the cluster and in the fore and background). The X-ray emission of the hot cluster gas was observed with the *Chandra* X-ray Observatory and is shown in pink. This component represents the majority of the baryonic matter. The total mass dominated by dark matter is shown in blue. Its distribution is reconstructed from gravitational lensing. The clear separation of dark and baryonic matter provides evidence for the existence of dark matter. Credit: X-ray: NASA/CXC/CfA/M.Markevitch et al.; Optical: NASA/STScI; Magellan/U.Arizona/D.Clowe et al.; Lensing Map: NASA/STScI; ESO WFI; Magellan/U.Arizona/D.Clowe et al.

bundles from distant sources when they travel through the gravitational potential of a foreground mass distribution. Clowe et al. (2006) presented the first proof of the existence of dark matter in a combined optical and X-ray analysis of the merging galaxy cluster system known as the 'Bullet' cluster. In the merger process, the dark matter mapped through gravitational lensing was separated from the bulk of the baryonic matter, which primarily consists of hot gas visible through its X-ray emission (see Figure 1.1). These observations provided strong evidence for the existence of dark matter. This component has dominated the energy budget of the Universe for the majority of its evolution and therefore considerably shaped the Universe as we observe it today.

At present times the energy budget is, however, dominated by the elusive dark energy. The first evidence for its existence was found independently by two research groups led by Riess et al. (1998) and Perlmutter et al. (1999). Their studies of the distance-redshift relation of Type Ia supernovae lead them to the insight that the Universe is expanding at an accelerated rate. Since then, many more complementary probes have been used to constrain and study the evolution of dark energy. These probes are baryonic acoustic oscillations (BAO), the CMB, weak gravitational lensing surveys, and galaxy cluster surveys.

Galaxy clusters are particularly interesting objects for cosmological studies because they are the most massive gravitationally bound structures in the Universe. As such, they represent the peaks in the large-scale matter distribution of the Universe. The number density of these massive objects as a function of mass and redshift can be predicted from theory or numerical simulations (e.g. Press & Schechter, 1974; Tinker et al., 2008). A comparison to the observed cluster number density is a powerful tool to constrain the structure formation and expansion history of the Universe. The multi-wavelength nature of galaxy clusters is an advantage because it enables complementary detection techniques. George Ogden Abell compiled the first cluster catalogue in 1958 from the National Geographic Society Palomar Observatory Sky Survey, identifying overdensities of galaxies with photographic plates. Since then, the cluster community has come a long way, not least due to the invention of the much more efficient CCD camera. More recent optical cluster surveys contain of the order of several 10,000 detected clusters (e.g. Gladders & Yee, 2005; Koester et al., 2007; Rykoff et al., 2016). In the 1990s, the ROSAT All-Sky Survey (Voges et al., 1999) was a breakthrough for the detection of clusters through their X-ray emission, providing X-ray flux-limited samples of galaxy clusters. Additionally, the detection of clusters through their Sunyaev Zeldovich (SZ) effect signal caused by inverse Compton scattering of CMB photons with free electrons in their hot intracluster medium has proven to be very valuable to generate nearly mass-limited cluster samples. This is possible because the signal is nearly redshift-independent. The most important SZ-detected cluster catalogues were obtained with the South Pole Telescope (Bleem et al., 2015, 2020), the *Planck* satellite (Planck Collaboration et al., 2016c), and the Atacama Cosmology Telescope (Hilton et al., 2021). In the future, the *Euclid*[1] satellite and the extended Roentgen Survey with an Imaging Telescope Array (eROSITA[2]) will provide even larger cluster samples aiming to understand dark matter and dark energy.

To obtain cosmological constraints, the observed number density of clusters must be tied to the theoretical predictions. For this, two prerequisites are critically needed: On the one hand, a thorough understanding of the selection function of the cluster sample and, on the other hand, a precise and accurate calibration of the relation between the observable and the underlying cluster mass over a wide redshift and mass range. Here, the observable serves both to detect the clusters and as a proxy for the cluster mass.

---

[1] `https://www.euclid-ec.org/`

[2] `https://www.mpe.mpg.de/eROSITA`

The selection function of a cluster sample is characterised by its completeness and purity. The former represents the probability that a cluster of a given mass and redshift is detected through the survey observable. The latter quantifies how many of the detections correspond to real clusters as opposed to noise-induced detections. My first thesis project contributes to the joint effort to understand the selection function of the second *Planck* catalogue of Sunyaev Zel'dovich sources (PSZ2, Planck Collaboration et al., 2016c). We exploit the multi-wavelength nature of galaxy clusters when we follow up a sample of 32 SZ-detected clusters with optical data from the William Herschel Telescope (WHT) to confirm the detections. We focus on the high redshift regime of cluster candidates with $z \gtrsim 0.7$ and the low signal-to-noise regime with $3.0 \lesssim \mathrm{S/N} \lesssim 6.0$, where a confirmation through external follow-up is especially needed due to decreasing reliability of detections at lower S/N.

My second thesis project is concerned with the calibration of observable-mass scaling relations. Constraining them in the high-redshift regime is particularly important because cluster properties evolve with time, which can cause a change of the observable-mass scaling relation. Mass measurements from weak gravitational lensing are a very useful method to obtain an absolute calibration of the normalisation of these scaling relations (e.g. Okabe et al., 2010b; Kettula et al., 2015; Dietrich et al., 2019; Schrabback et al., 2021). This method provides the most direct route to obtain this calibration because it directly probes the gravitational potential without any previous assumptions, for example, about the dynamical state of the cluster. Previous studies have constrained the mass calibration only up to $z \sim 1$ for SZ-selected clusters Schrabback et al. (2018, 2021). For my second thesis project, we obtained weak lensing mass constraints based on *Hubble Space Telescope* (*HST*) Advanced Camera for Surveys (ACS), Wide Field Camera 3 (WFC3), and Very Large Telescope (VLT) FORS2 data for nine massive, distant (SZ detection significances $\xi > 6$, redshifts $z \gtrsim 1.0$) clusters from the $2500\,\mathrm{deg}^2$ South Pole Telescope Sunyaev Zel'dovich (SPT-SZ) Survey (Bleem et al., 2015). The primary goal is to provide constraints on the redshift evolution of the SZ-mass scaling relation for clusters from the SPT-SZ survey.

This thesis is structured as follows: Chapter 2 provides an introduction into the cosmological framework. This includes basics about the expansion of the Universe, its thermal history, and the formation of structures. Chapter 3 describes several aspects relevant to the study of galaxy clusters. It summarises the different components and physical mechanisms giving rise to emission from clusters over the entire electromagnetic spectrum. A particular focus lies on the Sunyaev Zel'dovich effect. Additionally, the relevance of clusters in the context of cosmological studies is described. Chapter 4 gives an introduction to the gravitational lensing effect and elaborates in particular on weak gravitational lensing and how it can be used to measure cluster masses. Chapter 5 summarises important tools and techniques for optical observations. I present my first thesis project concerned with an optical follow-up study of a sample of *Planck* cluster candidates in Chapter 6. Subsequently, Chapter 7 is about my second thesis project, namely the *HST* weak lensing study of nine galaxy clusters at $z \gtrsim 1.0$ with strong SZ-signal in the South Pole Telescope Sunyaev-Zel'dovich Survey. Finally, I summarise and conclude in Chapter 8.

CHAPTER 2

Basic concepts in modern cosmology

Cosmology is the science about understanding the Universe as a whole. It asks about how the Universe originated, how structures formed, and how it has and will evolve. Cosmologists try to answer these questions using the known laws of physics in the framework of a cosmological model requiring that it consistently describes observations from the earliest of times to the local Universe and hence recent times. One of the most important observations guiding the onset and advancement of cosmology is the expansion of the Universe as first detected by Vesto Slipher (1917) and also studied by Edwin Hubble (1929) who deducted this from the fact that galaxies are receding from us as the observer in the Milky Way. Secondly, observations, for instance, of the cosmic microwave background (CMB) radiation or the distribution of galaxies in the sky indicate that there are no structures on very large scales, which suggests isotropy of the Universe. Paired with the assumption that we do not occupy a special position in the Universe, homogeneity can be inferred. This cornerstone of cosmology is summarised as the cosmological principle stating that the Universe is homogenous and isotropic on large scales.

Over the past decades, theoretical, numerical, and observational efforts have led to the current standard model of cosmology called ΛCDM model, where Λ is the so-called cosmological constant and CDM stands for cold dark matter, referring to the dynamical property of the majority of matter. This model is able to explain the key features throughout different epochs of the Universe with only six independent parameters. These are the Hubble constant H_0, the baryon density Ω_b, the matter density Ω_m, the optical depth to reionisation τ, the amplitude of the power-spectrum σ_8, and the spectral index of the linear power-spectrum n_s. Further related parameters include the sum of neutrino masses, the age of the Universe, and the redshifts of reionisation, matter-radiation equality, or recombination. All of them are relevant to the history of the Universe, its expansion or the formation of structures in it.

In the following sections, I will outline the most important concepts regarding the expansion of the Universe, its thermal history, and the process of structure formation. A thorough introduction is presented, e.g., in Peacock (1999), Dodelson (2003), Schneider (2015) and Tanabashi et al. (2018) [Section 'Astrophysics and Cosmology'].

2.1 The expansion of the Universe

Edwin Hubble discovered that the redshift of galaxies linearly increases with their distance (Hubble, 1929). He inferred that galaxies further away from us are receding with an increased velocity, a finding summarised as the Hubble law

$$cz \approx v = H_0 D \,, \tag{2.1}$$

where H_0 is the local Hubble constant, D is the distance to the galaxy, z is the redshift, and c is the speed of light. The local Hubble constant is often parametrised as $H_0 = 100\,h\,\mathrm{km\,s^{-1}\,Mpc^{-1}}$ with $h \approx 0.7$. Very recently, Planck Collaboration et al. (2020b) obtained $H_0 = 67.66 \pm 0.42\,\mathrm{km\,s^{-1}\,Mpc^{-1}}$ when assuming the ΛCDM model. The definition of the redshift z based on the observed (λ_{obs}) and the emitted wavelength (λ_{em}) reads

$$z = \frac{\lambda_{\mathrm{obs}} - \lambda_{\mathrm{em}}}{\lambda_{\mathrm{em}}} \,. \tag{2.2}$$

The important consequence of the Hubble law is that it implies an expansion of the Universe. The (radial) expansion can conveniently be expressed with the help of the cosmic scale factor $a(t)$ relating the physical coordinate $\boldsymbol{r}$ to the comoving coordinate $\boldsymbol{x}$ via

$$\boldsymbol{r}(t) = a(t)\boldsymbol{x} \,. \tag{2.3}$$

The cosmic scale factor is normalised to today at time t_0 with $a(t = t_0) = 1$. From this, the expansion rate follows as

$$H(t) = \frac{\dot{a}(t)}{a(t)} \quad \text{and} \quad H(t = t_0) = \frac{\dot{a}(t = t_0)}{a(t = t_0)} \equiv H_0 \,. \tag{2.4}$$

Additionally, the cosmic scale factor is related to the redshift via

$$a = \frac{1}{1 + z} \,. \tag{2.5}$$

Metrics connect coordinate distances to physical distances and determine the geodesics, which correspond to the free paths followed by test particles and light-rays when no force acts upon them. Since the Universe is neutral on average, the only force acting on large scales is gravity. It governs the expansion of the Universe and can be incorporated into a metric. Then, instead of describing gravity as a force, we can think of particles moving freely in a distorted space-time defined by the metric. In particular, the metric for a homogeneous and isotropic world model in the framework of General Relativity (GR) is given by the Robertson-Walker metric (Robertson, 1935; Walker, 1937)

$$\mathrm{d}s^2 = c^2\mathrm{d}t^2 - a^2(t)[\mathrm{d}\chi^2 + f_K^2(\chi)(\mathrm{d}\theta^2 + \sin^2\theta\mathrm{d}\varphi^2)]\,. \tag{2.6}$$

It includes the cosmic time t, the speed of light c in vacuum, the radial comoving distance χ, and the angular coordinates on a unit sphere θ and φ. The transverse comoving distance is defined as

$$f_K(\chi) = \begin{cases} K^{-1/2}\sin[K^{1/2}\chi] & \text{for} \quad K > 0 \\ \chi & \text{for} \quad K = 0 \\ (-K)^{-1/2}\sinh[(-K)^{1/2}\chi] & \text{for} \quad K < 0\,, \end{cases} \tag{2.7}$$

where K is the curvature parameter. In GR, Einstein's field equation

$$G_{\mu\nu} \equiv R_{\mu\nu} - \frac{1}{2}g_{\mu\nu}\mathcal{R} - \Lambda g_{\mu\nu} = -\frac{8\pi G}{c^4}T_{\mu\nu} - \Lambda g_{\mu\nu} \tag{2.8}$$

connects the geometry of the four dimensional space-time to the matter and energy content of the Universe. The tensor $G_{\mu\nu}$ is the Einstein tensor and G is the gravitational constant. On one side of the equation, the Ricci tensor $R_{\mu\nu}$ depends on the metric $g_{\mu\nu}$ and its derivatives. The Ricci scalar is the contraction of the Ricci tensor ($\mathcal{R} \equiv g^{\mu\nu}R_{\mu\nu}$). On the other side, $T_{\mu\nu}$ is the energy-momentum tensor, which holds information on the density $\rho(t)$ and pressure $p(t)$ of the constituents of the Universe. Inserting the Robertson-Walker metric into Einstein's field equation leads to the first and second Friedmann equations:

$$\left(\frac{\dot{a}}{a}\right)^2 = \frac{8\pi G}{3}\rho - \frac{Kc^2}{a^2} + \frac{\Lambda}{3}\,, \tag{2.9}$$

$$\frac{\ddot{a}}{a} = -\frac{4\pi G}{3}\left(\rho + \frac{3p}{c^2}\right) + \frac{\Lambda}{3}\,. \tag{2.10}$$

The first Friedmann equation is derived from the law of energy conservation. It essentially describes the evolution of the cosmic scale factor. The second Friedmann equation can be understood as an equation of motion of the cosmic scale factor and can be derived from the first equation in combination with the adiabatic equation

$$\mathrm{d}(\rho c^2 a^3) = -p\mathrm{d}(a^3) \quad \text{or} \quad \dot{\rho}c^2 + 3\frac{\dot{a}}{a}(\rho c^2 + p) = 0\,. \tag{2.11}$$

World models obeying the Robertson-Walker metric and with a scale factor following Equations (2.9) and (2.11) are called Friedmann-Lemaître models. From these equations it is obvious that the pressure and density of the constituents of the Universe play an important role for its geometry and the dynamics of its expansion. The equation of state (EOS)

$$p = wc^2\rho\,, \tag{2.12}$$

with the dimensionless EOS parameter w, provides further information on the relation between pressure and density. In principle, all components in the equation can be time-dependent. Inserting the EOS into the adiabatic equation (2.11) leads to the differential equation

$$\frac{\dot{\rho}}{\rho} = -3\frac{\dot{a}}{a}(1+w)\,. \tag{2.13}$$

A general solution (assuming no time-dependency of the EOS parameter) is

$$\rho = \rho_0 a^{-3(1+w)}\,. \tag{2.14}$$

The value of the EOS parameter w takes different values depending on the component considered. Cosmologists commonly distinguish between pressureless matter ($w = 0$), radiation ($w = 1/3$) and vacuum energy ($w = -1$, assumed in the ΛCDM model). Consequently, the respective densities are given by

$$\begin{aligned} \text{matter}: \quad & \rho_\mathrm{m}(t) = \rho_{\mathrm{m},0}\, a^{-3}(t)\,, \\ \text{radiation}: \quad & \rho_\mathrm{r}(t) = \rho_{\mathrm{r},0}\, a^{-4}(t)\,, \\ \text{vacuum energy}: \quad & \rho_\Lambda(t) = \rho_{\Lambda,0} = \mathit{const.} \end{aligned} \tag{2.15}$$

Here, the constants of proportionality $\rho_{\mathrm{m},0}$, $\rho_{\mathrm{r},0}$, and $\rho_{\Lambda,0}$ are chosen such that they correspond to the values of today at $t = t_0$. The total density is given as a sum of the components $\rho_\mathrm{tot} = \rho_\mathrm{m} + \rho_\mathrm{r} + \rho_\Lambda$. The average total density required for a flat geometry of the universe (with curvature parameter $K = 0$) is

$$\rho_\mathrm{cr}(t) = \frac{3H^2(t)}{8\pi G} \quad \text{and} \quad \rho_\mathrm{cr}(t = t_0) = \frac{3H_0^2}{8\pi G} \equiv \rho_{\mathrm{cr},0} \tag{2.16}$$

with $\rho_{\mathrm{cr},0} \approx 1.88 \times 10^{-29}\, h^2\,\mathrm{g/cm}^3$ (Schneider, 2015). This allows us to introduce the dimensionless density parameters

$$\Omega_{\mathrm{m},0} = \frac{\rho_{\mathrm{m},0}}{\rho_{\mathrm{cr},0}}\,, \quad \Omega_{\mathrm{r},0} = \frac{\rho_{\mathrm{r},0}}{\rho_{\mathrm{cr},0}}\,, \quad \Omega_{\Lambda,0} = \frac{\rho_{\Lambda,0}}{\rho_{\mathrm{cr},0}}\,, \quad \text{and} \quad \Omega_0 = \sum_i \Omega_{\mathrm{i},0}\,. \tag{2.17}$$

Figure 2.1 shows the contributions from these components as a function of the cosmic scale factor. It illustrates which components dominate at different epochs. The first Friedmann equation (2.9) can then be expressed as

$$H^2(a) = \left(\frac{\dot{a}}{a}\right)^2 = H_0^2\left[\frac{\Omega_{\mathrm{m},0}}{a^3} + \frac{\Omega_{\mathrm{r},0}}{a^4} + \Omega_{\Lambda,0} + \frac{(1-\Omega_0)}{a^2}\right]. \tag{2.18}$$

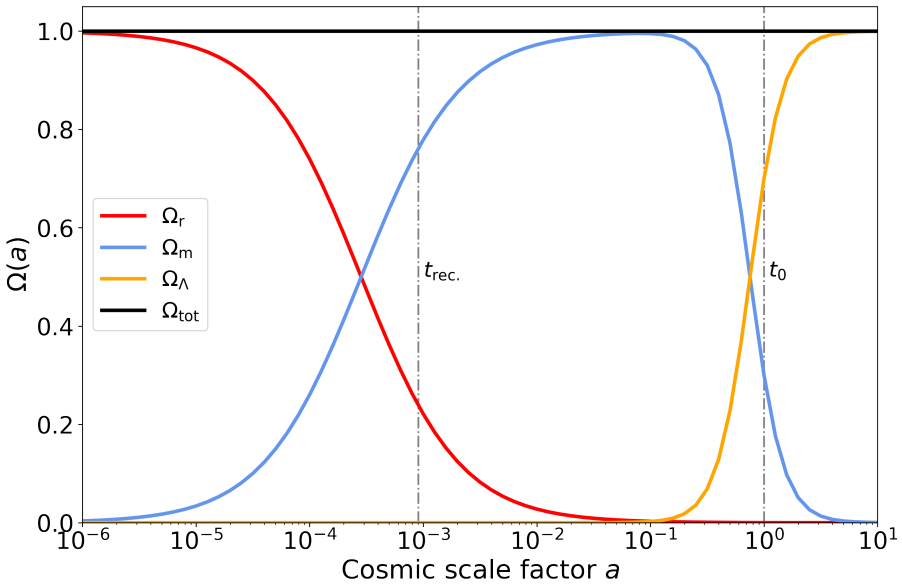

Figure 2.1 – The evolution of the density parameters as a function of the cosmic scale factor is displayed for a flat ΛCDM Universe with $h = 0.7$ and $\Omega_{\mathrm{m},0} = 0.3^{\dagger}$. At early times, the Universe was dominated by radiation. A phase of matter domination followed. After this, dark energy took over, which still is the dominant component today. The dash-dotted lines indicate the time of recombination at $z \approx 1100$ and today at redshift $z = 0$.
† I made use of the python package `astropy.cosmology` (Astropy Collaboration et al., 2018) for the computation of the displayed curves.

This representation of the equation directly shows how the expansion depends on the energy densities of pressureless matter, radiation, and vacuum energy. Additionally, the geometry of the Universe as characterised by the curvature parameter $K = (\Omega_0 - 1)H_0^2/c^2$, which directly depends on them. Sometimes the expansion is notated in terms of the cosmic evolution function $E(z)$ as $H(z) = H_0\,E(z)$ with

$$E(z) = \left(\Omega_{\mathrm{m},0}(1+z)^3 + \Omega_{\mathrm{r},0}(1+z)^4 + \Omega_{\Lambda,0} + (1-\Omega_0)(1+z)^2\right)^{1/2} . \tag{2.19}$$

From Equation (2.18) and the latest constraints of the density parameters it is inferred that for $t \to 0$ follows $a \to 0$. From this, one infers that the Universe has always expanded and that it must have been extremely small and dense in the past. In fact, $a = 0$ corresponds to a singularity where matter and radiation densities diverge. The evolution of the Universe from this state is called the Big Bang. The age of the Universe as a function of the cosmic scale factor can then be defined as

$$t(a) = \int_0^a \frac{\mathrm{d}a'}{a' H(a')} . \tag{2.20}$$

Our current best estimate for the age of the Universe today at $a = 1$ is 13.787 ± 0.020 billion years (Planck Collaboration et al., 2020b).

2.1.1 Constituents of the Universe

Baryonic matter

Baryonic matter consists of protons, neutrons, and electrons[1] and makes up the luminous matter in the Universe, which is detectable through electromagnetic radiation. The baryon density Ω_b can be measured from the deuterium abundance in the Ly-α forest or from CMB temperature fluctuations. These methods reveal that baryonic matter makes up around five per cent of the energy content of the Universe ($\Omega_{\mathrm{b},0} = 0.0489 \pm 0.0003$ according to Planck Collaboration et al., 2020b). Around 10 per cent of the baryonic matter are found in stars and galaxies (Fukugita & Peebles, 2004) and 50 to 60 per cent are distributed in the so-called circum-galactic medium (Shull et al., 2012). The missing 30 to 40 per cent were postulated to be part of the so-called warm-hot intergalactic medium, but until recently, this could not be confirmed. However, Nicastro et al. (2018) and Tanimura et al. (2019) detected warm-hot gas filaments through X-ray and Sunyaev Zel'dovich observations, which are consistent with predictions from theory and simulations. These observations could be the key to solving the 'missing baryon problem' (Fukugita et al., 1998; Shull et al., 2012).

Dark matter

Investigations of the power spectra with redshift surveys of galaxies, of the anisotropies of the CMB temperature, and of the baryon fraction in galaxy clusters (assumed to be representative of the cosmic mean) show that the baryon fraction in the Universe $\Omega_{\mathrm{b},0}/\Omega_{\mathrm{m},0}$ is of the order of $\Omega_{\mathrm{b},0}/\Omega_{\mathrm{m},0} \approx 0.15$ (e.g. Schellenberger & Reiprich, 2017; Planck Collaboration et al., 2020b). Consequently, baryonic matter cannot fully account for the total matter density in the universe ($\Omega_{\mathrm{m},0} = 0.3111 \pm 0.0056$ according to Planck Collaboration et al., 2020b). These findings strongly suggest that dark matter contributes the rest. As of now, its exact nature is still unknown. Macroscopic candidates like the suggested MACHOs (Massive Compact Halo Objects, e.g., primordial black holes or brown dwarfs) as the primary dark matter component could be excluded from microlensing experiments (Alcock et al., 2000; Tisserand et al., 2007; Niikura et al., 2019). Since dark matter substantially outnumbers baryonic matter, it is reasonable to assume that it mainly consists of a (as of yet unknown) particle. Weakly interacting massive particles (WIMPs) have been postulated to be a potential main constituent of dark matter. To explain cosmological observations, they need to be dynamically cold and electrically neutral particles with an energy of the order of 100 GeV to 10 TeV. The former property allows for a bottom-up formation of structures as observed in our Universe.

---

[1] Cosmologists include electrons into their nomenclature of baryonic matter, even though electrons are in fact leptons.

Currently, several experiments aim to detect WIMPs directly through their collisions with regular atoms (e.g. Aprile et al., 2017; Armengaud et al., 2019). However, a direct detection is very challenging due to the small expected cross-section of such a weakly interacting particle. So far, the ongoing experiments can only exclude certain regions in the parameter space of cross-section and mass of the WIMPs. Schumann (2019) gives an extensive review about direct detection experiments.

Another path to investigate the WIMP postulation is their indirect detection. Assuming that WIMPs are their own anti-particles, their self-annihilation should produce high-energy photons, which could in principle be detected especially towards the highest dark matter concentrations at the centres of galaxies and galaxy clusters (e.g. Jeltema et al., 2009; Bringmann & Weniger, 2012; Funk, 2015).

Radiation

Particles with zero rest mass (i.e., photons) and all relativistic, massive particles contribute to the radiation energy density of the Universe. As the Universe cools, more and more relativistic, massive particles become non-relativistic. Since the radiation energy density decreases rapidly with cosmic scale factor a following $\rho_\mathrm{r} \propto a^{-4}$, it is negligible in the current epoch with $\Omega_{\mathrm{r},0} \approx 10^{-5} - 10^{-4}$ (Planck Collaboration et al., 2020b). The majority of the radiation energy density consists of CMB photons, which follow a blackbody spectrum with a measured temperature of $T_0 = 2.7255\,\mathrm{K}$ today (Fixsen, 2009). The second important contributor to the energy density are relativistic neutrinos.

Neutrinos

According to the standard model of particle physics, neutrinos are massless particles. Hence, they would contribute to the radiation energy density of the Universe. However, flavour oscillation experiments have shown that neutrinos have a non-zero mass, where each neutrino flavour or family has a different mass (Ahmad et al., 2001; Fukuda et al., 1998). The standard model of cosmology predicts a neutrino background at a slightly lower black-body temperature $T_{\nu,0} = 1.9\,\mathrm{K}$ than the CMB (also see Section 2.2). As the Universe expands and cools, neutrino families may become non-relativistic. While they are part of the radiation content at relativistic velocities, neutrinos contribute to the dark matter content in the form of hot dark matter (HDM) at non-relativistic speeds. Since this implies that they still move at very high velocities, they are able to escape gravitational potential wells of matter overdensities, an effect called free-streaming. This property of neutrinos affects gravitational clustering and the growth of structure (J. Lesgourgues and L. Verde, 'Neutrinos in Cosmology' review in Tanabashi et al., 2018). Therefore, the number of neutrino families and their total mass can be constrained from observations of the CMB anisotropies and the matter power spectrum (Lesgourgues & Pastor, 2006). Recently, Planck Collaboration et al. (2020b) constrained the number of neutrino families to $N_{\text{eff}} = 2.99 \pm 0.17$ and their total mass to $\sum m_\nu < 0.12\,\text{eV}$ under the assumption of the ΛCDM model. Particle physicists also obtain tight, model-independent constraints for instance from measurements of the kinematics of electrons from beta-decay of tritium (^{3}H). Aker et al. (KATRIN, 2019) find an effective neutrino mass square value of $(-1.0^{+0.9}_{-1.1})\,\text{eV}^2$. At least two of the neutrino families are non-relativistic in the current epoch, which can be concluded from a comparison of the neutrino temperature today and the lower bound for the sum of neutrino masses at $\sum m_\nu > 0.06\,\text{eV}$ inferred from neutrino oscillation experiments (J. Lesgourgues and L. Verde, 'Neutrinos in Cosmology' review in Tanabashi et al., 2018). Excellent further reviews on neutrino cosmology are provided, for example, by Lesgourgues & Pastor (2006) and Gerbino & Lattanzi (2018).

Dark Energy

In the 1990s, two research groups by Riess et al. (1998) and Perlmutter et al. (1999) studied the expansion history of the Universe using the distance-redshift relation of type Ia supernovae. They independently found that the Universe is expanding at an accelerated rate. Dark energy, the dominant constituent of the energy budget of the Universe today with $\Omega_\Lambda = 0.6889 \pm 0.0056$ (Planck Collaboration et al., 2020b), has been introduced as a possible explanation for the accelerated expansion. Considering the second Friedmann equation reveals that an accelerated expansion with $\ddot{a} > 0$ can only be achieved when there is a component with negative pressure, i.e., its EOS parameter fulfils $w < -1/3$. In the context of the current standard ΛCDM model of cosmology, the EOS parameter of dark energy is $w = -1.0$, corresponding to an energy density ρ_Λ, which is constant in time. In this case, dark energy can be identified as the positive cosmological constant Λ from the Friedmann equations. Consequently, its dimensionless density today would be given by $\Omega_{\Lambda,0} = \Lambda c^2/3H_0^2$. In fact, the EOS state parameter of dark energy is not precisely known, but measurements from independent probes covering a wide range in redshift agree remarkably well and are consistent with a constant energy density (see Figure 2.2). However, investigating a possible time-dependent evolution is the main science driver for upcoming so-called Stage IV experiments like the Legacy Survey of Space and Time (LSST) performed by the Vera C. Rubin Observatory (LSST Science Collaboration et al., 2009), *Euclid* (Laureijs et al., 2011), or the *Nancy Grace Roman Space Telescope* (formerly known as WFIRST, Spergel et al., 2015). In that case, the EOS parameter is typically parametrised as

$$w(a) = w_0 + w_a(1 - a)\,, \tag{2.21}$$

where $w_0 = -1$ and $w_a = 0$ correspond to the case of a constant energy density. To date, the exact nature of dark energy remains one of the biggest unsolved questions in physics. Huterer & Shafer (2018) review recent knowledge about dark energy.

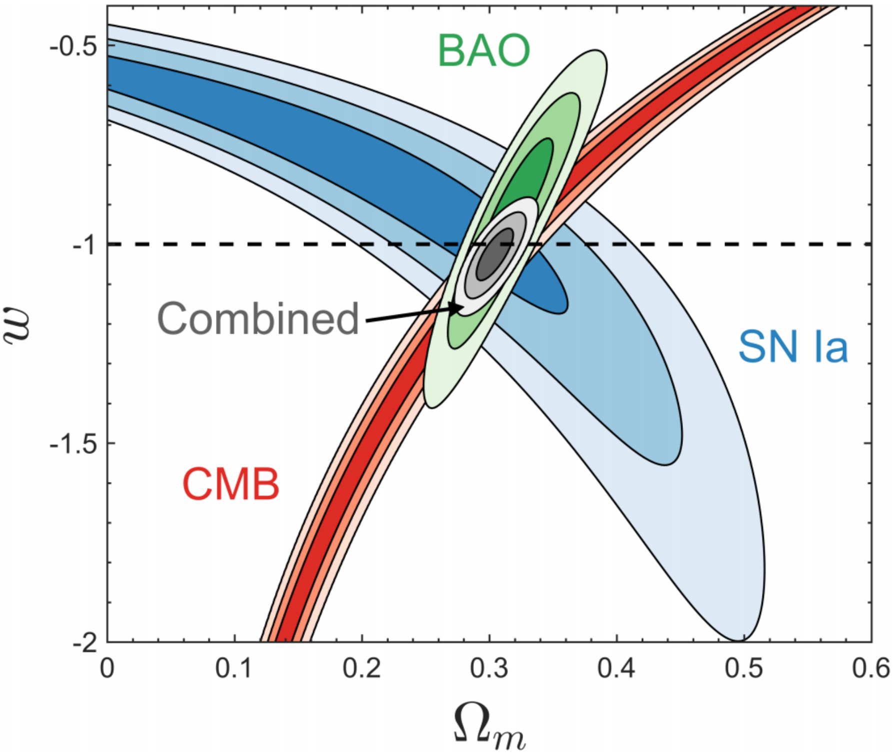

Figure 2.2 – This figure from Huterer & Shafer (2018) shows constraints on the EOS parameter for dark energy w and the matter density Ω_{m} under the assumption of a flat universe. Observational constraints from three probes are displayed with CMB measurements in red (Planck Collaboration et al., 2016a), baryonic acoustic oscillation (BAO) measurements in green (Alam et al., 2017), and SN Ia measurements in blue (Betoule et al., 2014). The contours indicate 68.3%, 95.4%, and 99.7% of the likelihood.

2.1.2 Distances in the expanding Universe

In a flat and non-expanding space, or Euclidean space, a uniquely defined distance between two points exists. From an observer's point of view, it is intuitive to derive distance measures based on observational information such as the flux in relation to the intrinsic luminosity or the angular extent on the sky in relation to the physical size of a source. Depending on the geometry of the space-time, different distance measures differ from each other. Of course, distances are also not generally constant in time in an expanding (or contracting) universe. Hogg (1999) gives a very instructive introduction to different distance measures in cosmology. All commonly used distance measures are related to the line-of-sight or radial comoving distance

$$\chi(z) = D_{\mathrm{H}} \int_0^z \frac{\mathrm{d}z'}{E(z')} , \tag{2.22}$$

where $D_{\mathrm{H}} = c/H_0$ is the Hubble radius.

The angular diameter distance is defined as

$$D_{\mathrm{A}} = \frac{d}{\theta} = \frac{f_K(\chi)}{1+z} = a f_K(\chi)\,. \tag{2.23}$$

It is based on the ratio of the intrinsic diameter d of a distant object and the angle θ it subtends on the sky. It can also be expressed in terms of the transverse comoving distance $f_K(\chi)$ as introduced in Equation (2.7). The angular diameter distance is not a monotonously increasing function of redshift, but instead exhibits a maximum at redshift $z \approx 1.7$ (for a flat Universe with $h = 0.7$ and $\Omega_{\mathrm{m},0} = 0.3$, see Figure 2.3). It also has to be noted that angular diameter distances are not generally additive, i.e., $D(z_1, z_2) = a(z_2) f_K(\chi(z_1, z_2)) \neq D(z_2) - D(z_1)$.

The luminosity distance to a source with flux S and intrinsic luminosity L is given by

$$D_{\mathrm{L}} = \sqrt{\frac{L}{4\pi S}} = (1+z) f_K(\chi) = (1+z)^2 D_{\mathrm{A}}\,. \tag{2.24}$$

Only if space is static, the introduced distance measures take the same value. The difference between luminosity and angular diameter distance leads to the cosmological surface brightness dimming of the observed surface brightness I_{obs} in comparison to the emitted surface brightness I_{emit} because the solid angle $\mathrm{d}\Omega$ covered by an object is given by $\mathrm{d}\Omega \propto D_{\mathrm{A}}^{-2}$. Consequently, we find

$$I_{\mathrm{obs}} = \frac{I_{\mathrm{emit}}}{(1+z)^4}\,. \tag{2.25}$$

2.2 Thermal history

As the Universe expands, the temperature of the CMB blackbody spectrum changes according to

$$T(a) = T_0/a\,. \tag{2.26}$$

Here, $T_0 = 2.7255\,\mathrm{K}$ is the temperature of the CMB measured today. According to Big Bang theory, the Universe originates from a singularity at $a \to 0$. Following Equation (2.26), the Universe must have been extremely hot and dense then. Physics at such high temperatures or equivalently at such high energies as immediately after the Big Bang is poorly understood. Most likely, the four fundamental forces we know in physics, i.e., gravitation, electromagnetism, weak nuclear force, and strong nuclear force, were combined in a single fundamental force during an era called the Planck epoch. It was followed by an epoch, where gravitation decoupled from the single fundamental force due to a phase transition as the Universe cooled. The Grand Unification Theory describes the remaining electrostrong force. Subsequently, a period of rapid exponential expansion called inflation followed, which was dominated by a vacuum energy density much higher than today.

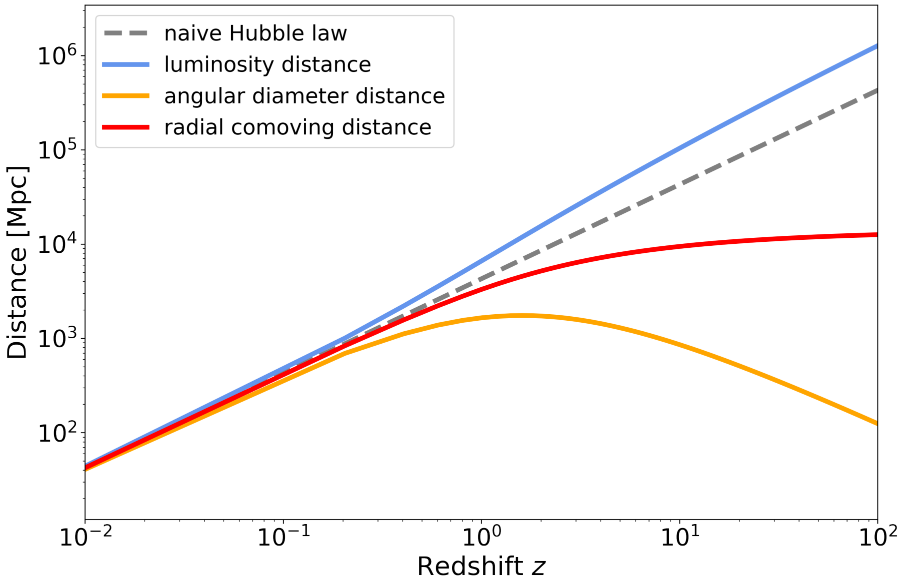

Figure 2.3 – Different cosmological distance measures are illustrated as a function of redshift employing a flat ΛCDM cosmology with $h = 0.7$ and $\Omega_{\mathrm{m},0} = 0.3$ [†]. The naive Hubble law is computed according to Equation (2.1). At small redshifts all distance measures agree. For example they differ by about 1 per cent at redshift $z = 0.005$. At large redshifts the luminosity distance diverges, the radial comoving distance converges towards the size of the observable Universe, and the angular diameter distance decreases after reaching the maximum at $z \approx 1.7$. [†] I made use of the python package `astropy.cosmology` (Astropy Collaboration et al., 2018) for the computation of the displayed curves.

When the Universe reaches energies of $\lesssim 100\,\mathrm{GeV}$, we enter into a regime of physics, which is fairly well-understood. At this point, the Universe is in the radiation-dominated era. It is populated by relativistic particles such as electrons, positrons, photons, and neutrinos, and their respective anti-particles. Additionally, there are non-relativistic particles such as protons and neutrons. Whenever the energy exceeds the rest mass of a particle species, particle - anti-particle pairs are either created or annihilated thereby creating a pair of photons. Particles are held in equilibrium with each other through various reactions, for instance Compton scattering, pair creation and annihilation, neutrino - anti-neutrino scattering or neutrino - electron scattering:

$$\begin{aligned} e^{\pm} + \gamma &\leftrightarrow e^{\pm} + \gamma\,, \\ e^{+} + e^{-} &\leftrightarrow \gamma + \gamma\,, \\ \nu + \bar{\nu} &\leftrightarrow e^{+} + e^{-}\,, \\ \nu + e^{\pm} &\leftrightarrow \nu + e^{\pm}\,. \end{aligned} \tag{2.27}$$

Relevant processes for involving nucleons are

$$n + \nu \leftrightarrow p + e^{-} \quad \text{and} \quad p + \bar{\nu} \leftrightarrow n + e^{+}\,. \tag{2.28}$$

As the Universe expands, the number density of particles decreases. Therefore, the reactions need to happen at a faster reaction rate than the expansion and cooling of the Universe to maintain equilibrium. Around one second after the Big Bang at $T \leq 10^{10}\,\mathrm{K}$ the reaction rates for neutrinos do not fulfil this condition anymore. Hence they decouple or 'freeze out'. From this moment on they propagate freely maintaining their thermal distribution at a decreasing temperature of $T_\nu = T_{\nu,0}/a$ with $T_{\nu,0} = 1.9\,\mathrm{K}$.

At temperatures $T \leq 5 \times 10^9\,\mathrm{K}$, the photons are not energetic enough anymore to create electron-position pairs. However, the annihilation of electron-positron pairs continues without hindrance. Consequently, the electron and positron densities decrease rapidly while their energy is added to the photon gas. This increases the temperature of the photons. After the annihilation, the baryon and photon densities n_b and n_γ stay at a constant ratio $\eta = n_\mathrm{b}/n_\gamma = 2.74 \times 10^{-8}(\Omega_\mathrm{b}h^2)$ (Schneider, 2015).

The next important step in the thermal history is a process called Big Bang nucleosynthesis (BBN). Since the reactions for nucleons in Equation (2.28) involve neutrinos, they become increasingly rare after neutrino decoupling. Due to the slightly higher rest mass of the neutron, they can decay into a proton, an electron, and an anti-neutrino. Consequently, more and more neutrons decay and thus the neutron-to-proton ratio $n_\mathrm{n}/n_\mathrm{p}$ decreases. This continues until the temperature has cooled enough ($T \approx 8 \times 10^8\,\mathrm{K}$), so that practically all the neutrons are bound in deuterium nuclei, which in turn are transformed to helium nuclei. Since the latter consist of two protons and two neutrons, there is the same amount of protons and neutrons bound in helium nuclei. The remaining amount of protons form the basis for hydrogen atoms. The mass fraction of helium nuclei with respect to the total mass of baryons is given by

$$Y = \frac{4n_\mathrm{He}}{4n_\mathrm{He} + n_\mathrm{H}} = \frac{2n_\mathrm{n}}{n_\mathrm{n} + n_\mathrm{p}} \approx 0.25\,, \tag{2.29}$$

where n_He and n_H denote the helium and hydrogen number densities, respectively. It is, therefore, expected that around 25 per cent of the baryonic mass should be bound in helium. This is in very good agreement with observations of low metallicity regions, which best represent the primordial conditions. The fraction Y and the residual amount of deuterium are sensitive probes for the baryon density Ω_b, because an increase of the baryon density implies that deuterium can form earlier and, in turn, fewer neutrons would have decayed by then. This would increase $n_\mathrm{n}/n_\mathrm{p}$ and thereby also Y. At the same time, a higher baryon density implies a more efficient transformation from deuterium to helium, which means less deuterium would be left.

At a redshift of $z = z_\mathrm{eq} \approx 23900\,\Omega_\mathrm{m}h^2 \approx 3500$ corresponding to a_eq, matter starts to dominate the expansion of the Universe. After further cooling, nuclei and electrons combine to form atoms. This is referred to as recombination. It competes with the ionisation process, where photons cause electrons to be released from atoms. Only at temperatures $T \leq 3000\,\mathrm{K}$, the majority of photons are not energetic enough anymore to ionise the newly formed atoms. At the redshift of recombination $z \approx 1100$ photons and baryonic matter decouple. After the last scattering, the photons propagate freely, forming the cosmic microwave background (CMB) and following a blackbody spectrum.

Today the Universe is largely ionised again. This is due to the formation of the first generation of stars and galaxies whose radiation ionised the atoms (Wise, 2019). The period between recombination and reionisation is referred to as the dark ages due to the lack of visible light, for example, from stars. The reionisation produces numerous free electrons. CMB photons interact with these electrons via Thomson scattering, which effectively causes an opacity source suppressing the amplitude of the CMB anisotropies (NASA/LAMBDA Archive Team, 2021). At the same time, this scattering also polarises the CMB radiation. The optical depth to reionisation τ quantifies the line-of-sight free-electron opacity to the CMB radiation, where a larger value of τ implies a higher redshift at reionisation. The optical depth can be measured from the polarisation of the CMB. Planck Collaboration et al. (2020b) constrained the optical depth to reionisation to $\tau = 0.0561 \pm 0.0071$ and the redshift of reionisation to $z_{\mathrm{reion}} = 7.82 \pm 0.71$.

2.3 Structure formation

We know that the Universe is isotropic on large scales, i.e., in observations of the CMB or in galaxy redshift surveys covering large areas on the sky such as the 2 degree Field Galaxy Redshift Survey (2dFGRS, Colless et al., 2001) or the extended Baryon Oscillation Spectroscopic Survey (eBOSS, Dawson et al., 2016), we do not find any structures larger than $\sim 200\,h^{-1}\,\mathrm{Mpc}$. However, there are small anisotropies in the CMB of the order of $\Delta T/T \sim 10^{-5}$. These reflect an early epoch of the Universe at $z \approx 1100$. The local Universe is considerably inhomogeneous on smaller scales with a large-scale structure where galaxy clusters represent the densest regions and voids, regions with a strong underdensity of galaxies, the least dense regions. Consequently, the Universe has grown increasingly inhomogeneous. The field of structure formation explains how the large-scale structure in late times has emerged from small density fluctuation at early times. Such small inhomogeneities in the density can be characterised by the density contrast $\delta(\mathbf{x}, t)$ at a given position $\mathbf{x}$ and time t via

$$\delta(\mathbf{x}, t) = \frac{\rho(\mathbf{x}, t) - \bar{\rho}(t)}{\bar{\rho}(t)} \,. \tag{2.30}$$

Hence, the average density $\bar{\rho}(t)$ governs the general expansion of the Universe, while $\Delta\rho = \rho(\mathbf{x}, t) - \bar{\rho}(t)$ contributes an additional small gravitational field. The concept of gravitational instability then states that such density fluctuations $|\delta|$ will grow in time due to self-gravity, i.e., slightly overdense regions will become denser, while slightly underdense regions will become less dense. This concept forms the basis for structure formation.

2.3.1 Linear perturbation theory

When we aim to describe how the density contrast evolves with the expansion, or in other words as a function of the cosmic scale factor, we need to consider the equations of motion of a fluid with velocity $\mathbf{v}$ and pressure p:

$$\text{Continuity equation}: \quad \frac{\partial \rho}{\partial t} + \nabla(\rho \mathbf{v}) = 0\,, \tag{2.31}$$

$$\text{Euler equation}: \quad \frac{\partial \mathbf{v}}{\partial t} + (\mathbf{v}\nabla)\mathbf{v} = -\frac{\nabla p}{\rho} - \nabla\Phi\,, \tag{2.32}$$

$$\text{Poisson equation}: \quad \nabla^2\Phi = 4\pi G\rho - \Lambda\,. \tag{2.33}$$

The gravitational potential is given by Φ. The continuity equation describes the matter conservation of a fluid, and the Euler equation contains momentum conservation. Hence, the latter connects the motion of a particle (left-hand side) to the acceleration by a gravitational potential (right-hand side). Finally, the Poisson equation connecting the density and the gravitational potential is modified with a cosmological constant. Generally, the behaviour of the density contrast depends on a variety of conditions. This includes whether we consider the radiation or matter-dominated era, whether the matter is subject to pressure, and whether the scale of the perturbation is larger or smaller than the horizon scale. This scale can be approximated by the local Hubble radius

$$d_\mathrm{H} = \frac{c}{aH(a)}\,. \tag{2.34}$$

It distinguishes the subhorizon scale and the superhorizon scale. No physical effects like pressure act on the latter, while they are relevant for the former. For every scale λ of a perturbation, there exists a time when $d_\mathrm{H} = \lambda$. From this moment on, the horizon scale becomes larger than the perturbation scale, and hence the perturbation changes from super to subhorizon scale. This moment is denoted by a_enter.

For a simplified treatment, the matter is assumed to behave as a pressureless fluid with $p = 0$. So we consider dark matter here, which is governed by gravity. Additionally, a Newtonian description is applicable for small scales $\lambda \ll d_\mathrm{H}$. Equations (2.31), (2.32), and (2.33) are more conveniently expressed with comoving coordinates $\mathbf{r}(t) = a(t)\mathbf{x}$. As a result, the velocity is rewritten as

$$\mathbf{v}(\mathbf{r}, t) = \frac{\dot{a}}{a}\mathbf{r} + \mathbf{u}\left(\frac{\mathbf{r}}{a}, t\right)\,. \tag{2.35}$$

Here, the first term describes the homogeneous expansion, while the second term corresponds to the peculiar velocity $\mathbf{u}$. The transformed set of equations reads

$$\frac{\partial\delta}{\partial t} + \frac{1}{a}\nabla[(1+\delta)\mathbf{u}] = 0\,, \tag{2.36}$$

$$\frac{\partial\mathbf{u}}{\partial t} + \frac{\mathbf{u}\nabla}{a}\mathbf{u} + \frac{\dot{a}}{a}\mathbf{u} = -\frac{1}{\bar{\rho}a}\nabla p - \frac{1}{a}\nabla\phi\,, \tag{2.37}$$

$$\nabla^2\phi(\mathbf{x},t) = 4\pi G a^2(t)\bar{\rho}(t)\delta(\mathbf{x},t)\,. \tag{2.38}$$

The density is given by $\rho = (1+\delta)\bar{\rho}$, the gravitational potential is $\Phi(\mathbf{x},t) = \phi(\mathbf{x},t) + \ddot{a}a/2\,|\mathbf{x}|^2$. The term $-1/(\bar{\rho}a)\nabla p$ vanishes for $p = 0$. The homogeneous solution to these equations is given by $\delta \equiv 0$, $\mathbf{u} \equiv 0$, $\rho \equiv \bar{\rho}$, and $\phi \equiv 0$. For a small deviation from the homogeneous case, Equations (2.36), (2.37), and (2.38) can be linearised by expanding to the first order in the density contrast δ and peculiar velocity $\mathbf{u}$. Combining the linearised equations leads to the second-order differential equation

$$\ddot{\delta} + 2\frac{\dot{a}}{a}\dot{\delta} - 4\pi G\bar{\rho}\delta = 0\,, \tag{2.39}$$

describing the temporal evolution of the density contrast. Since this equation does not depend on $\mathbf{x}$ or any spatial derivatives, it can be factorised like this:

$$\delta(\mathbf{x},t) = D(t)\tilde{\delta}(\mathbf{x})\,. \tag{2.40}$$

Here, $\tilde{\delta}(\mathbf{x})$ captures the spatial dependence, while $D(t)$ follows

$$\ddot{D} + 2\frac{\dot{a}}{a}\dot{D} - 4\pi G\bar{\rho}D = 0\,. \tag{2.41}$$

Two linearly independent solutions exist, which are typically denoted by $D_+(t)$, a function growing with time, and $D_-(t)$, a decreasing function. $D_+(t)$, also called the growth factor, is the one relevant for structure formation, characterising how structures grow over time. Therefore, structures grow according to

$$\delta(\mathbf{x},t) = D_+(t)\delta_0(\mathbf{x})\,, \tag{2.42}$$

where the growth factor $D_+(t)$ represents the amplitude, which grows over time and whose differential equation can be solved for different cosmologies with a normalisation of $D_+(t=t_0) = 1$. Then, it can be shown that $D_+(a) \approx a$ for $a_{\text{eq}} \ll a \ll 1$, independent of the cosmological parameters. Additionally, $\delta_0(\mathbf{x})$ describes the time-independent spatial distribution of the density fluctuations. It would be the distribution of density fluctuations today if the evolution was indeed linear. However, this approximation breaks down as soon as $|\delta| \approx 1$.

Extensions to the simplified treatment

During the radiation-dominated era ($a < a_{\mathrm{eq}}$), Equation (2.41) still holds for the behaviour of matter perturbations. However, the term $\dot{a}/a$ now follows the expansion for the radiation-dominated phase. According to the first Friedmann equation we find:

$$\left(\frac{\dot{a}}{a}\right)^2 = \frac{8\pi G}{3}(\rho_{\mathrm{m}} + \rho_{\mathrm{r}}) \,. \tag{2.43}$$

The density contrast is then governed by the ratio of matter density and radiation density as follows

$$\delta \propto \frac{\rho_{\mathrm{m}}}{\rho_{\mathrm{r}}} + \frac{2}{3} = \frac{a}{a_{\mathrm{eq}}} + \frac{2}{3} \,. \tag{2.44}$$

Thus, the density contrast remains nearly constant ($\delta \propto$ const.) for $a \ll a_{\mathrm{eq}}$ and transitions to a behaviour proportional to the scale factor ($\delta \propto a$) when matter-domination is approached. This result means that matter density perturbations do not grow in the radiation-dominated era.

As soon as the scales of perturbations are close to or larger than the horizon scale, the Newtonian description is no longer applicable. In principle, a treatment within the framework of GR would be necessary. However, it is instead also possible to infer the evolution of the density contrast as a function of the cosmic scale factor by considering the growth of a homogeneous spherical perturbation, which behaves similarly to the expanding Universe. This works because the density contrast can be factorised into a spatial and a temporal component. Distinguishing properly between the radiation and matter-dominated eras, one finds that the density contrast grows as $\delta \propto a^2$ or $\delta \propto a$, respectively.

Transfer function

Concluding from the previous sections, we find that at first, when matter perturbations are on superhorizon scales in the radiation-dominated phase ($a \ll a_{\mathrm{enter}} < a_{\mathrm{eq}}$), their density contrast grows as $\delta \propto a^2$. If a perturbation of fixed scale gets to the subhorizon scale during the radiation-dominated phase ($a_{\mathrm{enter}} < a < a_{\mathrm{eq}}$), its growth stops as $\delta \propto$ const. Only when the Universe transitions to the matter-dominated phase, this perturbation continues to grow with $\delta \propto a$. If a perturbation gets to the subhorizon scale in the matter-dominated phase ($a > a_{\mathrm{eq}}$), it continues to grow according to $\delta \propto a$. As a consequence, small-scale matter perturbations with $a_{\mathrm{enter}} < a_{\mathrm{eq}}$ are suppressed in comparison to large-scale perturbations. The transfer function $T(k)$ accounts for this scale dependence of the growth. Here, $k = 2\pi/\lambda$ is the wavenumber of a perturbation with scale λ. The transfer function is defined based on the relation between the density contrast δ_{i} at early times, when all perturbations were at superhorizon level, and the density contrast δ_0 extrapolated linearly to today:

$$\frac{\delta_0(k)}{\delta_0(k_\mathrm{s})} = T(k)\frac{\delta_\mathrm{i}(k)}{\delta_\mathrm{i}(k_\mathrm{s})}\,, \tag{2.45}$$

where k_s denotes the wavenumber in Fourier-space of a large-scale perturbation that enters the horizon during the matter-dominated area and therefore never suffered from a stopped growth.

Baryons and radiation

In the previous considerations, the pressure was disregarded. This is a reasonable assumption for pressureless matter such as dark matter and certainly an appropriate approximation to describe the evolution of the density contrast considering that dark matter is about five times more abundant than baryonic matter. However, before recombination, baryons and photons (and neutrinos before their freeze-out) were coupled, forming a single fluid due to the electromagnetic interactions between them by scattering off free electrons. The electrons were in turn coupled to protons and helium nuclei. As a consequence, the pressure was relevant for the baryons, preventing them from falling into potential wells from dark matter. Essentially, gravity and pressure can be understood as two counterparts in this situation. While gravity causes overdense regions to contract, pressure counteracts this contraction. When gravity dominates, density perturbations grow. When pressure dominates, the perturbations oscillate. Thus, the density fluctuations attributed to the baryons only start growing with $\delta \propto a$ after the decoupling of photons and baryons, i.e., when the baryons are not affected by pressure anymore. Note that the considerations in this section apply for perturbations on subhorizon scales.

2.3.2 Correlation function and power spectrum

Correlation functions are a statistical tool, which quantifies the correlation between two random variables. For the context of an isotropic and homogeneous universe, the two-point correlation function

$$\xi(|\mathbf{x} - \mathbf{y}|) = \langle \delta(\mathbf{x})\delta^*(\mathbf{y}) \rangle \tag{2.46}$$

provides an insight on how much the density contrast at two locations ($\mathbf{x}$ and $\mathbf{y}$) in the Universe is correlated. It is, therefore, a tool to characterise the structure of the matter distribution statistically. The * symbol denotes the complex conjugate. Due to homogeneity, the correlation function is only a function of the distance between two points. Isotropy requires that it must be independent of the direction, i.e., the absolute value $|\mathbf{x} - \mathbf{y}|$ is the argument of the function. The correlation function $\xi(|\mathbf{x}-\mathbf{y}|)$ is closely linked to the power spectrum $P(|\mathbf{k}|)$ through a Fourier transformation

$$P(|\mathbf{k}|) = \int_{\mathbb{R}^3} \mathrm{d}^3 y\, \xi(|\mathbf{y}|) \exp(-\mathrm{i}\mathbf{y}\cdot\mathbf{k})\,. \tag{2.47}$$

The power spectrum is equivalent to the correlation function, but expresses how the Universe is structured as a function of the wavenumber $k = 2\pi/L$, with L as the considered length scale.

In the standard model of cosmology, the initial power spectrum is given by the Harrison-Zel'dovich spectrum. It is applicable for very early times when all matter perturbation scales were still larger than the horizon scale. Since this implies that there is no characteristic scale, the power spectrum follows a power law

$$P(k) \propto k^{n_\mathrm{s}}\,, \tag{2.48}$$

with the scalar index $n_\mathrm{s} = 1$. The theory of inflation predicts a slightly smaller value, because tiny quantum fluctuations were inflated to large scales and thereby causing a deviation from scale independence. Thus, one expects to measure a value $n_\mathrm{s} \leq 1$. The scalar index is constrained most tightly from measurements of the CMB temperature and polarisation finding $n_\mathrm{s} = 0.9665 \pm 0.0038$ (Planck Collaboration et al., 2020b), consistent with the expectations. Alternatively, less tight constraints are obtained from a Lyα forest analysis (Palanque-Delabrouille et al., 2015). In the framework of linear perturbation theory, the evolution of the power spectrum is given by

$$P(k,a) = A k^{n_\mathrm{s}} T^2(k) D_+^2(a)\,. \tag{2.49}$$

The amplitude A has to be constrained from observations. One common way to normalise the power spectrum is through the parameter σ_8, which quantifies the standard deviation of matter fluctuations with respect to a radius of $R = 8h^{-1}\,\mathrm{Mpc}$. The choice of this radius originates from the finding that $\Delta N/N \approx 1$ when counting galaxies in spheres of radius $R = 8h^{-1}\,\mathrm{Mpc}$. The standard deviation of a density field smoothed at a scale R is

$$\sigma^2(R) = \int \frac{\mathrm{d}^3 k}{(2\pi)^3} |\tilde{W}(R,k)|^2 P(k)\,. \tag{2.50}$$

The smoothing is achieved with the top-hat filter function

$$\tilde{W}(R,k) = 3\frac{\sin(kR) - kR\cos(kR)}{(kR)^3}\,. \tag{2.51}$$

The parameter σ_8 can be obtained from various probes such as from galaxy cluster counts, galaxy velocity fields, CMB power spectrum modelling, weak lensing, and SZ measurements. For many of these methods, degeneracies between σ_8 and other cosmological parameters, mainly Ω_m, exist which can partially be broken by combining different methods or with an extension of the respective study to higher redshifts

(e.g. Addison et al., 2013; More et al., 2015; Planck Collaboration et al., 2020b). Interestingly, there seems to be a slight tension between early-time probes and late-time probes (e.g. Douspis et al., 2019). It is not yet clear if this is attributed to systematics in the analysis techniques or if it is a hint towards new physics. Planck Collaboration et al. (2020b) find a value of $\sigma_8 = 0.8102 \pm 0.0060$ from the CMB as an early-time probe, while Heymans et al. (2021) obtain $\sigma_8 = 0.76^{+0.025}_{-0.020}$ from weak gravitational lensing and spectroscopic galaxy clustering as a late-time probe.
In case the galaxies follow the dark matter distribution, one would expect $\sigma^2(R = 8h^{-1}\,\mathrm{Mpc}) \equiv \sigma_8^2 \approx 1$. In reality galaxies do not perfectly trace dark matter, which leads to a bias

$$\frac{\Delta n}{n} = b\frac{\Delta \rho}{\rho} = b\delta\,, \tag{2.52}$$

with b as the bias factor.

2.3.3 Dark matter halos

So far, we have considered structure growth at linear scales $|\delta| \ll 1$. As soon as the density contrast approaches unity, non-linear effects become significant. In particular, linear perturbation theory cannot explain how structures like galaxies or galaxy clusters evolved. Generally, an understanding of non-linear structure formation requires detailed numerical simulations. Early simulations focussed mainly on the behaviour of dark matter particles, which only interact gravitationally (e.g. Millennium, Springel et al., 2005). More recent, larger N-body simulations include the Quijote simulations (Villaescusa-Navarro et al., 2020). As computational capacities grew, it was also possible to include hydrodynamic effects related to baryons into so-called (magneto-)hydrodynamical simulations (e.g. IllustrisTNG, Marinacci et al., 2018; Naiman et al., 2018; Nelson et al., 2018; Pillepich et al., 2018; Springel et al., 2018).

Still, some analytical models can describe non-linear structure formation, at least to some extent. The following sections cover both important analytical approaches to non-linear structure formation and insights from cosmological simulations.

Spherical collapse model

The spherical collapse model is a simple, analytical model for the non-linear evolution of density fluctuations, which broadly reproduces the features of gravitational collapse also found in numerical simulations. It considers the special case of a homogeneous, spherical overdensity embedded in an otherwise homogeneous density field. Since its density $\rho(t) > \bar{\rho}(t)$ is larger than the average density of the Universe, the sphere expands more slowly than the average expansion of the Universe. The expansion continues until time $t_{\max}$ when the sphere reaches its maximum radius. Subsequently, it decouples from expanding at all and collapses under the impact of self-gravity to a singular point. Due to the symmetry of the collapse the time required is $t_{\mathrm{coll}} = 2t_{\mathrm{max}}$. It can be shown that for a collapse to have occurred before the redshift z the condition (Schneider, 2015)

$$\delta_0 \geq \delta_{\mathrm{c}}(1+z) \tag{2.53}$$

must be fulfilled. For an Einstein-de-Sitter universe with $\Omega_{\mathrm{m}} = 1$ and $\Omega_\Lambda = 0$, one finds $\delta_{\mathrm{c}} = 1.69$, which is a good approximation for our Universe as well since the majority of structure formation happened in the matter-dominated phase.

It has to be noted that a collapse into a single point is not realistic. Instead of following a perfectly radial motion, the particles scatter and eventually virialise. The reason for this is that the matter distribution in the sphere is not perfectly homogeneous and particles do not strictly follow a radial motion. Therefore, the particles virialise in a timescale shorter than the time to collapse, so that the collapsed sphere has an average density of (Schneider, 2015)

$$\langle \rho \rangle \simeq 178 \bar{\rho}(t_{\mathrm{coll}}) \,. \tag{2.54}$$

Such a collapsed, virialised mass concentration is referred to as a dark matter halo.

Number density of dark matter halos

Based on the spherical collapse model, it is possible to infer the expected number density n of dark matter halos at a given mass and redshift as first done by Press & Schechter (1974). This is called the halo mass function (HMF) and it takes the general form

$$\frac{\mathrm{d}n}{\mathrm{d}M}(M,z) = \frac{\Omega_{\mathrm{m}}\rho_{\mathrm{cr}}(z=0)}{M} \frac{\mathrm{d}\ln\sigma^{-1}(R,z)}{\mathrm{d}M} f\left(\frac{\delta_{\mathrm{c}}}{\sigma(R,z)}\right) \,. \tag{2.55}$$

The function $\sigma(R,z)$ is the dispersion of the matter field smoothed at a scale R relating to the typical radius of a dark matter halo and evaluated at redshift z as introduced in Equation (2.50). Since it is a function of the power spectrum $P(k)$, it also sensitively depends on the cosmological parameters. Additionally, $f(\delta_{\mathrm{c}}/\sigma(R,z))$ is a mass function, which can be written as

$$f\left(\frac{\delta_{\mathrm{c}}}{\sigma(R,z)}\right) = \sqrt{\frac{2}{\pi}} \frac{\delta_{\mathrm{c}}}{\sigma} \exp\left[-\frac{\delta_{\mathrm{c}}^2}{2\sigma^2}\right] \,, \tag{2.56}$$

following Press & Schechter (1974).

Density profile of dark matter halos

Investigating numerical simulations, Navarro et al. (1996, 1997) found that dark matter halos follow a universal radial density profile, namely

$$\rho(r) = \frac{\rho_{\mathrm{s}}}{(r/r_{\mathrm{s}})^{\alpha}(1+r/r_{\mathrm{s}})^{3-\alpha}}\,, \tag{2.57}$$

where $\alpha \approx 1$, r_{s} is the characteristic radius where the slope of the profile changes, and ρ_{s} corresponds to the amplitude of the density profile. The latter can be rewritten more conveniently in terms of the concentration parameter $c \equiv r_{200}/r_{\mathrm{s}}$ via

$$\rho_{\mathrm{s}} = \frac{200}{3}\rho_{\mathrm{cr}}(z)\frac{c^3}{\ln(1+c) - c/(1+c)}\,. \tag{2.58}$$

Here, r_{200} denotes the radius within which the density is 200 times the critical density. This function is called the Navarro-Frenk-White (NFW) profile. The concentration is, in turn, a function of mass and redshift.

CHAPTER 3

Galaxy clusters

3.1 General properties

Galaxy clusters are the most massive objects bound by gravity in the Universe. They reside in the peaks of the cosmic large-scale matter distribution and can be identified as overdensities of galaxies located at the nodes of the cosmic web, which emerged from initial matter density fluctuations through structure formation (see Section 2.3). Galaxy clusters are extremely versatile multi-component objects observable throughout the entire electromagnetic spectrum. This makes them ideal targets for both astrophysical and cosmological studies. This section provides a summary of the composition and observation of galaxy clusters mainly guided by the more in-depth treatment of these topics in Allen et al. (2011), Schneider (2015), and Pratt et al. (2019).

3.1.1 Composition of galaxy clusters

While clusters were historically first detected from an overdensity of galaxies, these only make up about three per cent of the total cluster mass. Most baryonic matter is found in hot gas, which contributes approximately 12 per cent. The remaining 85 per cent are attributed to dark matter. Together these components amount to cluster masses of up to $\sim 10^{15}\,\mathrm{M}_{\odot}$ for the most massive clusters. This section gives an overview of these cluster components.

Galaxies

Galaxy clusters contain between $\gtrsim 50$ and ~ 1000 galaxies with a typical velocity dispersion of $\sim 1000\,\mathrm{km/s}$. Gatherings of $\lesssim 50$ galaxies are referred to as galaxy groups. The majority of the cluster member population consists of elliptical galaxies, particularly towards the cluster centre and at lower redshifts. The most prominent of them is the brightest cluster galaxy (BCG), the most massive and brightest galaxy, as the name indicates. It is an elliptical located close to the kinematic cluster centre and thought to be formed by mergers of smaller galaxies.

Ellipticals are also often referred to as early-type galaxies according to a morphological classification scheme introduced by Edwin Hubble (1926). Other classifications include late-type galaxies (spirals) and irregular galaxies. Elliptical galaxies exhibit prominent spectral features such as the 4000 Å-break (also called Balmer break), which is a sharp drop of intensity at wavelengths $\lambda < 4000\,\text{Å}$. Common absorption line features are caused by the calcium K and H doublet at 3934.8 Å and 3969.6 Å, by the G-band at 4305.6 Å (a collection of absorption lines in CH molecules), by magnesium at 5176.7 Å, and by sodium at 5895.6 Å. Additionally, the Lyman break in star-forming galaxies is a drop of intensity at rest-frame wavelengths $\lambda < 912\,\text{Å}$. The neutral hydrogen gas in these galaxies or on the line-of-sight absorbs photons below this wavelength. Common emission lines in late-type galaxies are the [OII] line at 3728.3 Å, the [OIII] emission line doublet at 4960.3 Å and 5008.2 Å, and the Hα line at 6564.6 Å. All of these features in early and late-type galaxies help to measure spectroscopic or photometric redshifts. While emission and absorption line features enable secure spectroscopic redshift measurements, the 4000 Å-break and the Lyman break can be used to obtain photometric redshifts. We provide more details on spectroscopic and photometric redshift measurements in Section 4.3.1.

In the context of photometric redshifts of galaxy clusters, their so-called red-sequence is an important tool. It refers to the tight correlation of magnitude and colour for early-type galaxies in clusters with a small scatter of $< 0.1\,\mathrm{mag}$ (Bower et al., 1992). The red-sequence assembles over time as more and more ellipticals form through mergers of smaller galaxies. The red-sequence also exhibits a redshift dependent slope and intercept (Gladders et al., 1998), where the slope is observed to be negative because faint galaxies tend to be bluer, while bright ones are redder (Stott et al., 2009). This is thought to emerge from a mass-metallicity relation of these early-type galaxies, which occurs because the ejection of gas by supernovae is more efficient in smaller galaxies with a more shallow potential well. As a consequence, less massive (and thus fainter) galaxies are also more metal-poor (and thus bluer; Carlberg, 1984). The intercept of the red-sequence changes with redshift. This can easily be understood considering that the 4000 Å-break is shifted to ever redder colours with redshift, therefore affecting the galaxy colour and the intercept of the red-sequence. At a given redshift, however, slope and intercept vary only very little, implying that they are largely independent of the exact conditions in the cluster environment. Therefore, one can generate empirical red-sequence templates by measuring the slope and intercept of the red-sequence of clusters with known redshifts (e.g., from spectroscopy). The colours and magnitudes of galaxies from clusters with unknown redshift can be compared to these templates to constrain the cluster redshift.

Aside from the red-sequence, cluster galaxies also follow a characteristic luminosity function called the Schechter function (Schechter, 1976). It describes the number of galaxies as a function of luminosity per comoving volume, which is analytically approximated based on a self-similar stochastic model for the origin of galaxies. It is expressed as a function of the galaxy luminosity L via

$$\Phi(L)\mathrm{d}L = \Phi^* \left(\frac{L}{L^*}\right)^{\alpha} \exp\left(-\frac{L}{L^*}\right) \mathrm{d}L\,. \tag{3.1}$$

The characteristic luminosity L^* marks where the slope of the function changes. The faint-end slope is given by α, and Φ^* is the number of galaxies per unit volume. For a more practical application, the Schechter function can be rewritten in terms of magnitude m and the redshift-dependent characteristic magnitude $m^* = m^*(z)$ according to

$$\Phi(m)\mathrm{d}m = 0.4\ln(10)\Phi^* 10^{-0.4(m-m^*)(\alpha+1)} \exp(-10^{-0.4(m-m^*)})\mathrm{d}m\,. \tag{3.2}$$

Intracluster medium

The hot, optically thin gas in galaxy clusters is smoothly distributed as it gathers in the deep potential well associated with the cluster. This gas is referred to as the intracluster medium (ICM). Due to compression by gravity and shock heating, the gas has temperatures of 10^7 to 10^8 K (e.g. Pratt et al., 2019). This implies that the main elements in the ICM – hydrogen and helium – are fully ionised. The ICM is additionally enriched by metals, i.e., heavier elements[1]. The reasons for this include supernova explosions in galaxies, which eject gas into the ICM or ram pressure stripping of the interstellar medium in a galaxy as it undergoes infall into the cluster (e.g. Renzini, 1997). Typical metallicities of the ICM are $Z \sim 0.3 - 0.5\,Z_\odot$ (e.g. Mantz et al., 2017).

Dark matter

The majority of the cluster content consists of dark matter. While it does not interact electromagnetically and thus is not directly detectable, the most striking evidence for the existence can be traced in merging clusters as in the famous example of the Bullet cluster (Clowe et al., 2006). When two large clusters collide and

---

[1] Astronomers commonly refer to elements heavier than helium as metals.

merge, the ICM (observed through X-ray emission) can get separated temporarily from the dark matter haloes (traced through gravitational lensing with optical data, see Section 4) and galaxies (observed with optical data), which interact nearly in a collisionless manner.

Relativistic particles

Galaxy clusters form through highly energetic merger events. This energy is dissipated through shocks and turbulence heating the ICM, which in turn leads to an acceleration of particles to relativistic speeds (van Weeren et al., 2019). These particles are often also referred to as cosmic rays (CRs). Additionally, supernovae and outflows from active galactic nuclei (AGNs), whose jets interact with the ICM can serve as particle accelerators (Brunetti & Jones, 2014). The contribution of relativistic particles to the total mass of clusters is, however, negligible.

3.1.2 Observations of galaxy clusters

The variety of components in clusters implies that different wavelength regimes each offer a unique view of a specific component and its emission mechanisms. Their multi-component nature makes clusters ideal targets for multi-wavelength observations complementing each other (see Figure 3.1 for an example). This chapter presents an overview of observations at the different wavelength regimes.

X-rays

X-ray telescopes observe galaxy clusters as extended sources with typical sizes of a few arcminutes and with luminosities on the order of $\sim 10^{44}\,\mathrm{erg\,s^{-1}}$ in soft X-rays[2]. The ICM gas with densities of 10^{-1} (in centres of bright cool core clusters) to $10^{-5}\,\mathrm{cm^{-3}}$ (in cluster outskirts) emits X-ray radiation mainly through three emission mechanisms (Allen et al., 2011): line emission from the decay of a collisionally excited ion to the ground state (bound-bound), emission from the recombination of free electrons with an ion (free-bound), and thermal bremsstrahlung emission from free electrons (free-free). The latter is the dominant mechanism in massive clusters. The total emissivity of thermal bremsstrahlung is related to the temperature T and the electron density n_e via

$$\epsilon^{\mathrm{ff}} \propto n_e^2 T^{1/2}\,. \tag{3.3}$$

X-ray spectra can be used to measure profiles of the density, temperature, and metallicity. Other frequently used observables are the X-ray flux, spectral hardness, and spatial extent. X-ray observations can only be performed with space-based telescopes because Earth's atmosphere is not transparent for X-ray radiation. Despite

---

[2] Soft X-rays have energies of about 0.5 to 2 keV, hard X-rays have energies of about 2 to 10 keV.

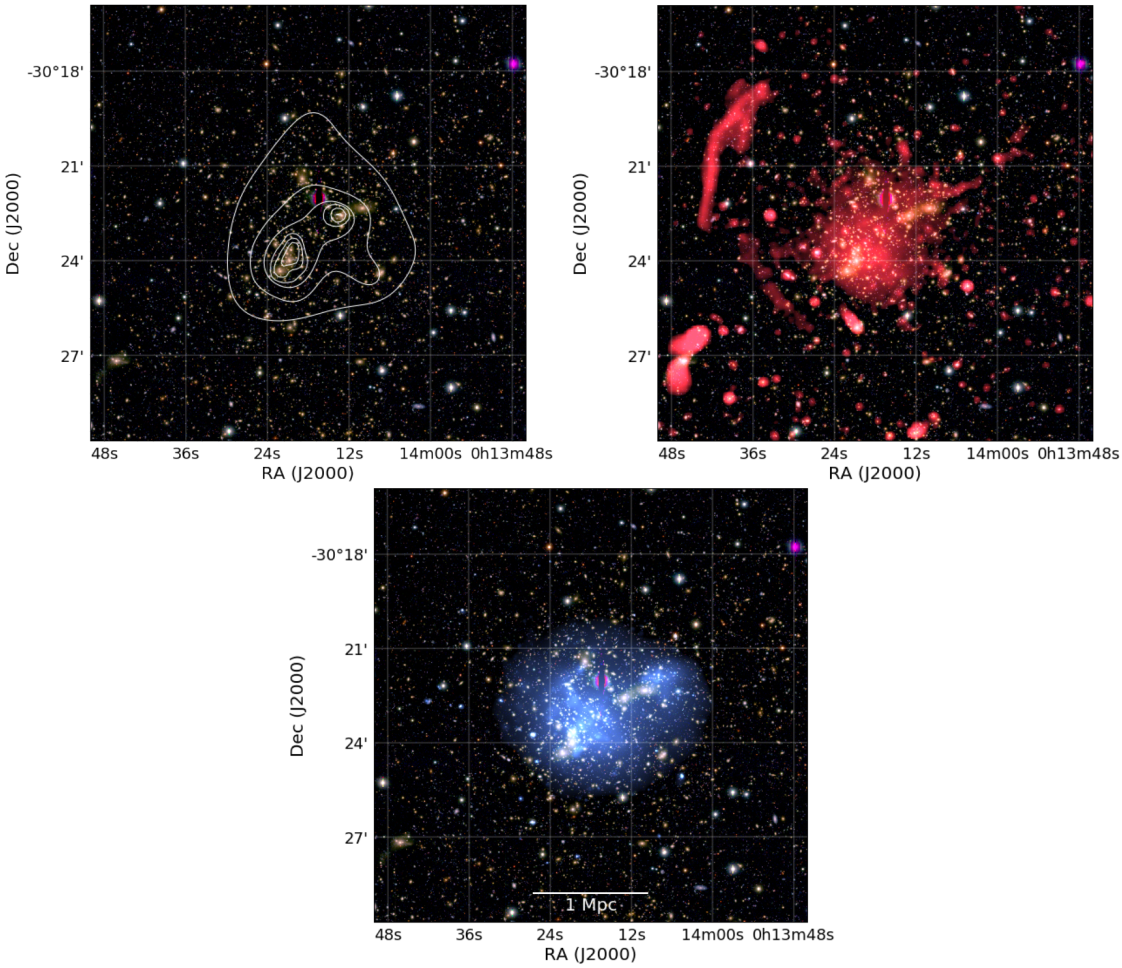

Figure 3.1 – Multi-wavelength observations of the galaxy cluster Abell 2744. All panels show an optical image based on the Subaru filters B, R, and z. *Upper left:* White contours represent the surface mass density derived from a weak lensing study tracing the total matter content (galaxies, gas, dark matter). *Upper right:* The red colour shows the radio emission as measured with the $1-4\,$GHz Very Large Array (VLA) tracing the thermal plasma. *Bottom:* The blue colour represents the X-ray emission as measured by *Chandra* tracing cosmic rays and magnetic fields. All three images are adapted from van Weeren et al. (2019).

this slight disadvantage, the detection of clusters with X-ray observations is a well-developed method to assemble X-ray flux selected cluster samples with excellent purity and completeness and with a tight relation between observable and mass (see Section 3.2.2 for more details on purity, completeness, and scaling relations).

For around 30 years, the ROSAT All-Sky Survey (RASS, Voges et al., 1999) has been the most important and largest resource for X-ray cluster catalogues providing the basis for cluster samples such as HIFLUGCS (Reiprich & Böhringer, 2002), REFLEX I and II (Böhringer et al., 2001, 2013), or NORAS I and II (Böhringer et al., 2000, 2017). Additionally, Pacaud et al. (2016) present the XXL cluster sample based on *XMM-Newton* observations. Very recently, the eROSITA (Predehl et al., 2014) X-ray satellite was launched and is expected to detect $\sim 100\,000$ galaxy clusters in a full-sky survey. Liu et al. (2021) present the first eROSITA-selected sample of galaxy clusters and groups in an area of $140\,\mathrm{deg}^2$. The satellite's main objective is to shed light on the nature of dark energy. Additionally, instruments like *Chandra* and *XMM-Newton* continue to be invaluable for X-ray studies of galaxy clusters, for example, providing deeper observations over smaller sky fractions.

Microwaves

Galaxy clusters are observable through the Sunyaev Zel'dovich (SZ) effect caused by inverse Compton scattering of CMB photons by the thermal population of hot electrons of the ICM. This causes a distortion in the observed spectrum of the CMB towards a galaxy cluster that is proportional to $\propto n_e T$. It is referred to as the thermal Sunyaev Zel'dovich effect (Sunyaev & Zeldovich, 1972). If a cluster has a non-zero peculiar velocity in the rest frame of the CMB, an additional but weaker CMB anisotropy can be observed towards a cluster. This is the kinetic Sunyaev Zel'dovich effect.

The SZ effect is observable at microwave frequencies both from space, for instance, with the *Planck* satellite as well as from Earth's surface with ground-based telescopes such as the Atacama Cosmology Telescope (ACT) or the South Pole Telescope (SPT). Since the SZ effect is not subject to cosmological surface brightness dimming, the high-redshift regime of clusters is more easily accessible than other probes, enabling cluster surveys and samples complementary to X-ray cluster surveys and samples (e.g. Planck Collaboration et al., 2016c; Bleem et al., 2015, 2020; Hilton et al., 2021). Section 3.3 gives a more in-depth overview of the SZ effect.

Optical and Near-Infrared

Optical and near-infrared (NIR) radiation is predominantly emitted either from stars in cluster member galaxies or from the intracluster light (ICL), i.e., from stars not bound by a galaxy. Investigating the colour, distribution, and morphology of galaxies through optical and NIR observations can give insights into the star formation in galaxies and into the evolution of galaxies in a cluster environment. Furthermore, optical observations do not only enable studies of the cluster member galaxies but they can also be used to measure systematic (small) distortions of background galaxies behind the cluster caused by (weak) gravitational lensing. The latter is a powerful method for mass measurements, which I introduce in more detail in Chapter 4.

Aside from X-ray and SZ-detections, the magnitudes and colours of galaxies can be used as well to detect clusters and perform surveys to obtain samples for cosmological analyses. In order to reduce projection effects, it is useful to identify clusters through an overdensity of galaxies of the same colour. Sophisticated cluster finders based on the red-sequence have led to catalogues with several thousands of detected clusters, e.g., RCS (Gladders & Yee, 2005), MaxBCG (Koester et al., 2007), and RedMaPPer (Rykoff et al., 2016). An important inferred quantity is the richness, a measure for the number of cluster member galaxies with varying definitions in the literature.

Radiowaves

Diffuse extended radio emission from clusters traces cosmic rays and magnetic fields in the ICM. The emission mechanism is synchrotron radiation occurring when relativistic particles gyrate around magnetic field lines. There is a classification into three types of diffuse radio sources:

1. Haloes are characterised by non-localised emission around the cluster centre with a brightness profile, which approximately follows the distribution of the ICM.
2. Shocks or relics reveal merger-induced shock waves in the ICM. They are observed as polarised and localised sources in the periphery of clusters.
3. Revived AGN fossil plasma sources exhibit radio-steep spectra and irregular morphologies.

Radio observations of galaxy clusters are a useful tool to trace the merger rate of clusters throughout different epochs. van Weeren et al. (2019) give a thorough review of this topic.

Gamma-rays

Proton cosmic rays in clusters have a long lifetime, and thus, they accumulate over time, storing energy in the non-thermal ICM. These trapped proton CRs produce pions when they collide inelastically with thermal protons. The pions, in turn, produce gamma radiation when they decay. Therefore, the observation of gamma rays can provide constraints on this cluster component. However, gamma rays are hard to detect, so that most studies so far can only provide upper limits for the flux of gamma radiation. An in-depth review is provided by Brunetti & Jones (2014).

3.2 Cosmological measurements with galaxy clusters

The mass and redshift are the fundamental properties of galaxy clusters connecting observations and theory, since the halo mass function (see Section 2.3.3) predicts the number density of clusters as a function of these two parameters. Studying the distribution and content of galaxy clusters as a function of mass and redshift provides an excellent probe for structure formation and the underlying cosmological parameters. Accurate and precise mass measurements are the key ingredient to obtain tight constraints. This section provides an overview about mass measurements of galaxy clusters, using both direct methods and mass proxies related to cluster mass through observable-mass scaling relations. These mass measurements form the basis for cosmological constraints from cluster number counts and from their baryonic matter content. For a thorough review of cosmological parameters from galaxy clusters, the reader is referred to Allen et al. (2011). Furthermore, Pratt et al. (2019) and Giodini et al. (2013) give detailed insights into mass measurements in the context of cosmological studies and into observable-mass scaling relations, respectively.

3.2.1 Mass measurements

There are several ways to obtain direct constraints on the masses of clusters. The cluster member galaxies can be used as test particles whose velocity dispersion is determined by the cluster's gravitational potential. Under the assumption of dynamical equilibrium, the dynamical mass can be inferred from the three-dimensional velocity dispersion $\sigma_{\mathrm{r}}(r)$ and number density profile $\nu(r)$ through the Jeans equation (e.g. Carlberg et al., 1997)

$$M(r) = -\frac{r\sigma_{\mathrm{r}}^2(r)}{G}\left[\frac{\mathrm{d}\ln\sigma_{\mathrm{r}}^2(r)}{\mathrm{d}\ln r} + \frac{\mathrm{d}\ln\nu(r)}{\mathrm{d}\ln r} + 2\beta\right] , \tag{3.4}$$

where β is the velocity anisotropy parameter. The three-dimensional quantities can be inferred from the projected velocity dispersion and number density profile through a number of model assumptions such as for instance spherical symmetry.

Instead of using the galaxies, the mass can also be inferred from gas properties using X-ray data. The key assumption here is that the ICM is in hydrostatic equilibrium. Then, the gas pressure P, gas density ρ, and the gravitational potential fulfil the hydrostatic equilibrium equation

$$\frac{1}{\rho}\frac{\mathrm{d}P}{\mathrm{r}} = -\frac{GM(<r)}{r^2} , \tag{3.5}$$

with $\rho = \mu m_{\mathrm{p}} n$, where μm_{p} is the mean molecular weight and n is the number density of the gas. In case of spherical symmetry, the radial temperature $T(r)$ and number density $n(r)$ profiles of the gas are related to the total mass via (e.g. Allen et al., 2008)

$$M(r) = -\frac{rk_{\mathrm{B}}T(r)}{G\mu m_{\mathrm{p}}}\left[\frac{\mathrm{d}\ln n(r)}{\mathrm{d}\ln r} + \frac{\mathrm{d}\ln T(r)}{\mathrm{d}\ln r}\right] , \tag{3.6}$$

where k_{B} is the Boltzmann constant. The radial number density profile $n(r)$ can be obtained from a deprojection of the X-ray surface brightness measured in thin annuli, while the temperature profile $T(r)$ can be obtained from X-ray spectra.

Generally, the cluster gas is never completely in hydrostatic equilibrium. This is due to the continuous growth of clusters through mergers and accretion, as well as due to bulk motions and turbulence in the ICM. Additionally, non thermal-pressure support for instance through random and rotational gas motions can play a significant role (Pratt et al., 2019). Deviations from hydrostatic equilibrium are typically more severe for disturbed or merging clusters. This leads to a bias between the hydrostatic equilibrium mass M_{HSE} and the true mass M_{true} quantified by the hydrostatic mass bias $b_{\mathrm{M}} = (M_{\mathrm{HSE}} - M_{\mathrm{true}})/M_{\mathrm{true}}$. The impact of deviations from hydrostatic equilibrium has been investigated from a simulation perspective (recent examples include Nelson et al., 2014b,a; Biffi et al., 2016; Shi et al., 2015, 2016), as well as by a comparison of hydrostatic equilibrium masses and masses based on weak gravitational lensing (e.g. Mahdavi et al., 2013; Smith et al., 2016; Applegate et al., 2016; Miyatake et al., 2019).

The outstanding advantage of mass measurements through weak gravitational lensing is that no prior assumptions about the dynamical state of the cluster or hydrostatic equilibrium are required. Instead, weak lensing probes the total projected matter content of a cluster by measuring the tangential distortions of background galaxies as a function of cluster-centric radius. These distortions occur when the light from background galaxies travels through the gravitational potential of a massive cluster. This allows for the reconstruction of the two-dimensional projected mass distribution of the galaxy cluster. Since the mass measurement of galaxy clusters through weak gravitational lensing is the main method used in this work, it is more thoroughly introduced in Chapter 4.

3.2.2 Observable-mass scaling relations

The methods for mass measurements described in the previous section can be rather time-consuming and expensive to obtain. A valuable alternative can be to probe the gravitational potential through more easily accessible mass proxies, which are expected to be tightly related to the cluster mass. Such proxies are commonly used to detect clusters in a survey, for example, based on the X-ray luminosity, the Comptonisation parameter from the Sunyaev-Zel'dovich effect, or the cluster richness. The survey observables are linked to the cluster mass through observable-mass scaling relations. The expected form of these relations can be predicted from the simplest model of structure formation, which states that the evolution and formation of structures are solely governed by gravity. In Section 2.3.2, we have seen that there is no characteristic scale for gravitational collapse in the initial power spectrum. From this, self-similarity of the galaxy cluster population can be inferred because galaxy clusters emerged from the initial density fluctuations. This means that small clusters are scaled-down versions of their larger counterparts, where all clusters have a very similar internal structure within R_{500}. Since this also implies that the gas properties follow from the dark matter properties, it is possible to predict the general relation between an observable gas property Q and the mass M_Δ (with a density Δ times higher than the critical density) via (e.g. Pratt et al., 2019)

$$Q \propto A(z) M_\Delta^\alpha \,, \tag{3.7}$$

where $A(z)$ quantifies the redshift dependent evolution of the dark matter density, which is related to the evolution function $E(z)$ introduced in Equation (2.19). For example X-ray observables are predicted to follow the scaling laws $T_\mathrm{X} \propto E^{2/3}(z) M_\Delta^{2/3}$ or $L_\mathrm{X} \propto E^{7/3}(z) M_\Delta^{4/3}$. Of course, these scaling relations will exhibit intrinsic scatter given the individual formation histories of clusters. Additionally, deviations from these self-similar predictions are expected in the presence of non-gravitational processes, which affect the normalisation, slope, scatter, and evolution of the scaling laws. Numerous studies investigating clusters in hydrodynamic simulations have found that especially AGN feedback is a key feature for realistic models (see e.g. Le Brun et al., 2017; Truong et al., 2018). These effects are the reason why observable-mass scaling relations need to be carefully calibrated when they are used for cosmological studies with cluster samples selected based on a specific observable. Uncertainties in scaling relations are currently the limiting factor for cosmological constraints from galaxy clusters (Dietrich et al., 2019). Weak lensing masses are frequently used in this context to calibrate X-ray or SZ effect observable-mass scaling relations (see e.g. Okabe et al., 2010b; Kettula et al., 2015; Dietrich et al., 2019) or the richness-mass scaling relation (Rozo et al., 2009a), where quantifying the scatter around these relations is also of particular interest. Only with an accurate and well-understood calibration of scaling relations, is it possible to properly relate the theoretical cluster mass function to observed number counts as required to obtain meaningful cosmological constraints.

Furthermore, the understanding of the scaling relations is directly linked to the selection function of cluster samples. This function describes how well the detected sample represents the underlying cluster population as a function of mass and redshift. It has two important contributions: completeness and purity. The completeness quantifies the probability that a cluster of given mass and redshift is detected through its baryonic signal, i.e., the survey observable. The purity reflects the probability that a detection corresponds to a real cluster and not to a noise peak. It is closely related to the signal-to-noise ratio of detections.

Part of characterising the selection function is determining how much the survey might be affected by different biases. Most commonly, this includes the Eddington bias and the Malmquist bias. The Eddington bias (Eddington, 1913) is a purely statistical effect caused by the fact that the measurements of the survey observable inherently exhibit some level of noise. Paired with the shape of the halo mass function, this implies that low-mass systems are more likely to scatter into a source sample with a given signal-to-noise ratio cut than high-mass sources scattering out. Consequently, masses measured based on the same observable that was used for detection will be overestimated. However, the impact of the Eddington bias can be quantified when follow-up observations of the detected clusters with an independent observable are available. The Malmquist bias, as first reported on for stars by Gunnar Malmquist (1925), is especially relevant for X-ray flux-limited cluster samples. It states that systems of a given mass that are intrinsically X-ray brighter will appear more numerous in a sample because they can be detected out to larger distances. Since such biases depend on the cluster mass function as well as the survey selection function, it has become common practice to perform joint analyses of scaling laws and cosmological parameters (see e.g. Mantz et al., 2014; de Haan et al., 2016; Bocquet et al., 2019).

3.2.3 Cosmological constraints from cluster number counts

The number density of galaxy clusters follows the halo mass function (HMF) introduced in Section 2.3.3, quantifying the number density of dark matter haloes as a function of mass and redshift. This function is particularly sensitive to the normalisation σ_8 of the power-spectrum. In principle, a single very massive cluster exceeding the expectation of the HMF computed for a given cosmology could falsify said cosmology. An example of a comparison between the measured number density of clusters and the HMF based on a given cosmology is shown in Figure 3.2 and provides constraints on cosmological parameters. Recent examples of studies with cluster counts include Planck Collaboration et al. (2016b) and Bocquet et al. (2019) using SZ selected samples, Mantz et al. (2015), Schellenberger & Reiprich (2017), and Pacaud et al. (2018) using X-ray selected samples, Hamana et al. (2015) using a weak-lensing detected sample, and Lesci et al. (2020) and Costanzi et al. (2021) using optically detected samples. These studies tend to measure a lower amplitude σ_8 of the matter fluctuations from these low-redshift probes than results obtained from CMB observations by *Planck* (see Figure 3.3). It remains an open question if unaccounted systematic uncertainties in the analyses cause this tension or if it could hint at new physics.

3.2.4 Cosmological constraints from the baryon fraction

Due to the strong gravitational potential and the large extent of galaxy clusters, it is thought that their baryon fraction $f_\mathrm{b} = (M_\star + M_\mathrm{gas})/M_\mathrm{tot}$, i.e., the ratio of stellar and gas mass with respect to the total mass, should represent the cosmic ratio $\Omega_\mathrm{b}/\Omega_\mathrm{m}$. As Ω_b can be determined from external probes related to CMB or BBN measurements, measuring the baryon fraction from X-ray and optical data allows for constraints on the total matter density Ω_m of the Universe.

Alternatively, the assumption that the gas mass fraction $f_\mathrm{gas} = M_\mathrm{gas}/M_\mathrm{tot}$ is constant over cosmic time offers a standard ruler, which allows for tests of the expansion history of the Universe. This is because the X-ray measurements of the gas mass require knowledge of the cosmology-dependent distance $D_\mathrm{A}(z)$ of the clusters. Sasaki

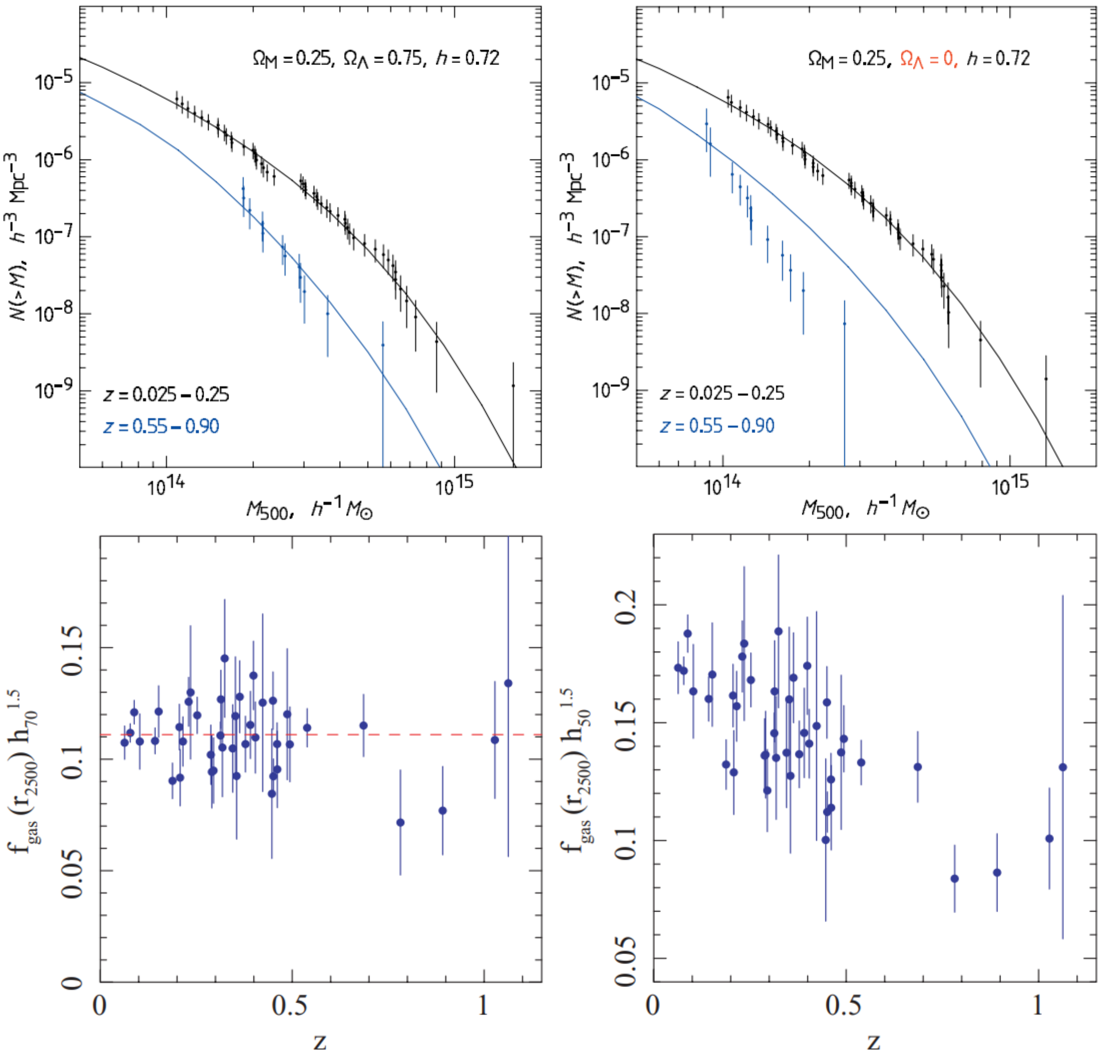

Figure 3.2 – Examples of obtaining cosmological constraints from measurements with galaxy cluster samples. *Top panels:* Both figures show the measured cluster mass function (employing *Chandra*-based hydrostatic mass estimates) at low (black data points) and high (blue data points) redshift. The solid lines represent the predicted HMF at low (black line) and high (blue line) redshift for different cosmological parameters. On the left-hand panel, employing a flat ΛCDM cosmology results in a good match between data and model. In contrast to that, using a model with $\Omega_\Lambda = 0$ leads to clear mismatch at high redshift on the right-hand panel. Such a cosmology is clearly disfavoured by the measured cluster distribution. Both panels are adapted from Vikhlinin et al. (2009). *Bottom panels:* The gas mass fraction $f_{\rm gas}$ is measured as a function of redshift. The gas mass fraction is assumed to be constant with redshift. In the left-hand panel, a standard ΛCDM cosmology ($\Omega_{\rm m} = 0.3$, $\Omega_\Lambda = 0.7$, $h = 0.7$) was used, resulting in a flat distribution of $f_{\rm gas}$ with redshift. This indicates that the 'correct' cosmology was assumed in the analysis. In the right-hand panel an alternative model ($\Omega_{\rm m} = 1.0$, $\Omega_\Lambda = 0.0$, $h = 0.5$) leads to a decrease of $f_{\rm gas}$ with redshift. Both panels are adapted from Allen et al. (2008).

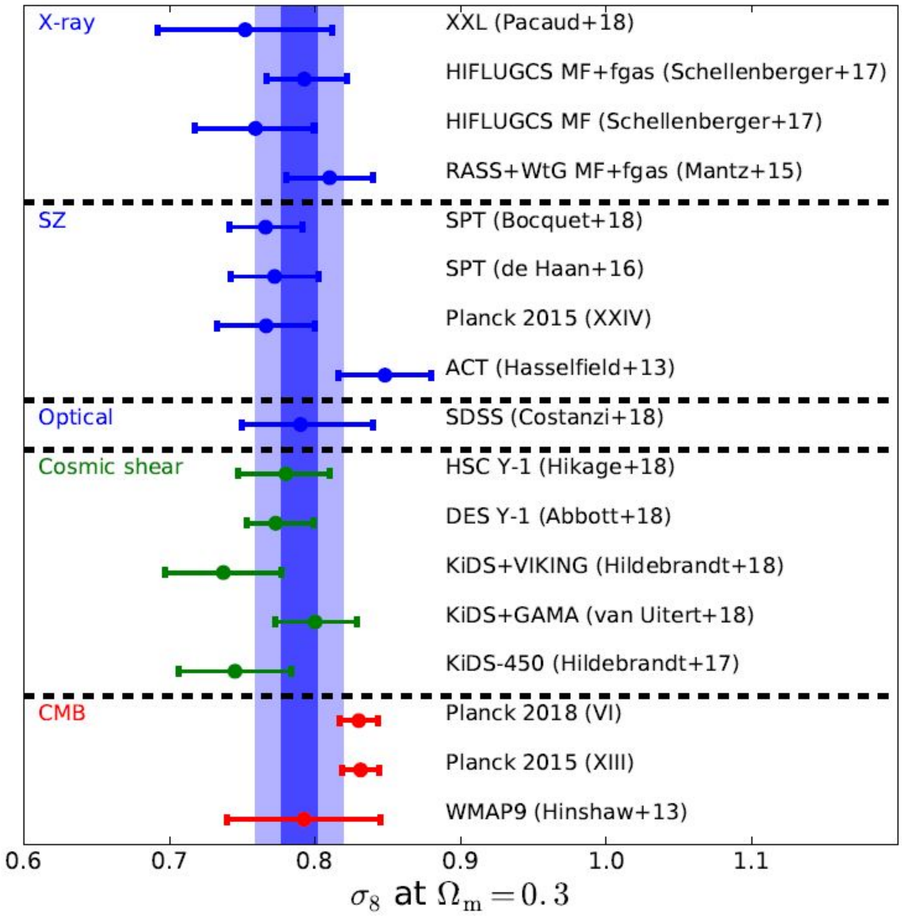

Figure 3.3 – Differences between measurements of σ_8 from different cosmological probes. The blue symbol correspond to constraints of σ_8 (at $\Omega_\mathrm{m} = 0.3$) from the cluster mass function, partially in combination with f_gas measurements. The light (dark) blue shaded bands show the standard deviation of 0.033 (error of 0.012) around the unweighted mean of $\sigma_8 = 0.789$. The green symbols present constraints from weak lensing, cosmic shear, or galaxy clustering. The red symbols show constraints from the CMB. The figure was taken from Pratt et al. (2019).

(1996) and Pen (1997) found that the gas mass fraction is proportional to the angular diameter distance according to $f_\mathrm{gas} \propto D_\mathrm{A}^{3/2}(z)$. Hence, measuring a constant gas mass fraction as a function of redshift implies that the 'correct' cosmology was employed in the analysis. An example of this method is shown in Figure 3.2. Recent examples exploiting the gas mass fraction to obtain cosmological results include Mantz et al. (2014) and Schellenberger & Reiprich (2017) who combined measurements of cluster counts and the gas mass fraction.

3.3 Cluster surveys based on the Sunyaev Zel'dovich effect

The Sunyaev Zel'dovich effect (Sunyaev & Zeldovich, 1972) summarises what happens when CMB photons are inverse Compton scattered by free electrons in the potential well of clusters or generally in the diffuse plasma on large scales. One can distinguish between four different types of the SZ effect (Mroczkowski et al., 2019):

- The thermal Sunyaev Zel'dovich effect (tSZ) is related to scattering with thermal electrons (see also Section 3.1.2).
- The kinetic Sunyaev Zel'dovich effect (kSZ) is caused by a bulk motion of a galaxy cluster in the rest frame of the CMB (see also Section 3.1.2).
- The relativistic Sunyaev Zel'dovich effect (rSZ) describes specific corrections to the tSZ and kSZ effect in case the electrons approach relativistic velocities.
- The non-thermal Sunyaev Zel'dovich effect (ntSZ) is caused by electrons with a non-thermal velocity distribution.

The remainder of this section solely discusses the tSZ effect as it is most relevant to this thesis in the context of cluster surveys based on the SZ effect. We refer the reader to Carlstrom et al. (2002) and Mroczkowski et al. (2019) for detailed insights on all types of the SZ effect and their role for cosmology.

The tSZ effect occurs when CMB photons encounter the hot thermal distribution of electrons in the intracluster medium (ICM). The CMB photons interact with energetic thermal electrons via inverse Compton scattering and gain energy. Consequently, the CMB spectrum is slightly distorted (see Figure 3.4) in such a way that a decrease of intensity is observed at frequencies below $\lesssim 218\,\mathrm{GHz}$, while an increase can be seen above. This change in observed intensity is equivalent to a change in observed CMB temperature. The signal of this tSZ effect is proportional to the line-of-sight integral of the electron pressure:

$$\frac{\Delta T_{\mathrm{SZE}}}{T_{\mathrm{CMB}}} = f(x)\, y = f(x) \int n_e \frac{k_{\mathrm{B}} T_e}{m_e c^2} \sigma_{\mathrm{T}}\, \mathrm{d}l \,, \tag{3.8}$$

where $x = \frac{h\nu}{k_{\mathrm{B}} T_{\mathrm{CMB}}}$, and y is the Compton y-paramter, which in turn depends on the electron density n_e and the electron temperature T_e. Further constants include the Boltzmann constant k_{B}, the Thomson cross section σ_{T}, and the electron rest mass energy $m_e c^2$. The frequency dependency of the tSZ effect is given by

$$f(x) = \left(x \frac{e^x + 1}{e^x - 1} - 4 \right) \left(1 + \delta_{\mathrm{SZ}}(x, T_e)\right) , \tag{3.9}$$

where $\delta_{\mathrm{SZ}}(x, T_e)$ is an electron-temperature-dependent relativistic correction to the spectrum of the tSZ effect, which is small even for massive clusters and will be neglected in this work.

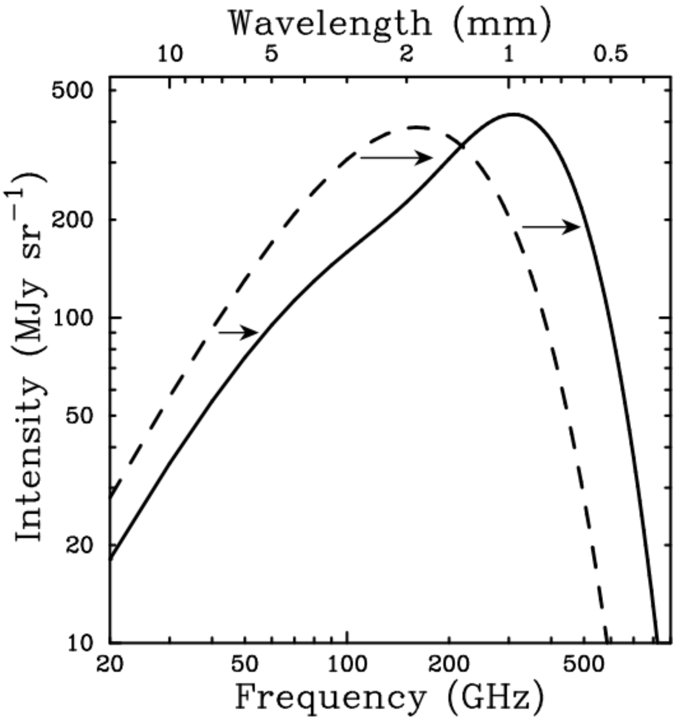

Figure 3.4 – Impact of the SZ effect on the CMB spectrum. The dashed line represents the undistorted spectrum. The solid line illustrates the shift caused by the SZ effect. For illustration purposes, the effect is displayed for a galaxy cluster that is ~ 1000 times more massive than a typical cluster. Below the frequency of $\lesssim 218\,\mathrm{GHz}$, the SZ effect causes a decrease of the observed CMB intensity, while it causes an increase at higher frequencies. Figure from Carlstrom et al. (2002).

The integral of the tSZ effect signal over the solid angle of a galaxy cluster $\mathrm{d}\Omega$ is proportional to the cluster mass M weighted by the temperature according to

$$\int \Delta T_{\mathrm{SZE}} \mathrm{d}\Omega \propto \frac{M\langle T_e \rangle}{D_{\mathrm{A}}^2} \,. \tag{3.10}$$

As a consequence, it is possible to obtain nearly mass-limited samples of galaxy clusters when they are detected through the tSZ effect since its signal does not depend on redshift (see Eq. 3.8).

Important surveys that detected galaxy clusters with the help of the tSZ effect were performed with the Atacama cosmology telescope (Hilton et al., 2021), the South Pole Telescope (Bleem et al., 2015), and the *Planck* satellite (Planck Collaboration et al., 2016c). We present further details on surveys conducted with the latter two telescopes in the following two subsections.

3.3.1 The South Pole Telescope Sunyaev Zel'dovich survey

The South Pole Telescope (SPT) has detected galaxy clusters through their tSZ effect signal. It has systematically surveyed an area of 2500 deg^2 at 95, 150, and 220 GHz from the geographic south pole between 2008 and 2011. From this 2500 deg^2 SPT-SZ survey Bleem et al. (2015) assembled a catalogue of detected cluster candidates. It includes 667 candidates detected above a signal-to-noise threshold of $\xi = 4.5$. This sample of candidates has a median mass of $M_{500} \approx 3.5 \times 10^{14}\, M_{\odot} h_{70}^{-1}$ and median redshift of $z_{\mathrm{med}} = 0.55$, where the highest redshifts extend to $z > 1.4$. Bleem et al. (2015) report a lower limit for the sample purity of ≥ 76 per cent at a signal-to-noise threshold of $\xi = 4.5$.

The detection of the clusters is performed on calibrated maps of the SZ-data obtained at the three survey frequencies 95, 150, and 220 GHz with a spatial-spectral matched filter and simple peak finding algorithm. At these frequencies, the primary mirror of the 10 m South Pole Telescope provides beam sizes of about 1.6 arcmin, 1.1 arcmin and 1.0 arcmin, respectively. This is exactly the size regime expected for the angular size of massive clusters at high redshifts. The signal in the calibrated tSZ maps includes several contributions. Apart from the frequency-dependent tSZ signal of interest, there are effects from the beam and previous filtering steps and different noise contributions. On the one hand, the astrophysical noise originates from lensed primary CMB fluctuations, the kinetic and thermal SZ signal from clusters below the detection threshold, as well as dusty extragalactic sources. On the other hand, there are residual instrumental and atmospheric noise contributions. A matched multi-filtering technique is applied to extract detections of galaxy clusters from the SZ-maps following Melin et al. (2006). This technique makes use of the known spatial and spectral characteristics of galaxy clusters. In particular, Bleem et al. (2015) assume a projected isothermal β-model (Cavaliere & Fusco-Femiano, 1976) as a source template:

$$\Delta T = \Delta T_0 (1 + \theta^2/\theta_{\mathrm{c}}^2)^{-1}\,, \tag{3.11}$$

with ΔT_0 as the normalisation, θ as the angular separation from the cluster centre, and θ_{c} as the core radius. There are 12 different matched filters applied, each with a different core radius between 0.25 and 3 arcmin. A peak detection algorithm then extracts cluster candidates from the maps. Ultimately, the location and maximum detection significance ξ are determined. All candidates with $\xi \geq 4.5$ are added to the list of galaxy cluster candidates. Recently, Bocquet et al. (2019) published an analysis deriving cosmological constraints with galaxy clusters from the 2500 deg^2 SPT-SZ survey and providing updated redshift and SZ mass estimates for the SPT cluster sample. Furthermore, Bleem et al. (2020) and Huang et al. (2020) present extended/new cluster samples detected with the SPTpol receiver (Austermann et al., 2012) installed at the SPT, which will be valuable for future cosmological studies.

3.3.2 The *Planck* Sunyaev Zel'dovich survey PSZ2

The second data release of the *Planck* catalogue of Sunyaev Zel'dovich sources (PSZ2) is the largest systematic SZ all-sky survey to date (Planck Collaboration et al., 2016c). It comprises 1653 detections of galaxy cluster candidates with a signal-to-noise ratio $\mathrm{S/N} \geq 4.5$, detected in the 29 month full mission data. 1203 of the sources were confirmed from auxiliary data sets in radio, microwave, infrared, optical, and X-ray wavelengths, and 1094 sources have redshift estimates. This corresponds to a lower limit for the catalogue purity of 83 per cent.

The *Planck* satellite performed observations in a total of nine frequency channels: the frequencies 30, 44, and 70 GHz are part of *Planck* LFI, the frequencies 100, 143, 217, 353, 545, and 857 GHz are part of *Planck* HFI, where the latter has a beam size between 9.7 arcmin at the lowest frequency and 4.2 arcmin at the highest frequency. The PSZ2 catalogue was produced based on *Planck* HFI. Planck Collaboration et al. (2016c) employed three different detection algorithms, namely `MMF1`, `MMF3`, and `PwS` for PowellSnakes, and constructed the PSZ2 catalogue as the combination of all sources detected by at least two of them. Any reported parameter estimates are derived from the detection method with the highest signal-to-noise ratio for the respective source. `MMF1` and `MMF3` are similar algorithms employing the same matched multi-filtering technique (also equivalent to the technique employed by the SPT team in Bleem et al., 2015), which detects galaxy clusters based on their characteristic spatial and spectral signature in *Planck*'s frequency bands. Matched-multi-filtering means that prior knowledge about the cluster pressure profile (spatial signature) and thermal SZ spectrum (spectral signature) are incorporated in the filtering process. The all-sky maps are subdivided into patches and then filtered by a matched multi-filter, which linearly combines the six frequencies. In particular, the maps are filtered several times with varying assumed cluster sizes between $\theta_\mathrm{s} = 0.8$ arcmin to 32 arcmin. Peaks in the filtered maps with signal-to-noise ratios larger than four represent the positions of cluster candidates. The `MMF1` and `MMF3` algorithms differ mainly regarding the size of the patches that the full-sky map is divided into. `MMF1` uses 640 patches with $14.66 \times 14.66\,\mathrm{deg}^2$, while `MMF3` uses 504 patches with $10 \times 10\,\mathrm{deg}^2$. The implied smaller overlap of patches in `MMF3` is compensated for with an additional iteration of the procedure to increase the reliability of the detections. While both algorithms are very similar, e.g., the choice of patch sizes impacts the signal-to-noise ratio and can, therefore, lead to noticeable differences in the peak detection.

The `PwS` algorithm is particularly potent with regards to identifying and characterising SZ sources in a diffuse background, and it is especially robust to variations of the background. The detection is facilitated through a combination of multichannel filtering, Bayesian posterior sampling, and evidence ratio evaluation to detect cluster candidates. The reader is kindly referred to Planck Collaboration et al. (2016c) as well as Melin et al. (2006), Carvalho et al. (2009), and Carvalho et al. (2012) for more detailed information on the detection algorithms.

The survey observable of the PSZ2 catalogue is the integrated Compton parameter $Y_{\rm SZ}$. It is obtained by integration of the Compton parameter y introduced in Equation(3.8). Planck Collaboration et al. (2016c) measure this quantity within $5R_{500,\rm c}$, with $R_{500,\rm c}$ as the radius where the average density equals 500 times the critical density of the Universe. The size of this radius is chosen such that it provides close to unbiased estimates and is still small enough to minimise confusion effects from nearby objects. Additionally, the SZ signal of the clusters is assumed to follow a generalised NFW (GNFW) profile (Nagai et al., 2007) with the universal pressure profile parameters provided by Arnaud et al. (2010). It has a concentration $c_{500,\rm c}$ and a characteristic angular radius $\theta_{\rm s}$, where $\theta_{\rm s} = \theta_{500\rm c}/c_{500,\rm c}$. Each detection by one of the algorithms results in a probability distribution in the ($\theta_{\rm s}$, $Y_{5\rm R500}$) plane. These two parameters exhibit a degeneracy, which can be broken using two ingredients: firstly, an X-ray based scaling relation between $Y_{500\rm c}$ and the mass $M_{500\rm c}$ within $R_{500\rm c}$ (the mass scale is calibrated with hydrostatic masses from *XMM-Newton* observations, Planck Collaboration et al., 2014a), and secondly, Equation (9) from Planck Collaboration et al. (2014a) relating $M_{500\rm c}$ and $\theta_{500\rm c}$. Both require prior knowledge about the redshift. The parameters best matching the prior information result in a mass estimate for $M_{500\rm c}$ from the SZ signal. This mass can be understood as the hydrostatic mass of a cluster that follows the assumed scaling relation at a given redshift, because the relation was calibrated against hydrostatic masses from *XMM-Newton*.

CHAPTER 4

Gravitational lensing

According to Einstein's theory of General Relativity, massive objects distort their surrounding space-time. Such objects are called gravitational lenses because they distort the light-rays from sources behind them, similar to convex glass lenses. Consequently, the observer sees an image of the source that is distorted, (de-)magnified, and displaced with regards to the true position in the sky. The gravitational tidal field can be traced by measuring the amplitude of the distortions. This information encapsulates the contribution of all matter, both dark matter and baryonic matter. It allows for constraints on the mass of the lens without any previous assumptions, for example, about the dynamical state of the lens. One distinguishes between strong and weak gravitational lensing. For strong gravitational lensing, the distortions are strong enough so that multiple images of the same source can occur. This enables mass measurements of the inner regions of the lens, roughly on the scales enclosed by the multiple images. We enter the regime of weak gravitational lensing when the radial distances of the sources increase. At a large radial distance from the lens, its gravitational field only slightly distorts the shape of the sources in the background. In this case, the coherent alignment caused by this can only be measured statistically.

This chapter follows Bartelmann & Schneider (2001) and Bartelmann & Maturi (2017) who provide an instructive and thorough introduction to the theory of strong and weak gravitational lensing. Proofs of the equations introduced in this section can be found therein. Additionally, Hoekstra et al. (2013) address gravitational lensing in the context of mass measurements of galaxy clusters. Another recent and insightful review is provided by Umetsu (2020).

4.1 Lensing geometry

We can describe the geometry of a gravitational lensing system through a sketch as shown in Figure 4.1. The light rays of a source at angular diameter distance D_S from the observer and true angular position $\boldsymbol{\beta}$ pass by a lens at angular diameter distance D_L and get deflected by it. If the distances between source, lens, and observer are much larger than the source's extent, the Born approximation is applicable, i.e., the light rays are assumed to travel on a straight path, whose direction only changes when crossing the lens plane. Additionally, the small-angle approximation applies. The image of the source is observed at angular position $\boldsymbol{\theta}$. True source position $\boldsymbol{\beta}(\boldsymbol{\theta})$ and observed position $\boldsymbol{\theta}$ are geometrically connected via the lens equation

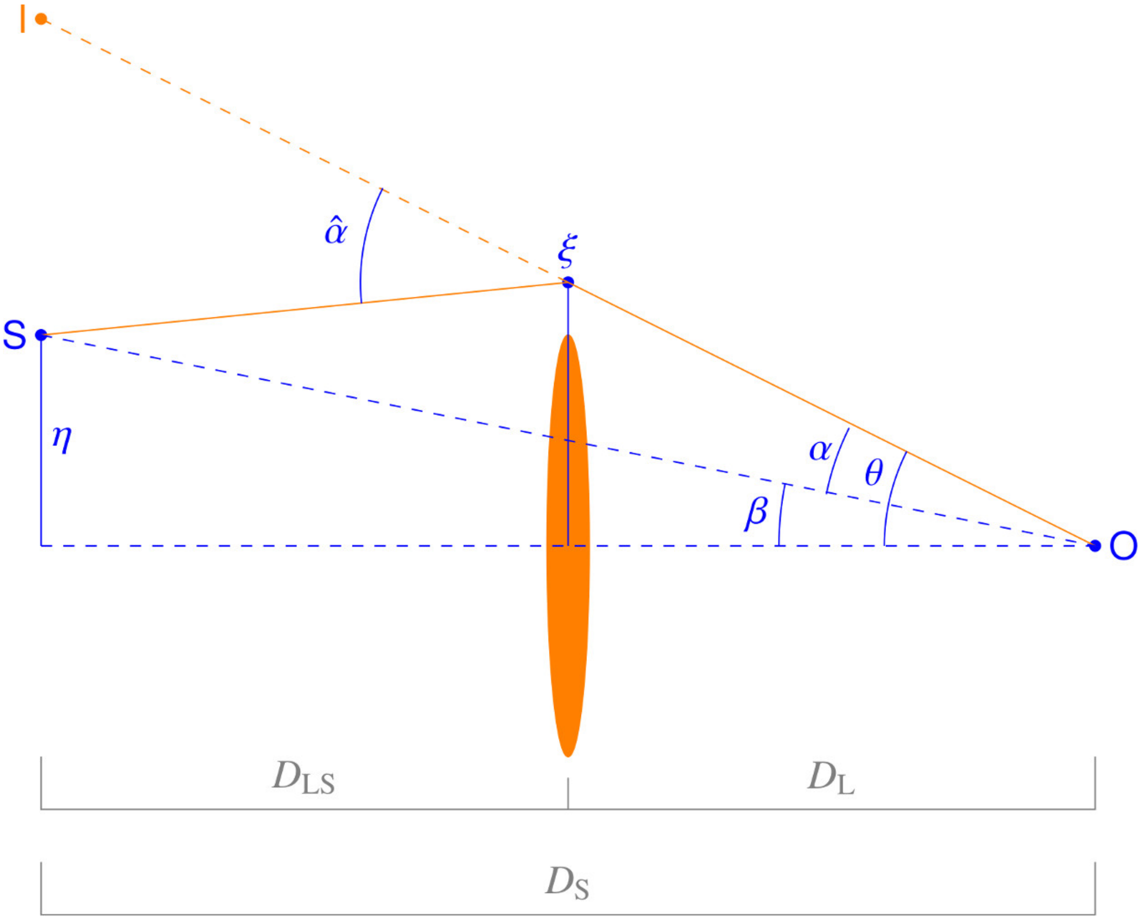

Figure 4.1 – Geometry of a lens system. The angles $\hat{\boldsymbol{\alpha}}$, $\boldsymbol{\alpha}$, $\boldsymbol{\beta}$, and $\boldsymbol{\theta}$ are two dimensional quantities. $\boldsymbol{\eta}$ and $\boldsymbol{\xi}$ are vectors in the source plane at angular diameter distance D_S and in the lens plane at angular diameter distance D_L from the observer at 'O', respectively. The image is taken from Bartelmann & Maturi (2017).

$$\boldsymbol{\beta}(\boldsymbol{\theta}) = \boldsymbol{\theta} - \boldsymbol{\alpha}(\boldsymbol{\theta})\,. \tag{4.1}$$

Here $\boldsymbol{\alpha}(\boldsymbol{\theta})$ is the scaled deflection angle as shown in Figure 4.1. It is linked to the true deflection angle $\hat{\boldsymbol{\alpha}}(D_\mathrm{L}\boldsymbol{\theta})$ via the ratio of angular diameter distances:

$$\boldsymbol{\alpha}(\boldsymbol{\theta}) = \frac{D_\mathrm{LS}}{D_\mathrm{S}}\hat{\boldsymbol{\alpha}}(D_\mathrm{L}\boldsymbol{\theta})\,, \tag{4.2}$$

where D_LS is the angular diameter distance between lens and source. For a source at given true position $\boldsymbol{\beta}$ the lens equation (4.1) can have several solutions $\boldsymbol{\theta}_i$. This means that there are multiple images of the same source.

In general, the imaging properties of a gravitational lens are captured by the deflection potential

$$\psi(\boldsymbol{\theta}) = \frac{1}{\pi}\int \mathrm{d}^2\,\theta'\,\kappa(\boldsymbol{\theta'})\ln|\boldsymbol{\theta}-\boldsymbol{\theta'}|\,, \tag{4.3}$$

where the convergence κ is the dimensionless surface mass density defined as

$$\kappa(\boldsymbol{\theta}) = \frac{\Sigma(D_\mathrm{L}\boldsymbol{\theta})}{\Sigma_\mathrm{crit}} \quad \text{with} \quad \Sigma_\mathrm{crit} = \frac{c^2}{4\pi G}\frac{D_\mathrm{S}}{D_\mathrm{L}D_\mathrm{LS}} = \frac{c^2}{4\pi G}\frac{1}{\beta D_\mathrm{L}}\,. \tag{4.4}$$

In the second equation, we introduced the geometric lensing efficiency

$$\beta = \frac{D_\mathrm{LS}}{D_\mathrm{S}}H(z_\mathrm{s}-z_\mathrm{l})\,. \tag{4.5}$$

This definition accounts for the fact that only sources with redshift z_s behind the lens with redshift z_l get lensed. Here, the Heavyside step function is defined as $H(x) = 1$ for $x > 0$, and $H(x) = 0$ for $x \leq 0$. Therefore, the geometric lensing efficiency is set to zero when $D_\mathrm{LS}/D_\mathrm{S}$ is ill-defined because of $D_\mathrm{S} < D_\mathrm{L}$. The scaled deflection angle can be written in terms of the convergence as

$$\boldsymbol{\alpha}(\boldsymbol{\theta}) = \frac{1}{\pi}\int \mathrm{d}^2\theta'\,\kappa(\boldsymbol{\theta}')\frac{\boldsymbol{\theta}-\boldsymbol{\theta}'}{|\boldsymbol{\theta}-\boldsymbol{\theta}'|^2} = \nabla\psi(\boldsymbol{\theta})\,. \tag{4.6}$$

4.2 Weak gravitational lensing

We can understand the mapping of light rays from the source plane to the image plane in the weak lensing regime through the following consideration. In case of a small source, the variation of the deflection angle across this source will also be small. We can then calculate how the angular separation $\delta\boldsymbol{\beta}$ from the centre of the source to a point at the outer contour of the source relates to the corresponding angular separation in the image plane via the linearised equation (Bartelmann & Maturi, 2017)

$$\delta\boldsymbol{\beta} \approx \mathcal{A}\,\delta\boldsymbol{\theta}\,. \tag{4.7}$$

In this equation the Jacobian matrix

$$\mathcal{A} = \delta_{ij} - \frac{\partial^2\psi(\boldsymbol{\theta})}{\partial\theta_i\partial\theta_j} = \begin{pmatrix} 1-\gamma_1-\kappa & -\gamma_2 \\ -\gamma_2 & 1+\gamma_1-\kappa \end{pmatrix} \tag{4.8}$$

describes the distortions of small light bundles, where the complex components of the shear $\gamma = \gamma_1 + \mathrm{i}\gamma_2$ are given by

$$\gamma_1 = \frac{1}{2}\left(\frac{\partial^2\psi}{\partial\theta_1^2} - \frac{\partial^2\psi}{\partial\theta_2^2}\right), \gamma_2 = \frac{\partial^2\psi}{\partial\theta_1\partial\theta_2}\,. \tag{4.9}$$

The mapping by the Jacobian matrix in Equation (4.8) summarises an isotropic and an anisotropic contribution to the distortions of source shapes. This can be understood by taking the trace of $\mathcal{A}$:

$$\mathrm{tr}\mathcal{A} = 2 - \vec{\nabla}^2\psi = 2(1-\kappa)\,, \tag{4.10}$$

which corresponds to the isotropic part of $\mathcal{A}$. The anisotropic, trace-free part is given by the shear matrix Γ:

$$\Gamma := -\left(\mathcal{A} - \frac{1}{2}(\mathrm{tr}\mathcal{A})\mathcal{I}\right) = \begin{pmatrix}\gamma_1 & \gamma_2\\ \gamma_2 & -\gamma_1\end{pmatrix}, \tag{4.11}$$

where $\mathcal{I}$ denotes the unit matrix. Thus, the convergence κ holds information on the isotropic distortion in the form of contraction or dilation of the source shape. The shear describes the anisotropic distortion. Overall this means that the Jacobian matrix transforms a circular shape into an ellipse (as illustrated in Figure 4.2) with axis ratio $(1-|g|)/(1+|g|)$ and position angle $\alpha = \arctan(g_2/g_1)/2$, where we introduced the reduced shear as $g = \gamma/(1-\kappa)$. In contrast to the unobservable shear γ, the reduced shear g is the central observable quantity in weak lensing studies.

Going back to Equations (4.3) and (4.9), we can see that both the convergence and the shear can be derived from the deflection potential. Based on this, it can be shown that the convergence, i.e., information on the surface mass density, can be obtained from the shear via (Kaiser & Squires, 1993)

$$\kappa(\boldsymbol{\theta}) - \kappa_0 = \frac{1}{\pi}\int \mathrm{d}^2\theta'\,\chi(\boldsymbol{\theta}-\boldsymbol{\theta}')\boldsymbol{\gamma}(\boldsymbol{\theta}')\,, \tag{4.12}$$

where the function $\chi(\boldsymbol{\theta}-\boldsymbol{\theta}')$ denotes an appropriate convolution kernel and κ_0 is a constant indicating that the convergence can only be recovered up to a constant. Consequently, there is no shear in case of a constant convergence. In fact, the mass-sheet degeneracy states that the reduced shear remains unchanged for a transformation of the form $\kappa' = \lambda\kappa + (1-\lambda)$ (Bartelmann & Schneider, 2001).

Furthermore, the surface brightness of a source is conserved when it undergoes gravitational lensing since this process does not involve any absorption or emission of light. The distortion of the source shape leads to a change of the solid angle ω and hence of the observed flux S. Therefore, we observe a magnification μ of the the source

$$\mu = \frac{S}{S_0} = \frac{1}{\det\mathcal{A}} = \frac{1}{(1-\kappa)^2 - |\gamma|^2} = \frac{1}{(1-\kappa)^2(1-|g|^2)}\,. \tag{4.13}$$

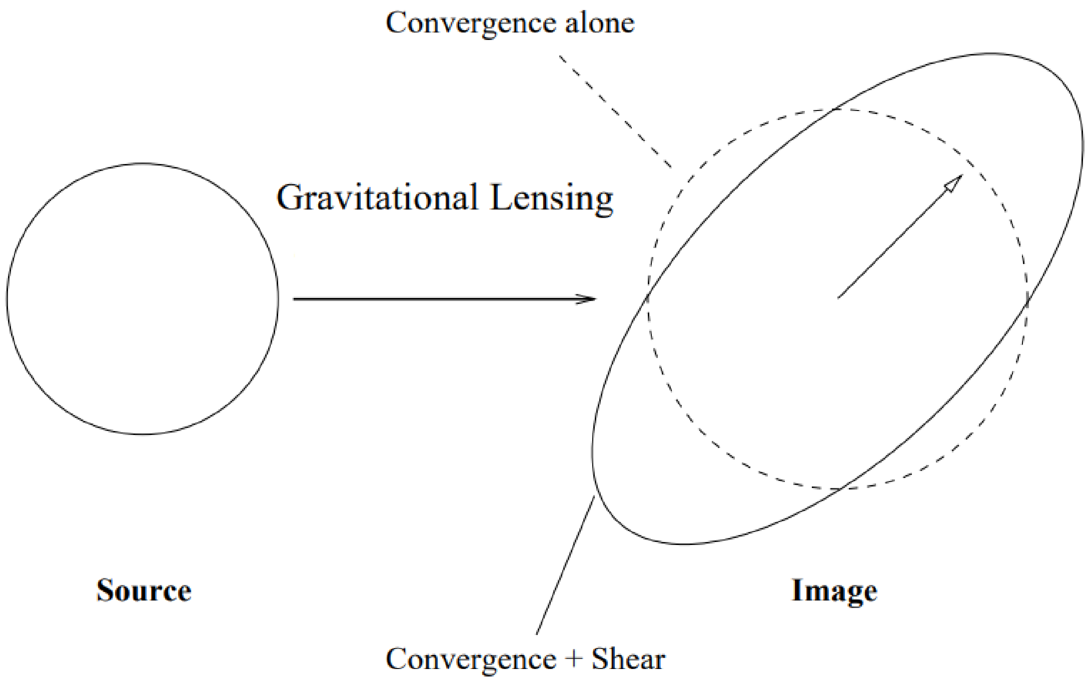

Figure 4.2 – Effects of gravitational lensing on an intrinsically circular source. Convergence causes an isotropic distortion, while shear causes an anisotropic distortion. Figure taken from Umetsu (2010).

In weak gravitational lensing, shear and convergence are very small, i.e., $\kappa \ll 1$ and $|\gamma| \ll 1$. In this case, the distortions of source shapes are significantly smaller than their intrinsic ellipticity. Therefore, this effect can only be measured with a sufficiently high source density of distorted sources. With deep space-based observations, source densities between a few 10 and a few 100 arcmin^{-2} can be achieved for high-redshift clusters (e.g. Jee et al., 2017; Schrabback et al., 2018, with varying source densities depending on the method). In the weak lensing regime, we can approximate the observed ellipticity as the sum of the intrinsic ellipticity and the shear:

$$\epsilon_{\mathrm{obs}} = \frac{\epsilon_{\mathrm{orig}} + g}{1 + g^{*}\epsilon_{\mathrm{orig}}} \approx \epsilon_{\mathrm{orig}} + \gamma \, . \tag{4.14}$$

According to the cosmological principle, the intrinsic orientation of the galaxies should have no preferred direction. Therefore, we expect that, when we average over many galaxies, we should find $\langle \epsilon_{\mathrm{orig}} \rangle = 0$. In contrast to that, the weak lensing effect causes a tangential alignment of the galaxy images with respect to the lens. Since $g \approx \gamma$ for the weak lensing regime, this implies $\langle \epsilon_{\mathrm{obs}} \rangle \approx g$. The uncertainty in the measurement of the shear components γ_i depends on the number N of galaxies involved in the measurement and the dispersion of their intrinsic ellipticities

$$\sigma_{\gamma,i} = \sqrt{\frac{\langle \epsilon_i^2 \rangle}{N}} \,. \tag{4.15}$$

We can infer the ellipticity of a galaxy image from its brightness distribution $I(\boldsymbol{\theta})$ with the help of the tensor of second-order brightness moments

$$Q_{ij} = \frac{\int \mathrm{d}^2\theta \, W(\boldsymbol{\theta}) I(\boldsymbol{\theta}) \theta_i \theta_j}{\int \mathrm{d}^2\theta \, W(\boldsymbol{\theta}) I(\boldsymbol{\theta})} \,, \tag{4.16}$$

with $W(\boldsymbol{\theta})$ as a weight function. Finally, the ellipticity is defined by the components of Q_{ij} via

$$\epsilon = \epsilon_1 + \mathrm{i}\epsilon_2 \equiv \frac{Q_{11} - Q_{22} + 2\mathrm{i}Q_{12}}{Q_{11} + Q_{22} + 2(Q_{11}Q_{22} - Q_{12}^2)^{1/2}} \,, \tag{4.17}$$

or alternatively via

$$e = e_1 + \mathrm{i}e_2 \equiv \frac{Q_{11} - Q_{22} + 2\mathrm{i}Q_{12}}{Q_{11} + Q_{22}} \,. \tag{4.18}$$

Both definitions can be used for shear measurements as they both respond (differently) to it in a well-defined way (Mandelbaum, 2018). When measuring the ellipticity from observations, the signal-to-noise ratio can be improved by applying a weighted average for the ellipticity components with $\alpha \in \{1, 2\}$ according to

$$\langle \epsilon_\alpha \rangle = \frac{\sum \epsilon_{\alpha,i} w_i}{\sum w_i} \,. \tag{4.19}$$

In this work, we employ weights that approximately related to the shear measurement uncertainty per galaxy $\sigma_{\epsilon,i}$ as $w_i = 1/\sigma_{\epsilon,i}^2$. Here, $\sigma_{\epsilon,i}$ includes measurement noise as well as intrinsic shape noise.

Since gravitational lensing causes a tangential alignment of sources with respect to the lens position, it is useful to distinguish a tangential (‘t’) and a cross (‘×’) component of the (reduced) shear, as follows

$$\begin{aligned} g_\mathrm{t} &= -g_1 \cos 2\phi - g_2 \sin 2\phi \,, \\ g_\times &= +g_1 \sin 2\phi - g_2 \cos 2\phi \,, \end{aligned} \tag{4.20}$$

with the azimuth angle ϕ with respect to the lens centre. While the tangential component g_t traces the lensing signal, the cross component $g_\times$ should be consistent with zero. Therefore, it can serve as a cross-check for systematics. The average shear $\langle \gamma_\mathrm{t} \rangle(r)$ at radius r can be written in terms of the convergence as (e.g. Hoekstra et al., 2013)

$$\langle \gamma_\mathrm{t} \rangle(r) = \bar{\kappa}(< r) - \bar{\kappa}(r) = \frac{\bar{\Sigma}(< r) - \bar{\Sigma}(r)}{\Sigma_\mathrm{crit}} \,. \tag{4.21}$$

Here, $\bar{\kappa}(< r)$ and $\bar{\kappa}(r)$ denote the average convergence within an aperture of radius r and the azimuthally averaged convergence at distance r, respectively. This quantity can thus be interpreted as a mass contrast and can be used to reconstruct the projected matter distribution.

4.2.1 Shear measurements with the KSB+ formalism

The observed shape of a galaxy does not only reflect the gravitational shearing of the intrinsic galaxy shape due to the presence of a gravitational lens. Instead, the galaxy image is also modified when the light passes through the atmosphere and telescope optics, an effect, which can be described by a convolution. Additionally, the pixelised sampling of the image and different sources of noise complicate the measurement of the shear. The Kaiser-Squires and Broadhurst (KSB) formalism (Kaiser et al., 1995; Luppino & Kaiser, 1997; Hoekstra et al., 1998) is a widely used method to obtain shear measurements from galaxy images by modelling the impact of the atmosphere and telescope optics using stars in the field as reference sources. Furthermore, Heymans et al. (2006) give detailed insights when they compare different implementations of this method. The work presented here focuses on an extension called KSB+ originally introduced by Hoekstra et al. (1998), and further modified by Erben et al. (2001), Schrabback et al. (2007), and Schrabback et al. (2010).

KSB+ is a moment-based algorithm where objects are parametrised by their weighted second-order brightness moments (analogous to Equations (4.16) and (4.18))

$$Q_{ij} = \int \mathrm{d}^2\theta \, I(\boldsymbol{\theta}) W_{r_\mathrm{g}}(|\boldsymbol{\theta}|)\theta_i\theta_j \,, \tag{4.22}$$

where $W_{r_\mathrm{g}}(|\boldsymbol{\theta}|)$ is a circular Gaussian weight function with scale r_g. In this work, the scale is given by the half-light radius parameter `FLUX_RADIUS` from `Source Extractor` (Bertin & Arnouts, 1996). Weighting helps to reduce biasing of the second-order brightness moments due to noise. The complex ellipticity is given by $e = e_1 + \mathrm{i}e_2$ with

$$e_1 = \frac{Q_{11} - Q_{22}}{Q_{11} + Q_{22}} \,, \quad e_2 = \frac{2Q_{12}}{Q_{11} + Q_{22}} \,. \tag{4.23}$$

This definition is also often referred to as polarisation to distinguish it from the one in Equation (4.17) since both respond differently to shearing.

A detailed understanding of the point-spread function (PSF) is a corner stone of the KSB+ algorithm. The PSF represents the light distribution of an observed point-like source in the image plane. For an ideal, diffraction-limited system, the PSF is characterised by an Airy disc. However, the PSF is blurred in realistic observations and can be approximated better by a two-dimensional Gaussian or a

Moffat profile. For the latter, the intensity $I(r)$ as a function of radius r follows (Moffat, 1969)

$$I(r) = I_0 \left[1 + \left(\frac{r}{\alpha}\right)^2\right]^{-\beta} . \tag{4.24}$$

Here, I_0 represents the amplitude, and the two parameters α and β depend on the observational setup and observation conditions. Typically, the size of the PSF is quantified by its Full-Width at Half Maximum (FWHM), which is also called seeing. It is a measure for the resolution of an observation and can be estimated from stars as representatives of point sources in an image.

To model the effects of PSF smearing and shearing (i.e., how a convolution of a galaxy shape with the PSF distorts the galaxy's shape isotropically and anisotropically, respectively), the KSB+ formalism assumes that the image PSF is represented by a convolution of an isotropic distortion with an anisotropic kernel. The total response of a galaxy image with intrinsic ellipticity e^{s} to both reduced shear g and PSF effects is expressed as

$$e^{\mathrm{obs}}_{\alpha} - e^{\mathrm{s}}_{\alpha} = P^{g}_{\alpha\beta} g_{\beta} + P^{\mathrm{sm}}_{\alpha\beta} q^{*}_{\beta} , \tag{4.25}$$

with $e^{\mathrm{obs}}_{\alpha}$ and e^{s}_{α} ($\alpha \in \{1,2\}$) as components of the observed and intrinsic PSF isotropy-convolved ellipticity, respectively. This equation incorporates both isotropic and anisotropic contributions, which I will describe in more detail in the following.

The observed ellipticity can be corrected for anisotropic effects from the PSF via

$$e^{\mathrm{cor}}_{\alpha} = e^{\mathrm{obs}}_{\alpha} - P^{\mathrm{sm}}_{\alpha\beta} q^{*}_{\beta} . \tag{4.26}$$

The smear polarisability tensor P^{sm} can be measured from higher-order brightness moments (Hoekstra et al., 1998). The anisotropy kernel $q^{*}(\boldsymbol{\theta})$ corrects for PSF anisotropies. It is measured from stellar images (the $*$ denotes quantities referring to stars) in the same frame as the galaxies of interest. Since stars are not affected by the gravitational shear, they follow $e^{\mathrm{s},*} = 0$. Thus, the anisotropy kernel is defined as

$$q^{*}_{\alpha} = (P^{\mathrm{sm},*})^{-1}_{\alpha\beta} e^{\mathrm{obs},*}_{\beta} . \tag{4.27}$$

The isotropic effects from the atmosphere and weight function can be corrected with the help of the pre-seeing shear polarisability tensor P^{g} via

$$e^{\mathrm{cor}}_{\alpha} = e^{\mathrm{s}}_{\alpha} + P^{g}_{\alpha\beta} g_{\beta} , \tag{4.28}$$

with

$$P^{g}_{\alpha\beta} = P^{\mathrm{sh}}_{\alpha\beta} - P^{\mathrm{sm}}_{\alpha\gamma} [(P^{\mathrm{sm},*})^{-1}_{\gamma\delta} P^{\mathrm{sh},*}_{\delta\beta}] . \tag{4.29}$$

Just like P^{sm}, the shear polarisability tensor P^{sh} can be measured from higher-order brightness moments (Hoekstra et al., 1998). If there were no PSF effects, this tensor would describe the total response of a weighted galaxy ellipticity to a gravitational shear (Erben et al., 2001). The tensor P^g includes an additional term to account for the circular smearing from the PSF. Since the trace-free elements are negligible compared to the trace (Erben et al., 2001), an approximation can be used

$$[(P^{\mathrm{sm},*})^{-1}_{\gamma\delta} P^{\mathrm{sh},*}_{\delta\beta}] \approx \frac{\mathrm{Tr}[P^{\mathrm{sh},*}]}{\mathrm{Tr}[P^{\mathrm{sm},*}]}\delta_{\gamma\beta}\,, \quad (P^g)^{-1}_{\alpha\beta} \approx \frac{2}{\mathrm{Tr}[P^g]}\delta_{\alpha\beta}\,. \tag{4.30}$$

The tensors $P^{\mathrm{sm},*}$ and $P^{\mathrm{sh},*}$ are the stellar smear and shear tensors, which are measured from stellar images. Finally, the fully corrected ellipticity

$$e_\alpha = (P^g)^{-1}_{\alpha\beta}[e^{\mathrm{obs}}_\alpha - P^{\mathrm{sm}}_{\beta\gamma} q^*_\gamma] \tag{4.31}$$

serves as the shear estimator in KSB+. Under the assumption of randomly distributed intrinsic ellipticities e^{s} and for $\kappa \ll 1$, we find $\langle e_\alpha \rangle = g \simeq \gamma$.

In practice, some additional considerations need to be taken into account. Firstly, the PSF properties can only be measured at the position of stars, while $q^*(\boldsymbol{\theta})$ and $(P^{\mathrm{sm},*})^{-1}P^{\mathrm{sh},*}$ actually need to be known at the position of the galaxies. However, interpolation with a low-order polynomial is usually a sufficiently good description (Erben et al., 2001). Secondly, measurements are always affected by noise. One can combat this with an appropriate weighting scheme where galaxies are weighted individually according to the accuracy of their ellipticity measurement (Erben et al., 2001). Thirdly, the assumption that the PSF can be described by an isotropic part convolved with an anisotropic kernel may no be a good approximation for some realistic PSF types (Kaiser, 2000). In fact, Heymans et al. (2006) show that the choices regarding the weight functions, PSF modelling, and approximations have a large impact on the performance of shear measurement methods. In their collaborative project called the Shear Testing Programme (STEP), different methods are used to measure the shear of galaxies with a known input shear in simulated ground-based data. They quantify multiplicative calibration biases and additive PSF contaminations in the comparison of measured shear γ and input shear γ^{true} via

$$\gamma - \gamma^{\mathrm{true}} = q(\gamma^{\mathrm{true}})^2 + m\gamma^{\mathrm{true}} + c\,. \tag{4.32}$$

If no calibration biases such as selection bias or weighting bias and no measurement or noise biases are present, one expects $m = 0$. In the absence of PSF anisotropy-related systematics, such as a poor correction for the PSF distortion, one finds $c = 0$. A linear response of the method to the shear is indicated by $q = 0$.

4.2.2 From shear measurements to cluster mass estimates

Following Equation (4.12), it is possible to retrieve the convergence holding information on the surface mass density from the shear field with the help of an appropriate convolution kernel Kaiser & Squires (1993). However, the resulting surface mass map does not provide any information on the total cluster mass due to the mass sheet degeneracy. Additionally, the shear field can only be measured at the discrete locations of the galaxies, making smoothing a requirement. Still, a mass map provides insights into the general distribution of matter. In particular, substructures or a relaxed/disturbed state of a galaxy cluster can be identified (Hoekstra et al., 2013). The peak of the matter distribution can be measured and compared to observations mapping, for example, the distribution of cluster member galaxies or of the ICM to measure positional offsets between different cluster components. This is an especially valuable tool for the investigation of cluster mergers. However, it has to be noted that mass maps represent the projected matter distribution. Therefore, any additional mass concentrations along the line-of-sight such as filaments or other clusters, as well as triaxiality of the cluster itself can hamper the proper interpretation of a mass map (e.g. Israel et al., 2012). Furthermore, the highest peak in the reconstructed mass maps does not necessarily coincide with the projected position of the 3D cluster centre as found in simulations (Dietrich et al., 2012). While the offsets are very small in noise-free simulations, they are increased significantly by smoothing and shape noise.

The total cluster mass can be constrained by fitting the tangential shear measurements with a reduced shear profile model assuming a suitable density profile for the cluster mass distribution. A spherical NFW density profile is used frequently for this purpose. The fit reduces to a one-parameter model fit with the cluster mass as free parameter when a fixed concentration-mass relation is assumed. For instance, Diemer & Kravtsov (2015) find a general form for the concentration of

$$c_{200,\mathrm{c}} = \frac{c_{\mathrm{min}}}{2}\left[\left(\frac{\nu}{\nu_{\mathrm{min}}}\right)^{-\alpha} + \left(\frac{\nu}{\nu_{\mathrm{min}}}\right)^{\beta}\right] , \tag{4.33}$$

where $c_{200,\mathrm{c}}$ denotes the concentration for a spherical halo with a mean density 200 times higher than the critical density at the cluster redshift, and ν is the halo mass expressed as a peak height $\nu \equiv \delta_\mathrm{c}/\sigma(M, z)$ with the critical overdensity for collapse $\delta_\mathrm{c} = 1.686$ (see Section 2.3.3) and the r.m.s. density fluctuation σ in a sphere of radius R.

Deviations of the cluster from an NFW profile, triaxial or complex mass distributions (e.g. due to mergers), correlated large scale structure, and miscentering of the fitted reduced shear profile can lead to systematic biases of masses measured based on weak gravitational lensing with respect to the unobservable true mass (e.g. Sommer et al., 2022). This bias is quantified in terms of the factor

$$b_{\Delta,\mathrm{WL}} = \frac{M_{\Delta,\mathrm{WL}}}{M_{\Delta,\mathrm{true}}} , \tag{4.34}$$

with the measured weak lensing mass $M_{\Delta,\mathrm{WL}}$ at an overdensity Δ, which is typically smaller than the true mass $M_{\Delta,\mathrm{true}}$. This bias also depends on the specific properties of the cluster like mass and redshift and on the measurement setup regarding the employed concentration-mass relation and radial fitting range. Furthermore, fitting the tangential shear measurements requires accurate knowledge of the true cluster centre for which centres from X-ray or SZ observations are commonly used as a proxy. However, these usually do not coincide with the 3D halo centre, and a miscentered fit will bias the mass measurement low.

Therefore, the miscentering distribution has to be carefully modelled and incorporated into the estimation of the weak lensing mass bias from simulations. This way, it is possible to account for systematic biases of the mass constraints and to properly take the resulting uncertainties into account (e.g. van Uitert et al., 2016; Zhang et al., 2019; Schrabback et al., 2021; Sommer et al., 2022; Grandis et al., 2021).

4.3 Background source selection

When measuring the shear of sources that have been distorted by gravitational lensing, it is important to include primarily (and ideally only) sources behind the gravitational lens. Only background galaxies are affected by the lensing signal while galaxies in the foreground and particularly at the cluster redshift dilute the signal and ultimately bias the weak lensing mass estimate low. Redshift information of galaxies enables a distinction between foreground or cluster galaxies and the background galaxies. Additionally, the redshifts of the lens and the redshift distribution of the sources are required to calculate the critical surface mass density Σ_{crit}. In turn, this allows relating the measured shear signal to the physical quantity of interest, i.e., the mass.

4.3.1 Spectroscopic and photometric redshifts

Measuring the redshift of a galaxy requires observing its spectral energy distribution (SED, i.e., continuum and absorption/emission line features), which is redshifted according to Equation (2.2). Spectroscopic redshifts are considered to be the most precise. Here, the full spectrum of the flux as a function of the wavelength of a galaxy is obtained. It is possible to identify characteristic absorption or emission lines and then infer the spectroscopic redshift by comparing the observed wavelength and the wavelength at emission. A robust spectroscopic redshift measurement requires the identification of at least two spectral lines (Salvato et al., 2019). Then, the redshift can be constrained with an uncertainty of the order of 10^{-3} at $R = \lambda/\Delta\Lambda > 200$ (e.g. Le Fèvre et al., 2005). However, these measurements require long exposures and are limited in depth. Consequently, they are not practical for most observations that involve large numbers of faint galaxies (e.g. weak lensing studies).

Photometric redshifts provide a more accessible alternative. These measurements are based on multi-band photometry of galaxies representing a sparse sampling of the SED. While spectral lines cannot be identified, the Balmer and Lyman breaks imply characteristic colours, especially if the employed filter bands bridge one or both of the respective breaks. This allows for redshift constraints, which are improved when a broader wavelength coverage is available. To infer a photometric redshift, a mapping between colours and redshifts is required. The two primary methods to obtain the mapping are template fitting and machine learning techniques.

The former makes use of templates for SEDs of galaxies. These can either be inferred from theory through stellar synthesis models or from observations through measured spectra from galaxies. There are different templates for different types of galaxies. Using the transmission curves of the filters employed for the photometric redshift measurement, the expected flux of a galaxy following the template SED can be predicted at a given redshift. Comparing the observed fluxes to the expected fluxes enables the photometric redshift measurement in the form of a probability distribution function, indicating the most likely redshift of the galaxy. Popular template fitting codes include `EAZY` (Brammer et al., 2008) and `BPZ` (Benítez, 2000).

Machine learning algorithms do not rely on galaxy SED templates. Here, the mapping between colours and redshifts is directly ‘learned’ from a training sample. Consequently, the accuracy of machine learning algorithms depends on the quality of the training sample. This includes wavelength coverage, depth of the data, and how well the training sample represents the properties of the sample for which photometric redshift measurements are desired. Salvato et al. (2019) provide a detailed review on redshift measurements, focussing primarily on photometric redshifts.

4.3.2 Estimation of the source redshift distribution

If the photometric redshifts of the background galaxies are well-known (i.e., we can safely assume negligible scatter and bias), one can easily compute their redshift distribution and geometric lensing efficiency β. In particular, the slope $\partial\beta/\partial z$ of the galaxy sample quantifies the sensitivity to the source redshift distribution and its errors or statistical variations (Hoekstra et al., 2013). The reason is that for a large slope, even a small change in the source redshift leads to a relatively large change in β (which is proportional to the lensing amplitude).

Unfortunately, high-quality photometric redshifts are not always available, as they require observations in as many filter bands as possible. There are, however, a few approaches that still allow for a distinction between the background sources of interest and the contaminating foreground and cluster galaxies (Hoekstra et al., 2013).

1. Statistical correction:
   This method assumes that the number density of galaxies is not affected by cluster members at large distances from the cluster centre. The number density there represents a background level of galaxies. A statistical correction for the contamination by cluster galaxies can be inferred by quantifying the excess of

galaxy counts towards the cluster centre. This method is only applicable when the observations have a large field of view. A small field of view would result in high systematic uncertainties.

2. Colour-magnitude diagram:
   Early-type galaxies in galaxy clusters typically follow the so-called red-sequence (see Section 3.1.1). This means that these galaxies populate a line in a colour versus magnitude plane whose slope and intercept depend on the cluster redshift and the filters involved. These red-sequence galaxies are redder than the other cluster members and the foreground galaxies. Hence, a selection of galaxies with redder colour than the red-sequence galaxies enables to discard contaminating foreground and cluster galaxies. However, this also removes blue background galaxies and, in turn, this method suffers from a low source density of selected background galaxies.

3. Colour-colour diagram:
   Due to the typical shape of the SEDs of different galaxy types, they populate different regions in colour-colour space depending on the given redshift and on the colours involved. This allows a distinction of the background galaxy population from galaxies in the foreground and galaxies at the cluster redshift by applying suitable cuts based on colour (see Chapter 7 for a detailed example of an application of this method). It is possible to identify these regions occupied by background galaxies with the help of a well-measured photometric or spectroscopic reference catalogue of galaxies at various redshifts. The cuts applicable in the reference catalogue can be transferred to any other field under the assumption that the average redshift distribution is the same independent of the line-of-sight. In this context, it is necessary to characterise the reference catalogue as precisely as possible regarding possible systematics, for example, due to cosmic variance, limited field coverage, limited completeness, or systematic redshift errors.

Independent of the applied method, it is important to know the source redshift distribution to measure the cluster mass with weak gravitational lensing. A photometric redshift reference catalogue allows for an estimate of the source redshift distribution by applying the same source selection as in one of the three methods described above. Then, one can compute the average geometric lensing efficiency $\langle\beta\rangle$ of the background galaxy population, which is typically sufficient for a weak lensing mass analysis.

CHAPTER 5

Tools and techniques in optical observations

We rely on observations with telescopes to investigate various scientific questions. Depending on the goal, different telescopes are most suitable. This work focuses on either weak lensing studies or follow-up observations of galaxy clusters detected through their SZ signal. Both of these require optical observations.

For weak lensing studies, there are two important aspects, which the optical images have to fulfil. Firstly, deep observations are required to detect as many faint background galaxies as possible with a high signal-to-noise ratio. Secondly, shape measurements of galaxies form the basis of weak lensing analyses. Hence, the observations must provide a sufficiently high resolution. These requirements are best met by a space-based telescope such as the *Hubble Space Telescope* (*HST*).

For follow-up observations that aim to confirm galaxy clusters, rather the colours than the shapes of galaxies are of interest because they allow for measurements of photometric redshifts. This can very well be achieved with ground-based telescopes, such as, in particular, the Willliam Herschel Telescope (WHT), which was used for the follow-up study of galaxy clusters presented in this work (see Chapter 6).

In this section, I address some of the key concepts in the context of optical observations. For a more in-depth introduction the reader is referred to, e.g., Howell (2006) or Chromey (2010).

5.1 Imaging with CCDs

Charge-coupled device (CCD)

CCDs are two-dimensional semiconductor detectors. When a CCD is exposed to light, the photoelectric effect generates charges, i.e., electrons. These gather in potential wells, which correspond to the pixels of the detector. Here, the pixel scale indicates the angle in the sky covered by one pixel (unit: ″/pix). After a defined amount of time called the integration time, the CCD is read out. This means that the collected charges are transferred to an amplifier via parallel and serial shifts by manipulating the potential wells of the pixels. The charges per pixel are converted into a digital number by an analogue-to-digital converter (ADC) and have the analogue-to-digital unit (ADU). Notable advantages of CCDs include their high quantum efficiency of $\gtrsim 90$ per cent, geometric stability, robustness concerning over-exposure, and linear response over the full large dynamic range. These make them the most widely used detectors for imaging in astronomy.

Calibration frames

Calibration frames are applied to raw observation frames to remove detector signatures, which would otherwise affect the astronomical signal of interest.

- Bias frame:
  A bias frame has zero exposure time. This means that an unexposed CCD is read out, and from this, the bias level and read-out noise can be determined. The bias level is an offset, which is added on purpose to ensure that the signal always remains positive even in the presence of noise fluctuations. This is necessary because the amplifiers in the CCDs work logarithmically and cannot handle negative values. The bias level is an additive effect. Hence, typically the median of around ten bias frames is subtracted from the scientific frame. The read-out noise is caused by the electronics during the read-out process. It limits the detector sensitivity at low count rates.

- Dark frame:
  CCDs are affected by thermal noise. This can generate free electrons, which gather in the potential wells, just like the ones initially produced by the photoelectric effect. Since the effect is temperature-dependent, cooling is an efficient way to mitigate the problem. The remaining excess charge from thermal noise can be accounted for with a dark frame. To obtain a dark frame, the CCD is exposed for the same exposure time[1] as the scientific frames, but the shutter is closed. After subtraction of the bias, the median of around ten dark frames is subtracted from the scientific frame to remove the dark current signature.

---

[1] It is also possible to take a different exposure time, but then the dark frame has to be rescaled to obtain the correct level for the scientific frame.

- Flat frame:
  The quantum efficiency of a CCD may vary on a pixel-to-pixel basis. Additionally, vignetting effects, dust, or other imperfections may also cause that an identical signal does not produce an identical response across all pixels. The flat frame can account for this. Here, the CCD is illuminated uniformly by observing the twilight sky or a screen within the dome. Around ten flat frames are median combined and then normalised by rescaling to the mode of the frame. For calibration, the scientific frames are divided by this master flat frame.

5.2 Photometry

Magnitudes

Magnitudes are a measure of the (apparent) brightness of an astronomical source. It is logarithmically related to the flux of the source. In particular, one can find the difference in magnitude between two sources with fluxes f_1 and f_2 and magnitudes m_1 and m_2 through

$$m_1 - m_2 = -2.5 \log_{10} \left(\frac{f_1}{f_2} \right) . \tag{5.1}$$

If the magnitude refers to the total flux of a source it is called the bolometric magnitude. However, magnitudes are more commonly measured with respect to a restricted band-pass. In the frequently used AB-magnitude system, the magnitude m_{AB} for a source with monochromatic flux f_ν is

$$m_{\mathrm{AB}} = -2.5 \log_{10}(f_\nu) - 48.60 . \tag{5.2}$$

Here, f_ν is given in the unit of $\mathrm{ergs\,sec^{-1}\,cm^{-2}\,Hz^{-1}}$ and the constant fulfils the requirement $m_{\mathrm{AB}} = m_{\mathrm{Vega}}$ for a flat-spectrum source (Oke & Gunn, 1983). In practice, this definition is applied by integration over the relevant bandpass of an observation.

There are different ways to measure magnitudes from an image. Such measurements are commonly conducted with the software `Source Extractor` (Bertin & Arnouts, 1996). It distinguishes flux and inferred magnitude measurements within either fixed or adaptive apertures. For a fixed aperture magnitude measurement (referred to as `MAG_APER` within the software `Source Extractor`), the entire flux above the background level within a circular aperture of fixed size is taken into account independent of the source properties. This method is considered to be robust in particular for colour measurements of galaxies (e.g. Skelton et al., 2014).

Within the framework of `Source Extractor`, the `AUTO` flux measures the 'total flux' from a source in a given filter band within an adaptively scaled aperture, which is defined based on the first moment of a source according to (Kron, 1980)

$$r_1 = \frac{\sum r I(r)}{\sum I(r)} , \tag{5.3}$$

where $I(r)$ is the light distribution function as a function of radius r. It is expected that $\gtrsim$ 90 per cent of the source flux of a star or galaxy profile convolved with Gaussian PSF is contained within $2r_1$.

Photometric zeropoint

The flux f is measured in the unit of counts per second in the instrument system. To properly convert this value into a meaningful, instrument-independent magnitude m the instrument-specific zeropoint ZP has to be calibrated. This zeropoint is defined as the magnitude of an object that produces 1 count per second on the detector (Baggett et al., 2002), so that we can calculate

$$m = \mathrm{ZP} - 2.5\log_{10}(f)\,. \tag{5.4}$$

PSF-homogenisation

Especially for ground-based telescopes, the PSF size or seeing strongly depends on the Earth's atmosphere, whose refractive index varies on temporal and spatial scales due to turbulence. Additionally, the airmass, i.e., the amount of atmosphere along the line-of-sight, affects the seeing. The airmass a amounts to $a \approx 1/\cos z$, with z as the angle with respect to the zenith. Space-based observations typically exhibit a much higher resolution due to the lack of atmosphere along the line-of-sight. The PSF size can vary significantly across imaging from different filter bands, especially when comparing ground-based and space telescopes. This poses a problem for colour measurements with fixed aperture photometry because the aperture does not measure the flux from the same intrinsic part of the galaxies. In such a case, a PSF homogenisation is required. As a first step, the PSF size in each observation is measured from stars in the image. Then the images with smaller PSF sizes are convolved with a suitable kernel (e.g. obtained using`PSFEx`, Bertin, 2011) to broaden the PSF size to match the one from the image with the largest PSF size. After the PSF homogenisation, consistent photometric measurements with fixed apertures can be performed.

5σ-depth

The depth of an observation quantifies the magnitude of the faintest detectable objects. In principle, longer integration times imply deeper observations. The depth is commonly expressed in terms of the 5σ limiting magnitude. The flux of a source at this magnitude is five times as high as the noise level σ.

5.3 Common units

- Solar masses: Masses are typically expressed in reference to the mass of our Sun $\mathrm{M}_\odot$. One solar mass corresponds to $\mathrm{M}_\odot \approx 2.0 \times 10^{30}\,\mathrm{kg}$.

- Parsec: Distances in astronomy are most commonly measured in the unit of parsecs (short pc). It is defined as the distance to an object with a parallax angle of 1 arcsecond (1/3600 degrees), i.e., $1\,\mathrm{pc} = 3.0857 \times 10^{16}\,\mathrm{m}$ in SI-units.

- R_Δ: The density within the radius R_Δ is Δ times higher than the critical density at the given redshift.

- M_Δ: The mass enclosed in a sphere of radius R_Δ is called M_Δ.

CHAPTER 6

Optical follow-up study of 32 high-redshift galaxy cluster candidates from *Planck* with the William Herschel Telescope

---

Preface

This chapter reproduces the article 'Optical follow-up study of 32 high-redshift galaxy cluster candidates from *Planck* with the William Herschel Telescope', which was first published as Zohren et al. (2019) in the journal Monthly Notices of the Royal Astronomical Society (MNRAS), Volume 488, Issue 2, September 2019, Pages 2523 – 2542. The manuscript is reproduced following the guidelines by MNRAS granting the author of an article the right to include said article in full or in part in a thesis or dissertation. The reproduction includes minor editorial changes to fit the format of this document, but none of the content from the published article is changed.

The article comprises results previously documented in my master thesis 'Spectroscopic and Photometric Analysis of Observational Data of a Sample of Galaxy Cluster Candidates from the Planck SZ2 Catalogue' (2018), as well as refined steps of the analysis conducted as a continuation of the project within the framework of my Ph.D. For clarity, I provide a summary here of the research conducted as part of the master thesis and as part of the Ph.D. thesis, respectively.

Contributions to the article conducted in the context of the master thesis include:

- Spectroscopic analysis of ACAM data: reduction of raw data with `IRAF`, extraction and calibration of spectra, preliminary estimate of spectroscopic redshift by eye.

- Photometric analysis of ACAM data: reduction of ACAM data in r, i, and z bands, PSF-homogenisation with `PSFEx`, photometric calibration (zeropoints and colour terms) with the help of the Pan-STARRS 1 catalogues, measurement of seeing and data quality (5σ limiting magnitudes).

- Setup of red-sequence models as the basis to estimate photometric redshifts and richnesses of galaxy cluster candidates (the models themselves were developed by co-author Remco van der Burg), obtaining preliminary estimates of photometric redshifts and richnesses including a background subtraction, a completeness correction, magnitude cuts, and colour and radial weights.

- Obtaining preliminary richness-based mass estimates $M_{500\mathrm{c},\lambda}$ (based on the richness-mass scaling relation by Rozo et al., 2015) and SZ-mass estimates $M_{500\mathrm{c,SZ}}$ (inferred with the help of the preliminary photometric redshift estimates; the SZ-mass estimates were calculated by co-authors Monique Arnaud and Jean-Baptiste Melin), estimates of the distances between optical and SZ-centres.

- Preliminary comparison of spectroscopic redshifts (measured and from the literature) and measured photometric redshifts, identifying the overestimation of photometric redshifts.

Contributions to the article conducted in the context of the Ph.D. thesis include:

- Obtaining improved estimates of spectroscopic redshifts via cross-correlation of the extracted spectra with an absorption or emission line template and improved estimates of the uncertainties by fitting a Gaussian to the peak in the cross-correlation.

- Improving the consistency by using the i-band as the reference band for the red-sequence models instead of the z-band (as done in the master thesis).

- In-depth comparison of photometric and spectroscopic redshifts including a full reanalysis of photometric data from Buddendiek et al. (2015) obtaining photometric redshifts for 15 of their observed clusters with our pipeline and comparing them to the reported spectroscopic redshifts.

- Performing an iterative recalibration of red-sequence models with the help of spectroscopic redshifts.

- Calculating the 80 per cent depth limits of the observed cluster fields and including them into the pipeline for the estimation of photometric redshifts, richnesses, and richness-based masses.

- Re-evaluating the photometric redshifts, richnesses, richness-based masses, and SZ-based masses (the latter were calculated by co-authors Monique Arnaud and Jean-Baptiste Melin).
- Adding detailed notes on individual cluster candidates including a comparison to information from the literature.

I am the leading author of the article mentioned above and collaborated with the co-authors, whose contributions I summarise as follows: Tim Schrabback was my day-to-day supervisor for this project, he is the PI of the two visitor mode observation runs at the William Herschel Telescope (WHT) and participated in one of them. Remco van der Burg developed the original red-sequence models and modified them to match the Pan-STARRS-based photometric system. He also participated in both visitor mode observation runs. Monique Arnaud and Jean-Baptiste Melin calculated the SZ-based masses using the photometric redshifts measured in the study. Jan Luca van den Busch participated in both visitor mode observation runs and contributed to the data reduction of the WHT observations. Henk Hoekstra is the PI of the two service mode observation runs at the WHT. The red-sequence analysis and inference of the richness is adapted from the works by Klein et al. (2018), Klein et al. (2019), and van der Burg et al. (2016). Matthias Klein and Remco van der Burg helped to refine the analysis to be applicable for the study presented here, specifically. All co-authors were involved in proof-reading and refining the article itself.

6.1 Abstract

The *Planck* satellite has detected cluster candidates via the Sunyaev Zel'dovich (SZ) effect, but the optical follow-up required to confirm these candidates is still incomplete, especially at high redshifts and for SZ detections at low significance. In this work, we present our analysis of optical observations obtained for 32 *Planck* cluster candidates using ACAM on the 4.2-m William Herschel Telescope. These cluster candidates were preselected using SDSS, WISE, and Pan-STARRS images to likely represent distant clusters at redshifts $z \gtrsim 0.7$. We obtain photometric redshift and richness estimates for all of the cluster candidates from a red-sequence analysis of r-, i-, and z-band imaging data. In addition, long-slit observations allow us to measure the redshifts of a subset of the clusters spectroscopically. The optical richness is often lower than expected from the inferred SZ-mass when compared to scaling relations previously calibrated at low redshifts. This likely indicates the impact of Eddington bias and projection effects or noise-induced detections, especially at low SZ-significance. Thus, optical follow-up provides not only redshift measurements but also an important independent verification method. We find that 18 (7) of the candidates at redshifts $z > 0.5$ ($z > 0.8$) are at least half as rich as expected from

scaling relations, thereby clearly confirming these candidates as massive clusters. While the complex selection function of our sample due to our preselection hampers its use for cosmological studies, we do provide a validation of massive high-redshift clusters particularly suitable for further astrophysical investigations.

6.2 Introduction

One of the core challenges in contemporary astrophysics is to explain the nature of dark matter and dark energy. Past efforts in understanding the parameters that govern our Universe have led to our fiducial Lambda-cold-dark-matter (ΛCDM) cosmological model, which includes a hierarchical structure formation, where dark energy takes the form of a spatially uniform and non-evolving energy density. In order to constrain the cosmological model from an observational point of view, galaxy clusters have proven to be valuable objects to study. They are the most massive gravitationally bound structures, which reside in the densest regions of the cosmic large-scale structure. Driven by gravity, the large-scale structure emerged from small over-densities in the density field of the early Universe. Probing the growth of the densest fluctuations, the number of clusters as a function of mass and redshift sensitively depends on cosmological parameters (e.g. Allen et al., 2011).

Samples of galaxy clusters form the foundation for such cosmological investigations. In order to compare their properties to theoretical predictions, they should ideally be selected based on their mass. Unfortunately, the mass is not directly observable. However, galaxy clusters are multi-component objects observable in various wavelength regimes. They can be detected from their emission in the X-ray (e.g. Piffaretti et al., 2011; Pacaud et al., 2016), in the optical and near-infrared (e.g. Rykoff et al., 2016), via the Sunyaev Zel'dovich (SZ) effect (e.g. Bleem et al., 2015; Planck Collaboration et al., 2016c; Hilton et al., 2018), and recently through their gravitational lensing signal (e.g. Miyazaki et al., 2018). Scaling relations then allow to connect the cluster observables to their mass and make it possible to assemble samples of galaxy clusters with a known selection function (Pratt et al., 2019). The challenge in this context is to carefully calibrate these relations to connect the observables and still account for intrinsic scatter (Allen et al., 2011).

The detection of galaxy clusters via the SZ effect provides cluster samples that are nearly mass-limited. This is because the SZ effect, caused by an inverse Compton scatter of CMB photons by the hot electrons in the cluster plasma, is not subject to cosmic dimming (Carlstrom et al., 2002). Specifically, the *Planck* SZ Survey provides the first all-sky SZ detected cluster catalogue, including detections of massive clusters out to redshifts of $z \approx 1$. The full mission catalogue is called PSZ2 and was publicly released in 2016 (Planck Collaboration et al., 2016c). It contains SZ detections down to a significance of signal-to-noise ratio $\mathrm{S/N} \geq 4.5$. The follow-up and verification process is ongoing (Liu et al., 2015; Planck Collaboration et al., 2016c;

van der Burg et al., 2016; Burenin et al., 2018; Amodeo et al., 2018; Barrena et al., 2018; Streblyanska et al., 2018; Boada et al., 2018), but still incomplete, especially at high redshifts. The primary goal of this work is to help complete the follow-up of cluster candidates in the PSZ2 catalogue at high redshifts $z \gtrsim 0.7$ with the help of optical data from the William Herschel Telescope. In the redshift regime above $z \sim 0.7$ the PSZ2 catalogue has a completeness of about 80 per cent for massive clusters of $M_{500c} \gtrsim 7.5 \times 10^{14}\,\mathrm{M}_{\odot}$. The completeness decreases, however, to 20 per cent for masses of $M_{500c} \gtrsim 5 \times 10^{14}\,\mathrm{M}_{\odot}$ in that redshift regime (Fig. 26 in Planck Collaboration et al., 2016c). Considering cluster candidates at a lower S/N threshold is a way to raise the completeness and reveal more massive high-z clusters. The sample studied in this work therefore also includes low significance candidates detected from the *Planck* SZ-maps via the Matched Multi-Filter 3 (Melin et al., 2006, 2012) detection method with a SZ-significance down to S/N $\gtrsim$ 3. Since a lower S/N threshold also implies a lower reliability of the sources, confirmation using additional data is critically required. In this work, we apply a preselection of cluster candidates based on optical and infrared data as suggested in van der Burg et al. (2016). This helps to exclude those SZ sources that are likely spurious detections because they lack a counterpart in the optical and infrared data. As a result of these considerations, this work deals with the analysis of spectroscopic and photometric data of a sample of 32 cluster candidates, which originate either from the PSZ2 or from detection in the *Planck* maps below the PSZ2 significance cut with the primary aim of confirming massive galaxy cluster candidates at high redshifts.

We structure this paper as follows. In Section 6.3 we present the *Planck* SZ-Survey, which builds the foundation for the cluster candidate sample that we follow-up optically in this work. We focus on the photometric observations in Section 6.4 explaining the data reduction and the strategy to obtain redshift and richness estimates. We present the analysis of the spectroscopic observations in Section 6.5. In Section 6.6, we discuss which cluster candidates are likely counterparts to the SZ detections by comparing our richness estimates to the SZ-masses inferred from the SZ-signal. We give notes on individual cluster candidates and briefly discuss our results in Sections 6.7 and 6.8. Finally, we give a summary and conclusions of our work in Section 6.9.

Unless otherwise noted, we adopt a flat ΛCDM cosmology with $\Omega_\mathrm{M} = 0.3$, $\Omega_\Lambda = 0.7$, and $H_0 = 70\,\mathrm{km\,s^{-1}Mpc^{-1}}$ in this work, as approximately consistent with recent CMB results (e.g. Hinshaw et al., 2013; Planck Collaboration et al., 2016a). All magnitudes are given in the AB magnitude system.

6.3 The *Planck* catalogue as basis for the cluster candidate sample

Most of the cluster candidates in our sample originate from the second *Planck* catalogue of Sunyaev Zel'dovich (SZ) sources (PSZ2). This catalogue represents the largest SZ-selected sample of galaxy clusters to date[1] and it is the deepest systematic all-sky survey of galaxy clusters (Planck Collaboration et al., 2016c). It includes 1653 detections in the 29 month full mission data, 1203 of which are confirmed with identified counterparts in external data sets and 1094 of which have redshift estimates. Clusters are included in the public PSZ2 catalogue down to a signal-to-noise ratio of $S/N = 4.5$, defined via three different detection methods: MMF1, MMF3 and PwS. We refer the reader to Planck Collaboration et al. (2016c) for a more detailed description. The parameter estimates are taken from the detection pipeline with the highest S/N ratio for a given detection.

The remainder of cluster candidates in our sample is assembled from SZ detections in the *Planck* maps with $S/N \geq 3$ that are solely based on the MMF3 detection method. The masses and S/N ratios in the PSZ2 catalogue are by construction always larger than or equal to the corresponding values obtained from the MMF3 detection method.

We selected targets from the PSZ2 with the prospect of contributing to a complete follow-up of all targets down to $S/N = 4.5$. A complete follow-up is essential to understand the selection function including the completeness and purity of the PSZ2 catalogue in order to use it for cosmological studies. In particular, we focus on the high-redshift regime at $z \gtrsim 0.7$ among the PSZ2 candidates that were still unconfirmed at the time of target selection. We inspect optical and NIR data from SDSS (Aihara et al., 2011), Pan-STARRS (Chambers et al., 2016) and WISE $3.4\,\mu$m (Wright et al., 2010) to help us identify the high-redshift targets. Images in the r-, i- and z-band from SDSS and Pan-STARRS should display colours that are consistent with early-type galaxies at $z \gtrsim 0.7$. Here, particularly a missing counterpart in the r-band provides hints at a high-redshift candidate. In principle, a reliability of ≈ 90 per cent is expected for cluster candidates from the PSZ2 catalogue (see Fig. 11 in Planck Collaboration et al., 2016c). We also expect a positional uncertainty of approximately 1.5 arcmin for the PSZ2 cluster candidates (Planck Collaboration et al., 2016c).

The *Planck* maps can be exploited further by exploring the lower S/N regime for massive high-redshift clusters suitable for astrophysical investigations. We additionally selected targets detected through the MMF3 detection method for our study with this purpose in mind. Here, we focused on the regime $3 < S/N < 4.5$, which is not covered by the PSZ2 catalogue, to look for rich cluster candidates at redshifts above $z \gtrsim 0.7$. Due to the decreasing reliability in the low S/N regime of the MMF3

---

[1] At the time the article was published in September 2019.

detected clusters, an identification of likely cluster candidates from among the numerous detections down to S/N = 3, requires an adequate preselection. For this, we focused on the Pan-STARRS/SDSS i-band and the WISE 3.4 μm band, looking for over-densities of red galaxies by eye. These complex selection criteria make it hard to assess the reliability of our MMF3 cluster candidates and render the MMF3 sample unsuitable for cosmological studies. Our investigated sample finally includes a total of 32 cluster candidates, with 23 candidates from the PSZ2 catalogue and 9 candidates detected with the MMF3 method.

The PSZ2 catalogue includes an additional parameter Q_{neural}, which is an indicator for the quality of a detection, i.e., $Q_{\mathrm{neural}} < 0.4$ marks detections of low reliability (Planck Collaboration et al., 2016c; Aghanim et al., 2015; Hurier et al., 2017). This quantity is based on the spectral energy distribution for each detection over the different frequency bands, as assessed by a neural network. It is sensitive to IR-induced spurious detections but is not constructed to flag detections caused by noise, which are more likely to occur in the low S/N regime. We examine the use of Q_{neural} in this regime in Section 6.6.

Noise-induced detections or projection effects of multiple clusters contributing to the SZ signal can cause a discrepancy between optical and SZ measurements. Apart from that, we expect Eddington bias to play a significant role for our cluster candidate sample. This purely statistical type of bias leads to a distorted view of the underlying distribution of objects when a cut in significance is applied (Eddington, 1913). It can be comprehended from the following considerations: galaxy clusters follow a steep halo mass function (Tinker et al., 2008) with numerous low-mass haloes but only a few high-mass haloes. When these haloes are detected in the *Planck* maps, they carry an additional (approximately Gaussian) noise contribution (Planck Collaboration et al., 2016c). Accordingly, it is expected that more low-mass clusters scatter over the SZ-significance threshold for detection than high-mass clusters scatter below the threshold. This implies that sources at low S/N are more likely to be up-scattered and hence their SZ-based mass will be overestimated. This causes a systematic bias, which depends on the significance threshold and the redshift (van der Burg et al., 2016).

6.4 Photometric observations

We use imaging data in the Sloan r-, i- and z-band obtained with the Auxiliary-port CAMera (ACAM, Benn et al., 2008) at the 4.2-m William Herschel Telescope (WHT) to optically follow-up the 32 cluster candidates in our selected sample. In imaging mode, ACAM has a circular field of view of 8.3 arcmin diameter with a pixel scale of $0\farcs25$/pix on a red-optimised chip with 2148 × 2500 pixels. The filters are especially useful for the red-sequence analysis, because they bridge the 4000 Å-break in the targeted redshift regime (z $\gtrsim$ 0.7).

The observations were completed in four separate runs: two service mode observation runs (PI: Hoekstra) on 2015 December 12 and 2016 January 19, and two visitor mode runs (PI: Schrabback) with two nights on 2016 October 6 and 2016 October 7 and three nights from 2017 March 20 to 2017 March 22. We observed the clusters with a total integration time between 630 s and 1800 s per filter depending on the roughly estimated redshift of the cluster and the observing conditions of the night.

6.4.1 Data reduction and calibration

For the data reduction of the WHT imaging data, we employ the `GUI` version of the THELI[2] pipeline (Erben et al., 2005; Schirmer, 2013). The reduction includes a bias subtraction, flat-field correction, and a subtraction of a background and a fringe model. For the background model, we make use of the dither pattern that was applied between exposures. This allows us to distinguish between features at a fixed position on the CCD and sky-related signals. The astrometric solution is calculated in THELI with the help of the SDSS DR8 or the USNO-B1 reference catalogue. Finally, the images are co-added.

We decide to use aperture magnitudes for the colour measurement of the galaxies, because they are reasonably robust at the low S/N regime of faint galaxies. For reliable colours, we need to make sure to always consider the flux from the same intrinsic part of the galaxy in each band. The image quality in the co-added images varies depending on the night of observation and on the band that was used (see Table 6.1). On average we find a FWHM PSF size of $1\farcs21$ in the r-band, $1\farcs20$ in the i-band and $1\farcs14$ in the z-band. To enable robust photometric measurements, we therefore perform a PSF homogenisation of the co-added images using the software PSFEx (Bertin, 2011). The PSF profile in our observations is best described by a Moffat profile:

$$I(r) = I_0 \left[1 + \left(\frac{r}{\alpha} \right)^2 \right]^{-\beta} . \tag{6.1}$$

We target a PSF profile with a 10 per cent larger FWHM than the largest PSF size measured in the r-, i- or z-band. Here, $\alpha = \frac{\mathrm{FWHM}}{2\sqrt{2^{1/\beta}-1}}$ and we use $\beta = 2.5$. With this setup we make sure that no deconvolution is required because the targeted PSF will always be broader than the original PSF.

The PSF-homogenised images provide the basis for the colour measurements. We measure the colours in circular apertures of $2''$ diameter with the software Source Extractor (Bertin & Arnouts, 1996). Here, we make use of the dual image mode, where we take the i-band unconvolved co-added image as a detection image and the PSF-homogenised r-, i- or z-band image as the measurement image. We check the result of the PSF-homogenisation by comparing the flux of stars in a fixed $2''$ aperture

---

[2] https://astro.uni-bonn.de/~theli/gui/index.html

to the flux measured in a flexible elliptical aperture (‘FLUX_AUTO’ in Source Extractor). In case of a successful PSF-homogenisation, the average ratio of the two fluxes should be the same in all three bands. We assess the performance with the quantity Δf_{loss}, which denotes the maximum difference between the average flux ratios in stars in the r-, i- and z-bands.

We perform a photometric calibration by matching the instrumental magnitudes from the ACAM instrument to the magnitudes in the Pan-STARRS (PS1) catalogue (Chambers et al., 2016) based on the stars in the observed fields. We chose this catalogue as a reference because of its depth and because its footprint covers all of our targets. We obtain the zeropoints and colour terms, which account for slightly different filter curves in ACAM and PS1. For the colour terms, we fit a linear relation to the PS1 colour and the ACAM colour in $r-i$ and $i-z$ and apply a 5σ clipping to exclude outliers. In the following, we refer to calibrated total magnitudes (Kron magnitudes) as m_r, m_i and m_z and to calibrated colour measurements as $r-i$, $r-z$ and $i-z$. All given magnitudes are in the AB magnitude system.

We characterise the quality of our data with 5σ limiting magnitudes defined as:

$$m_{\mathrm{aplim}} = \mathrm{ZP} - 2.5\,\log_{10} 5\sigma_{\mathrm{sky}}\,, \tag{6.2}$$

where ZP is the zero-point of the field and σ_{sky} is the standard deviation of the sky background measured in 1000 randomly placed apertures of $2''$ diameter that do not contain any detected source (Klein et al., 2018). We measure averaged 5σ limiting magnitudes of $m_{r,\mathrm{aplim}} = 24.93$ in the r-band, $m_{i,\mathrm{aplim}} = 24.54$ in the i-band and $m_{z,\mathrm{aplim}} = 23.82$ in the z-band.

We also quantify the depth limit of our observations. To do so, we inject simulated galaxies into our images and define the 80 per cent detection limit of the respective observation as the magnitude at which we still recover 80 per cent of the injected sources. For these sources, we assume a Sérsic light profile with a constant Sérsic parameter of $n = 4$ and give them a random half-light radius drawn from a uniform distribution of 1–3 kpc (which we convert into the corresponding angular diameter assuming a redshift of $z = 0.7$). The resulting detection limit for our detection band (i-band) is called $m_{\mathrm{i,totlim}}$. An example of recovery fraction $N_{\mathrm{detected}}/N_{\mathrm{injected}}$ of sources as a function of the i-band magnitude m_i is presented in Figure 6.7. On average the detection limit is $m_{i,\mathrm{totlim}} = 23.43$.

Additionally, we define a corresponding limiting redshift as the redshift at which the detection limit $m_{\mathrm{i,totlim}}$ in the i-band coincides with the limit $m_i^*(z) + 1.25$. Here, $m_i^*(z)$ is the redshift-dependent characteristic i-band magnitude of the stellar mass function as measured in Muzzin et al. (2013b) and Ilbert et al. (2013). A redshift-dependent characteristic mass of quiescent galaxies in the redshift range of interest can be deduced, which is expressed as $\log M^*_{\mathrm{star}}/\mathrm{M}_\odot = 10.95 - 0.167 \times z$. We infer a corresponding i-band magnitude as expected from a quiescent galaxy with stellar mass M^*_{star}, which formed at redshift $z = 3$. We adopt this magnitude as our redshift-dependent characteristic magnitude $m_i^*(z)$. The limiting redshift therefore indicates the redshift at which the faintest and still detectable galaxies have a magnitude of $m_{\mathrm{i,totlim}} = m_i^*(z) + 1.25$. On average our observations are limited at redshifts of 0.80. The limiting magnitudes, detection limits, and limiting redshifts of our observed fields are reported in Table 6.1. We base our photometric redshift analysis on a catalogue of galaxies in our observations, detected with the software Source Extractor (Bertin & Arnouts, 1996). We include all objects with the internal flags `FLAG`=0, `FLAG`=1 and `FLAG`=2, to reduce the number of blend rejections.

As a final step, we apply an extinction correction to the colours and magnitudes of the galaxies. We base the extinction correction on the method described in Tonry et al. (2012), who use the value of $E(B-V)$ by Schlafly & Finkbeiner (2011)[3].

---

[3] https://irsa.ipac.caltech.edu/applications/DUST/

Table 6.1 – Properties of the imaging data in the r-, i- and z-band from the WHT.

ID	Name	r-band IQ[a] [″]	$m_{r,\mathrm{aplim}}$[b] [mag$_{\mathrm{AB}}$]	i-band IQ[a] [″]	$m_{i,\mathrm{aplim}}$[b] [mag$_{\mathrm{AB}}$]	z-band IQ[a] [″]	$m_{z,\mathrm{aplim}}$[b] [mag$_{\mathrm{AB}}$]	$m_{i,\mathrm{totlim}}$[c] [mag$_{\mathrm{AB}}$]	limiting redshift[d]	Δf_{loss}[e] [%]
115	PSZ2 G032.31+66.0	0.93	24.96	1.06	24.81	1.04	24.10	23.95	0.90	2.39
277	PSZ2 G066.34+26.1	1.46	24.67	1.47	24.35	1.65	23.56	22.75	0.67	1.73
378	PSZ2 G085.95+25.2	1.41	25.10	1.05	24.08	1.06	23.75	23.05	0.73	1.96
381	PSZ2 G086.28+74.7	1.07	25.35	0.86	24.94	0.74	23.93	23.85	0.88	4.95
420	PSZ2 G092.64+20.7	0.91	24.00	0.83	23.90	0.79	22.69	23.15	0.75	3.23
421	PSZ2 G092.69+59.9	1.10	24.90	1.23	24.96	1.26	23.95	23.75	0.86	2.48
483	PSZ2 G100.22+33.8	1.38	25.29	1.35	24.68	1.13	24.17	23.25	0.77	1.39
545	PSZ2 G112.54+59.5	1.12	25.07	1.21	24.45	1.23	24.43	23.25	0.77	4.45
623	PSZ2 G126.28+65.6	0.92	25.21	0.89	24.50	0.87	23.76	23.55	0.82	1.81
625	PSZ2 G126.57+51.6	1.08	25.01	1.16	24.38	1.20	23.65	23.25	0.77	1.20
667	PSZ2 G136.02–47.1	0.79	24.66	0.75	24.50	0.81	23.67	23.75	0.86	1.24
681	PSZ2 G139.00+50.9	1.44	25.44	1.42	24.91	1.15	24.00	23.55	0.82	1.94
690	PSZ2 G141.98+69.3	0.98	25.56	0.99	25.09	0.91	24.38	24.15	0.93	3.13
740	PSZ2 G152.47+42.1	1.45	25.02	1.52	24.49	1.29	23.80	22.95	0.72	0.91
769	PSZ2 G160.94+44.8	1.00	24.74	1.29	24.35	1.00	24.10	23.35	0.79	1.72
789	PSZ2 G165.41+25.9	1.81	24.98	1.66	23.71	1.65	23.93	23.25	0.77	2.26
1074	PSZ2 G237.68+57.8	1.46	25.19	1.49	24.77	1.53	24.04	23.15	0.75	0.22
1121	PSZ2 G246.91+24.6	1.64	22.21	1.59	24.49	1.76	22.55	23.15	0.75	2.25
1441	PSZ2 G305.76+44.7	1.52	25.07	1.41	23.92	1.45	23.53	22.65	0.66	0.99
1493	PSZ2 G316.43+54.0	0.76	25.03	1.18	24.58	0.74	24.02	23.55	0.82	5.34
1512	PSZ2 G321.30+50.6	1.28	24.95	1.30	24.61	1.20	23.79	23.25	0.77	1.28
1539	PSZ2 G326.73+54.8	1.25	25.16	1.22	24.52	1.02	23.61	23.35	0.79	0.42
1606	PSZ2 G343.46+52.6	1.20	25.06	1.18	24.80	1.15	24.16	23.45	0.81	0.24

Table 6.1 – Properties of the imaging data in the r-, i- and z-band from the WHT. (continued)

-	PLCK G55.00–37.0	0.99	24.91	1.02	24.38	0.93	23.47	23.55	0.82	1.73
-	PLCK G58.14–72.7	1.15	25.14	1.00	24.39	0.94	23.86	23.65	0.84	2.83
-	PLCK G82.51+29.8	1.48	25.20	1.32	24.80	1.27	23.99	23.55	0.82	1.07
-	PLCK G98.08–46.4	1.70	25.26	1.68	24.84	1.29	24.42	23.45	0.81	1.81
-	PLCK G122.62–31.9	1.31	25.02	1.19	24.64	1.10	23.77	23.55	0.82	0.47
-	PLCK G150.77+17.1	1.16	24.80	1.19	24.43	1.33	23.62	23.35	0.79	0.67
-	PLCK G164.82–47.4	1.27	24.79	1.30	24.44	1.19	23.75	23.35	0.79	1.10
-	PLCK G174.14–27.5	1.01	25.32	0.92	24.76	0.93	23.94	23.85	0.88	1.86
-	PLCK G184.49+21.1	0.77	24.79	0.67	24.68	0.76	23.93	23.95	0.90	3.74

Notes. ^{a} FWHM of the PSF (seeing). ^{b} 5σ limiting magnitudes as defined by Equation (6.2). ^{c} Detection limit at which 80 per cent of the simulated, injected galaxies are still recovered in the source detection in the i-band with SOURCE EXTRACTOR. ^{d} Limiting redshifts of the observations defined as the redshift at which $m_{i,\mathrm{totlim}} = m_i^*(z) + 1.25$. ^{e} Maximum difference between the average flux ratios (comparing $2''$ aperture flux and FLUX_AUTO) in stars in the r-, i- and z-bands after the PSF-homogenisation (see Section 6.4.1).
We indicate the PSZ2 ID of the candidates in column 1 and the full name in column 2 (Planck Collaboration et al., 2016c). In case this is not available, we give the candidates generic names starting with 'PLCK' followed by a notation of the galactic coordinates.

6.4.2 Red-sequence models and redshift estimates

We aim to extract redshift and richness information about the galaxy clusters from the available optical data. For this, we make use of the fact that early-type galaxies, which are the dominant population in massive galaxy clusters, follow a tight correlation between colour and magnitude with a typically very small intrinsic scatter of $< 0.1\,\mathrm{mag}$ (Bower et al., 1992). These galaxies are host to stellar populations that have evolved passively since $2 < z < 5$ (e.g. Bower et al., 1992; Lin et al., 2006). This so-called red-sequence is characterised by its slope and intercept, which depend on the redshift (Gladders et al., 1998). For the galaxy clusters detected with *Planck* at redshifts up to $z \sim 1$, there are enough red-sequence galaxies in the clusters to present an excess to the background field galaxies. This allows us to estimate the redshift of the cluster by comparing the colours of the galaxies with the colours of empirical red-sequence models, which predict the colour of red-sequence galaxies as a function of their magnitude and redshift. We construct the empirical red-sequence models analogously to the work by van der Burg et al. (2016) on the basis of the deep 30-band photometric data of the COSMOS/UltraVISTA field (Muzzin et al., 2013a). This provides us with a catalogue of galaxies down to faint magnitudes and with high-quality photometric redshifts allowing us to constrain the red-sequence models over the full magnitude range of interest. We select quiescent galaxies based on their rest-frame $U - V$ and $V - J$ colours up to redshifts of 1.2 and down to a magnitude of $m_i = 24.0$. These galaxies have similar properties as the cluster red-sequence galaxies. The r-, i-, and z-band magnitudes in the UltraVISTA catalogue were obtained with the Subaru filters, which do not match the filters of PS1. Therefore, we transform the UltraVISTA colours to the PS1 photometric system. As a result, a set of quiescent galaxies is available with COSMOS/UltraVISTA redshifts and colours and total magnitudes corresponding to the PS1 system.

As described in van der Burg et al. (2016), we then divide the galaxies into redshift bins with width 0.04 and step size 0.01 and fit a linear relation to the colours ($r - i$, $r - z$ or $i - z$) as a function of the total i-band magnitude m_i. This provides us with a slope, intercept (at magnitude $m_i = 22.0$) and scatter for each redshift step. We show the models for the three available colour combinations in Figure 6.1. The models have the highest sensitivity at redshifts where the two involved filters enclose the 4000 Å-break. Hence, the $(r - i)$ vs. m_i, $(r - z)$ vs. m_i, and $(i - z)$ vs. m_i model is most sensitive to redshifts of $(0.3 \lesssim z \lesssim 0.7)$, $(0.4 \lesssim z \lesssim 0.9)$, and $(0.6 \lesssim z \lesssim 1.1)$, respectively.

For our task to estimate the redshifts empirically with the help of our red-sequence models, we conduct several steps, which are largely based on works by Klein et al. (2018), Klein et al. (2019), and van der Burg et al. (2016). Our basic strategy is to count how many galaxies in an 0.5 Mpc radius around the cluster centre agree with the red-sequence models at different redshift steps. This way, we obtain a histogram of counted galaxies versus redshift, which exposes an over-density of galaxies at the

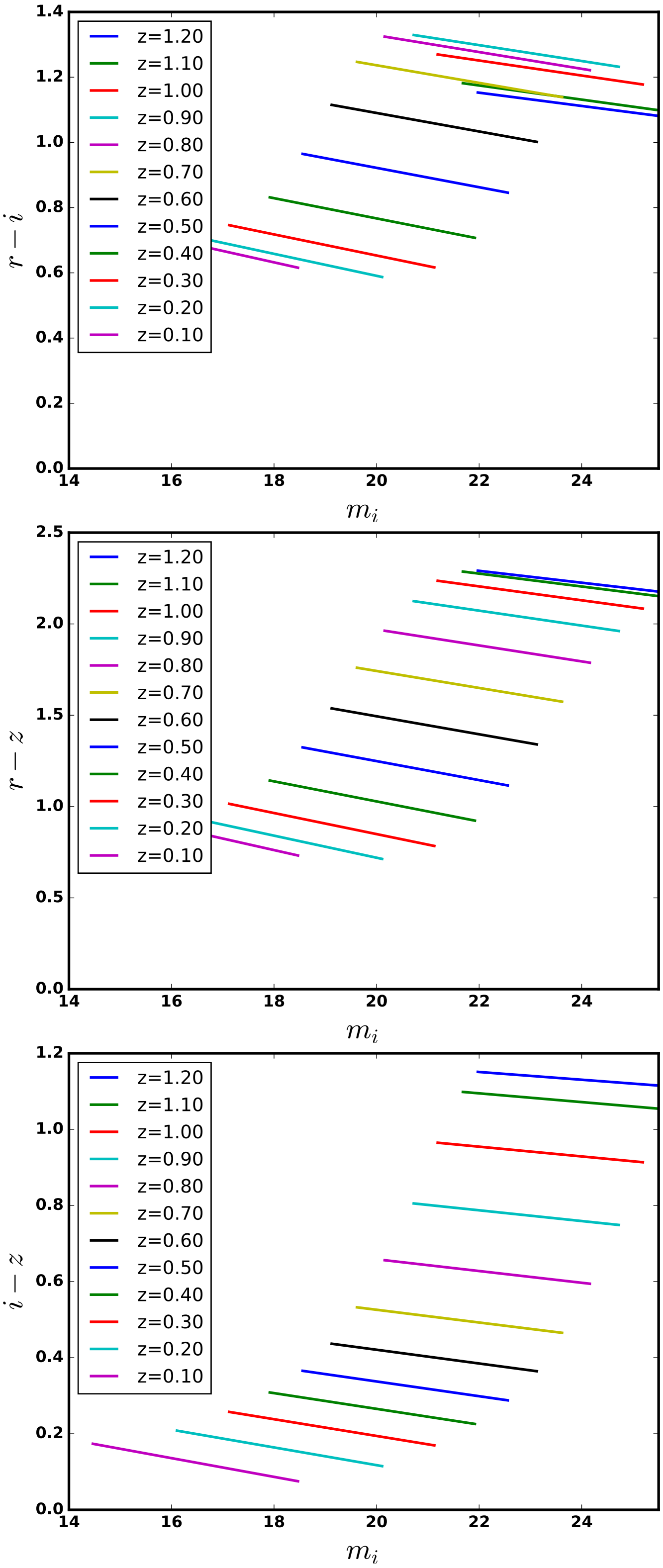

Figure 6.1 – Empirical red-sequence models for three colours (recalibrated, see Section 6.4.2). *Top*: $r - i$ vs m_i, highest sensitivity in regime $0.3 \lesssim z \lesssim 0.7$, *Middle*: $r - z$ vs m_i, highest sensitivity in regime $0.4 \lesssim z \lesssim 0.9$, *Bottom*: $i - z$ vs m_i, highest sensitivity in regime $0.6 \lesssim z \lesssim 1.1$. Each line covers the range $m_i^* - 2.0 \leq m_i \leq m_i^* + 2.0$.

cluster redshift because of the red-sequence galaxies in the cluster. To enhance this over-density, we apply certain filters and weighting techniques to the galaxies. We describe these below.

Magnitude cuts and colour weights

In a first step, we identify a candidate for the brightest cluster galaxy (BCG) of the cluster candidate from a colour image in the r-, i- and z-band. Considering the galaxies in a 0.5 Mpc radius around the BCG (a value adapted from Buddendiek et al., 2015), we then count all galaxies p as a match to the red-sequence models at a given redshift step if they fulfil all of these criteria:

1. The colour of galaxy p agrees with all three red-sequence models at the same time within three times the standard deviation of the respective red-sequence model
$$\Delta c_{p,k} = |c_{p,k} - \langle c(z, m_i) \rangle_k| < 3\sigma_{c_k}(z)\,. \tag{6.3}$$
Here, the colour combinations are described by the index $k \in 1, 2, 3$ with $(c_1, c_2, c_3) = (r - i, i - z, r - z)$, $c_{p,k}$ is the measured colour k of galaxy p and $\langle c(z, m_i)\rangle_k$ is the model colour k at redshift z with a scatter of the model $\sigma_{c_k}(z)$. We also use galaxies if they only fall in the $3\sigma_{c_k}(z)$ range of the red-sequence models taking their 1σ photometric errors into account.
2. The galaxy is brighter than the detection limit $m_i < m_{i,\mathrm{totlim}}$.
3. The galaxy is brighter than $m_i < m_i^*(z) + 1.25$, where $m_i^*(z)$ is the characteristic magnitude at the respective redshift.

We then weight each galaxy by its colour. At each redshift step we assign a weight $w_p(z)$ to the galaxy depending on how close the galaxy's colour is to the colour predicted by the red-sequence models at that step (Klein et al., 2019):

$$w_p(z) = \frac{\prod_{k=1}^{3} G(\Delta c_{p,k}\,, \sigma_{c_k}(z))}{N(\sigma_{c_1}(z), \sigma_{c_2}(z), \sigma_{c_3}(z))}\,. \tag{6.4}$$

$G(\Delta c_{p,k}, \sigma_{c_k}(z))$ is the value of a normalised Gaussian function at colour offset $\Delta c_{p,k}$. The normalisation N is defined as

$$N(\sigma_{c_1}(z), \sigma_{c_2}(z), \sigma_{c_3}(z)) = \prod_{k=1}^{3} G(0, \sigma_{c_k}(z))\,. \tag{6.5}$$

Completeness correction

In the third criterion of our list, we apply a magnitude cut-off to the galaxies that we take into consideration. However, it is possible that the detection limit $m_{i,\mathrm{totlim}}$ (second criterion), which represents a limit to the completeness of the detections, is brighter than the limit $m_i < m_i^*(z) + 1.25$. In that case, we have to account for the galaxies that we miss due to the limited depth of our data. Following Klein et al. (2018), we estimate the amount of galaxies, which we expect to miss, by extrapolating the Schechter function down to our magnitude cut-off. The Schechter function $S(m, m_i^*, \alpha)$ is defined via

$$S(m, m_i^*, \alpha)\,\mathrm{d}m = 0.4\,\ln(10)\,\Phi^* 10^{-0.4(m-m_i^*)\cdot(\alpha+1)} \cdot \exp\left[-10^{-0.4(m-m_i^*)}\right]\mathrm{d}m\,. \tag{6.6}$$

We chose a value for the faint-end slope of $\alpha = -1.0$ adapted from Klein et al. (2018). This results in a completeness correction factor

$$c_{\mathrm{cmp}} = \frac{\int_{-\infty}^{m_i^*+1.25} S(m, m^*, \alpha)\,\mathrm{d}m}{\int_{-\infty}^{m_{i,\mathrm{totlim}}} S(m, m^*, \alpha)\,\mathrm{d}m} \tag{6.7}$$

(Klein et al., 2018). We only apply this correction factor in case that the detection limit $m_{i,\mathrm{totlim}}$ is brighter than $m_i^*(z) + 1.25$. Otherwise, we set $c_{\mathrm{cmp}} = 1.0$.

In addition, it is possible to correct for the magnitude-dependent fraction of retrieved versus injected galaxies from the estimation of the 80 per cent depth of the data (see Section 6.4.1 and Appendix 6.10). However, we only apply this type of correction when we estimate the cluster richness (see Section 6.4.3).

Radial weights

The galaxies in a cluster are typically more abundant towards the centre. To include this information in our analysis, we follow an approach by Klein et al. (2019). We weight galaxies according to their distance from the cluster centre (characterised by the BCG position) with the help of a Navarro Frenk White (NFW) profile (Navarro et al., 1997). Although originally intended to describe the distribution of dark matter in N-body simulations, it also provides a good description of the number density profile of cluster galaxies (e.g. Lin et al., 2004; Hansen et al., 2005). The surface density of galaxies can be expressed as

$$\Sigma(R) \propto \frac{1}{(R/R_\mathrm{S})^2 - 1} f(R/R_\mathrm{S}) \tag{6.8}$$

(Bartelmann, 1996). Here, we set $R_\mathrm{S} = 0.15h^{-1}$ Mpc (Rykoff et al., 2012) as the characteristic scale radius and

$$f(x) = \begin{cases} 1 - \frac{2}{\sqrt{x^2-1}} \arctan\sqrt{\frac{x-1}{x+1}} & (x > 1) \\ 1 - \frac{2}{\sqrt{1-x^2}} \operatorname{arctanh}\sqrt{\frac{1-x}{x+1}} & (x < 1)\,. \end{cases} \tag{6.9}$$

Below the minimum radius of $0.1h^{-1}$ Mpc we set the radial weight to be constant, to avoid a singularity for $R = 0$ (Rykoff et al., 2012). The profile is truncated at a cutoff radius $R_\mathrm{C} = 0.5$ Mpc for the redshift estimates, because we consider all galaxies out to this radius for the estimate. Accordingly, we normalise the profile with the help of a correction term C_{rad} as

$$1 = C_{\mathrm{rad}} \int_0^{R_{\mathrm{C}}} \mathrm{d}R \; 2\pi R_p \Sigma(R_p) \tag{6.10}$$

(Klein et al., 2019). Thus, the radial weight for a galaxy p at distance R_p from the estimated centre is

$$n_p(z) = C_{\mathrm{rad}}(z) 2\pi R_p \Sigma(R_p)\,. \tag{6.11}$$

Masking and statistical background estimate

As a next step, we account for the contribution of field galaxies that do match the models but do not actually belong to the cluster itself. Since the field of view of ACAM is too small to estimate the local background contribution from the available images, we make use of the UltraVISTA catalogue from Muzzin et al. (2013a), which we matched to the PS1 photometric system. This field covers around 1.62 deg^2 corresponding to more than 100 times the field of view of ACAM. The deep photometric data in a field of this size provide a good basis for an estimate of the background contribution from field galaxies. However, this approach cannot account for a variation of this contribution over large spatial scales.

In order to mimic similar conditions as for the observations with the ACAM instrument, we add Gaussian noise to the flux of the galaxies with a standard deviation equal to the one from the sky background σ_{sky}. Next, we count the number of galaxies that agree with the available red-sequence models at the different redshift steps. Here, we apply the same criteria and weighting steps (see Sections 6.4.2, 6.4.2, 6.4.2) as during the analysis of the galaxies in the actual co-adds. We estimate the contribution of background galaxies this way in 75 ACAM-sized, non-overlapping apertures covering the UltraVISTA field. For each galaxy q in an aperture, we calculate the quantities $w_q(z)$ and $n_q(z)$ analogously to Equations (6.4) and (6.11). We average the results from 75 apertures, calculate the standard deviation and normalise the values to an area of 1 arcmin^2, so that we can subtract our statistical background estimate from the weighted number of galaxies in differently sized areas in the co-added image.

Additionally, we mask bright foreground objects in the field of view that potentially cover galaxies in the cluster. We subtract the area covered by these masks from the total area within a 0.5 Mpc radius.

Iteration of the redshift estimate

Evaluating the weighting and masking schemes described in the previous sections at each redshift step, provides us with the so-called filtered richness (Klein et al., 2018, 2019)

$$\begin{aligned}\lambda_{\mathrm{MCMF}}(z) = & \, c_{\mathrm{cmp}}(z) \cdot \Sigma w_p(z) n_p(z) \\ & - c_{\mathrm{cmp}}(z) \cdot A_{\mathrm{cl}}(z) \cdot \Sigma w_q(z) n_q(z) \, . \end{aligned} \tag{6.12}$$

Here, A_{cl} is the area within a 0.5 Mpc radius (with the masked regions excluded). The index p denotes galaxies from the observations and the index q indicates galaxies from the estimate of the (average) background from the UltraVISTA field. The filtered richness quantifies how many galaxies are consistent with the red-sequence models at different redshift steps. For an initial redshift estimate, we take the BCG as the centre of the cluster and identify the most prominent over-density in the distribution of filtered richness $\lambda_{\mathrm{MCMF}}(z)$ as a function of redshift. We fit a Gaussian function to this over-density and take the peak position of the Gaussian as our initial redshift estimate. At this point, we set $n_p(z) = n_q(z) = 1$. We do this because we want to account for different cluster morphologies, where the BCG is not necessarily always right in the centre for a cluster. To obtain an estimate of the centre of the galaxy over-density, we then identify all galaxies in the field of view that agree with the initial redshift estimate and pick that galaxy as a new centre that has the maximum number of neighbours within a 0.5 Mpc radius. Afterwards, we repeat the redshift estimate analogously now around the new centre and including the radial weights $n_p(z)$ and $n_q(z)$. An overview of the redshift estimation procedure is given in Figure 6.2. We obtain statistical errors for the estimated redshifts by bootstrapping the catalogue of galaxies in the respective observation. Here, we assemble a new catalogue by drawing galaxies from the original catalogue at random until we have a catalogue of the same length again, where it is possible that some galaxies enter the new catalogue multiple times and others do not enter it at all. We create 1000 new catalogues and re-estimate the redshift a thousand times per cluster candidate. To account for variation in the background of field galaxies, we only pick one position in the UltraVISTA catalogue per bootstrap step for the background subtraction. Thus, the statistical errors also mirror the variation of the background. The symmetric 68 per cent uncertainty can be calculated via

$$\sigma^2_{\mathrm{sym}} = \frac{\sum_{i=1}^{B} \left(z(\mathbf{x}_i^*) - \bar{z}(\mathbf{x}^*) \right)^2}{B-1} \, . \tag{6.13}$$

Here, $B = 1000$ is the number of bootstrap iterations, z is the measured quantity, i.e., the redshift, $\mathbf{x}$ represents the original catalogue of galaxies and then $\mathbf{x}_i^*$ is the i-th bootstrapped version of this catalogue. Finally, $\bar{z}(\mathbf{x}^*)$ is the average of all redshifts that result from the bootstrap iterations. We find an average uncertainty of $\sigma_{z_{\mathrm{phot}}} = 0.062$ for the photometric redshift measurements.

Calibration of the redshift estimate

Since our red-sequence models are based on galaxies in the field, which may differ from the cluster member galaxies in age or metallicity and thus in broadband

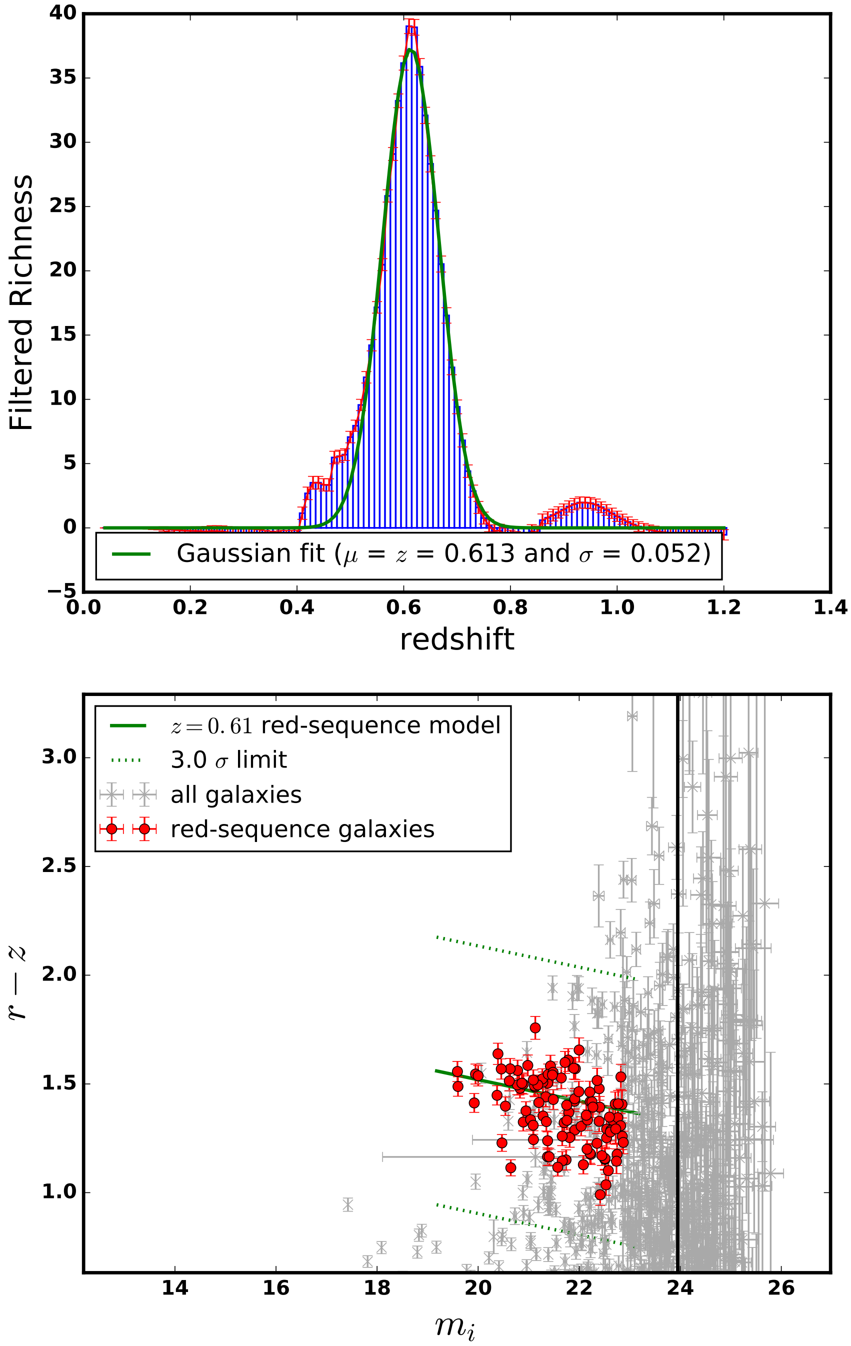

Figure 6.2 – *Top:* Filtered richness λ_{MCMF} versus redshift with Gaussian fit in green for cluster candidate PSZ2 G032.31+66.07. The blue bars display λ_{MCMF} at the different redshift steps. The red error bars display the uncertainties that emerge from the background subtraction. *Bottom:* Diagram of $(r - z)$ colour versus i-band magnitude for cluster candidate PSZ2 G032.31+66.07. The grey points mark all galaxies observed in the image. The red points are the red-sequence galaxies within R_{C} consistent with the (recalibrated) red-sequence model at $z = 0.61$, that is indicated by a green, solid line. The green, dotted lines mark the $\pm 3\sigma$ band around that model. The red dots only display red-sequence galaxies that are brighter than the limit $m_i < m_i^* + 1.25$. The vertical, black line represents the detection limit $m_{i,\mathrm{totlim}}$ of this observation.

colour, we perform a correction to our best-fit photometric redshifts based on a direct comparison with spectroscopically determined redshifts. Apart from our own spectroscopic redshift estimates (see Section 6.5) for two clusters with a sufficiently well-defined red-sequence, we include results from several other authors. Burenin et al. (2018) measured spectroscopic redshifts with the BTA 6-m telescope using the instruments SCORPIO and SCORPIO-2 for five of the clusters in our sample, namely PSZ2 G092.69+59.92, PSZ2 G126.28+65.62, PSZ2 G126.57+51.6, PSZ2 G237.68+57.83 and PSZ2 G343.46+52.65. Amodeo et al. (2018) provide a spectroscopic redshift for PSZ2 G085.95+25.23 with Keck/LRIS spectroscopy. Streblyanska et al. (2018) list spectroscopic redshifts originating from the SDSS DR12 spectroscopic information for PSZ2 G032.31+66.07 and PSZ2 G086.28+74.76. Additionally, we resort to data by Buddendiek et al. (2015), who measured spectroscopic and photometric redshifts with the help of observations also obtained at the WHT using ACAM. Buddendiek et al. (2015) investigate a sample originating from the *ROSAT* All Sky Survey. It therefore does not relate to the PSZ2 follow-up pursued here and we only use this sample for calibration purposes of the photometric redshifts. We estimate red-sequence based redshifts using their r-, i- and z-band observations of 15 galaxy clusters and compare these photometric redshifts to the corresponding spectroscopic redshift results found by Buddendiek et al. (2015). From the overall comparison of spectroscopic and photometric redshifts, we find that we overestimate the redshift by a median offset of $\Delta z = (z_{\mathrm{phot}} - z_{\mathrm{spec}})_{\mathrm{median}} = 0.104 \pm 0.045$. We decide to recalibrate our red-sequence models in an iterative manner. For this purpose, we compare the colours of the red-sequence models at the photometric redshift and at the spectroscopic redshift. We then adjust the intercepts of our three red-sequence models in a redshift dependent way. For this, we fit a line to the colour offset as a function of redshift and modify the intercepts of the red-sequence models accordingly. Subsequently, we re-estimate the photometric redshifts. We repeat this process until we minimise the scatter between photometric and spectroscopic redshifts given by

$$\sigma_z = \sqrt{\frac{1}{N} \sum \left(\frac{z_{\mathrm{spec}} - z_{\mathrm{phot}}}{1 + z_{\mathrm{spec}}} \right)^2} \,. \tag{6.14}$$

Here, N is the number of galaxy clusters with available spectroscopic redshifts and z_{spec} and z_{phot} are the spectroscopic and red-sequence redshifts of the clusters, respectively. Table 6.2 gives an overview of the calibrated red-sequence redshifts of our complete cluster sample. In Figure 6.3, we plot the calibrated photometric redshift versus the corresponding spectroscopic redshift of all clusters used for the recalibration. From this, we can see that the systematic bias has been removed. The remaining scatter is $\sigma_z = 0.021$ as compared to the average uncertainty of $\sigma_{z_{\mathrm{phot}}} = 0.062$ for the photometric redshift measurements.

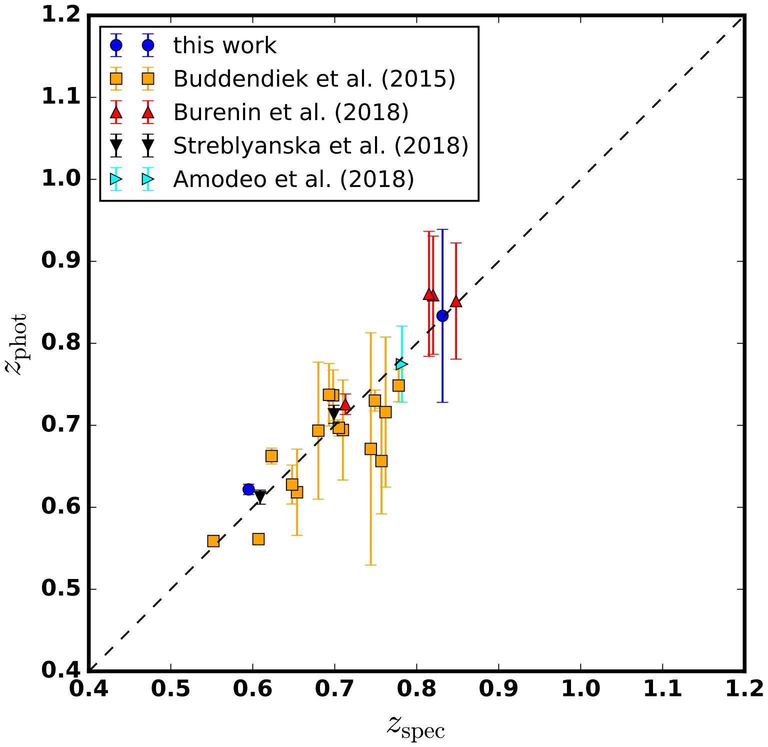

Figure 6.3 – Comparison of red-sequence redshifts (obtained through the analysis steps described in this work) after recalibration of the red-sequence models and spectroscopic redshifts from this work, Buddendiek et al. (2015), Burenin et al. (2018), Streblyanska et al. (2018) and Amodeo et al. (2018). The error bars show the statistical 68 per cent errors, which result from a bootstrapping according to Equation (6.13). We find a scatter of $\sigma_z = 0.021$.

6.4.3 Richness and mass estimates

We want to relate the results from our optical data to the SZ-based results (in particular the mass $M_{\rm 500c,SZ}$) inferred from the *Planck* measurements. In this work, we make use of the richness-mass scaling relation established by Rozo et al. (2015), which connects the richness estimated from optical data of the SDSS DR8 `redMaPPer` catalogue (Rykoff et al., 2014) to the SZ-mass from the PSZ1 catalogue (Planck Collaboration et al., 2014b), the progenitor of the PSZ2 catalogue. This scaling relation was already used for comparison of optical observations to SZ-observations, e.g., by Planck Collaboration et al. (2016c) and van der Burg et al. (2016). Additionally, this scaling relation is suitable for our work in contrast to other richness-mass scaling relations because it directly relates the mass estimate inferred from the SZ-signal (in particular from PSZ1, which is very similar to PSZ2) to a richness, that is inferred from a red-sequence analysis. Both of these quantities are available for the cluster candidates in our sample. It also extends to relatively high redshifts ($z \leq 0.5$) compared to other richness-mass scaling relations and uses a relatively large sample size of 191 cluster to base their results on.

The scaling relation by Rozo et al. (2015) is based on the richness as defined in Rykoff et al. (2014). Therefore, we aim to estimate the richness in a similar way. The richness is estimated by counting all the galaxies that agree with the redshift estimate above a certain magnitude threshold and within some cut-off radius R_{C}. However, the cut-off radius itself depends on the richness as well. In particular, Rykoff et al. (2014) assume a power-law relation between the richness λ and the cut-off radius R_{C} of the following shape

$$\lambda(R_{\mathrm{C}}) = 100\left(\frac{R_{\mathrm{C}}}{R_0}\right)^{1/\beta} . \tag{6.15}$$

The cut-off radius R_{C} characterises the circular area around the cluster centre within which the galaxies contributing to the richness are counted. It is, however, not comparable to common radii describing an over-density like $R_{500\mathrm{c}}$ (the radius within which the density is 500 times higher than the critical density of the Universe at a given redshift). In the above equation, we have $R_0 = 1.0\,h^{-1}\,\mathrm{Mpc}$ and $\beta = 0.2$ according to Equation (4) in Rykoff et al. (2014). Rozo et al. (2009b) determine the optimal choice of the parameters β and R_0 empirically by minimising the scatter in the relation between richness and X-ray luminosity of their investigated galaxy cluster sample. In their work, Rykoff et al. (2012) report that the optimal richness measurements are obtained when considering galaxies with luminosities $L \geq 0.2L^{*}$, which translates to apparent magnitudes as $m_i \leq m_i^{*}(z) + 1.75$. Thus, the richness λ can be calculated as

$$\lambda(R_{\mathrm{C}}) = [N(R_{\mathrm{C}}) - N_{\mathrm{BG}}(R_{\mathrm{C}})] \cdot c_{\mathrm{cmp}}(z)/0.95\,, \tag{6.16}$$

where N is the number of galaxies in a circle with radius R_{C} in the co-added frame with a magnitude $m_i < m_i^{*}(z)+1.75$ and $m_i < m_{i,\mathrm{totlim}}$ that agree within $2\sigma_{c_k}(z)$ with the red-sequence model of the estimated redshift. We count the galaxies correcting for the magnitude-dependent fraction of retrieved versus injected galaxies from the estimation of the 80 per cent depth of the data (see Section 6.4.1 and Appendix 6.10). N_{BG} is the corresponding number of background galaxies. The completeness correction is applied in case $m_{i,\mathrm{totlim}} < m_i^{*}(z) + 1.75$. Additionally, we divide the result by 0.95 in order to account for galaxies with a larger scatter than $2\sigma_{c_k}(z)$. Assuming Gaussian scatter, their number is expected to be 5 per cent of the total.

Since it is not clear what the cut-off radius is beforehand, we estimate the richness within a range of different values of R_{C}. We then compare the richness $\lambda(R_{\mathrm{C}})$ we obtain this way to the richness we expect from Equation (6.15). Thus, the richness estimate is the unique point where the two values coincide. We estimate the uncertainty of the richness in a purely statistical way. This means that we consider the Poisson errors on the number counts of galaxies in the observation and on the background counts. Any uncertainty introduced by the redshift uncertainty is therefore not included. It has to be noted, however, that the richness is closely linked to the redshift estimate since it builds the basis for the richness estimate and can also have an impact on a possible completeness correction.

The $\lambda - M_{\mathrm{500c,SZ}}$ scaling relation is described by

$$\langle \ln \lambda | M_{\mathrm{500c,SZ}} \rangle = a + \alpha \ln \left(\frac{M_{\mathrm{500c,SZ}}}{5.23 \times 10^{14}\,\mathrm{M}_{\odot}} \right) , \tag{6.17}$$

with $a = 4.572 \pm 0.021$ and $\alpha = 0.965 \pm 0.067$, and an intrinsic scatter in richness of $\sigma_{\ln \lambda | M_{\mathrm{500c,SZ}}} = 0.266 \pm 0.017$ (Rozo et al., 2015). Assuming that there is no redshift-dependent evolution of this relation, we apply this scaling relation to our sample in order to infer a corresponding mass (we call this mass $M_{\mathrm{500c},\lambda}$) from the richness we measured. Given that the red-sequence assembles over time, it is possible for the normalisation of the richness-mass scaling relation to change with redshift (van Uitert et al., 2016). However, there are also studies indicating only little evolution of the scaling relation out to redshifts of $z = 0.6$ (Andreon & Congdon, 2014) or even $z = 0.8$ (Saro et al., 2015).

Based on the obtained redshift estimates and central positions, it is also possible to estimate the mass based on the SZ signal in the *Planck* maps, as detailed in Section 6.6. It refers to the mass within a radius of R_{500c}. The measured redshifts, richnesses and masses are summarised in Table 6.2.

Table 6.2 – Results of the photometric analysis of the cluster sample studied here.

	ID	Name	RA [°]	Dec [°]	z_{spec}	z_{RS}	λ	$M_{500\mathrm{c},\lambda}$ [$10^{14}\mathrm{M}_\odot$]	c_{cmp}	$M_{500\mathrm{c,SZ}}$ [a] [$10^{14}\mathrm{M}_\odot$]	S/N	D_{blind} [b] [arcmin]	Q_{neural} [c]
$\frac{M_{500\mathrm{c},\lambda}}{M_{500\mathrm{c,SZ}}} > 0.5$	115	PSZ2 G032.31+66.0	219.348	24.407	0.609^g	0.61 ± 0.01	71 ± 13	3.81 ± 0.72	1.00	$5.64^{+0.77}_{-0.84}$	5.14	3.18	0.98
	277	PSZ2 G066.34+26.1	270.268	39.876	-	0.62 ± 0.02	79 ± 14	4.22 ± 0.78	1.16	$4.81^{+0.67}_{-0.74}$	5.63	2.71	0.96
	378	PSZ2 G085.95+25.2 ⋆	277.648	56.892	0.782 ± 0.003^f	0.77 ± 0.05	160 ± 21	8.86 ± 1.22	1.66	$4.97^{+0.58}_{-0.63}$	5.55	1.96	0.98
	420	PSZ2 G092.64+20.7	289.196	61.665	0.545^h	0.58 ± 0.02	36 ± 11	1.87 ± 0.61	1.00	$4.45^{+0.46}_{-0.49}$	5.12	1.10	0.92
	483	PSZ2 G100.22+33.8	258.417	69.355	0.598^h	0.56 ± 0.06	35 ± 9	1.78 ± 0.49	1.00	$4.04^{+0.51}_{-0.55}$	5.69	1.13	0.99
	623	PSZ2 G126.28+65.6	190.599	51.443	0.820^e	0.83 ± 0.07	79 ± 16	4.21 ± 0.87	1.46	$5.00^{+0.67}_{-0.71}$	4.77	2.51	0.92
	625	PSZ2 G126.57+51.6	187.444	65.354	0.815^e	0.80 ± 0.08	81 ± 16	4.35 ± 0.91	1.60	$5.82^{+0.56}_{-0.60}$	6.35	0.53	0.91
	690	PSZ2 G141.98+69.3 ⋆	183.109	46.395	0.714^g	0.71 ± 0.03	40 ± 8	2.08 ± 0.45	1.00	$2.74^{+0.96}_{-1.33}$	4.71	7.96	0.84
	1074	PSZ2 G237.68+57.8 † ⋆	163.336	10.877	0.894 ± 0.007^d	0.97 ± 0.05	148 ± 27	8.15 ± 1.55	2.94	$5.38^{+0.76}_{-0.81}$	5.36	4.48	0.94
	1493	PSZ2 G316.43+54.0	200.820	-7.998	-	0.53 ± 0.02	72 ± 13	3.82 ± 0.74	1.00	$5.82^{+0.75}_{-0.82}$	5.18	0.87	0.73
	1512	PSZ2 G321.30+50.6 ⋆	204.611	-10.550	-	0.79 ± 0.04	131 ± 19	7.18 ± 1.07	1.53	$5.28^{+0.94}_{-1.08}$	4.63	1.08	0.96
	1539	PSZ2 G326.73+54.8	206.320	-5.526	-	0.60 ± 0.02	76 ± 14	4.05 ± 0.76	1.00	$5.98^{+0.81}_{-0.89}$	5.92	3.57	1.00
	1606	PSZ2 G343.46+52.6	216.094	-2.731	0.713^e	0.72 ± 0.01	115 ± 15	6.28 ± 0.87	1.02	$6.26^{+0.89}_{-0.98}$	4.90	0.99	0.96
	-	PLCK G58.14–72.7 † ⋆	356.394	-18.803	0.938 ± 0.003^d	1.03 ± 0.10	60 ± 16	3.15 ± 0.90	2.23	$3.90^{+0.88}_{-1.08}$	4.20	2.64	0.99
	-	PLCK G82.51+29.8	268.725	54.478	-	0.86 ± 0.10	25 ± 11	1.25 ± 0.57	1.67	$2.83^{+0.96}_{-1.34}$	3.51	4.49	0.71
	-	PLCK G98.08–46.4 † ⋆	355.524	13.023	0.983 ± 0.005^d	1.06 ± 0.04	53 ± 21	2.80 ± 1.17	3.47	$2.63^{+1.20}_{-1.20}$	3.34	4.38	0.98
	-	PLCK G174.14–27.5	59.050	16.448	0.834 ± 0.005^d	0.84 ± 0.11	15 ± 8	0.73 ± 0.44	1.22	$2.30^{+1.55}_{-1.55}$	3.81	4.44	-
	-	PLCK G184.49+21.1	111.081	34.045	0.596 ± 0.007^d	0.62 ± 0.01	121 ± 15	6.64 ± 0.89	1.00	$5.88^{+0.80}_{-0.87}$	4.26	0.21	0.99
$\frac{M_{500\mathrm{c},\lambda}}{M_{500\mathrm{c,SZ}}} > 0.25$	381	PSZ2 G086.28+74.7	204.480	38.900	0.699^g	0.71 ± 0.01	36 ± 10	1.87 ± 0.55	1.00	$5.47^{+0.69}_{-0.75}$	5.07	1.78	0.96
	421	PSZ2 G092.69+59.9 ⋆	216.646	51.268	0.848^e	0.86 ± 0.07	20 ± 10	0.99 ± 0.51	1.42	$3.38^{+0.78}_{-0.95}$	4.90	1.16	0.96
	1121	PSZ2 G246.91+24.6	141.495	-15.162	-	0.60 ± 0.14	35 ± 9	1.81 ± 0.50	1.00	$5.67^{+0.71}_{-0.77}$	4.80	2.13	0.97
	-	PLCK G55.00–37.0	325.138	-0.432	-	0.62 ± 0.14	23 ± 9	1.19 ± 0.50	1.00	$5.30^{+0.78}_{-0.85}$	3.85	0.58	0.90
	-	PLCK G122.62–31.8	12.583	30.990	-	0.91 ± 0.06	28 ± 13	1.42 ± 0.69	2.15	$4.99^{+0.93}_{-1.07}$	3.32	1.96	0.81
	-	PLCK G150.77+17.1	87.435	62.406	-	0.59 ± 0.05	32 ± 10	1.63 ± 0.54	1.00	$4.94^{+0.93}_{-1.05}$	3.6	2.30	0.98

Table 6.2 – Results of the photometric analysis of the cluster sample studied here. (continued)

$\frac{M_{500c,\lambda}}{M_{500c,SZ}} < 0.25$	545	PSZ2 G112.54+59.5 ⋆	202.464	56.797	-	0.83 ± 0.06	4.4 ± 5.4	0.21 ± 0.27	1.89	$5.32^{+0.60}_{-0.64}$	5.10	1.14	0.90
	667	PSZ2 G136.02–47.1 ⋆	22.008	14.756	-	0.61 ± 0.07	5.8 ± 6.6	0.28 ± 0.34	1.00	$5.65^{+0.95}_{-1.07}$	4.64	1.98	0.56
	681	PSZ2 G139.00+50.9	170.075	63.248	-	0.71 ± 0.10	12 ± 7	0.59 ± 0.38	1.00	$4.61^{+0.72}_{-0.81}$	4.98	1.90	0.78
	1441	PSZ2 G305.76+44.7	195.003	-18.022	-	0.76 ± 0.13	20 ± 11	0.99 ± 0.59	2.29	$7.17^{+0.71}_{-0.76}$	5.72	1.73	0.97
$\frac{M_{500c,\lambda}}{M_{500c,SZ}}$ unknown	740	PSZ2 G152.47+42.1 ◇	142.409	61.660	-	-	-	-	-	-	4.81	3.34	1.00
	769	PSZ2 G160.94+44.8 ⋆	143.418	54.992	-	0.74 ± 0.10	2.3 ± 5.2	0.10 ± 0.26	1.16	-	4.98	3.83	0.06
	789	PSZ2 G165.41+25.9 ⋆	110.990	52.160	-	0.67 ± 0.11	-4.8 ± 3.6	-	1.00	$4.04^{+0.97}_{-1.15}$	4.51	0.35	0.99
	-	PLCK G164.80-47.4 ◇	39.918	6.450	-	-	-	-	-	-	4.24	1.51	0.99

Notes. All the values to the left of the solid line result from the analysis of the optical data, values to the right are based on the SZ-signal from the *Planck* maps. We sort the cluster candidates into three categories of validation: conservative confirmation with $M_{500c,\lambda}/M_{500c,SZ} > 0.5$, loose confirmation with $M_{500c,\lambda}/M_{500c,SZ} > 0.25$ and unconfirmed with $M_{500c,\lambda}/M_{500c,SZ} < 0.25$ (each within the 1σ uncertainties). Cluster where results for $M_{500c,\lambda}$ or $M_{500c,SZ}$ could not be measured are categorised as 'unknown'.

[a] The SZ-mass is inferred from the *Planck* maps based on the photometric redshift and position information from the optical data. [b] Distance from optical centre to position of SZ blind detection. [c] The values of $Q_{\rm neural}$ for the MMF3 detected candidates (identifier 'PLCK' and S/N < 4.5) were computed by G. Hurier (private communication) following the method described in Aghanim et al. (2015) and Hurier et al. (2017). Spectroscopic redshifts $z_{\rm spec}$ are indicated as published in *d*) this work (BCG candidate) with a detailed description in Section 6.5, *e*) Burenin et al. (2018), *f*) Amodeo et al. (2018), *g*) Streblyanska et al. (2018), *h*) Streblyanska et al. (2019).

[†] For these candidates we found very high completeness correction factors of $c_{\rm cmp} > 3.5$ when using the photometric redshift. We therefore resort to the spectroscopic redshifts for the indicated richness λ and richness-based mass $M_{500c,\lambda}$. In Table 6.5, we list similar results based on the spectroscopic redshifts when available for the other cluster candidates.

◇ For these candidates the analysis did not lead to a conclusive redshift result because the red-sequence models do not have enough constraining power. The reason is that we do not have a sufficiently deep detection limit in these cases. We only report the position of the potential brightest cluster galaxy and available quantities related to the SZ-based measurements.

⋆ More remarks on these candidates in Section 6.7.

6.5 Spectroscopic observations

For nine out of 32 cluster candidates in our sample, we performed spectroscopic observations with the long-slit of the ACAM instrument at the WHT during the visitor mode observation runs in October 2016 and March 2017. We selected these targets based on a preliminary reduction of the r-, i- and z-band images obtained in the same night. In case of a galaxy over-density at a likely high redshift and with a visible BCG candidate, we conducted three spectroscopic exposures of 1200 s each per cluster. We positioned the slit such that it covered the BCG candidate and at least one other candidate cluster galaxy. We used a V400 grating and the GG495A order-sorting filter in combination with a slit width of $1\farcs0$. Thus, we obtained observations at 3.3 Å/pixel with a resolution of $R \approx 450$ at $\lambda = 6000$ Å covering a wavelength range between 4950 and 9500 Å. This agrees well with the range of expected emission and absorption features in the targeted redshift regime.

6.5.1 Data reduction

The data reduction of the spectroscopic observations includes a bias subtraction and flat-fielding. We remove cosmic rays with the help of the algorithm LA-cosmic (van Dokkum, 2001) for all of the spectroscopic frames. We then co-add three frames of the same target, respectively, and employ IRAF for the further reduction of the co-added spectroscopic frames. We extract spectra using the task `apall`, which follows the ‘Optimal Extraction Algorithm for CCD Spectroscopy’ by Horne (1986). This includes a background subtraction and trace fitting of the position of the spectrum in the spatial direction of the frame. For the background subtraction a polynomial is fitted to the sky background along the spatial direction at each wavelength step and subsequently subtracted to remove the contribution of the night sky to the spectrum. The tasks `identify` and `dispcor` allow us to perform a wavelength calibration with the help of well-known sky emission lines[4]. Finally, we perform a flux calibration using the tasks `sensfunc` and `calibrate`. Our primary goal here is not to get an absolute flux calibration but to find the correct relative fluxes over the range of the spectrum. We use standard star observations of the star BD+332642 (observed by us on 2017 March 21, slit width: $0\farcs75$, exposure time: 150 seconds). They enable us to estimate the sensitivity function (`sensfunc`), which connects the measured spectra (e.g. of the standard stars) to reference spectra of the same object. When applied to the wavelength-calibrated spectra (`calibrate`), the sensitivity function allows us to obtain the flux-calibrated spectra.

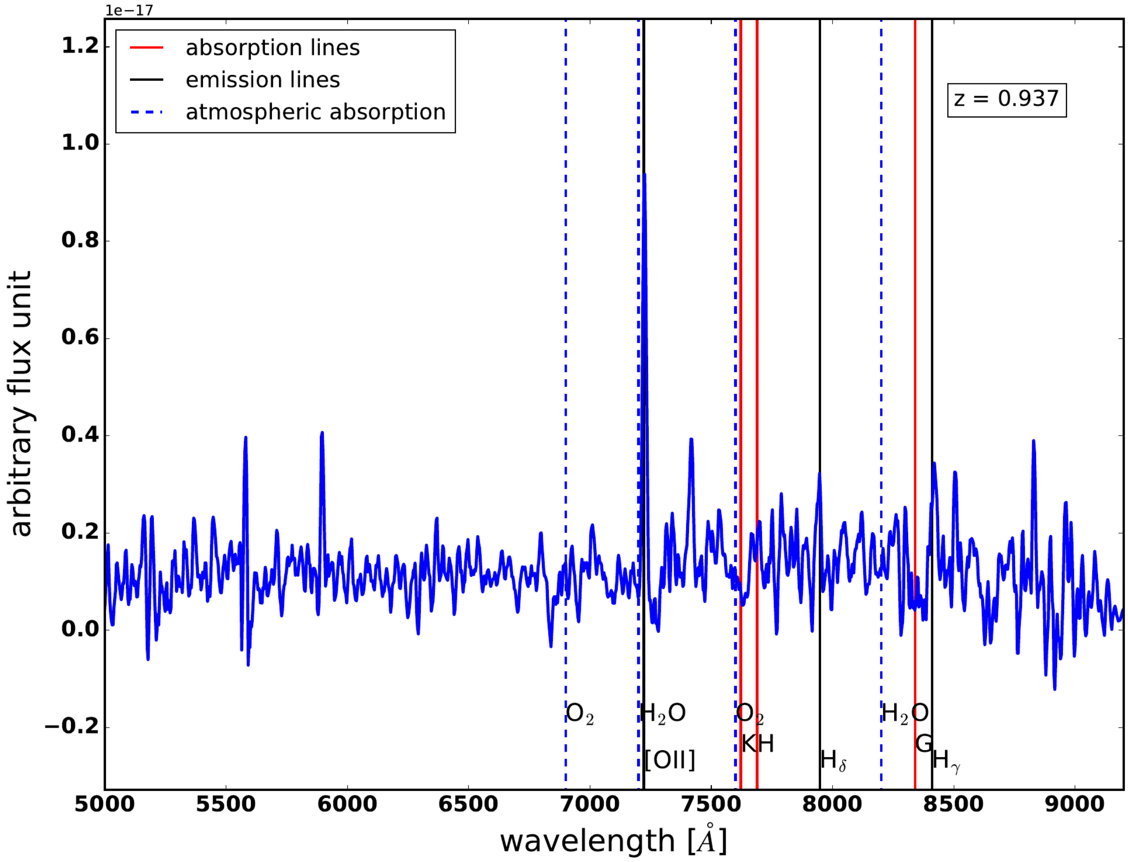

Figure 6.4 – Spectrum of the BCG candidate in cluster PLCK G58.14–72.7. The vertical, dashed blue lines indicate where atmospheric absorption lines caused by water and oxygen molecules are to be expected. The vertical, solid black lines represent the position of emission lines. The vertical, solid red lines represent the position of absorption lines that may occur especially in elliptical galaxies. The original wavelength at emission/absorption is shifted to the redshift indicated in the upper right corner of the plot. The [OII] line is the only feature we clearly identified for this spectrum.

6.5.2 Spectroscopic redshifts

We examine the fully extracted and calibrated spectra of the candidate BCGs and other cluster member galaxies for prominent emission and absorption line features in order to obtain a rough spectroscopic redshift estimate. The Calcium H and K absorption lines at about 3935 Å and 3970 Å and the 4000 Å-break are the main features that we can identify in the majority of the galaxies[5]. Additionally, we have one galaxy (in PLCK G58.14–72.7) with a prominent emission line (see Figure 6.4).

---

[4] https://www.astrossp.unam.mx/misc/obstools/standards/NightSky/skylines.html

[5] We use the lines listed at the SDSS homepage as a reference http://classic.sdss.org/dr6/algorithms/linestable.html.

We perform a cross-correlation with the absorption line template `spDR2-023`[6] and the emission line template `femtemp97`[7] following these steps:

1. We fit a polynomial of order 7 to the spectrum and the template, to subtract the continuum contribution.

2. We mask wavelength regimes that include known intense sky lines and atmospheric lines to minimise the impact of residuals from the sky background subtraction and to prevent the cross-correlation with atmospheric features. The most common molecules to cause atmospheric absorption are H_2O (at 7200 Å) and O_2 (at 6900 Å and 7600 Å).

3. We perform the cross-correlation with the function `crosscorrRV()` from the `PyAstronomy.pyasl` package in python. While the spectroscopic data are relatively shallow, we were able to fine-tune the redshift using the photo-z information as a prior. The cross-correlation gives us a spectroscopic redshift estimate.

4. We estimate the uncertainty of the spectroscopic redshift result by fitting a Gaussian to the correlation peak and by taking the half width at half maximum as the uncertainty.

The spectroscopic redshift estimates from the cross-correlation analysis are in close agreement with our estimates by eye. In particular, we can identify the emission line from the BCG candidate of PLCK G58.14–72.7 (see Figure 6.4) as the [OII] emission line with a rest frame wavelength of 3727 Å based on our photometric redshift result and an estimate by eye upon inspection of the spectrum. Additionally, when two galaxies falling on the same (long-)slit have both a reliable redshift measurement, we also find a good consistency between those two measurements. We report spectroscopic redshifts for five cluster candidates in Table 6.3. The spectra from galaxies in the remaining cluster candidates were unfortunately too noisy to extract a reasonable redshift by eye or with the cross-correlation technique. This was, however, fully expected given the relatively short spectroscopic integration times used in this study.

---

[6] http://classic.sdss.org/dr5/algorithms/spectemplates/

[7] http://tdc-www.harvard.edu/iraf/rvsao/Templates/

Table 6.3 – Redshift results for the spectroscopic sub-sample.

ID	Name	RA	Dec	z_{spec}	$f^{\star}_{\mathrm{peak}}$	features
1074	PSZ2 G237.68+57.83	163.3244	10.8770	$z_1 = 0.894 \pm 0.007$	1.12	Ca H+K lines, 4000 Å-break
		163.3107	10.8834	$z_2 = 0.878 \pm 0.006$	1.84	Ca H+K lines, 4000 Å-break
-	PLCK G58.14–72.7	356.3987	-18.8019	$z_1 = 0.938 \pm 0.003$	2.98	[OII] emission line
		356.3982	-18.8020	$z_2 = 0.927 \pm 0.004$	2.37	Ca H+K lines, 4000 Å-break
-	PLCK G98.08–46.4	355.5238	13.0233	$z_1 = 0.983 \pm 0.005$	1.74	Ca H+K lines, 4000 Å-break
		355.5201	13.0139	$z_2 = 0.988 \pm 0.008$	1.38	Ca H+K lines, 4000 Å-break
-	PLCK G174.14–27.5	59.0335	16.4454	$z_1 = 0.834 \pm 0.005$	1.19	Ca H+K lines, 4000 Å-break
		59.0371	16.4443	$z_2 = 0.829 \pm 0.003$	2.31	Ca H+K lines, 4000 Å-break
-	PLCK G184.49+21.1	111.0799	34.0573	$z_1 = 0.596 \pm 0.007$	1.81	Ca H+K lines, 4000 Å-break, Mg-line
		111.0749	34.0465	$z_2 = 0.594 \pm 0.007$	1.85	Ca H+K lines, 4000 Å-break

Notes. Results of the spectroscopic analysis. z_1 and z_2 correspond to the redshifts of the first (= BCG candidate) and second galaxy spectrum on the slit.

In case of the clusters PSZ2 G112.54+59.53, PLCK G82.51+29.8, PLCK G122.62–31.9 and PLCK G164.82–47.4 the extracted spectra were not pronounced enough to obtain a reliable redshift estimate.

* f_{peak} is the ratio between the cross-correlation peak and the next weaker peak in the cross-correlation function. It characterises how reliable the redshift result is.

6.6 Confirmation of cluster candidates

To verify or invalidate the cluster candidates in our sample in a quantitative manner, we resort to the richness-mass relation by Rozo et al. (2015), which allows us to asses if our measured richness suggests a halo that can account for the SZ-signal in the *Planck* maps.

We derive the *Planck* SZ mass proxy $M_{500c,SZ}$ following mainly Section 7.2 in Planck Collaboration et al. (2014b). To do so, we filter the *Planck* maps at the position of the optical cluster centre from our analysis with the Matched Multi-Filter 3 (MMF3, Melin et al., 2006) varying the angular cluster size θ_s between 0.8 and 32 arcmin. Here, the six frequency channels are linearly combined, and the filtering takes into account the cluster pressure profile and thermal SZ spectrum as prior knowledge (Planck Collaboration et al., 2014b). For each cluster size we estimate the SZ flux, Y_{500}, within the radius R_{500} from the filtered maps. We can break the size-flux degeneracy with an X-ray scaling relation (see also Figure 16 in Planck Collaboration et al., 2016c). Since it is redshift dependent, we use our photometric redshift results as prior information to then obtain the SZ mass proxy $M_{500c,SZ}$.

We compare our estimates of λ and $M_{500c,SZ}$ in Figure 6.5, finding that the majority of clusters are close to the scaling relation by Rozo et al. (2015) or at least approximately half as rich as expected from the relation. This suggests that the richness-mass relation, which was established for systems measured at higher S/N and lower redshifts, may indeed be applicable even under the assumption that there is no redshift evolution and given slight differences in the richness definition. We also find a fraction of candidates that are clearly below the scaling relation.

Indeed, we even expect a fraction of cluster candidates to lie notably below the richness-mass relation because we investigate a sample in the low S/N regime. Even with our preselection it is possible that spurious detections or projection effects occur. Even more importantly, the Eddington bias starts to play a significant role at low S/N. As shown in van der Burg et al. (2016), this effect can even lead to an overestimation of the measured SZ-mass by a factor of 2 with respect to the real SZ-mass for clusters at $\mathrm{S/N} \lesssim 4.0$ and $z \gtrsim 0.6$.

In order to distinguish between confirmed and invalidated cluster candidates, it is necessary to find criteria to base this classification on. We expect that the measured SZ signal is predominantly caused by inverse Compton scattering of CMB photons instead of noise in the *Planck* maps. van der Burg et al. (2016) assume that this is the case when the richness-based mass amounts to 50 per cent or more of the SZ-based mass within the error bars.

From the sample in this work this criterion is met for 18 candidates (13 are in the PSZ2 catalogue, 5 were detected with the MMF3 method at lower S/N). However, there is a continuous transition between a SZ signal which is noise-dominated and one which is dominated by the presence of a cluster. Especially in the light

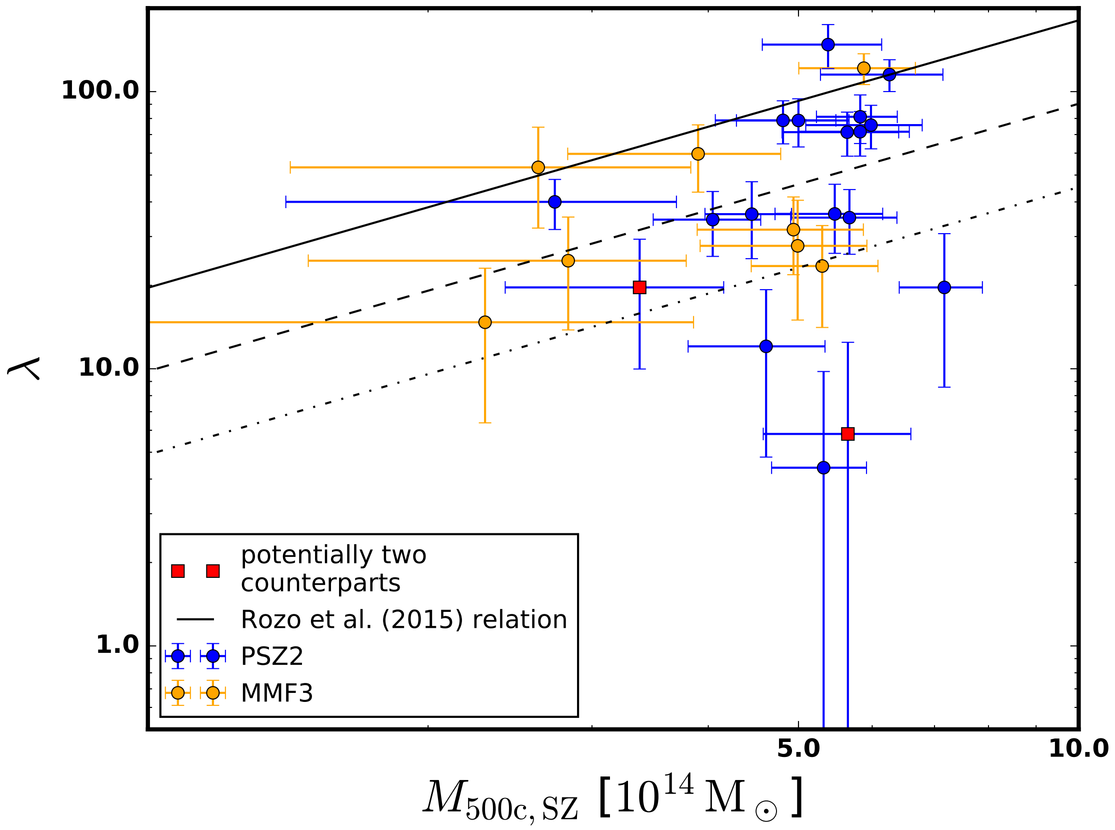

Figure 6.5 – Comparison of the richness λ obtained from our optical data and the SZ-based mass $M_{500\mathrm{c,SZ}}$ from the *Planck* measurements. The solid line marks the richness-mass relation from Rozo et al. (2015). The dashed (dash-dotted) line marks, where the richness is 50 per cent (25 per cent) of what is expected from the scaling relation. Red squares mark PSZ2 cluster candidates with two potential optical counterparts. In these cases, the SZ-based mass $M_{500\mathrm{c,SZ}}$ should be seen as an upper limit.

of the multiple effects that can lead to a discrepancy between richness-based mass and SZ-based mass (assumption of no redshift evolution of the scaling relation, potentially fewer galaxies on the red-sequence at higher redshifts, 25 per cent scatter in the richness-mass relation, Eddington bias especially at low S/N, projection effects with multiple clusters contributing to the SZ signal), the validation criterion of $M_{500\mathrm{c},\lambda}/M_{500\mathrm{c,SZ}} \geq 0.5$ might be too strict. Inspecting the distribution of candidates in the richness-mass-plane once again (see Figure 6.5), we see that there is a bulk of candidates above a limit of $M_{500\mathrm{c},\lambda}/M_{500\mathrm{c,SZ}} \geq 0.25$. Also inspecting the colour images, they are likely valid counterparts to the SZ-signal. For 24 (16 are in the PSZ2 catalogue, 8 were detected with the MMF3 method) out of 32 candidates the richness-based mass makes up at least 25 per cent of the SZ-based mass within the 1σ uncertainties and we conclude that they are likely optical counterparts to the SZ-signal. We distinguish a conservative cluster confirmation criterion with $M_{500c,\lambda}/M_{500c,SZ} \geq 0.5$ and a loose cluster confirmation criterion with $M_{500c,\lambda}/M_{500c,SZ} \geq 0.25$. It has to be noted that the mass ratio $M_{500c,\lambda}/M_{500c,SZ}$ as estimated here is not entirely applicable for clusters with multiple counterparts. The richness-based mass is inferred with the help of the richness-mass scaling relation by Rozo et al. (2015). Therefore, it only relates to one particular optical counterpart, assuming that it fully accounts for the SZ-signal. However, our estimates of the SZ-based mass are based on the SZ-signal, possibly with contributions from several counterparts. In these cases our reported mass ratio is biased low. Our sample includes two candidates with two potential counterparts (PSZ2 G092.69+59.92 and PSZ2 G136.02-47.15; see Section 6.7 for details). The mass ratios of these cluster candidates can be seen as a lower limit. Inspecting the additional available information in Table 6.2 beyond the richness-mass relation, we notice the following:

Figure 6.6 (*top, left panel*) displays that the fraction of loosely confirmed clusters is higher among the low S/N noise sources in our sample (MMF3 with $S/N < 4.5$) than among the high S/N sources (PSZ2 with $S/N > 4.5$). This is not necessarily to be expected since spurious detections are more likely to occur at lower S/N. However, we had a larger number of candidates to choose from considering the MMF3 detection method down to $S/N > 3$. This means we could identify particularly those candidates, which appeared very rich in the WISE, PS1 and/or SDSS data. It is possible that this preselection counterbalances the effect of Eddington bias. An additional explanation for the high fraction of confirmed MMF3 cluster candidates could be the fact that these low S/N candidates have a higher positional uncertainty, lower masses and there are a lot more candidates available than in case of the PSZ2 candidates. Consequently, the probability for super-positions by chance is increased. We check if richness λ and SZ-mass $M_{500c,SZ}$ are related with the help of Spearman's rank correlation coefficient r_s. We find $r_{s,MMF3} = 0.36$ for the MMF3 targets and $r_{s,PSZ2} = 0.23$ considering all PSZ2 targets available richness measurements or $r_{s,PSZ2,0.25} = 0.35$ considering only the PSZ2 targets with $M_{500c,\lambda}/M_{500c,SZ} \geq 0.25$. We conclude that there is a tendency towards a positive correlation between richness and SZ-mass. There is a comparable correlation between loosely confirmed PSZ2 and MMF3 targets.

With regard to the PSZ2 cluster candidates, we find that 16 out of 20 PSZ2 candidates (with available estimates for $M_{500c,\lambda}$ and $M_{500c,SZ}$) are above the limit $M_{500c,\lambda}/M_{500c,SZ} \geq 0.25$. This corresponds to 80 per cent. Considering the numerous different follow-up studies for the PSZ2 catalogue with confirmed as well as invalidated cluster candidates it is hard to quantify the expected fraction of confirmed clusters in our sample. We can, however, get a rough estimate based on the work by Planck Collaboration et al. (2016c). They report 1653 detections in PSZ2 with and expected reliability of about 90 per cent. Thus, 165 candidates are expected to be invalidated. Planck Collaboration et al. (2016c) report 1203 confirmed cluster candidates. Consequently, there should be 165 candidates to be invalidated among the remaining $1653 - 1203 = 450$ cluster candidates. This corresponds to an expected

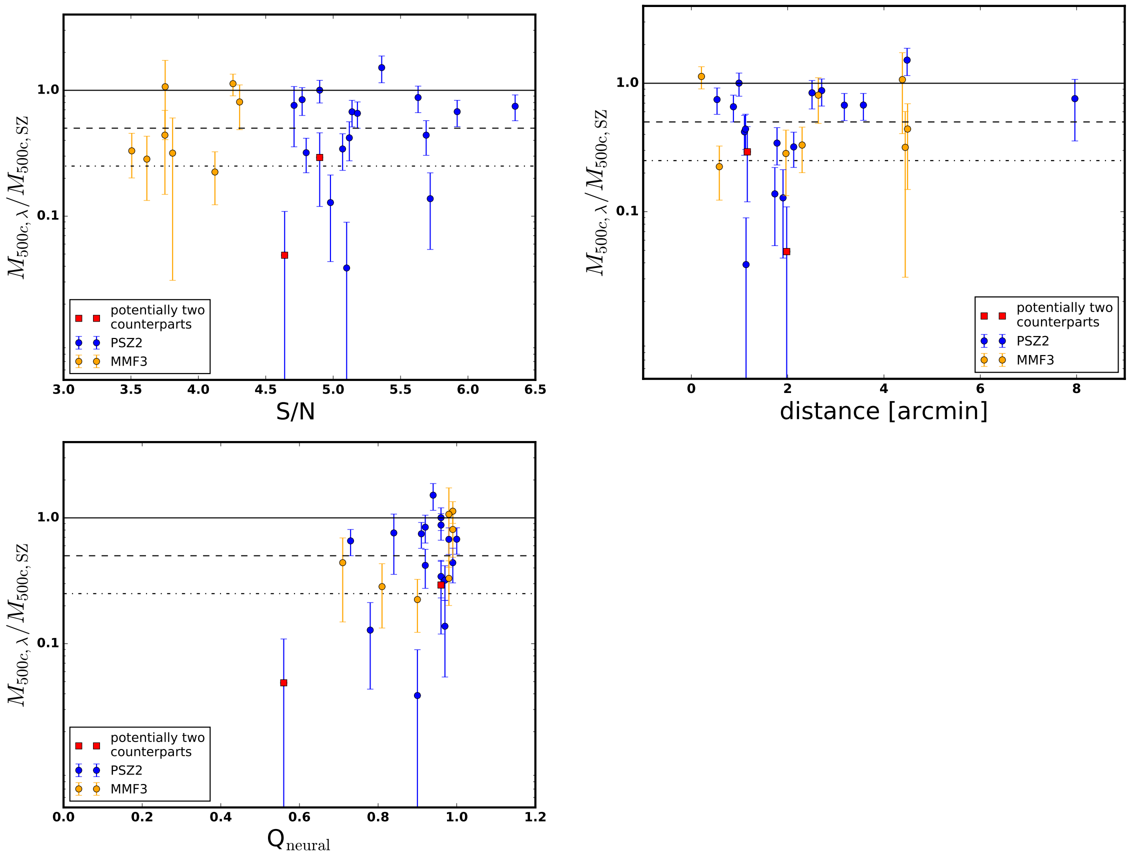

Figure 6.6 – Comparison of the mass ratio $M_{500c,\lambda}/M_{500c,SZ}$ versus S/N (*top, left*) of the *Planck* SZ detection, versus the distance between the optical centre and the SZ peak coordinates of the blind detection (*top, right*) and versus Q_{neural} (*bottom*). We only plot the candidates that have the corresponding information available in Table 6.2. The solid, dashed and dash-dotted line mark, where $M_{500c,\lambda}/M_{500c,SZ} = 1.0$, $M_{500c,\lambda}/M_{500c,SZ} = 0.5$, and $M_{500c,\lambda}/M_{500c,SZ} = 0.25$, respectively. Red squares mark PSZ2 cluster candidates with two potential optical counterparts. In these cases, the mass ratio $M_{500c,\lambda}/M_{500c,SZ}$ should be seen as a lower limit.

fraction of confirmed clusters of about 63 per cent if one were to randomly select candidates from the remaining 450 of unconfirmed candidates. This is slightly lower than the fraction of confirmed clusters that we find for the PSZ2 targets presented in this work. Our fraction is, however, comparable to the fraction of confirmed PSZ2 cluster candidates reported in van der Burg et al. (2016).

Figure 6.6 (*bottom panel*) illustrates that we find no confirmed clusters with values of $Q_{neural} < 0.7$. Additionally, the fraction of validated clusters and the ratio $M_{500c,\lambda}/M_{500c,SZ}$ both generally increase with increasing Q_{neural}. There are, however, also cluster candidates with a high value of $Q_{neural} > 0.7$ that do not fulfil our validation criteria. It is reasonable that this quantity becomes less reliable in the low

S/N regime (S/N < 5), since Q_{neural} is not suited to flag noise-induced detections (Planck Collaboration et al., 2016c).

Figure 6.6 (*top, right panel*) shows that all except one of the loosely confirmed clusters in our sample are within a distance of $\lesssim 5$ arcmin from the *Planck* SZ position. This corresponds to a cluster confirmation criterion used in several previous works (Barrena et al., 2018; Streblyanska et al., 2018; Boada et al., 2018). On average the distance is 2.4 arcmin, which is well within the size of the *Planck* beam. We also find that 68 per cent of the confirmed clusters with $M_{500\mathrm{c},\lambda}/M_{500\mathrm{c,SZ}} \geq 0.25$ are found within a distance of 2.6 arcmin from the respective detection in the *Planck* maps. This is less than 2 times larger than the positional uncertainty of ≈ 1.5 arcmin of the PSZ2 union catalogue (Planck Collaboration et al., 2016c). Additionally, this is in good agreement with values found for confirmed cluster candidates from PSZ2 by Streblyanska et al. (2018) with 68 per cent of confirmed clusters within 3.1 arcmin and from the first *Planck* data release PSZ1 by Barrena et al. (2018) with 68 per cent of confirmed clusters within 2.8 arcmin. From Figure 6.6 (*top, right panel*), we see that the optical positions of the PSZ2 targets tend to be closer to the position of the SZ detection than the optical positions of the MMF3 targets. This agrees with the fact that the positional uncertainty of the PSZ2 targets is smaller because they have a higher S/N.

6.7 Notes on individual cluster candidates

Table 6.2 summarises the estimated properties of the investigated sample and we present colour images of the confirmed cluster candidates in Appendix 6.13. In this section, we discuss some cluster candidates that are worth mentioning, for example, due to high redshifts, multiple counter parts or for special treatment in our analysis.

PSZ2 G085.95+25.23

This cluster candidate likely has a complex structure. We find an optical counterpart around the position RA $= 277.648°$, Dec $= 56.892°$ at a photometric redshift of $z_{\mathrm{phot}} = 0.77 \pm 0.05$. We can also measure the redshift from a second position at RA $= 277.599°$, Dec $= 56.885°$ with an estimated photometric redshift of $z_{\mathrm{phot}} = 0.74 \pm 0.03$ with a richness of $\lambda = 148 \pm 18$[8]. Both redshifts agree within their uncertainties. We report the results for the first position (with higher richness) in Table 6.2. The redshift of this optical counterpart is in good agreement with the spectroscopic redshift of $z_{\mathrm{spec}} = 0.782 \pm 0.003$ found by Amodeo et al. (2018) (see Table 6.4). Our richer (less rich) component has a distance of 1.98 arcmin (1.06 arcmin) to the optical cluster centre reported by Amodeo et al. (2018).

---

[8] Note that this richness is related to the richness measured at the first position because the measurements are close both in position and in redshift.

PSZ2 G092.69+59.92

According to Burenin et al. (2018), this cluster candidate consists of two optical counterparts in projection. They estimate a spectroscopic redshift of $z_{\mathrm{spec}} = 0.848$ for a counterpart at a position, which coincides with our own observations. They mention that a redshift of $z = 0.463$ was reported in the *redMaPPer* cluster survey (Rykoff et al., 2014). This agrees with the spectroscopic redshift of $z_{\mathrm{spec}} = 0.461$, which Streblyanska et al. (2018) mention in their work. However, the geometric centre of their optical cluster does not lie within the field of view of our observation. Since our photometric redshift estimate and position are in better agreement with the results by Burenin et al. (2018), we only make use of their spectroscopic redshift estimate for our red-sequence calibration. We note that the richness λ of the cluster candidate measured at a photometric redshift of $z_{\mathrm{phot}} = 0.86 \pm 0.07$ is lower than expected given the measured SZ signal. This is not indicative of a halo that may solely be responsible for the measured SZ signal, but it is a hint that an additional counterpart (at $z = 0.46$) may be contributing to the SZ signal.

PSZ2 G112.54+59.53

In the colour image, there are only a few cluster members visible and we find that some of them are fainter than the 80 per cent depth of our data. Accordingly, there is only a very weak peak in the histogram of filtered richness versus redshift resulting in a redshift estimate of $z_{\mathrm{phot}} = 0.83 \pm 0.06$.

Since the density of galaxies at the same redshift is so low, the step of finding the galaxy, which maximises the richness, is not reasonable. We therefore only report the redshift, richness and mass results at the position of the BCG identified by eye. The richness is not high enough to fulfil the confirmation criterion. However, deeper data might reveal more of the potential cluster galaxies and provide a more robust estimate of richness and mass.

PSZ2 G136.02–47.15

Streblyanska et al. (2018) list a spectroscopic redshift of $z_{\mathrm{spec}} = 0.465$ from SDSS DR12 for this cluster candidate. They categorise this counterpart as ‘potentially associated’, i.e., this candidate does not meet their richness/distance requirements for cluster confirmation. The possible counterpart we discuss in this paper is closer in sky position to the SZ detection, but has a richness-based mass that is also lower than expected for the SZ detection. Even though both sources (at $z = 0.47$ and $z_{\mathrm{phot}} = 0.61 \pm 0.07$ measured in this work) may have contributed to the measured SZ signal, it may be a largely noise-induced detection. We find that the given geometric centre from Streblyanska et al. (2018) does not lie within the field of view of our observation of this target. We therefore conclude that we do not investigate the same optical counterpart as Streblyanska et al. (2018). For this reason we do not use the spectroscopic redshift estimate for the recalibration of the red-sequence models.

PSZ2 G141.98+69.31

Streblyanska et al. (2018) identify an optical counterpart as potentially associated with PSZ2 G141.98+69.31 and report a spectroscopic redshift of $z_{\rm spec} = 0.714$. Since the given geometrical centre is about 3.5 arcmin from the centre we find in this work, we do not include this spectroscopic redshift for the recalibration of the red-sequence models. Our photometric redshift estimate of $z_{\rm phot} = 0.71 \pm 0.03$ is, however, close to the spectroscopic redshift from Streblyanska et al. (2018). We additionally find a quite large offset between the optical centre and the SZ detection of 7.96 arcmin. The similar redshift results and offsets between optical and SZ position could be a hint at the presence of large-scale structure.

PSZ2 G160.94+44.8

This candidate likely corresponds to a false detection when carefully reinspecting the *Planck* maps. This is supported by the fact that PSZ2 G160.94+44.8 has a quality flag of $Q_{\rm neural} = 0.06$. Additionally, we find a large distance of more than 10 arcmin between the SZ-peak and the optical position when we re-sample the *Planck* maps at the optical position for the SZ-mass measurement. This gives a second strong argument for a false *Planck* detection.

PSZ2 G165.41+25.93

Upon the inspection of the colour image, an optical counterpart to the SZ-signal is hardly identifiable. Accordingly, there is only a very weak peak in the histogram of filtered richness versus redshift resulting in a redshift estimate of $z_{\rm phot} = 0.67 \pm 0.03$. At this redshift, member galaxies of the cluster should be detectable in our imaging. We therefore believe that the optical counterpart is a small galaxy group at most.

Since the density of galaxies at the same redshift is so low, our pipeline is not able to reliably refine the cluster centre through identifying the galaxy, which maximises the richness. We therefore, only report the redshift, richness and mass results at the position of the BCG identified by eye.

PSZ2 G237.68+57.83

From our red-sequence analysis, we obtain a high photometric redshift estimate of $z_{\rm phot} = 0.97 \pm 0.05$. This is close to the highest redshifts for which clusters can still be detected in the *Planck* maps. However, our red-sequence models loose constraining power in this redshift regime. Additionally, we have a 80 per cent detection limit of $m_{i,\rm totlim} = 23.15$. This photometric redshift and detection limit cause a high completeness correction factor of $c_{\mathrm{cmp}} > 3.5$. We therefore resort to our spectroscopic redshift result for the estimate of the optical richness and inferred mass. The spectroscopic redshift of the BCG candidate of $z_{\mathrm{spec}} = 0.894$ is in good agreement with the spectroscopic redshift estimate of $z_{\mathrm{spec}} = 0.892$ reported by Burenin et al. (2018). Due to the problems with the photometric redshift measurement, we do not include this target in the recalibration of the red-sequence models.

PSZ2 G305.76+44.79

Our observations of this cluster candidate provide only a shallow 80 per cent detection limit of $m_{i,\mathrm{totlim}} = 22.65$, which means we have a limiting redshift of 0.66. We measure a photometric redshift of $z_{\mathrm{phot}} = 0.76 \pm 0.13$. However, this is a noisy measurement, which is based only on a few galaxies. Therefore, our pipeline cannot reliably refine the cluster centre and we only report the redshift, richness and mass results at the position of the BCG identified by eye. The richness is not high enough to fulfil the confirmation criterion. However, deeper data might reveal more of the potential cluster galaxies and provide a more robust estimate of richness and mass.

PSZ2 G321.30+50.63

Similar to cluster candidate PSZ2 G085.95+25.23, this cluster candidate likely has a complex structure. We measure a photometric redshift of $z_{\mathrm{phot}} = 0.79 \pm 0.04$ around the positio RA $= 204.611°$, Dec $= -10.550°$. Additionally, we find $z_{\mathrm{phot}} = 0.68 \pm 0.07$ around the position RA $= 204.661°$, Dec $= 10.566°$. Here, we measure a richness of $\lambda = 37 \pm 10$. The redshifts agree only within around 2σ. This could, however, also be connected to the broad photo-z peak in the distribution of filtered richness versus redshift. We report the results for the first, richer component in Table 6.2.

PLCK G58.14–72.7

Similar to PSZ2 G237.68+57.83, we measure a high photometric redshift of $z_{\mathrm{phot}} = 1.03 \pm 0.10$. This would require a high completeness correction factor of $c_{\mathrm{cmp}} > 3.5$. Thus, we do not include this cluster in the recalibration of the red-sequence models. Additionally, we use the spectroscopic redshift of the BCG candidate for our optical richness and mass estimates.

Concerning the spectroscopic redshifts estimated via cross-correlation with absorption and emission line templates we noticed that the O_2 atmospheric absorption line at 7600 Å coincides with the position of the 4000 Å-break (see Figure 6.4). The emission peak of the [OII] line is, however, prominent enough so that we are confident of our spectroscopic redshift results of $z_{\mathrm{spec}} = 0.938 \pm 0.003$ for the BCG and $z_{\mathrm{spec}} = 0.927 \pm 0.004$ for the second galaxy on the slit.

PLCK G98.08–46.4

For this cluster candidate, we measure a very high photometric redshift of $z_{\mathrm{phot}} = 1.06 \pm 0.04$. This is close to the highest redshifts for which clusters can still be detected in the *Planck* maps. Given the high redshift and an intermediate depth of the data, we have to apply a large completeness correction factor of $c_{\mathrm{cmp}} > 3.5$. In addition, the completeness curve describing how many of the injected sources are retrieved drops rather sharply in comparison to other observations. This could also lead to an overestimate of the richness. Since we have measured a spectroscopic redshift of $z_{\mathrm{spec}} = 0.983$ for the BCG candidate as well, we report the richness given this redshift estimate in Table 6.2. We do, however, not use the spectroscopic redshift result for the calibration of the red-sequence models.

6.8 Discussion

Planck is the only all-sky SZ survey presently available. The public PSZ2 catalogue provides galaxy cluster candidates down to a SZ-significance threshold of $\mathrm{S/N} = 4.5$, forming an excellent basis for cosmological investigations. In this context, all candidates must be systematically followed up to understand the selection function and to fully exploit *Planck*'s potential. For this, we provide a noticeable contribution in this work. We pursue slightly different and partly complementary methods and strategies for the confirmation of cluster candidates in comparison to similar follow-up studies of the PSZ2 catalogue.

For example, Streblyanska et al. (2018) inspect PSZ2 cluster candidates in the Compton y-maps and in SDSS data. Their confirmation criteria are based on the richness and distance of the optical centre to the position of the PSZ2-detection. Additionally, they provide photometric and partially spectroscopic redshift information. Due to the limited depth of the SDSS data, they estimate the richness taking into account galaxies close to the photometric redshift estimate with an r-band magnitude in the range of $(r_{\mathrm{BCG}}, r_{\mathrm{BCG}} + 2.5)$ in an 0.5 Mpc radius around the cluster centre. The limited depth allows them to provide this richness estimate only for clusters with $z < 0.6$. Streblyanska et al. (2018) require a richness of > 5 and a distance of the optical centre to the position of the SZ detection of $< 5'$ for a cluster to be confirmed. This way, they confirm 37 clusters from the PSZ2 catalogue and find 17 clusters as 'potentially associated' with a PSZ2 detection. Our sample overlaps with the one from Streblyanska et al. (2018) for 9 cluster candidates. Our redshift estimates are in good agreement with their results. In addition, we provide richness-based masses obtained using the scaling relation by Rozo et al. (2015) and SZ-mass results, which we inferred from the *Planck* maps based on the optical positions and photometric redshifts.

Boada et al. (2018) apply confirmation criteria, which are very similar to Streblyanska et al. (2018). They use optical data from the Kitt Peak National Observatory 4m Mayall telescope to provide photometric redshifts, richnesses and the distance from the optical centre to the PSZ2-detection for their sample of PSZ2 cluster candidates. They focus on the regime of high SZ-significance with S/N > 5 confirming clusters in a low to intermediate redshift range of $0.13 < z < 0.74$. Our study does not overlap with their sample but complements this with a sample of *Planck* cluster candidates at intermediate to high redshifts ($0.5 \lesssim z \lesssim 1.0$) and extending down to low SZ-significance S/N > 3.

The works by Amodeo et al. (2018) and Burenin et al. (2018) report precise spectroscopic redshifts for PSZ2 clusters, which are in part also included in our sample. Their spectroscopic information helps us with recalibrating our red-sequence models. As a result, we obtain photometric redshifts, which allow us to estimate the richness and richness-based mass from our observations. Additionally, we can infer the SZ-based mass and therefore supplement the spectroscopic redshift information from Amodeo et al. (2018) and Burenin et al. (2018).

Finally, our strategy of cluster confirmation is very similar to van der Burg et al. (2016) who confirm 16 clusters detected with *Planck*. Based on optical imaging with MegaCam at Canada-France-Hawaii Telescope (CFHT), they estimate photometric redshifts and richnesses, and infer SZ-based masses. They illustrate the benefit of preselecting cluster candidates from optical and NIR-data in order to reliably uncover massive clusters at low SZ detection significance. In addition, they point out the advantage of a secondary mass proxy from optical data because it is independent of Eddington bias. These strategies have proven equally useful for our follow-up study. The reliability is of the order of 80 per cent for our PSZ2 cluster candidates. This roughly meets our expectations (see Section 6.6) and is comparable to the findings of van der Burg et al. (2016). In particular, our selection was effective for the low S/N targets detected with the MMF3 method. We achieve a high reliability where only one of these targets remains unconfirmed. There is of course the possibility of an increased number of chance super-positions between MMF3 SZ detections and our selected optical counterparts for example due to the large number of candidates in the low S/N regime. However, we do not find that the optical positions of the MMF3 targets are particularly closer to the SZ detections than it is the case for the PSZ2 candidates. Additionally, the Spearman rank correlation coefficients of the richness and the SZ-mass show a very similar tendency towards a positive correlation both for the MMF3 and for the PSZ2 candidates. This gives us reason to believe that we did select cluster candidates in the optical, which are indeed related to the SZ detection in the *Planck* maps.

Moreover, the fact that our sample is not purely SZ-selected implies that we have a complex selection function, which is hard to quantify because it requires a careful modelling of the optical properties of the clusters. The consequential uncertainties in the selection function can easily present a problem for the use of such samples for precision cosmology. With our approach we do, however, increase the sample's purity especially towards lower SZ significance. It allows us to efficiently exploit the potential of the *Planck* SZ-survey to lower S/N to find more massive, high-redshift clusters. Indeed, our study extends the number of massive, high-redshift clusters including some of the highest-redshift clusters detected in *Planck* so far. These could be of particular interest for further astrophysical investigations in the context of clusters as laboratories for the interaction and evolution of galaxies, potential mergers or AGN feedback. Therefore, combining a SZ-significance cut with deeper auxiliary data might be the best option to obtain representative massive and high-redshift samples based on *Planck* as the only all-sky SZ survey presently available.

6.9 Summary and conclusions

We present a photometric (spectroscopic) follow-up analysis of a sample of 32 (9) galaxy cluster candidates observed with the 4.2-m William Herschel Telescope. The sample is selected from detections in the *Planck* maps (PSZ2 catalogue and MMF3 detection method) while the candidates were preselected to likely have counterparts at redshifts above $z \gtrsim 0.7$ based on SDSS, Pan-STARRS and WISE 3.4 μm data. From a red-sequence based analysis of galaxy over-densities in the r-, i- and z-band imaging data, we are able to obtain photometric redshift and richness estimates for the cluster candidates. We recalibrate our red-sequence models based on a comparison of our initial photometric redshift estimates with spectroscopic redshift estimates.

In combination with the richness-mass relation by Rozo et al. (2015), the richness estimate provides us with a quantitative measurement to assess if the detected cluster candidate is likely massive/rich enough to account for the detected SZ signal. We consider a cluster candidate to be a likely counterpart of a SZ detection in our sample according to quantitative and qualitative criteria. We require 1) that we can identify an over-density of cluster galaxies of the same colour in the colour images and 2) that the richness-based mass is high enough to account for the SZ signal considering the cluster should be at least 50 per cent as massive as expected from the SZ signal. We confirm 18 clusters out of 32 cluster candidates from the *Planck* maps in our sample. The confirmed clusters cover a redshift range of $0.5 \lesssim z \lesssim 1.0$ and a richness-based mass range of $1.0 \times 10^{14} \lesssim M_{500\mathrm{c},\lambda}/\mathrm{M}_{\odot} \lesssim 8.0 \times 10^{14}$.

There are, however, multiple effects that can lower the ratio of richness-based mass to SZ-based mass. Among them are projection effects, the assumption of no redshift evolution of the richness-SZ-mass scaling relation, the 25 per cent scatter in the richness-SZ-mass relation, and Eddington bias especially at low S/N. Applying a less strict criterion where the cluster should be 25 per cent as massive as expected from the SZ signal, we find 24 optical clusters, which are likely counterparts to the SZ-signal.

Investigating candidates down to S/N ≥ 3 in the *Planck* maps, we find that the SZ-based mass proxy is clearly influenced by Eddington bias. In this context, the richness-based mass represents a valuable quantity because it is independent of the SZ-signal and hence not subject to Eddington bias.

While our sample has a complex selection function due to the preselection with auxiliary optical and infrared data, and is therefore not suitable for precision cosmology, our approach is still efficient in uncovering rich, high-z clusters in the low S/N regime from the *Planck* all-sky survey.

6.10 Appendix A: 80 per cent depth limits

In this appendix, we show an example of the distribution of the recovery fraction $N_{\mathrm{detected}}/N_{\mathrm{injected}}$ of sources as a function of the i-band magnitude m_i (see Figure 6.7). We define the 80 per cent depth limits $m_{i,\mathrm{totlim}}$ in the i-band as the faintest magnitude where we could still recover 80 per cent or more of the injected galaxies.

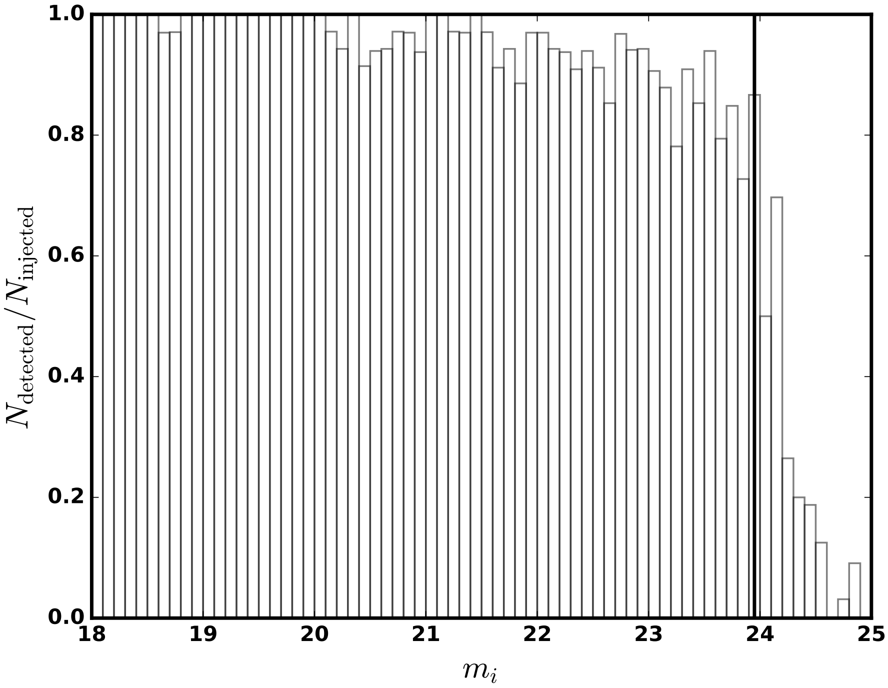

Figure 6.7 – Distribution of the recovery fraction $N_{\mathrm{detected}}/N_{\mathrm{injected}}$ of sources as a function of the i-band magnitude m_i for cluster candidate G032.31+66.07. The black line indicates the 80 per cent depth limit $m_{i,\mathrm{totlim}}$ for this particular observation.

6.11 Appendix B: External information about the candidates

In this appendix, we summarise results from the literature where targets from our sample have been investigated (see Table 6.4). This concerns spectroscopic redshifts and optical cluster centres.

Table 6.4 – Results from independent follow-up studies of cluster candidates from our sample.

ID	Name	RA [°]	Dec [°]	$z_{\rm spec}$	comments
115	PSZ2 G032.31+66.07	219.3540	24.3986	0.609	confirmed cluster from Streblyanska et al. (2018), spec-z from 6 galaxies
277	PSZ2 G066.34+26.14	270.2772	39.8685	-	confirmed cluster from Streblyanska et al. (2018)
378	PSZ2 G085.95+25.23	277.6164	56.8823	0.782 ± 0.003	from Amodeo et al. (2018)
381	PSZ2 G086.28+74.76	204.4745	38.9019	0.699	confirmed cluster from Streblyanska et al. (2018), spec-z from 1 galaxy
420	PSZ2 G092.64+20.78	289.1893	61.6782	0.545	confirmed cluster from Streblyanska et al. (2019) spec-z from 39 galaxies
421	PSZ2 G092.69+59.92	216.5355	51.2373	0.461	potentially associated cluster from Streblyanska et al. (2018), spec-z from 3 galaxies, optical pos. outside the FOV of our observation
		216.6504	51.2642	0.848	from Burenin et al. (2018), spec-z from 2 galaxies, other close by cluster at $z = 0.463$ mentioned
483	PSZ2 G100.22+33.81	258.4232	69.3626	0.598	confirmed cluster from Streblyanska et al. (2019) spec-z from 18 galaxies
623	PSZ2 G126.28+65.62	190.5975	51.4394	0.820	from Burenin et al. (2018), spec-z from 7 galaxies
625	PSZ2 G126.57+51.61	187.4492	65.3536	0.815	from Burenin et al. (2018), spec-z from 1 galaxy
667	PSZ2 G136.02–47.15	22.0984	14.6871	0.465	potentially associated cluster from Streblyanska et al. (2018), spec-z from 1 galaxy, optical pos. outside the FOV of our observation
681	PSZ2 G139.00+50.92	170.0707	63.2500	-	confirmed cluster from Streblyanska et al. (2018)
690	PSZ2 G141.98+69.31	183.1693	46.3564	0.714	potentially associated cluster from Streblyanska et al. (2018), spec-z from 2 galaxies
1074	PSZ2 G237.68+57.83	163.3242	10.8770	-	confirmed cluster from Streblyanska et al. (2018)
		163.3179	10.8794	0.892	from Burenin et al. (2018), spec-z from 1 galaxy
1606	PSZ2 G343.46+52.65	216.0963	-2.7178	0.713	from Burenin et al. (2018), spec-z from 3 galaxies

Column 1: ID of cluster in PSZ2, column 2: name of the cluster, column 3 and 4: optical centre from the respective work, column 5: spectroscopic redshift if available, column 6: comments on the origin of the results.

6.12 Appendix C: Alternative Richness and Mass Results at the Spectroscopic Redshifts

In this appendix, we present our richness and mass results inferred from the optical data when using the spectroscopic redshifts (when available) instead of the photometric redshifts (see Table 6.5).

Table 6.5 – Alternative richness and mass results at the spectroscopic redshifts.

ID	Name	z_{spec}	λ	$M_{500\text{c},\lambda}$ $[10^{14}\text{M}_\odot]$	c_{cmp}	$M_{500\text{c,SZ}}$ $[10^{14}\text{M}_\odot]$
115	PSZ2 G032.31+66.07	0.609^d	71 ± 13	3.81 ± 0.72	1.00	$5.70^{+0.76}_{-0.84}$
378	PSZ2 G085.95+25.23	0.782 ± 0.003^c	167 ± 22	9.24 ± 1.27	1.74	$5.41^{+0.55}_{-0.59}$
381	PSZ2 G086.28+74.76	0.699^d	36 ± 10	1.88 ± 0.55	1.00	$5.32^{+0.70}_{-0.76}$
420	PSZ2 G092.64+20.7	0.545^e	32 ± 11	1.64 ± 0.57	1.00	$4.40^{+0.45}_{-0.49}$
421	PSZ2 G092.69+59.92	0.848^b	$18 \pm 9.$	0.91 ± 0.50	1.36	$3.39^{+0.77}_{-0.95}$
483	PSZ2 G100.22+33.8	0.598^e	37 ± 10	1.94 ± 0.51	1.00	$4.09^{+0.51}_{-0.56}$
623	PSZ2 G126.28+65.62	0.820^b	76 ± 15	4.04 ± 0.84	1.38	$5.06^{+0.66}_{-0.71}$
625	PSZ2 G126.57+51.61	0.815^b	83 ± 17	4.45 ± 0.94	1.68	$5.83^{+0.56}_{-0.60}$
690	PSZ2 G141.98+69.31	0.714^d	40 ± 8	2.08 ± 0.45	1.00	$4.05^{+0.79}_{-0.90}$
1074	PSZ2 G237.68+57.83	0.894 ± 0.007^a	148 ± 27	8.15 ± 1.55	2.94	$5.47^{+0.75}_{-0.80}$
1606	PSZ2 G343.46+52.65	0.713^b	115 ± 15	6.29 ± 0.86	1.00	$6.35^{+0.87}_{-0.95}$
-	PLCK G58.14–72.7	0.938 ± 0.003^a	60 ± 16	3.15 ± 0.90	2.23	$4.13^{+0.85}_{-1.01}$
-	PLCK G98.08–46.4	0.983 ± 0.005^a	53 ± 21	2.80 ± 1.17	3.47	$3.24^{+1.06}_{-1.46}$
-	PLCK G174.14–27.5	0.834 ± 0.005^a	15 ± 8	0.75 ± 0.43	1.17	$3.09^{+1.33}_{-2.15}$
-	PLCK G184.49+21.1	0.596 ± 0.007^a	118 ± 15	6.41 ± 0.87	1.00	$5.80^{+0.79}_{-0.87}$

Column 1: ID of the cluster in PSZ2, column 2: name of the cluster, column 3: spectroscopic redshift: z_{spec} a) from this work (BCG candidate), b) from Burenin et al. (2018), c) from Amodeo et al. (2018), d) from Streblyanska et al. (2018), e) from Streblyanska et al. (2019), column 4 and 5: richness and inferred mass based on z_{spec}, column 6: completeness correction factor at z_{spec}, column 7: SZ-mass using z_{spec} and the optical position of the BCG in this work or the optical centre indicated in the literature.

6.13 Appendix D: Colour Images of Cluster Candidate Sample

Here, we provide colour images of all clusters investigated in this work (see Figures 6.8 to 6.12). All images have north up and east left orientation and the same colour scale. The images display roughly 4 arcmin by 3.4 arcmin fields.

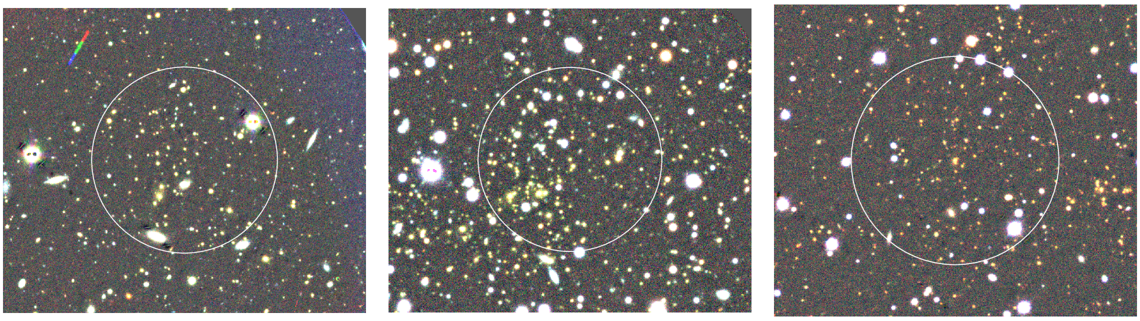

(a) PSZ2 G032.31+66.07 (b) PSZ2 G066.34+26.14 (c) PSZ2 G085.95+25.23

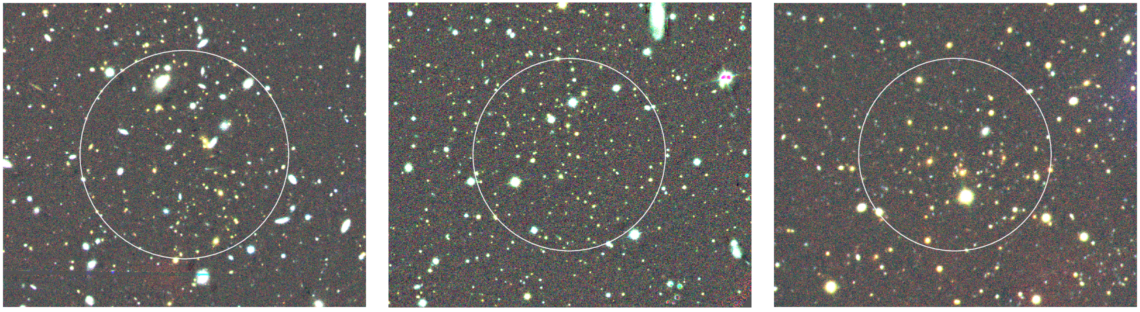

(d) PSZ2 G086.28+74.76 (e) PSZ2 G092.64+20.78 (f) PSZ2 G092.69+59.92

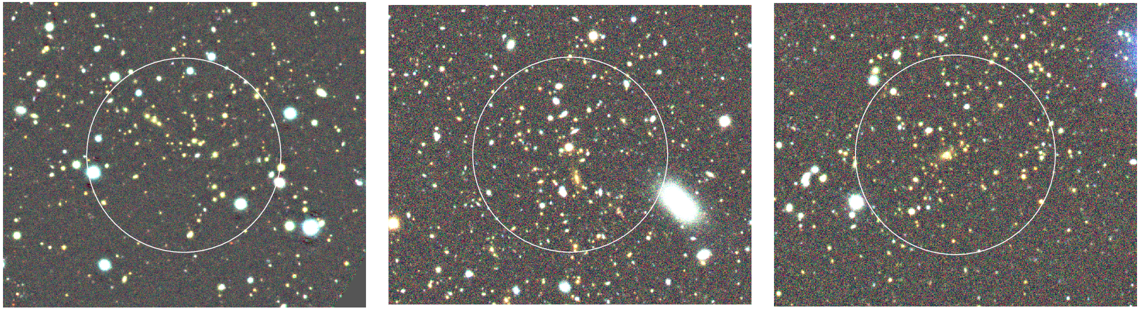

(g) PSZ2 G100.22+33.81 (h) PSZ2 G126.28+65.62 (i) PSZ2 G126.57+51.61

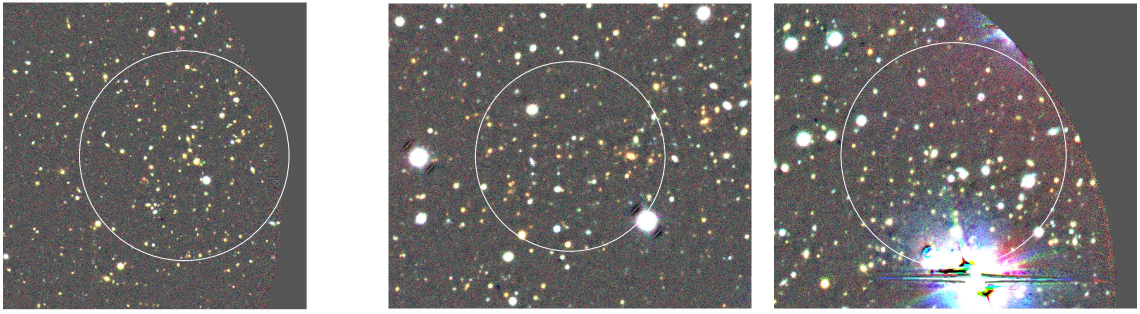

(j) PSZ2 G141.98+69.31 (k) PSZ2 G237.68+57.83 (l) PSZ2 G246.91+24.65

Figure 6.8 – Clusters with $M_{500\mathrm{c},\lambda}/M_{500\mathrm{c,SZ}} > 0.25$. The white circles equal 0.5 Mpc in radius around the cluster centre at the estimated redshift.

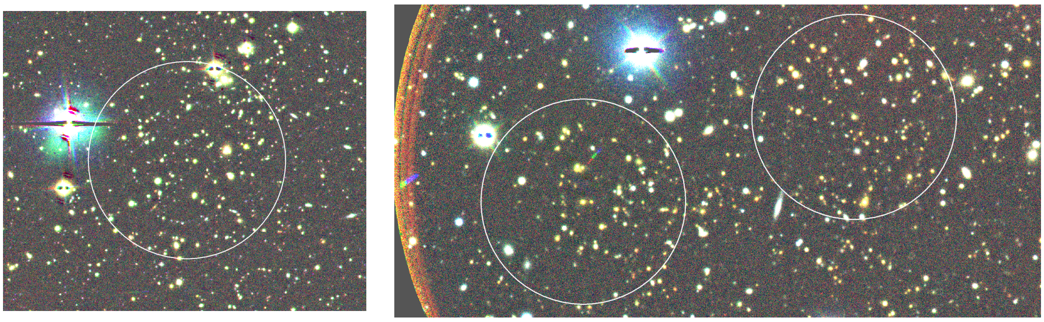

(a) PSZ2 G316.43+54.02 (b) PSZ2 G321.30+50.63

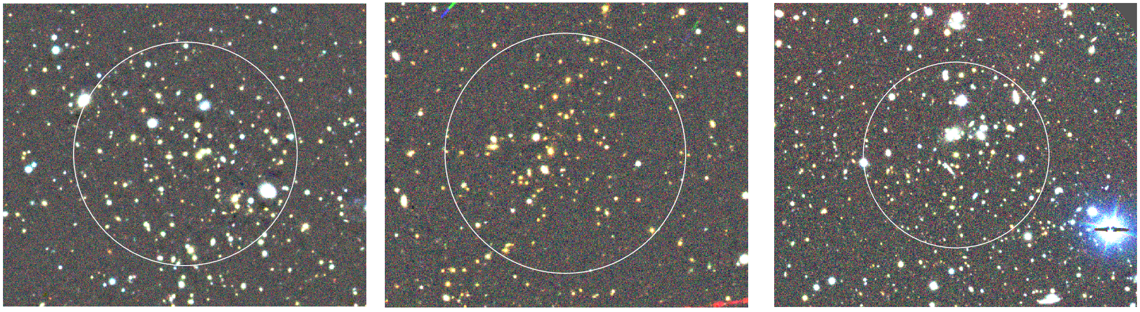

(c) PSZ2 G326.73+54.80 (d) PSZ2 G343.46+52.65 (e) PLCK G55.00–37.0

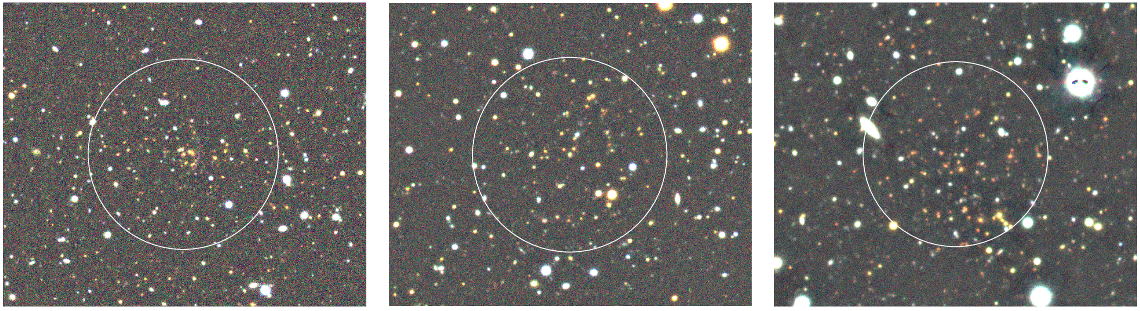

(f) PLCK G58.14–72.7 (g) PLCK G82.51+29.8 (h) PLCK G98.08–46.4

Figure 6.9 – Clusters with $M_{500c,\lambda}/M_{500c,SZ} > 0.25$ (continued). The white circles equal 0.5 Mpc in radius around the cluster centre at the estimated redshift. (b) We report the results for the cluster detection to the right of the image in Table 6.2. More comments on candidate PSZ2 G321.30+50.63 can be found in Section 6.7.

(a) PLCK G122.62–31.9 (b) PLCK G150.77+17.1 (c) PLCK G174.14–27.5

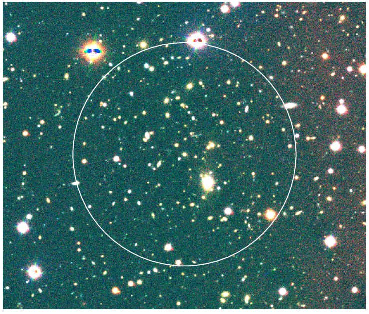

(d) PLCK G184.49+21.1

Figure 6.10 – Clusters with $M_{500\mathrm{c},\lambda}/M_{500\mathrm{c,SZ}} > 0.25$ (continued). The white circles equal 0.5 Mpc in radius around the cluster centre at the estimated redshift.

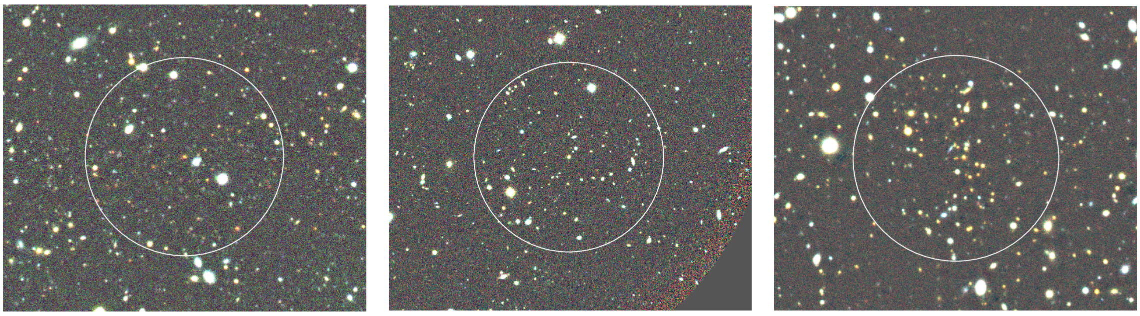

(a)PSZ2 G112.54+59.53 (b) PSZ2 G136.02–47.15 (c) PSZ2 G139.00+50.92

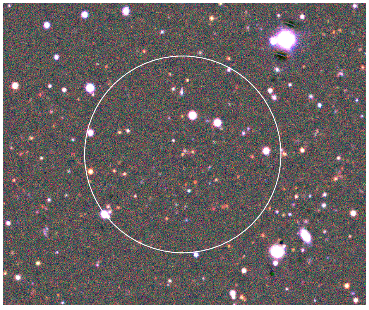

(d) PSZ2 G305.76+44.79

Figure 6.11 – Clusters with $M_{500c,\lambda}/M_{500c,SZ} < 0.25$. The white circles equal 0.5 Mpc in radius around the cluster centre at the estimated redshift.

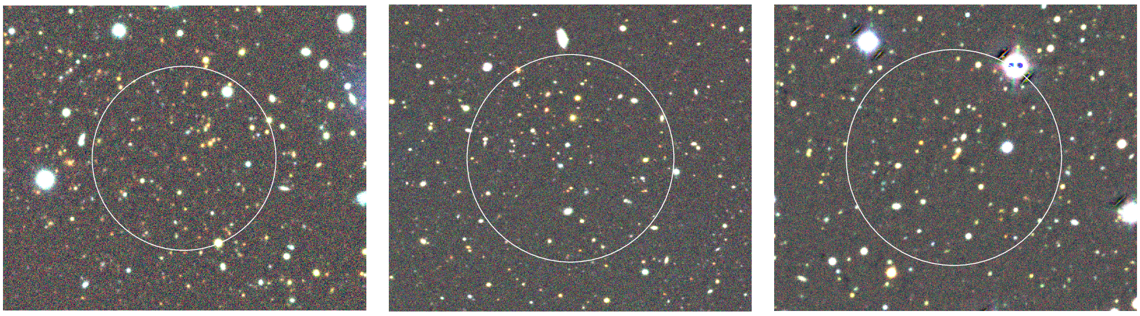

(a) PSZ2 G152.47+42.11 (b) PSZ2 G160.94+44.85 (c) PSZ2 G165.41+25.93

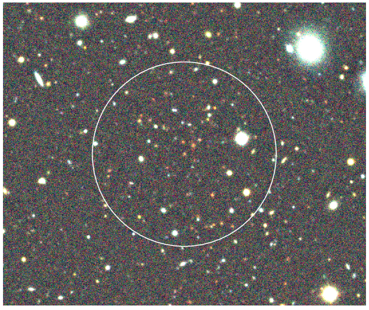

(d) PLCK G164.82–47.4

Figure 6.12 – Clusters with $M_{500c,\lambda}$ or $M_{500c,SZ}$ unknown. The white circles equal 0.5 Mpc in radius around the cluster centre at the estimated redshift.

CHAPTER 7

Extending empirical constraints on the SZ–mass scaling relation to higher redshifts via *HST* weak lensing measurements of nine clusters from the South Pole Telescope Sunyaev-Zel'dovic Survey at $z \gtrsim 1$

Preface

The research presented in this chapter is currently being finalised and to be submitted to the refereed journal Monthly Notices of the Royal Astronomical Society (MNRAS). The leading author of this study is Hannah Zohren (myself). I performed the following tasks for this project: data reduction of *HST*/ACS, *HST*/WFC3 and VLT/FORS2 observations, photometric measurements and calibration including several cross-checks, optimisation of the background source selection with the help of CANDELS/3D-HST photometric redshift catalogues from Skelton et al. (2014), computation of the geometric lensing efficiency and its variation, and a systematic and statistical error analysis. Additionally, there are several contributions from fellow scientists, which I summarise as follows: Tim Schrabback was my day-to-day supervisor for this project and conducted the shape measurements and weak lensing shear analysis as summarised in Sections 7.7, 7.8.1, and 7.8.2. Fatimah Raihan calculated the revised redshifts for the full CANDELS/3D-HST catalogues as described in Raihan et al. (2020). Martin Sommer calculated the mass modelling biases and the scatter listed in Tables 7.6 and 7.7. Sebastian Bocquet provided the results on the redshift-evolution of the SZ–mass scaling relation by combining the weak lensing results of the studied sample with results from clusters at lower redshifts (see

Section 7.9). Beatriz Hernández-Martín performed the visitor mode observations of the VLT/FORS2 imaging. I performed the data reduction of the *HST*/ACS data to obtain flt-images (calibrated, flat-fielded exposures) based on several scripts by Ole Markgraf, and I modified these scripts to apply them to the *HST*/WFC3 data in this study. Lindsey Bleem and Mike Gladders provided the spectroscopic redshift measurements for cluster SPT-CL $J0646-6236$. Thomas Erben, Florian Kleinebreil, Mischa Schirmer, and Angus Wright contributed several helpful discussions and advice on different, specific steps of this study.

7.1 Abstract

We present a *Hubble Space Telescope* (*HST*) weak lensing study of nine distant and massive galaxy clusters with redshifts $1.0 \lesssim z \lesssim 1.7$ ($z_{\mathrm{median}} = 1.4$) and SZ detection significance $\xi > 6.0$ from the South Pole Telescope Sunyaev Zel'dovich (SPT-SZ) Survey. We measure weak lensing galaxy shapes in *HST*/ACS F606W and F814W band images and use additional observations from *HST*/WFC3 in F110W and VLT/FORS2 in U_{HIGH} to preferentially select background galaxies at $z \gtrsim 1.8$, achieving a high purity. We combine recent redshift estimates from the CANDELS/3D-HST and HUDF fields to infer an improved estimate of the source redshift distribution. We measure weak lensing masses by fitting the tangential reduced shear profiles with spherical NFW models. We obtain the largest lensing mass in our sample for cluster SPT-CL $J2040-4451$, thereby confirming earlier results that suggest a high lensing mass of this cluster compared to X-ray and SZ-mass measurements. Combining our weak lensing mass constraints with results obtained by previous studies for lower redshift clusters, we expand the calibration of the scaling relation between the unbiased SZ detection significance ζ and the cluster mass for the SPT-SZ Survey out to higher redshifts. In particular, we find that the mass scale inferred for our highest redshift bin ($1.2 < z < 1.7$) is fully consistent with the constraints derived at lower redshifts. Thus, our results agree with previous findings indicating an offset between the mass scale preferred based on weak lensing data and based on a flat *Planck* $\nu\Lambda$CDM cosmology with the observed SPT-SZ cluster counts.

7.2 Introduction

Galaxy clusters trace the densest regions of the large-scale structure in the Universe. Studying their number density as a function of mass and redshift, therefore, provides insights on the cosmic expansion and structure formation histories, allowing for constraints of cosmological models (e.g. Haiman et al., 2001; Allen et al., 2011). Here, the halo mass function (HMF) predicts the expected number of dark matter haloes at a given mass and redshift. It can be obtained from numerical simulations (e.g. Tinker et al., 2008). A comparison of these predictions to observations of galaxy clusters as representatives of these haloes and their abundance serves as a probe, which is particularly sensitive to a combination of the cosmological parameters Ω_{m}, the matter energy density of the Universe, and σ_8, the standard deviation of fluctuations in the linear matter density field at scales of $8\,\mathrm{Mpc}/h$. At the same time, cluster studies can constrain the dark energy equation of state parameter w.

Such studies require samples of galaxy clusters ideally with a well-defined selection function and covering a large redshift range. Common methods for the assembly of such samples include detection via the overdensity of galaxies in the optical/near-infrared (NIR) regime (e.g. Rykoff et al., 2016), via the X-ray flux (e.g. Piffaretti et al., 2011; Pacaud et al., 2018), or via the signal from the Sunyaev Zel'dovich (SZ) effect (e.g. Bleem et al., 2015; Planck Collaboration et al., 2016b; Hilton et al., 2021).

The thermal SZ effect (Sunyaev & Zeldovich, 1972) describes a distortion of the CMB blackbody spectrum towards higher energy, caused when CMB photons experience an inverse Compton scattering with the energetic electrons in the intracluster medium. Since the signal is independent of redshift, detecting clusters through the SZ effect enables the assembly of cluster catalogues, which are nearly mass-limited and extending out to very high redshifts. Additionally, the uncertainties in the selection function are relatively low because the SZ-observable provides a mass proxy with a comparably low intrinsic scatter (~ 20 per cent, e.g. Angulo et al., 2012). These are excellent prerequisites for cosmological studies through the comparison of cluster counts and the HMF.

However, accurate and precise calibration of the scaling relations between the observable mass proxy and the underlying unobservable halo mass as predicted by the HMF over a wide redshift range is needed to obtain meaningful cosmological constraints. Especially since the remaining uncertainties in the observable-mass scaling relations are the limiting factor hampering the progress to tighter constraints (e.g. Dietrich et al., 2019). It is, therefore, imperative to improve the cluster mass calibration out to the highest redshifts that are now accessible in cluster samples (Bocquet et al., 2019; Schrabback et al., 2018, 2021). Mass measurements from weak gravitational lensing are a frequently used method to obtain an absolute calibration of the normalisation of these scaling relations (e.g. Okabe et al., 2010b; Kettula et al., 2015; Dietrich et al., 2019; Chiu et al., 2021; Schrabback et al., 2021). Weak gravitational lensing causes a systematic distortion of the shapes of background galaxies when their light travels through the gravitational field of a foreground mass distribution. The weak lensing reduced shear quantifies the tangential distortion with respect to the centre of the mass distribution. The differential projected cluster mass distribution can be inferred from measurements of the reduced shear. This technique is applied without the need for assumptions about the dynamical state of the clusters. This is especially advantageous for high-redshift clusters because these objects are still dynamically young and may not have settled into hydrostatic equilibrium yet.

Wide-field ground-based surveys like the Kilo Degree Survey (KiDS, Kuijken et al., 2015), the Dark Energy Survey (DES, The Dark Energy Survey Collaboration, 2005) and Hyper-Suprime-Cam Survey (HSC, Miyazaki et al., 2012) can calibrate the cluster masses at the few per cent level via weak lensing in the low to intermediate redshift regime, but they are not suitable to obtain the critically required cluster masses at high redshifts. Their limited depth and ground-based resolution are not capable to sufficiently resolve the small and faint background galaxies behind high-redshift clusters.

The previously mentioned studies using weak lensing mass measurements to calibrate the normalisation of scaling relations have also focused on the low to intermediate redshift regimes up to $z \sim 1$. It is important to extend the calibration of scaling relations to higher redshifts because cluster properties evolve over time. With this work, we present the first weak lensing constraints on the mass scale of SZ-selected clusters extending to such high redshifts above $z \gtrsim 1.2$. The median redshift of the sample with nine clusters studied here is $z = 1.4$. This is an expansion to the efforts of Schrabback et al. (2018, henceforth S18), Dietrich et al. (2019, henceforth D19), Bocquet et al. (2019, henceforth B19), and Schrabback et al. (2021, henceforth S21) to constrain the redshift evolution of the SZ-mass scaling relation based on clusters from the 2500 deg^2 South Pole Telescope SZ survey (Bleem et al., 2015). With our high-redshift sample, we aim to tighten the constraints on the scaling relation parameter C_{SZ}, describing its redshift evolution, which in particular helps to break the degeneracy of C_{SZ} with the dark energy equation of state parameter w.

The structure of this work is as follows: we provide a brief summary of the weak lensing theory and the studied cluster sample in Sections 7.3 and 7.4, respectively. We then present the data reduction of our optical observations and describe the photometric calibration steps in Section 7.5. Details about the selection of background galaxies based on four photometric bands and about the estimation of the source redshift distribution from photometric redshift catalogues are given in Section 7.6. We describe the details of weak lensing shape measurements in Section 7.7. We present our weak lensing mass constraints including an estimation of the weak lensing mass bias in Section 7.8. We constrain the observable-mass scaling relation incorporating the new lensing results for our high-redshift SPT cluster sample in Section 7.9. Finally, we discuss our results in Section 7.10 and summarise and conclude in Section 7.11.

Unless indicated otherwise, we assume a standard flat ΛCDM cosmology throughout this paper with $\Omega_{\mathrm{m}} = 0.3$, $\Omega_{\Lambda} = 0.7$, and $H_0 = 70 \ \mathrm{km\,s^{-1}\,Mpc^{-1}}$, as approximately consistent with CMB constraints (e.g. Planck Collaboration et al., 2020b). We express masses in terms of $M_{\Delta c}$ corresponding to a sphere within which the density is Δ times higher than the critical density at the given redshift.

Unless otherwise noted, all reported magnitudes in this work are AB-magnitudes. We generally correct all magnitude measurements for Galactic extinction with the extinction maps by Schlafly & Finkbeiner (2011).

7.3 Summary of weak lensing theory

Massive objects distort the space-time around them. The light bundles from sources behind such an object are affected by its tidal gravitational field such that an observer sees a distorted, (de-)magnified, and displaced image of the source. This effect is called gravitational lensing (see reviews e.g. by Bartelmann & Schneider 2001 and Bartelmann & Maturi 2017, as well as Hoekstra et al. 2013 regarding galaxy clusters). In the case of weak gravitational lensing, the tidal gravitational field of the lens only slightly distorts the shape of sources in the background. The coherent alignment caused by this can only be measured statistically from a large sample of background sources. Generally, the distortion of a source at observed position $\boldsymbol{\theta}$ can be described by two quantities: the convergence $\kappa(\boldsymbol{\theta})$ holds information on the isotropic distortion (i.e., contraction or dilation), while the shear $\gamma(\boldsymbol{\theta})$ describes the anisotropic distortions. The convergence is defined as

$$\kappa(\boldsymbol{\theta}) = \frac{\Sigma(\boldsymbol{\theta})}{\Sigma_{\text{crit}}} \,, \tag{7.1}$$

which is the ratio of the surface mass density $\Sigma(\boldsymbol{\theta})$ and the critical surface mass density

$$\Sigma_{\text{crit}}^{-1} = \frac{4\pi G}{c^2} D_{\text{l}} \beta \,. \tag{7.2}$$

Here, c is the speed of light, G is the gravitational constant, and β is the geometric lensing efficiency:

$$\beta = \frac{D_{\text{ls}}}{D_{\text{s}}} H(z_{\text{s}} - z_{\text{l}}) \,, \tag{7.3}$$

where D_{l}, D_{s}, and D_{ls} denote the angular diameter distances to the lens, the source, and between lens and source, respectively. The Heavyside step function is defined as $H(x) = 1$ if $x > 0$ and $H(x) = 0$ if $x \leq 0$, where z_{s} and z_{l} denote the source and lens redshifts, respectively.

The shear is a two-component quantity, which can conveniently be expressed as a complex number:

$$\gamma = \gamma_1 + \mathrm{i}\gamma_2 = |\gamma| \mathrm{e}^{2\mathrm{i}\varphi} \,, \tag{7.4}$$

with $|\gamma|$ as the amplitude of the distortion and φ as the angle with respect to the reference coordinate system. The shear is not directly observable, the reduced shear $g(\boldsymbol{\theta})$ however is. The reduced shear can be written as a function of the shear and the convergence via

$$g(\boldsymbol{\theta}) = \frac{\gamma(\boldsymbol{\theta})}{1 - \kappa(\boldsymbol{\theta})} \,. \tag{7.5}$$

Analogous as for the unobservable shear γ, it follows that

$$g = g_1 + \mathrm{i}g_2 = |g|\mathrm{e}^{2\mathrm{i}\varphi}\,. \tag{7.6}$$

The shape of a galaxy can be quantified by its ellipticity, as a complex number $\epsilon = \epsilon_1 + \mathrm{i}\epsilon_2$. The observed ellipticity ϵ_{obs} of a background galaxy can be related to the intrinsic ellipticity ϵ_{orig} and reduced shear g via (Bartelmann & Schneider, 2001)

$$\epsilon_{\mathrm{obs}} = \frac{\epsilon_{\mathrm{orig}} + g}{1 + g^{*}\epsilon_{\mathrm{orig}}} \approx \epsilon_{\mathrm{orig}} + g\,. \tag{7.7}$$

The latter approximation holds for $g \ll 1$. According to the cosmological principle, the intrinsic orientation of galaxies should have no preferred direction. Therefore, the expectation value for an average over many galaxies is that $\langle \epsilon_{\mathrm{orig}} \rangle = 0$. In conclusion, we can estimate the reduced shear from the ensemble-averaged PSF-corrected ellipticities of the background galaxies via

$$\langle \epsilon_{\mathrm{obs}} \rangle = g\,. \tag{7.8}$$

In practice, we include shape weights $w_i = 1/\sigma^2_{\epsilon,i}$ for each galaxy i when we measure the ellipticity components $\alpha \in \{1,2\}$ to improve the signal-to-noise ratio, i.e.,

$$\langle \epsilon_\alpha \rangle = \frac{\sum \epsilon_{\alpha,i} w_i}{\sum w_i}\,. \tag{7.9}$$

Here, $\sigma_{\epsilon,i}$ takes into account contributions from the measurement noise and the intrinsic shape distribution (S18).

When measuring the reduced shear signal with respect to the centre of a mass concentration such as a cluster, it is helpful to distinguish a tangential component g_{t} and a cross component $g_\times$ like this:

$$\begin{aligned} g_{\mathrm{t}} &= -g_1 \cos 2\phi - g_2 \sin 2\phi\,, \\ g_\times &= +g_1 \sin 2\phi - g_2 \cos 2\phi\,, \end{aligned} \tag{7.10}$$

with ϕ as the azimuthal angle with respect to the centre. The average tangential shear γ_{t} at a radial distance r from the centre holds information on the difference between the average convergence $\bar{\kappa}(<r)$ within r and the mean convergence $\bar{\kappa}(r)$ at r (Hoekstra et al., 2013):

$$\langle \gamma_{\mathrm{t}} \rangle(r) = \bar{\kappa}(<r) - \bar{\kappa}(r)\,. \tag{7.11}$$

Since the individual galaxies i behind a cluster typically have very different redshifts z_i, it is convenient to introduce a scaling of the shear, convergence, and geometric lensing efficiency as follows:

$$\gamma = \beta_{\mathrm{s}}(z_i)\gamma_\infty, \quad \kappa = \beta_{\mathrm{s}}(z_i)\kappa_\infty \quad \text{with} \quad \beta_{\mathrm{s}}(z_i) = \frac{\beta(z_i)}{\beta_\infty}\,. \tag{7.12}$$

Here, γ_∞, κ_∞, and β_∞ denote the respective quantities at infinite redshift. Therefore, we can express the average reduced shear for a sample of galaxies with a distribution in redshift as

$$\langle g \rangle = \left\langle \frac{\beta_\mathrm{s}(z_i)\gamma_\infty}{1 - \beta_\mathrm{s}(z_i)\kappa_\infty} \right\rangle . \tag{7.13}$$

An approximation to this is provided in Hoekstra et al. (2000):

$$g^\mathrm{model} = \left[1 + \left(\frac{\langle \beta_\mathrm{s}^2 \rangle}{\langle \beta_\mathrm{s} \rangle^2} - 1 \right) \langle \beta_\mathrm{s} \rangle \kappa_\infty^\mathrm{model} \right] \frac{\langle \beta_\mathrm{s} \rangle \gamma_\infty^\mathrm{model}}{1 - \langle \beta_\mathrm{s} \rangle \kappa_\infty^\mathrm{model}} \tag{7.14}$$

(see also Seitz & Schneider, 1997; Applegate et al., 2014), where

$$\langle \beta_\mathrm{s} \rangle = \frac{\sum \beta_\mathrm{s}(z_i) w_i}{\sum w_i} , \; \langle \beta_\mathrm{s}^2 \rangle = \frac{\sum \beta_\mathrm{s}^2(z_i) w_i}{\sum w_i} , \tag{7.15}$$

can be obtained from the source redshift distribution taking into account the shape weights.

7.4 The high-z SPT cluster sample and previous studies

We investigate nine massive and distant galaxy clusters at redshifts $1.0 \leq z \leq 1.7$ detected by the SPT via their SZ signal. They were originally selected to have $z > 1.2$ according to the best redshift estimate available at the time. However, the cluster SPT-CL $J0646{-}6236$ is only at redshift $z \sim 1$ based on more recent spectroscopic observations. Therefore, only the remaining eight clusters constitute the complete sample of galaxy clusters at very high redshifts $z \geq 1.2$ with the strongest detection significance of $\xi \geq 6$ from the 2500 deg^2 SPT-SZ survey (Bleem et al., 2015, see Table 7.1 for cluster properties). The sample has a median redshift of $z_\mathrm{med} = 1.4$. B19 derive cosmological constraints with galaxy clusters from the 2500 deg^2 SPT-SZ survey and provide updated redshift and SZ mass estimates for the SPT cluster sample, including the clusters studied here. The estimates incorporate a weak lensing mass calibration using data from D19 and S18.

The nine clusters in this work were also part of several previous studies. McDonald et al. (2017) examined *Chandra* X-ray data for eight of these clusters and investigated the redshift dependency and compatibility with self-similar evolution of the ICM in a large sample of galaxy clusters. Their study includes an estimation of the positions of the X-ray cluster centres (see also Table 7.1) and the X-ray-based masses (derived from the $M_\mathrm{gas} - M$ relation from Vikhlinin et al., 2009), as well as density profiles and morphologies of the clusters. Ghirardini et al. (2021) investigate thermodynamic properties, e.g., density, temperature, pressure, and entropy with combined *Chandra* and *XMM-Newton* X-ray observations of seven clusters in our

Table 7.1 – Properties of the galaxy cluster sample. We list cluster names, SZ significance ξ, SZ coordinates of the centre and SZ-masses as presented in B19. The X-ray coordinates correspond to the centroid positions estimated by McDonald et al. (2017).

Cluster name	z_l	ξ	Coordinates centres (deg J2000)				$M_{500c,SZ}$
			SZ α	SZ δ	X-ray α	X-ray δ	$[10^{14}\,M_\odot/h_{70}]$
SPT-CL J0156−5541	1.288^{a}	6.98	29.044903	−55.69801	29.0405	−55.6976	$3.96^{+0.57}_{-0.65}$
SPT-CL J0205−5829	1.322^{b}	10.40	31.442823	−58.485209	31.4459	−58.4849	$5.06^{+0.55}_{-0.68}$
SPT-CL J0313−5334	1.474^{a}	6.09	48.480902	−53.578085	48.4813	−53.5718	$3.31^{+0.55}_{-0.61}$
SPT-CL J0459−4947	1.7^{d}	6.29	74.926929	−49.78724	74.9240	−49.7823	$3.08^{+0.53}_{-0.53}$
SPT-CL J0607−4448	1.401^{a}	6.44	91.898408	−44.803329	91.8940	−44.8050	$3.60^{+0.57}_{-0.63}$
SPT-CL J0640−5113	1.316^{a}	6.86	100.06452	−51.22045	100.0720	−51.2176	$3.89^{+0.58}_{-0.65}$
SPT-CL J0646−6236	0.995^{e}	8.67	101.63906	−62.613595			$5.17^{+0.62}_{-0.74}$
SPT-CL J2040−4451	1.478^{c}	6.72	310.24832	−44.860228	310.2417	−44.8620	$3.76^{+0.58}_{-0.63}$
SPT-CL J2341−5724	1.259^{a}	6.87	355.35683	−57.415799	355.3533	−57.4166	$3.58^{+0.51}_{-0.59}$

Notes. [a] Spectroscopic redshifts by Khullar et al. (2019). [b] Spectroscopic redshift from Stalder et al. (2013). [c] Spectroscopic redshift from Bayliss et al. (2014). [d] Best redshift constraint currently available (Mantz et al., 2020). [e] Observation design and data reduction followed the same procedures as described in Khullar et al. (2019), more general results will be discussed in a future paper on high-z spectroscopic measurements of SPT clusters.

sample and compare them with the corresponding properties of low-redshift clusters. Additionally, Bulbul et al. (2019) included two of the clusters in their analysis of X-ray properties of SPT-selected galaxy clusters observed with *XMM-Newton*. They constrain the scaling relations between the X-ray observables of the ICM (luminosity L_X, ICM mass M_ICM, emission-weighted mean temperature T_X, and integrated pressure Y_X), redshift, and halo mass. Further X-ray studies investigating astrophysical properties featuring one or more clusters from our sample include McDonald et al. (2013), Sanders et al. (2018), and Mantz et al. (2020). There have also been efforts to obtain precise spectroscopic redshifts for the majority of clusters in our sample (Stalder et al., 2013; Bayliss et al., 2014; Khullar et al., 2019; Mantz et al., 2020), where some studies specifically investigated the galaxy kinematics and velocity distributions (Ruel et al., 2014; Capasso et al., 2019). Several multi-wavelength studies of cluster samples with varying size investigated different cluster components such as the baryon content (Chiu et al., 2016, 2018), the properties, growth and star formation in brightest cluster galaxies (BCGs, McDonald et al., 2016; DeMaio et al., 2020; Chu et al., 2021), the mass-richness relation (Rettura et al., 2018), environmental quenching of the galaxy populations in clusters (Strazzullo et al., 2019), and AGN-feedback (Hlavacek-Larrondo et al., 2015; Bîrzan et al., 2017). The cluster SPT-CL $J2040{-}4451$ was already studied in a weak lensing analysis by Jee et al. (2017), who employed infrared images from the Wide Field Camera 3 (WFC3) at the *HST* for shape measurements. We compare their analysis strategy and ours in detail in Section 7.10.

While the studies have been manifold covering various observation techniques and searching to answer various scientific questions, our study represents the first consistent weak lensing study of a cluster sample of this size with a clean SZ-based selection function at this high-redshift regime.

7.5 Data & Data reduction

7.5.1 HST ACS and WFC3 data

We use high-resolution imaging from the *Hubble Space Telescope* (*HST*) to measure weak lensing galaxy shapes as detailed in Section 7.7. The observational data analysed in our study were obtained during Cycles 19, 21, 23, and 24 as part of the SPT follow-up programmes 12477 (PI: F. High), 13412 (PI: T. Schrabback), 14252 (PI: V. Strazzullo), and 14677 (PI: T. Schrabback) in the filter bands F606W and F814W with the ACS/WFC instrument and F110W with the WFC3/IR instrument. We measure the shapes of galaxies for our weak lensing analysis in the observations in the filters F606W and F814W, which have a field of view of $202'' \times 202''$ at a pixel scale of $0\overset{''}{.}05$/pixel. The ACS observations correspond to a single pointing except for SPT-CL $J0205{-}5829$ for which an additional larger 2×2 mosaic was obtained in F606W as part of programme 12477. The field of view of the WFC3 instrument

Table 7.2 – Summary of the integration times, image quality, and depth from our observations with *HST*/ACS, *HST*/WFC3, and VLT/FORS2. For the image quality (IQ), we report the full width at half maximum of the PSF, based on measurements with `Source Extractor`. The depth corresponds to 5σ limiting magnitudes, computed from the standard deviation of 1000 non-overlapping apertures without flux from detected sources. We use apertures with diameters of $0\overset{''}{.}7$ for *HST* bands and $1\overset{''}{.}2$ for U_{HIGH}.

	F606W			F814W			F110W			U_{HIGH}		
Cluster name	t_{exp} [ks]	IQ [$''$]	depth [mag]	t_{exp} [ks]	IQ [$''$]	depth [mag]	t_{exp}[b] [ks]	IQ [$''$]	depth[b] [mag]	t_{exp} [ks]	IQ [$''$]	depth [mag]
SPT-CL *J*0156−5541	5.5	0.10	27.0	4.9	0.10	26.6	0.6	0.29	26.3	4.8	0.73	26.9
SPT-CL *J*0205−5829	3.7[a]	0.10	27.1[a]	3.7	0.08	26.5	0.6	0.29	26.3	4.8	0.85	26.8
SPT-CL *J*0313−5334	3.7	0.10	26.9	3.7	0.09	26.1	0.6	0.29	26.3	4.8	0.80	27.1
SPT-CL *J*0459−4947	2.3	0.11	26.7	4.8	0.10	26.5	0.6	0.28	26.3	6.0	0.81	26.9
SPT-CL *J*0607−4448	2.3	0.10	26.7	4.8	0.10	26.3	0.6	0.28	26.4	4.8	0.97	26.4
SPT-CL *J*0640−5113	5.6	0.10	26.7	3.3	0.10	26.2	0.6	0.26	26.1	2.4	0.97	26.3
SPT-CL *J*0646−6236	4.0	0.10	26.8	4.0	0.10	26.1	0.6	0.27	26.1	4.8	1.07	26.3
SPT-CL *J*2040−4451	2.1	0.10	26.6	4.8	0.10	26.1	0.6	0.28	26.1	4.8	0.88	26.5
SPT-CL *J*2341−5724	5.3	0.10	26.5	4.8	0.10	26.2	0.6	0.29	26.1	4.8	0.92	26.9
HUDF	–	–	–	–	–	–	–	–	–	6.6	1.03	26.6

Notes. [a] For cluster SPT-CL *J*0205−5829 a 2×2 ACS mosaic from programme 12477 and one single ACS pointing from programme 14677 are available in the F606W band. We have eight overlapping exposures in the region with the biggest overlap with our observations in the other bands. We report the integration time and depth based on this region.

[b] The F110W stacks are mosaics of eight exposures. The highest/intermediate/lowest depth is achieved, where eight/four/two exposures overlap, respectively. Since regions with only two overlapping exposures make up the most area in the stacks, we report integration times and depths equivalent to two exposures.

is $136'' \times 123''$ with a pixel scale of roughly $0\farcs128$/pixel (the pixels are not exactly square shaped). We observe 2×2 mosaics in the F110W filter, which roughly match the field of view of the ACS observations. We use the observations in the F110W filter exclusively for the photometric selection of the background galaxies carrying the weak lensing signal. The integration times range between 2.3 and 5.5 ks (F606W), 3.3 and 4.9 ks (F814W), and 2.4 ks (F110W, spread out over a 2×2 mosaic to reach a minimum depth of 0.6 ks over the full ACS footprint) (see Table 7.2).

We perform the basic image reduction steps for the *HST*/ACS imaging data with the ACS calibration pipeline `CALACS`. However, we deviate from the standardised processing steps regarding the correction for charge transfer inefficiency (CTI). This effect occurs because CCDs get damaged by radiation in space. This, in turn, introduces defects, which result in non-linear charge trails when the CCDs are read out. If not corrected properly, CTI systematically affects the *HST* weak lensing shape analyses. We perform the CTI correction with the algorithm by Massey et al. (2014) and apply it to both the *HST*/ACS imaging data and the respective dark frames. Furthermore, we perform a quadrant-based sky background subtraction, improve the bad pixels masks by manually flagging satellite trails and cosmic ray clusters, and compute accurately normalised RMS maps following the prescription in Schrabback et al. (2010).

The *HST*/WFC3 imaging data reduction is mostly performed similarly to the *HST*/ACS imaging data reduction. We download the pre-reduced `flt` frames, which have already undergone basic image processing via the WFC3 calibration pipeline `calwf3`. As a further difference, we do not perform a quadrant-based sky background subtraction because it does not make sense for the parallel read-out mechanism of WFC3. Instead, we use `Source Extractor` (Bertin & Arnouts, 1996) to obtain a background model, which we subtract. This allows us to account properly for gradients in the background level. These occasionally occur in particular due to a variable airglow line of He I at 10830 Å, which mostly affects the filter bands F105W and F110W (see Chapter 7.9.5 of the WFC3 instrument handbook[1] and WFC3 ISR 2014-03).

Subsequently to the initial data reduction, we employ the software `DrizzlePac`[2] for aligning and combining *HST* images in particular using the tasks `TweakReg` and `AstroDrizzle`. The `TweakReg` task computes residual shifts between input exposures, which can occur because of errors in guide-star positions, in particular when observations from different observing visits are combined. The task then modifies the WCS information in the headers of the exposures so that they can be properly combined using `AstroDrizzle`. In this process, the `AstroDrizzle` task identifies and removes cosmic rays, removes distortions, and performs a sky subtraction. For the stacking, we use the `lanczos3` kernel at the native pixel scale of $0\farcs05$ ($0\farcs128$) of the ACS (WFC3) images to distribute the flux onto the output image.

---

[1] https://hst-docs.stsci.edu/wfc3ihb

[2] https://www.stsci.edu/scientific-community/software/drizzlepac.html

This kernel is known to minimise correlated noise and causes less resolution loss than other kernels. Additionally, we employ the RMS image as the weighting image. We produce the stack for the imaging in the F606W band first and subsequently use this stack as the astrometric reference image for the stacks in the F814W and F110W bands to ensure optimal astrometric alignment between the stacks.

7.5.2 VLT FORS2 data

We use additional observations from VLT/FORS2 in the U_{HIGH} passband obtained as part of the ESO programme 0100.A-0204(A) (PI: Schrabback) between November 18 and November 20, 2017. Together with the *HST* imaging, these observations facilitate a robust photometric selection of background galaxies. The images were taken with the two blue-sensitive 2k × 4k E2V CCDs in standard resolution with 2×2 binning, providing observations over a field of view of $6\farcm8 \times 6\farcm8$ at a pixel scale of $0\farcs25$/pixel. We observe the nine galaxy clusters in our sample and additionally one pointing centred on the *Hubble Ultra Deep Field* (HUDF, Beckwith et al., 2006), which we use to assess the photometric calibration of the U_{HIGH} band. The integration times per cluster range between 2.4 ks and 6.6 ks (see Table 7.2).

We reduce the data with the software `THELI`[3] (Erben et al., 2005; Schirmer, 2013). We perform a bias subtraction, flat-field correction, and a subtraction of a background model. The latter is obtained by taking advantage of the dither pattern applied between exposures. The images are median combined, resulting in the background model. This enables us to distinguish features at a fixed detector position from sky-related signals. The background model is rescaled to the illumination level of the individual exposures and then subtracted from them. We apply a sky background subtraction using `Source Extractor` (Bertin & Arnouts, 1996). We obtain the astrometric calibration based on the Gaia DR1 catalogue (Gaia Collaboration et al., 2016b,a) as reference. Finally, the images are co-added.

7.5.3 Photometry

Photometric measurements with LAMBDAR

We perform photometric measurements on our fully reduced images with the Lambda Adaptive Multi-Band Deblending Algorithm in R (`LAMBDAR`[4], Wright et al., 2016). This algorithm can perform consistent and matched aperture photometry across images with varying pixel scales and resolutions. Therefore, it is ideally suited for our analysis, which requires accurate and precise colour measurements between the *HST* and VLT imaging with very different resolutions. In the follow-

---

[3] `https://www.astro.uni-bonn.de/theli/`

[4] `https://github.com/AngusWright/LAMBDAR`

ing, we give a brief summary of the `LAMBDAR` algorithm. We refer the reader to Wright et al. (2016) for a more in-depth description.

`LAMBDAR` requires at least two inputs: A FITS image and a catalogue of object locations and aperture parameters. Additionally, we provide a point-spread function (PSF) model for the FITS image. These files are read in as the first step, then the aperture priors from the catalogue are transferred onto the same pixel grid as the input FITS image. Subsequently, the aperture priors are convolved with the input PSF, and object deblending is executed based on the convolved aperture priors. Images are deblended via multiplication with a deblending function. For this, it is assumed that the total flux in a pixel equals the sum of the fluxes from sources with aperture models overlapping that pixel. The flux per source is distinguished with the help of the deblending function. This function is calculated using the second assumption that the PSF convolved aperture model is a tracer of the emission profile of each source. Taking into account the estimation of the local sky-backgrounds and noise correlation using random/blank apertures, `LAMBDAR` calculates the object fluxes with the help of the deblended convolved aperture priors. Here, the code accounts for aperture weighting and/or missed flux through an appropriate normalisation of fluxes. Finally, flux uncertainties in relation to all of the above steps are determined.

For our purposes, using `LAMBDAR` has two main advantages. Firstly, we can comfortably perform matched aperture photometry across our images with varying PSF sizes between $0\farcs08$ and $1\farcs07$. Secondly, the prior aperture definitions derived from high-resolution optical imaging allow for deblending of sources leading to more accurate flux measurements, in particular in comparison to conventional fixed aperture photometry.

We run `Source Extractor` on the F606W image to obtain the input catalogue with object locations and aperture parameters. We set the detection and analysis thresholds to 1.4σ. We require a minimum of 8 pixels for a source detection and set the deblending threshold to 32 with a minimum contrast parameter of 0.005. Before the detection, the images are smoothed with a Gaussian filter of 5 pixels with a FWHM of 2.5 pixels. We check for residual shifts in the astrometry of our images with respect to the F606W detection image and correct for them with a linear shift if necessary to avoid biases in the flux measurements with `LAMBDAR`. For the *HST* images, we use `TinyTim` (Krist et al., 2011) to obtain a PSF model for the photometric analysis. For the ACS images (i.e., in F606W and F814W), we look up the average focus from the duration of the observation at the *HST* Focus Model tool[5]. Since this tool does not offer an estimate for WFC3/IR (i.e., for the images in F110W), we assume a focus offset of 0.0 microns as default[6]. We use the central chip position as the position of reference for the estimation of the PSF model. In

---

[5] `http://focustool.stsci.edu/cgi-bin/control.py`

[6] To cross-check this assumption, we measured the photometry with an alternative PSF model with a very different focus offset of 4.0 microns. We find that both measurements differ by 0.001 mag (median), which is negligible for our purposes.

the case of the ACS instrument with two chips, we take the central pixel of chip 1 as a reference. For our VLT/FORS2 images, we obtain a PSF model with the help of the software `PSFEx` (Bertin, 2011).

Some of our fully reduced images exhibit slight residual gradients in the background level. Therefore, we perform an initial run with `Source Extractor` to obtain a background-subtracted image. We use these as the FITS input images to be analysed with `LAMBDAR`.

Photometric zeropoints

The photometric calibration for the *HST* bands is straightforward. We obtain a photometric zeropoint for each coadd with the help of the header keywords `PHOTFLAM` and `PHOTPLAM`:

$$\begin{aligned}\mathrm{ZP_{AB}} = &- 2.5 \cdot \log_{10}(\mathrm{PHOTFLAM}) \\ &- 5.0 \cdot \log_{10}(\mathrm{PHOTPLAM}) - 2.408\,.\end{aligned} \tag{7.16}$$

`PHOTFLAM` is the inverse sensitivity, which facilitates the transformation from an instrumental flux in units of electrons per second to a physical flux density and `PHOTPLAM` denotes the pivot wavelength in units of Å[7]. Afterwards, we account for Galactic extinction with the extinction maps by Schlafly & Finkbeiner (2011)[8].

The challenge in the photometric calibration of the U_{HIGH} band is the lack of an adequate reference catalogue with well-calibrated U band magnitudes for our cluster fields. We, therefore, resort to a calibration strategy based on a galaxy locus. We make use of the fact that galaxies have a characteristic distribution in colour-colour space, similar to stars that occupy the stellar locus (High et al., 2009). We find that a direct use of a stellar locus does not work well for our analysis due to the limited number of stars in the small fields of view. Additional large scatter results in substantial uncertainties of the stellar locus approach. Therefore, we resort to a galaxy locus method. We identify a reference galaxy locus from the 3D-HST photometric catalogues as presented in Skelton et al. (2014). They summarise photometric measurements in the five CANDELS/3D-HST fields (AEGIS, COSMOS, GOODS-North [abbreviated GN], GOODS-South [abbreviated GS], and UDS) over a total area of $\sim 900\,\mathrm{arcmin}^2$. Among others, this includes the following bands relevant for our reference galaxy locus: the *HST* bands F606W and F814W and U bands from various instruments such as CFHT/MegaCam (AEGIS, COSMOS, and UDS), KPNO 4 m/Mosaic (GOODS-North), and VLT/VIMOS (GOODS-South). We describe in Section 7.5.3 how we account for the differences in these effective band-passes. Compared to the CANDELS/3D-HST fields our cluster fields are overdense at the cluster redshift, changing the local galaxy distribution in colour-colour space. To account for this, we apply a preselection, which uses the well-calibrated *HST*-only colours

---

[7] https://www.stsci.edu/hst/instrumentation/acs/data-analysis/zeropoints

[8] obtained from the website https://irsa.ipac.caltech.edu/applications/DUST/

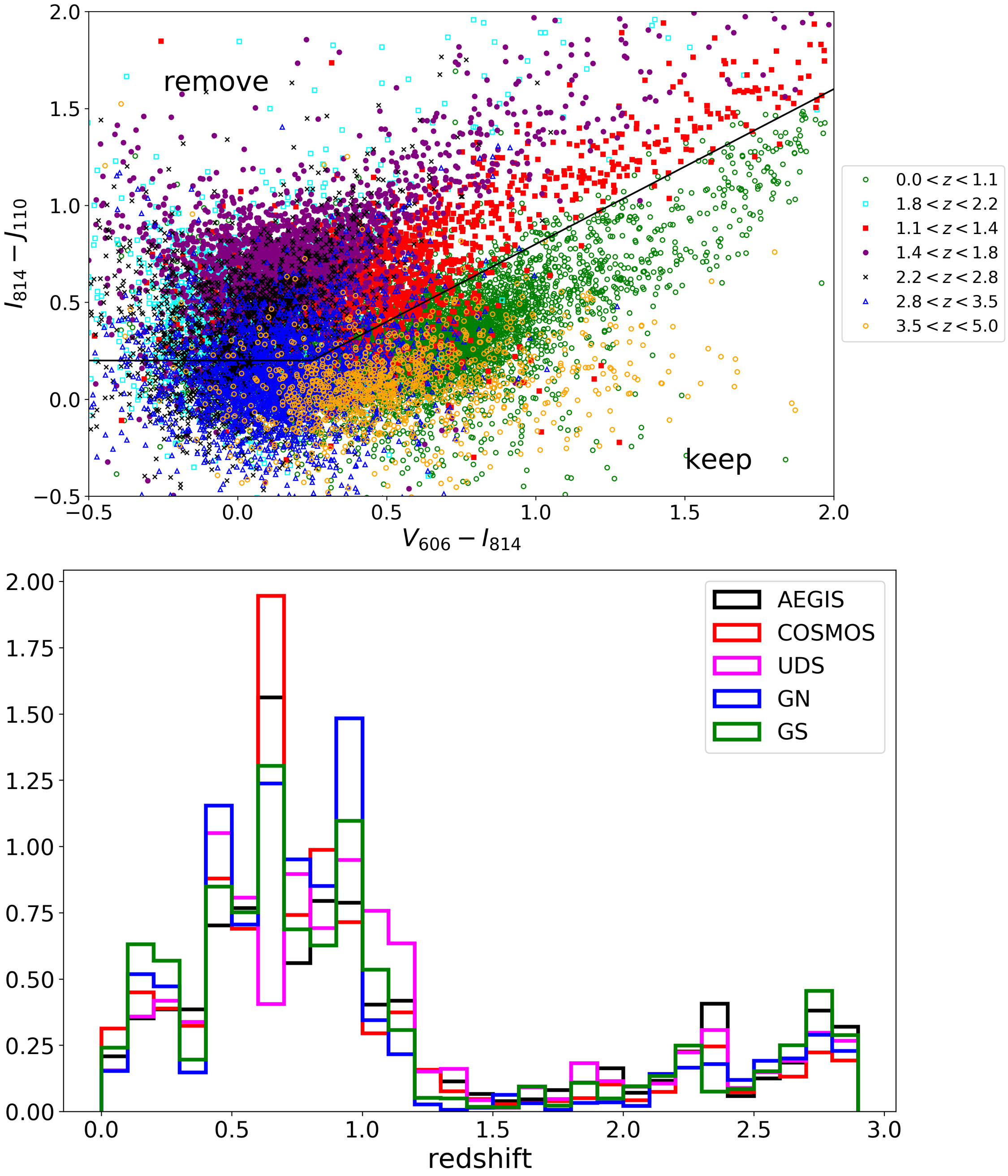

Figure 7.1 – Removal of galaxies in the cluster redshift regime from the galaxy locus at magnitudes of $24.2 < V_{606} < 27.0$. *Top:* Cut in the VIJ plane to remove galaxies with photometric redshifts $1.2 \lesssim z \lesssim 1.7$ according to the catalogues by Skelton et al. (2014) (i.e., galaxies in the regime of cluster redshifts of the sample studied here), illustrated for galaxies from the GOODS-South field with photometry from Skelton et al. (2014). Red and purple symbols roughly correspond to galaxies in the cluster redshift regime. *Bottom:* Redshift distribution of galaxies in our chosen galaxy locus from the five CANDELS/3D-HST fields.

to remove galaxies at the cluster redshift (see Figure 7.1). In addition, the galaxy distribution varies locally due to line-of-sight variations. We reduce the impact of these by employing relatively faint galaxies in the regime $24.2 < V_{606} < 27.0$ for the galaxy locus analysis. At the same time, this is the magnitude regime we focus on for the selection of background galaxies (see Section 7.6) so that we optimise the calibration in the targeted magnitude regime. Together, this allows us to calibrate $U - V_{606}$ colour estimates in the cluster fields by matching the galaxy distribution of the VIJ-selected galaxies in the $V_{606} - I_{814}$ versus $U - V_{606}$ colour-colour space.

For the calibration, we first account for Galactic extinction with the extinction maps by Schlafly & Finkbeiner (2011)[9]. We then smooth the distribution of the galaxies in the UVI colour-colour space with a Gaussian kernel (using scipy.stats.gaussian_kde in python) both for the galaxies of the reference galaxy locus and the galaxies in our observation. We identify the peak position of the highest density and apply a shift to the U_{HIGH} magnitudes according to the difference in $U - V_{606}$ of the peak positions. We quantify and propagate the statistical uncertainty of 0.08 mag of our colour calibration scheme (see Section 7.13 for a robustness test of the U_{HIGH} band zeropoint calibration with the help of the reference galaxy locus; see Table 7.3 for the effect of this statistical uncertainty on the average geometric lensing efficiency.)

Defining a common photometric system

When we investigate colour cuts for a suitable selection of background galaxies, we need to make sure to work in a consistent photometric framework. Regarding the U bands, we have measurements from four different instruments at hand: U_{HIGH} from VLT/FORS2 (our observations), U_{MEGACAM} from CFHT/MegaCam, U_{KPNO} from KPNO 4 m/Mosaic, and U_{VIMOS} from VLT/VIMOS (the latter three filters are employed in different CANDELS/3D-HST fields in Skelton et al., 2014). All of these have different effective filter curves. We, therefore, have to make sure that we employ these different bands to select consistent source populations, in particular regarding the $U - V_{606}$ colour. Comparing the $U - V_{606}$ colour of these populations, we find that there are small offsets among the CANDELS/3D-HST fields. We quantify these by identifying the peak position of the galaxy loci after smoothing the distribution with a Gaussian kernel (galaxies with $24.2 < V_{606} < 27.0$, where galaxies in the cluster redshift regime $1.2 \lesssim z \lesssim 1.7$ are excluded according to a cut in the VIJ colour plane; see Section 7.5.3). We apply a shift to the U bands to make the peak positions coincide with the peak position of the galaxy locus in GOODS-South as an anchor. We list the applied shifts in Table 7.9 in Section 7.13. As a cross-check, we compare the peak positions in the $U - V_{606}$ colour distribution for differently selected galaxy subsamples in Figure 7.2. Here, we generally find good agreement. For example, for the full population of galaxies with

---

[9] obtained from the website `https://irsa.ipac.caltech.edu/applications/DUST/`

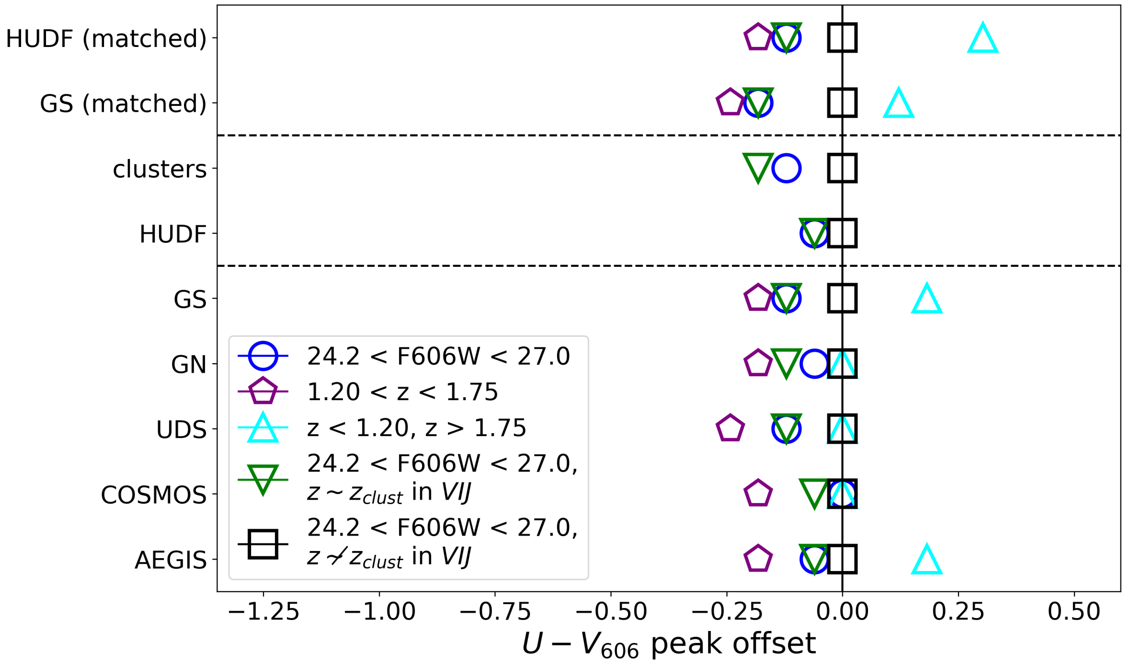

Figure 7.2 – Offsets between different populations of galaxies and the reference galaxy locus (galaxies with $24.2 < V_{606} < 27.0$ where galaxies at the cluster redshifts $1.2 \lesssim z \lesssim 1.7$ are excluded according to a cut in the VIJ colour plane; represented by black squares). Overall the populations exhibit quite similar offsets in $U - V_{606}$ colour despite relying on different U bands. *Bottom section:* Comparisons for five CANDELS/3D-HST fields. *Mid section:* Comparison of cluster fields (measurements from all nine cluster fields combined) and our measurements in the HUDF area, where we have U_{HIGH} imaging. Since we do not have photometric redshifts available, the populations relying on these are missing (purple pentagons and cyan triangles). *Top section:* Comparison of directly matched galaxies in the HUDF region based on our measurements and the catalogue in GOODS-South by Skelton et al. (2014).

$24.2 < V_{606} < 27.0$, we measure a standard deviation of the density peak positions between the five CANDELS/3D-HST fields of 0.045 mag. We conclude that the photometry is sufficiently comparable as a basis for the selection of background galaxies (we summarise systematic and statistical uncertainties connected to the photometry at the end of Section 7.6.2). In addition to these considerations for the U bands, we use *HST* bands for which we have available observations for our cluster fields, i.e., F606W, F814W, and F110W. Since not all reference catalogues have magnitude information on the galaxies in all of these bands, we need to apply a few interpolations to estimate the fluxes and magnitudes of galaxies in our photometric system of filters. In this case, we perform an interpolation based on the closest available filters in effective wavelength, where one filter is redder (R) and one is bluer (B) than the missing filter (X):

$$\begin{aligned} F_\mathrm{X} &= s \cdot (\lambda_\mathrm{eff,X} - \lambda_\mathrm{eff,B}) + F_\mathrm{B} \,, \\ m_\mathrm{X} &= -2.5 \cdot \log_{10}(F_\mathrm{X}) + \mathrm{ZP} \,, \\ \text{with} \quad s &= \frac{(F_\mathrm{R} - F_\mathrm{B})}{(\lambda_\mathrm{eff,R} - \lambda_\mathrm{eff,B})} \,, \end{aligned} \tag{7.17}$$

where F denotes the flux, m denotes the magnitude, ZP is the zeropoint (it is fixed to $\mathrm{ZP} = 25.0$ for all bands in the Skelton et al. (2014) CANDELS/3D-HST photometric catalogues), and λ_eff is the effective wavelength of the respective filter. In a catalogue that covers the sources in all filter bands, we can gauge how well the interpolation typically represents the actually measured magnitude. Overall, there is a good match between the interpolated and the actually measured magnitudes. We do, however, see that the interpolation becomes increasingly noisy and asymmetric for fainter magnitudes. This is likely related to the (potentially different) depths of the available bands.

None of the available reference catalogues provides measurements in the band F110W. Options for interpolation are to use a combination of either F105W and F125W, or F850LP and F125W, or F814W and F125W. Depending on the method used, we find that a light median offset of the order of 0.04 mag with a standard deviation of 0.07 mag can be introduced. We do not attempt to correct for such differences but we investigate the impact of systematic photometric offsets on the estimate of the average lensing efficiency in Section 7.14, finding that the impact of such a systematic offset can well be neglected given our current statistical uncertainties. We also check how well our photometry compares to measurements from Skelton et al. (2014) in Section 7.12. From this, we conclude that slight offsets in photometry can occur, and we include the expected uncertainties in the overall error budget of our analysis (summarised at the end of Section 7.6.2).

7.6 Photometric selection of source galaxies and estimation of the source redshift distribution

For a robust weak lensing analysis, it is important to preferentially select the galaxies at redshifts higher than the cluster redshifts. Only these galaxies behind the clusters carry the weak lensing signal, which we are interested in. A straightforward way to identify these galaxies would be based on their spectroscopic redshifts. High-quality photometric redshifts can also be helpful if examined carefully for systematic outliers. Such redshift information is, however, not available for the galaxies in our observed cluster fields. Instead, we aim to use only the photometry from our observations to identify background galaxies. For this, we need reference catalogues of galaxies providing redshift and magnitude information in different bands. This allows us to understand how to distinguish background galaxies from contaminating foreground and cluster galaxies solely based on their colours. In the following section, we will first describe the reference catalogues used in this work. After that, we will present suitable cuts in colour space to preferentially select background galaxies for the weak lensing analyses.

7.6.1 Redshift catalogues

UVUDF

The *Hubble Ultra Deep Field* (HUDF) is a region of the sky that has been studied extensively in various photometric filters by the *Hubble Space Telescope*. Rafelski et al. (2015) (henceforth R15) conduct a joint analysis of imaging ranging from near-ultraviolet (NUV) bands F225W, F275W, and F336W (UVUDF, Teplitz et al., 2013), over optical bands F435W, F606W, F775W, and F850LP (Beckwith et al., 2006), to near-infrared (NIR) bands F105W, F125W, F140W, and F160W (UDF09 and UDF12 Oesch et al., 2010b,a; Bouwens et al., 2011; Koekemoer et al., 2013; Ellis et al., 2013). These data sets cover an area of 12.8 arcmin^2, but only 4.6 arcmin^2 have full NIR coverage. R15 provide photometric redshifts obtained with the code `BPZ` (Benítez, 2000), which are highly robust due to the exquisite depth and high wavelength coverage of the data sets (e.g. demonstrated in Brinchmann et al., 2017). Given their accuracy, the R15 photo-zs provide an important benchmark for our computation of the average lensing efficiency. However, the small area covered in the sky leads to a substantial impact of sampling variance. Consequently, we also need to incorporate other data sets, which are shallower but cover a larger footprint in the sky (see Section 7.6.1).

3D-HST

Skelton et al. (2014) (henceforth S14) present catalogues with photometric measurements in filters covering a wide wavelength range and photometric redshifts for galaxies from the CANDELS/3D-HST fields over a total areal of ~ 900 arcmin^2. Their aim is to homogeneously combine various data sets available for these fields. Firstly, this includes the Cosmic Assembly Near-infrared Deep Extragalactic Legacy Survey (CANDELS, Grogin et al., 2011; Koekemoer et al., 2011). It is an imaging survey conducted with *HST*/WFC3 and *HST*/ACS in five fields of the sky, namely AEGIS, COSMOS, GOODS-North, GOODS-South, and UDS. Secondly, the 3D-HST program (Brammer et al., 2012) provides slitless spectroscopy obtained with the WFC3 G141 grism for galaxies across nearly 75 per cent of the CANDELS area and thus includes redshifts and spatially resolved spectral lines. Additionally, the WFC3 G141 grism spectroscopy data products are presented in Momcheva et al. (2016), who also developed a software to optimally extract spectra for the objects from the S14 photometric catalogues. S14 combine the photometric data sets from the CANDELS and 3D-HST programmes with available ancillary data sets in the five CANDELS/3D-HST fields by using a common WFC3 detection image, conducting consistent PSF-homogenised aperture photometry, and estimating photometric redshifts and redshift probability distributions with the code `EAZY` (Brammer et al., 2008).

S18 and Raihan et al. (2020) (henceforth R20) show that the photometric redshifts by S14 suffer from catastrophic outliers, which can significantly bias weak lensing mass measurements. Through the comparison of photometric redshift measurements from S14 and R15, R20 found that these outliers systematically bias the redshift distribution low. R20 were able to mitigate this by recomputing the photometric redshifts using the code `BPZ` instead of `EAZY`. In particular, the interpolation of the implemented SED template set helped reduce the bias[10]. For our weak lensing study, we use the updated R20 photometric redshift catalogues in the five CANDELS/3D-HST fields to estimate the average redshift distribution and lensing efficiency of our samples of selected background galaxies.

Additionally, S18 found some systematic deviations between the R15 photometric redshifts and the grism redshifts (Brammer et al., 2012; Momcheva et al., 2016). Upon revisiting this comparison, now including MUSE spectroscopic redshifts (Inami et al., 2017, see Section 7.6.1 below for details), R20 identified the affected redshift regimes and corrected the respective bias by subtracting the median offset. This bias amounts to 0.081 (0.162) for the photo-z regime $1.0 < z < 1.7$ ($2.6 < z < 3.2$). The resulting 'fixed' redshift catalogues are denoted as R15_fix catalogues.

HDUV

The Hubble Deep UV Legacy Survey (HDUV, Oesch et al., 2018, henceforth Oe18) is an imaging programme, which expands on the S14 catalogues with deeper UV observations in the WFC3/UVIS filters F275W and F336W. It targets $\sim 100\,\mathrm{arcmin}^2$ within the GOODS-North and GOODS-South field. Oe18 conducted consistent photometry as S14 regarding the detection image and flux measurements and recalculated photometric redshifts with the `EAZY` code including their deeper UV images.

MUSE

The MUSE Hubble Ultra Deep Field Survey (Bacon et al., 2015; Inami et al., 2017; Brinchmann et al., 2017) comprises spectroscopic redshift measurements of almost

---

[10] When recomputing the photo-zs, R20 employed an approximately homogeneous subset of broad-band filters (between U and H band), which are available for all five CANDELS fields. Since they dropped additional bands, this may increase the scatter in some of the photo-z estimates compared to the S14 catalogue. However, for our analysis it is more important to have accurate estimates of the overall redshift distribution of colour-selected high-z lensing source galaxies, as provided by the R20 catalogues.

1400 sources in the HUDF region. This increases the number of available spectroscopic redshifts in this region by a factor of eight. It was conducted with the Multi Unit Spectroscopic Explorer (MUSE) at the Very Large Telescope. Inami et al. (2017) provide spectroscopic redshifts for sources with a completeness of 50 per cent at 26.5 mag in F775W. The redshift distribution includes sources beyond $z > 3$ and up to a F775W magnitude of ~ 30 mag. This spectroscopic redshift catalogue is an excellent reference to judge the reliability of the photometric redshift catalogues used for the colour selection of background galaxies.

7.6.2 Selection of background galaxies through colour cuts

Defining the colour and magnitude cuts

We aim to find criteria based on colours and magnitudes that help us distinguish the background galaxies of interest from the contaminating foreground and cluster galaxies. To this end, we take a look at the S14/R20 catalogues providing photometry and photometric redshifts for the largest number of galaxies. Firstly, we decide to focus on the magnitude regime $24.2 < V_{606} < 27.0$ for the selection strategy. Inspecting the redshift distributions of galaxies in the CANDELS/3D-HST fields, we find that there is no significant amount of background galaxies at redshifts $z \gtrsim 1.8$ present at magnitudes brighter than $V_{606} < 24.2$. By focusing on galaxies fainter than this limit, we can exclude many bright foreground galaxies. Additionally, our cluster fields roughly reach limiting magnitudes of 27.0 mag in the F606W band.

Secondly, we inspect the colour-colour plots of different combinations of colours to identify a suitable strategy. We find that a combination of the colour plane including V_{606}, I_{814}, and J_{110} and the colour plane including U, V_{606}, and J_{110} provide a useful basis for a selection of background galaxies, i.e., galaxies at redshifts higher than the cluster redshifts of $1.2 \lesssim z \lesssim 1.7$. A strategic cut in the colour plane $V_{606} - I_{814}$ and $I_{814} - J_{110}$ (short VIJ plane) allows us to remove a significant fraction of foreground galaxies at $0.0 < z < 1.1$. We discard all galaxies to the right of this cut (redder in $V_{606} - I_{814}$, see the black line in Figure 7.3). With this cut, we do, however, still keep a lot of galaxies at the cluster redshift while discarding a substantial fraction of background galaxies at $z > 2.2$. The colour plane $U - V_{606}$ and $V_{606} - J_{110}$ (short UVJ plane) helps us to refine the selection. Here, we can remove almost all galaxies at the cluster redshift (galaxies that are blue in $U - V_{606}$ and red in $V_{606} - J_{110}$, they correspond to the upper left corner of the UVJ plane in Figure 7.4), and at the same time recover high-redshift sources we had discarded in the first selection step (galaxies that are red in $U - V_{606}$, they correspond to the lower right corner of the UVJ plane in Figure 7.4). Additionally, we slightly vary these cuts depending if the galaxies are bright ($24.2 < V_{606} < 25.75$) or faint ($25.75 < V_{606} < 27.0$). Fainter galaxies typically exhibit a larger photometric scatter than brighter galaxies. We can, therefore, apply slightly tighter cuts for brighter galaxies without a high risk

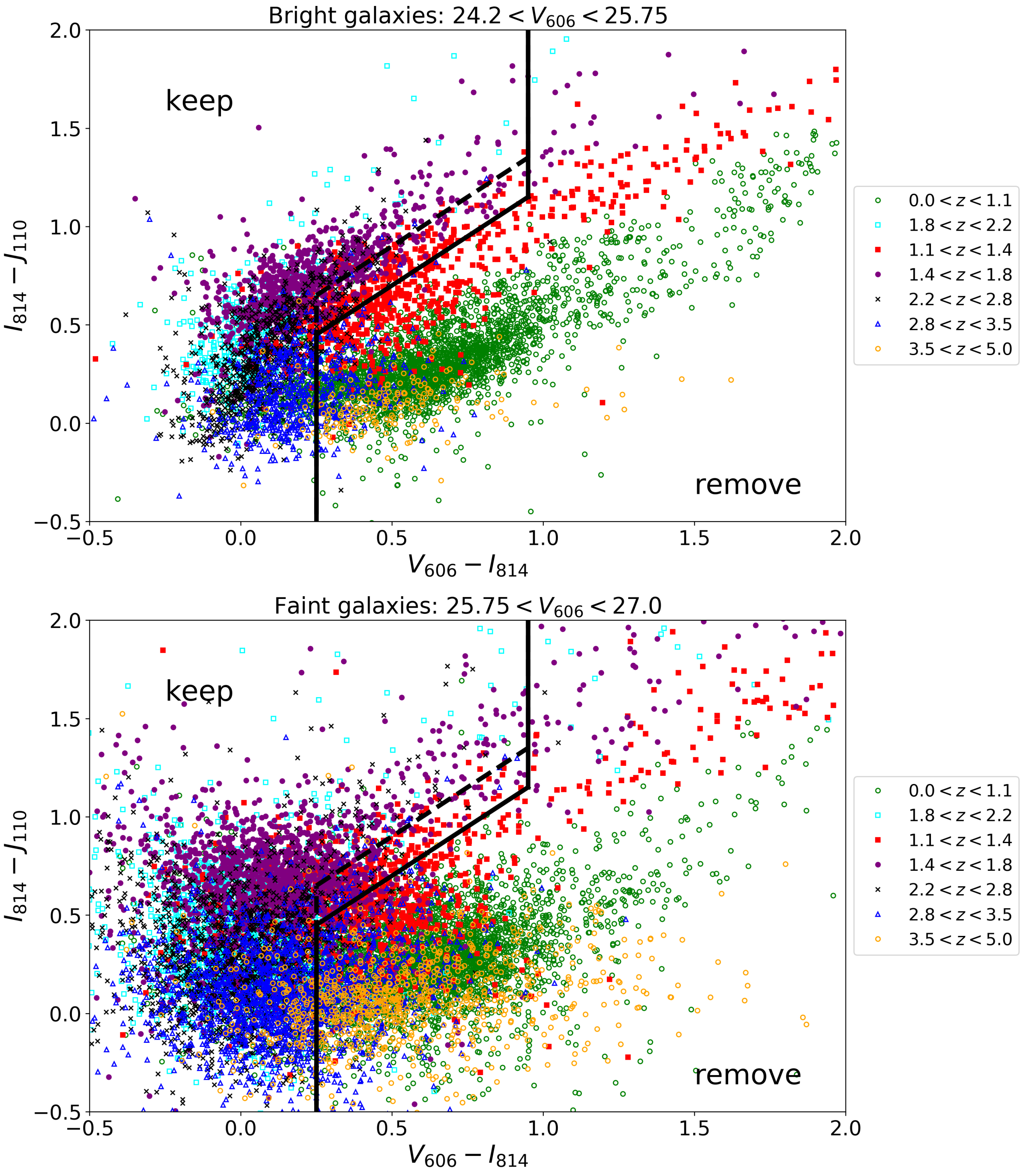

Figure 7.3 – Colour selection for galaxy clusters at redshift $1.2 \lesssim z \lesssim 1.7$. The selected source galaxies are at redshift $z \gtrsim 1.7$. We display galaxies based on their photometry from S14 in the GOODS-South field. The figures show the first selection step in the VIJ plane for bright galaxies at the top and faint galaxies at the bottom. The solid black lines indicate cuts applied for bright galaxies, the dashed black lines show cuts for faint galaxies.

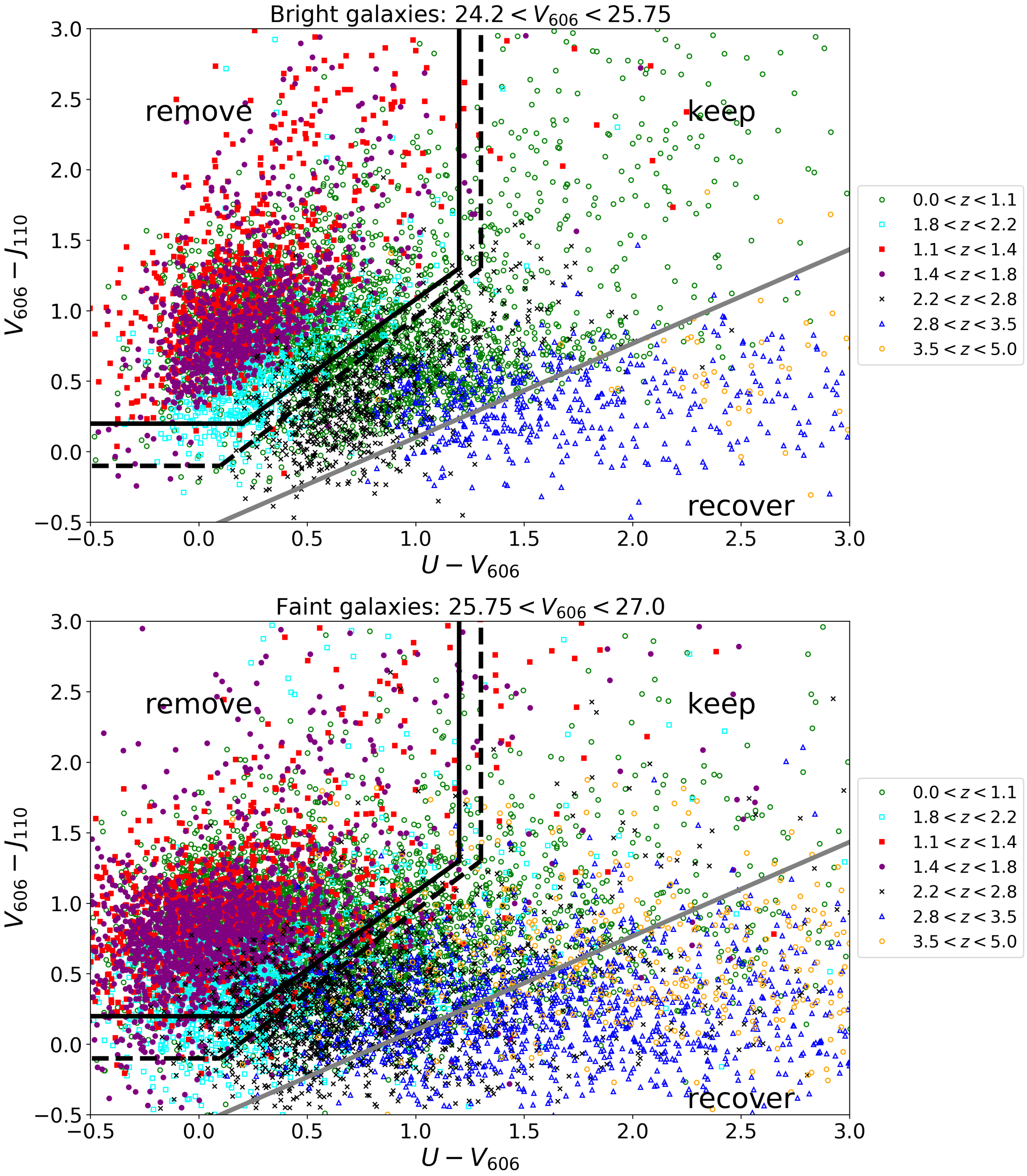

Figure 7.4 – Colour selection for galaxy clusters at redshift $1.2 \lesssim z \lesssim 1.7$. The selected source galaxies are at redshift $z \gtrsim 1.7$. We display galaxies based on their photometry from S14 in the GOODS-South field. The figures show the second selection step in the UVJ plane for bright galaxies at the top and faint galaxies at the bottom. The solid black lines indicate cuts applied for bright galaxies, the dashed black lines show cuts for faint galaxies. Galaxies below the diagonal grey line are recovered in both the bright and the faint regime.

of contamination by cluster galaxies due to scatter. Figures 7.3 and 7.4 illustrate our cuts in the two colour planes and for the bright and faint magnitude regimes for clusters at redshift $1.2 \lesssim z \lesssim 1.7$.

We have also investigated if it is possible to optimise the selection depending on the cluster redshift. For instance galaxies at redshift $1.3 < z < 1.7$ could be used for a cluster at redshift $z = 1.2$, but have to be removed for a cluster at redshift $z = 1.7$. Unfortunately, such an optimisation is not possible with the available filters because all the galaxies in the redshift regime $1.2 \lesssim z \lesssim 1.7$[11] occupy a very similar location in the UVJ plane (see red and purple symbols in Figure 7.4). We, therefore, decide to use common selection criteria for background galaxies, independent of the cluster redshift.

Additionally, we investigated how beneficial the use of the U band is for an efficient source selection since it is the band introducing the largest uncertainties. We find that it is possible to select sources with a similar average geometric lensing efficiency only based on the bands F606W, F814W, and F110W. However, the resulting source density of such a selection is significantly lower. In conclusion, the signal-to-noise ratio of the lensing measurement (proportional to the product of the average lensing efficiency and the square root of the source density) is about 1.4 times higher when the U band is included for the source selection (see Section 7.15).

Comparison of selections based on the S14 and the LAMBDAR photometry

We calculate the average lensing efficiency $\langle\beta\rangle$ for the selection based on the S14 photometry and for five catalogues with photometric redshift information, namely the original S14 redshifts, the updated R20 redshifts by R20, the redshifts given in R15, a modified version of the R15 redshifts from R20 called R15_fix, and the redshifts from Oe18. Throughout this section, we use the median lens redshift of our cluster sample of $z_l = 1.4$ for the calculation of $\langle\beta\rangle$. In addition to the selection as described in Section 7.6.2, we employ a signal-to-noise threshold of $S/N_{\mathrm{flux},606} > 10$ as applied for the shape measurements of galaxies (the signal-to-noise ratio is defined via the ratio of `FLUX_AUTO` and `FLUXERR_AUTO` from `Source Extractor`; see also Section 7.7). We note that R20 optimised the redshifts for a source selection targeting background galaxies behind clusters of $0.6 \lesssim z \lesssim 1.1$ (the cluster sample from S18). They apply a cut based on $V - I$ colour at $V - I < 0.3$ and a magnitude cut of $V_{606} < 26.5$. Even though these settings differ from ours, we find that the R20 catalogues are still applicable for our analysis because on average 84 per cent of galaxies in our selection in the cluster fields also fulfil the condition $V - I < 0.3$. Additionally, we find that the average lensing efficiency calculated based on R20 photo-zs for our colour-selected galaxies in the HUDF is

---

[11] Note that the cluster redshift of SPT-CL $J0646{-}6236$ is lower with $z \sim 1.0$. While a slightly different optimisation could be conducted here, we choose to apply the same colour selection scheme to keep the analysis homogeneous.

not significantly affected by a change of the magnitude limit from $V_{606} < 27.0$ to $V_{606} < 26.5$.

The five redshift catalogues (denoted R15, R15_fix, R20, S14, and Oe18) overlap in the HUDF region. We match the sources from our five reference catalogues based on their coordinates through the function `associate` from the `LDAC` tools[12]. For a match, we require a distance smaller than $0\farcs3$. In Figure 7.5, we show the redshift distribution of the galaxies, which we select with our strategy. Note that the depth of the S14 U band (5σ depth = 27.9) is considerably higher than the depth of our observations in the U_{HIGH} band in the HUDF (5σ depth = 26.6). To account for this difference, we add Gaussian noise to the S14 U band photometry and show the average redshift distribution derived from 50 noise realisations of galaxies in the HUDF for a U_{HIGH} band depth of 26.6 mag in Figure 7.5. Note that, when we estimate the average lensing efficiency for the cluster fields, we add Gaussian noise to both the U band and *HST* photometry from the S14 catalogues to account for the difference between the depths in the respective cluster fields and in the CANDELS/3D-HST fields. When we calculate the average lensing efficiency, we employ the shape weights from S18 that depend on the signal-to-noise ratio $(\mathrm{Flux}/\mathrm{Fluxerr})_{\mathrm{auto}}$ in V_{606}. Since the S14 catalogues do not provide measurements of `FLUX_AUTO`, we use the listed total fluxes and respective errors instead[13]. The redshift distributions show that S14 and Oe18 have an excess of galaxies at the cluster redshifts and in the foreground at $z < 0.4$ compared to the other catalogues. This is connected to the reported contamination by catastrophic redshift outliers (see Section 7.6.1). We can see this effect as well in Figure 7.5 where the S14 and Oe18 redshift catalogues yield lower values of the average lensing efficiency than the other redshift catalogues. In contrast to that, the results from the R20 redshift catalogues are in good agreement with the robust photometric redshift catalogues R15 and R15_fix. According to these catalogues, we expect nearly no contamination by cluster galaxies for our selection strategy (only ~ 1 per cent of selected galaxies are within the cluster redshift range). From a comparison of the average lensing efficiency based on R20 and R15_fix we infer a systematic uncertainty of $\Delta(\langle\beta\rangle)/\langle\beta\rangle_{\mathrm{R15\_fix}} = 5.6\%$.

Since we measure fluxes in our observations with LAMBDAR, we additionally inspect the redshift distributions, which we obtain when we use the LAMBDAR photometry measured from our observations of the HUDF in U_{HIGH} and from the S14 stacks in the *HST* filters F606W, F814W, F850LP and F125W[14] (we interpolate

---

[12] `https://marvinweb.astro.uni-bonn.de/data_products/THELIWWW/LDAC/`

[13] As a cross-check, we calculated the average lensing efficiency with the shape weights based on the total fluxes in the S14 catalogues and the `AUTO` fluxes in catalogues by S18. They have analysed shallower stacks in the CANDELS/3D-HST fields, including measurements of `FLUX_AUTO`, which allows us to draw a direct comparison. We find that the difference between both options is less than 1 per cent.

[14] `https://archive.stsci.edu/prepds/3d-hst/` ; (F606W + F850LP: programme 9425 with PI M. Giavalisco, F814W: programme 12062 with PI S. Faber, F125W: programme 13872 with PI G. Illingworth)

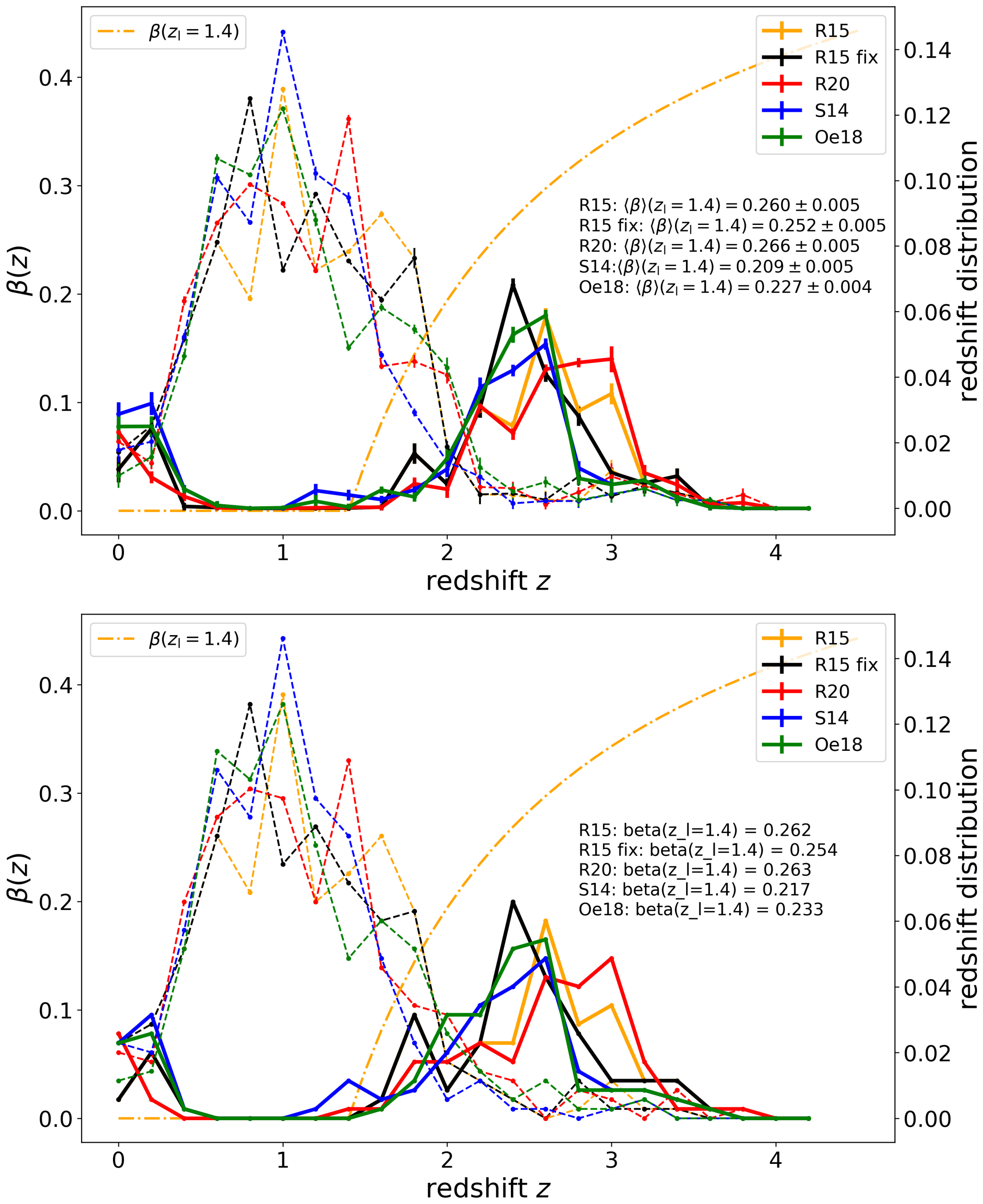

Figure 7.5 – Redshift distributions resulting from the colour selection for galaxy clusters at redshift $1.2 \lesssim z \lesssim 1.7$ in the HUDF region. The selected source galaxies (solid lines) are mostly at redshift $z \gtrsim 1.7$. Removed galaxies (dashed lines) are mostly at redshifts $z \lesssim 1.7$. The distributions only show galaxies matched between the five reference redshift catalogues (R15, R15_fix, R20, S14 and Oe18) and the photometric catalogue from this work. We additionally display the average lensing efficiency curve as a function of redshift (yellow dash-dotted line). *Top:* Redshift distributions for the five redshift catalogues and employing a colour selection based on the S14 photometry. The uncertainties represent the standard deviations from 50 noise realisations of the U band in the S14 photometry. *Bottom:* Redshift distributions for the five redshift catalogues and employing a colour selection based on the LAMBDAR photometry measured from our observations of HUDF in U_{HIGH} and from the S14 stacks in different *HST*-bands (see text).

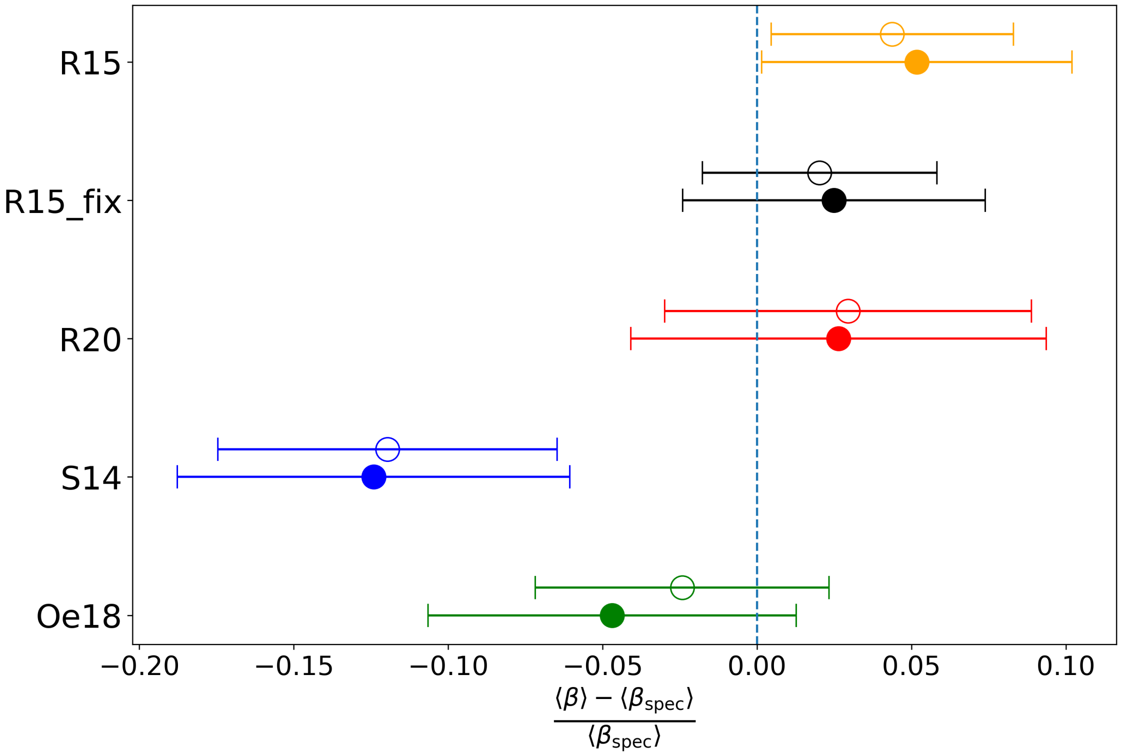

Figure 7.6 – Relative bias in the average lensing efficiency normalised to the result based on spectroscopic/grism redshifts. We perform the colour selection for all coordinate-matched galaxies in the HUDF with available spectroscopic/grism redshifts. The uncertainties represent the scatter from 1000 bootstrap resamples. Filled symbols represent source selections based on the S14 photometry, open symbols represent source selections based on the LAMBDAR photometry.

between the latter two filters to estimate the magnitude in the filter F110W). The resulting distribution is shown in the bottom panel of Figure 7.5.

This corresponds to a systematic uncertainty of $\Delta(\langle\beta\rangle)/\langle\beta\rangle_{\rm R15\_fix} = 3.5\%$. Overall, the average lensing efficiency results based on S14 and LAMBDAR photometry agree within the uncertainties (see Figure 7.5).

Comparison of selections based on photo-zs and spec-zs

As a cross-check for the photometric redshift catalogues, we retrieve spectroscopic/grism redshifts from the MUSE and 3D-HST catalogues, respectively, for all galaxies matched by their coordinates in the HUDF field. As a reference, we then calculate the average lensing efficiency of the colour-selected sources based on the spectroscopic/grism redshifts. Here, we only use the MUSE spec-zs with the highest quality flags 3 (secure redshift, determined by multiple features) and 2 (secure redshift, determined by a single feature, see Inami et al., 2017). In the case

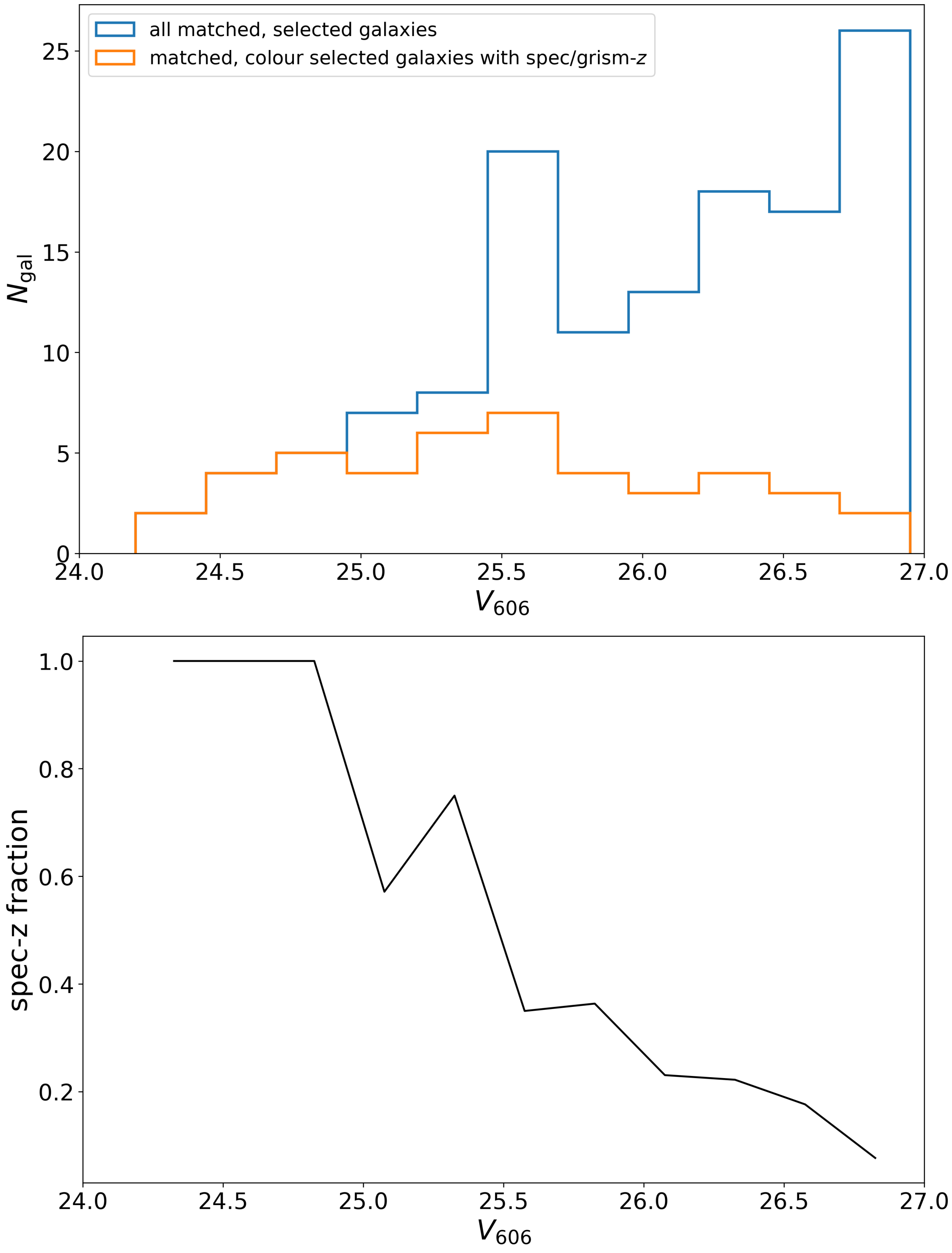

Figure 7.7 – *Top:* Histogram of all matched and colour-selected galaxies within the HUDF region (blue). The orange histogram shows how many of these have a robust spec-z from MUSE or grism-z. *Bottom:* Fraction of matched and colour-selected galaxies within the HUDF region with a robust spec-z from MUSE or grism-z, corresponding to the ratio of the orange and blue curve from the top panel.

of galaxies with both spectroscopic redshifts from MUSE and grism redshifts from 3D-HST, we use the former for the calculation of $\langle\beta_{\mathrm{spec}}\rangle$. To estimate the uncertainty, we bootstrap the colour-selected galaxies and recalculate the average lensing efficiency 1000 times. Figure 7.6 shows how the average lensing efficiency calculated from the five photometric redshift catalogues compares to the one calculated based on spectroscopic/grism redshifts. We do not find a bias within the uncertainties, but we notice that the average lensing efficiency based on R15_fix, R20 and Oe18 matches closest to the result based on the spectroscopic/grism redshifts. It also has to be noted that the spectroscopic/grism redshifts are only complete in comparison to the full sample of matched galaxies in the HUDF region up to a magnitude of $V_{606} \lesssim 25.0\,\mathrm{mag}$ (see Figure 7.7). We still decide to correct our measurements of the average lensing efficiency by the roughly three per cent offset between the R20 redshift-based and the spectroscopic redshift-based lensing efficiency.

Differences between the five CANDELS/3D-HST fields

Since we estimate the average lensing efficiency from all CANDELS fields, we want to evaluate the expected systematic uncertainties arising from differences in the depths, available filters, and calibrations in the five CANDELS/3D-HST fields. Additionally, we expect statistical sampling variance connected to line-of-sight variations.

We quantify the systematic uncertainties by measuring the average lensing efficiency for colour-selected galaxies independently in the five CANDELS/3D-HST fields (see Figure 7.8). We obtain an average lensing efficiency of $\langle\beta\rangle = 0.242$ with a standard deviation of $\sigma(\beta) = 0.014$ between the $N = 5$ fields (using the photometric redshifts from R20). This translates into a systematic uncertainty of $\sigma(\beta)/\langle\beta\rangle = 5.7\%$. We calculate this more conservative systematic uncertainty without dividing by $\sqrt{N-1}$ because we notice that the value of the GOODS-South field is notably higher, and thus, one field might not automatically be a good representation of the average of all. We add this uncertainty in quadrature to our systematic error budget (see Table 7.3). Note that this uncertainty also contains a statistical contribution as each CANDELS/3D-HST field represents a different line-of-sight. However, since the fields are each much larger than the small sub-patches studied in the paragraph below, we conservatively assume that the variations between the CANDELS/3D-HST fields are dominated by systematic uncertainties.

We gauge the expected statistical uncertainty from line-of-sight variations in the average lensing efficiency by placing non-overlapping apertures with the same area as the field of view of our observations (about 11 arcmin^2) in the CANDELS/3D-HST fields. We can fit eight apertures in each of the fields. We calculate the average lensing efficiency independently for all of the apertures, where we obtain on average $\langle\beta\rangle = 0.243$ with a scatter of $\sigma(\beta) = 0.017$. Hence, we add a statistical uncertainty of $\sigma(\beta)/\langle\beta\rangle = 6.9\%$ to our statistical error budget (see Table 7.3).

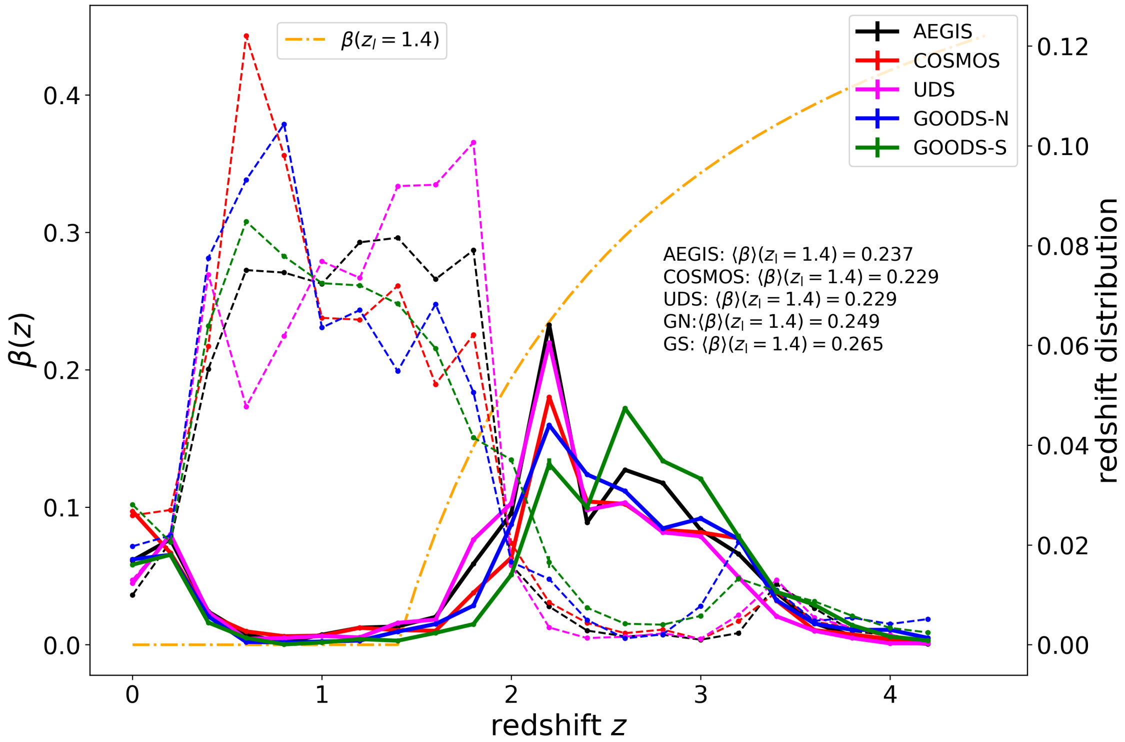

Figure 7.8 – Redshift distribution of the galaxies in the CANDELS/3D-HST fields for the colour selection for clusters at $1.2 \lesssim z \lesssim 1.7$, employing the R20 photometric redshift catalogues. See caption of Figure 7.5 for further details.

Regarding uncertainties of the source redshift distribution, we estimate a total statistical uncertainty of 8.0 per cent. This includes uncertainties in the U_{HIGH} band calibration (see Section 7.13) and line-of-sight variations (this Section), which we add in quadrature. Furthermore, we estimate a total systematic uncertainty of 8.6 per cent. Here, we take into account systematics for the F110W band (interpolation versus direct measurement, aperture photometry versus LAMBDAR photometry, see Appendices 7.12 and 7.14), uncertainties in the measurement of $V - I$ colours (see Sections 7.12 and 7.14), uncertainties of the R20 redshift catalogues (see Section 7.6.2), and variations between the CANDELS/3D-HST fields (differences of the filters, depths, availability of U bands, and usage of different bands to interpolate the J_{110} magnitudes, see this Section). Again, we add these contributions in quadrature. All uncertainties are summarised in Table 7.3.

7.6.3 Check for cluster member contamination

We aim to preferentially select background galaxies with our magnitude and colour cuts both in the cluster fields and the CANDELS/3D-HST fields. Investigating the total source density of the selected galaxies and their radial dependence allows us to

Table 7.3 – We summarise our systematic and statistical error budget. In the upper part of the table, we list all systematic uncertainties, which ultimately translate into an uncertainty in the weak lensing mass measurement, where we add the individual contributions in quadrature to obtain an estimate for the total uncertainty. We report the relative uncertainties in per cent in the second column, the resulting relative uncertainty on the mass in the third column, and refer the reader to the respective Sections listed in the last column for more detailed information about the contributions to the error budget. In the lower table, we list statistical uncertainties in the redshift distribution, which affect the calculation of the average geometric lensing efficiency $\langle\beta\rangle$. Note that the final statistical uncertainties reported in Tables 7.6 and 7.7 do include additional contributions from shape noise and uncorrelated large-scale structure projections.

Source of **systematic** uncertainties	Rel. error signal	Rel. error M_{500c}	Section
Redshift distribution:			
- R20 vs. R15_fix comparison	5.6 %	8.4 %	7.6.2
- Variations between CANDELS/3D-HST fields	5.7 %	8.6 %	7.6.2
- F110W band (LAMBDAR/S14, interpolation)	2.2 %	3.3 %	7.12/7.14
- $V-I$ colour (LAMBDAR/S14)	2.2 %	3.3 %	7.12/7.14
Shape measurements:			
- Shear calibration	2.3 %	3.4 %	7.7
Mass model:			
- $c(M)$ relation		4.0 %	
- Miscentering for			
X-ray centres		3.8 % /	7.8.3
SZ centres		9.2 %	7.8.3
total		14.4 % / 16.7 %	

Source of **statistical** uncertainties	Rel. error signal	Rel. error M_{500c}	Sect./App.
Redshift distribution:			
- Line-of-sight variations	6.9 %	10.4 %	7.6.2
- U_{HIGH} band calibration	4.1 %	6.2 %	7.13/7.14
total		12.1 %	

test if we have a substantial amount of contamination by cluster galaxies and if our method provides a consistent selection in the cluster fields and the CANDELS/3D-HST fields in the presence of noise (S18).

To this end, we add Gaussian noise to the S14 photometric catalogues according to the difference between the depth of the cluster observations and the depth of the CANDELS/3D-HST fields. This may vary depending on the field and filter. We only add Gaussian noise if the CANDELS/3D-HST observation in a filter is deeper than the corresponding observation in the cluster field. Occasionally, the cluster observations are slightly deeper than some of the CANDELS/3D-HST observations, but only by ~ 0.2 mag. We consider this negligible for the validity of this test.

We measure the source density of selected sources accounting for masks, for example, due to bright stars for the cluster fields and CANDELS/3D-HST fields. We only consider photometrically selected galaxies and do not consider potential flags from the shape measurement pipeline. We also do not apply the signal-to-noise ratio cut $S/N_{\mathrm{flux},606} > 10$ as mentioned in Sections 7.6.2 and 7.7 for this test, since the quantities `FLUX_AUTO` and `FLUXERR_AUTO` required to calculate the signal-to-noise ratio are not available in the CANDELS/3D-HST catalogues. In Figure 7.9 (upper panel), we show the average source density of selected galaxies as a function of the V_{606} band magnitude. We find a good agreement over the full magnitude range of interest in this study.

Additionally, we present the radial dependence of the source density of selected galaxies. In principle, an increase of the number density towards the cluster centre can indicate cluster member contamination. However, the profile can also be affected by blending and/or masking of background galaxies by cluster member galaxies, magnification, or selection effects. We account neither for blending and/or masking by cluster galaxies nor magnification in our analysis. The blending/masking by cluster galaxies should be less important than for clusters at lower redshifts since the cluster galaxies are more cosmologically dimmed. Additionally, we generously exclude the core region $r < 500\,\mathrm{kpc}$, when we measure the weak lensing masses so that this effect should not play a significant role. Regarding magnification, for S21 the application of a magnification correction had only a minor impact on the source density profile. Given the higher redshifts of our clusters, the lensing strength and, therefore, the expected impact of magnification are even lower, which is why we ignore it here.

Figure 7.9 (lower panel) displays the radial distance from the X-ray centre (except for cluster SPT-CL $J0646{-}6236$, where we use the SZ centre) in units of the radius $R_{500\mathrm{c,SZ}}$, which we derive from the SZ mass $M_{500\mathrm{c,SZ}}$. We find a very slight trend of a higher source density towards the centres of the clusters. However, the profile is consistent with flat within the uncertainties. Together, both measurements provide an important confirmation for the success of photometric background selection and cluster member removal.

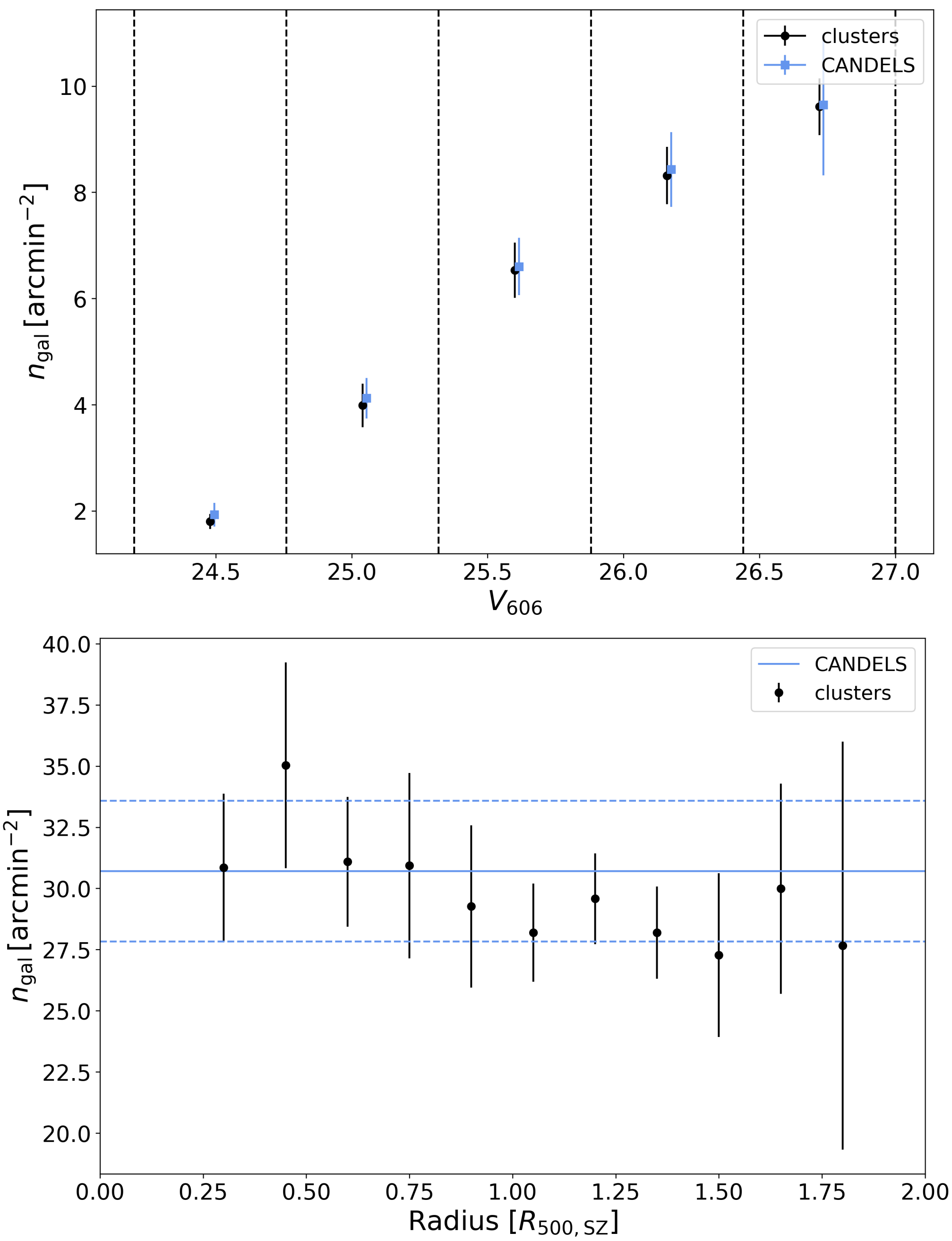

Figure 7.9 – *Top:* We show the number density of selected galaxies n_{gal} averaged over the nine cluster fields (black symbols) and averaged over the five 3D-HST/CANDELS fields (blue symbols). We take into account the masks, for example, from bright stars in the images, and we only consider photometrically selected galaxies, i.e., no flags from shape measurements or signal-to-noise ratio cuts are considered here. The error bars correspond to the uncertainty of the mean from the variation between the contributing cluster fields or 3D-HST/CANDELS fields, respectively. *Bottom:* Average density of selected sources as a function of the distance to the X-ray cluster centre (except for cluster SPT-CL $J0646{-}6236$, where we use the SZ centre). These distances are given in units of the radius $R_{500\mathrm{c,SZ}}$ based on the SZ-mass $M_{500\mathrm{c,SZ}}$. Blue lines indicate the average density and 1σ uncertainties from the five 3D-HST/CANDELS fields. The error bars correspond to the uncertainty of the mean from the variation between the contributing cluster fields or 3D-HST/CANDELS fields, respectively.

7.7 Shape measurements

We measure galaxy shapes in the ACS F606W (V) and F814W (I) images using the KSB+ formalism (Kaiser et al., 1995; Luppino & Kaiser, 1997; Hoekstra et al., 1998) as implemented by Erben et al. (2001) and Schrabback et al. (2007). We model the spatially and temporally varying ACS point-spread function using an interpolation based on principal component analysis, as calibrated on dense stellar fields (Schrabback et al., 2010, 2018). We correct for shape measurement and selection biases as a function of the KSB+ galaxy signal-to-noise ratio from Erben et al. (2001). This correction was derived by Hernández-Martín et al. (2020), who analysed custom `Galsim` (Rowe et al., 2015) image simulations with ACS-like image characteristics. Importantly, Hernández-Martín et al. (2020) tuned their simulated source samples such that the measured distributions in galaxy size, magnitude, signal-to-noise ratio, and ellipticity dispersion closely matched the corresponding measured distributions of the magnitude and colour-selected source samples from S18, while also incorporating realistic levels of blending. Varying the properties of the simulations, Hernández-Martín et al. (2020) estimated a (post-correction) multiplicative shear calibration uncertainty of the employed KSB+ pipeline of $\sim 1.5\%$. Our data are very similar to those analysed by S18, which is why we expect that the Hernández-Martín et al. (2020) shear calibration is also directly applicable for our analysis. However, our colour selection selects galaxies at slightly higher redshifts on average compared to the $V-I$ selection from S18. Some of our image stacks are also slightly deeper. We, therefore, conservatively increase the shear calibration uncertainty in our systematic error budget by a factor ×1.5 (see Table 7.3).

Given their greater average depth (see Table 7.2), we base our shear catalogue primarily on the F606W stacks. Here we include galaxies with a measured flux signal-to-noise ratio (defined as the ratio of the `FLUX_AUTO` and `FLUXERR_AUTO` parameters from `Source Extractor`) $S/N_{\mathrm{flux},606} > 10$. This single-band selection matches the one employed in Section 7.6.2 in the computation of the average geometric lensing efficiency. For galaxies that additionally have $S/N_{\mathrm{flux},814} > 10$, we combine the shape measurements from both filters to reduce the impact of measurement noise.

In order to compute shape weights and filter-combined estimates of the reduced shear, we make use of the $\log_{10} S/N_{\mathrm{flux}}$-dependent fits computed by S18, see their Appendix A for the total ellipticity dispersion $\sigma_{\epsilon,V/I}$, the intrinsic ellipticity dispersion $\sigma_{\mathrm{int},V/I}$, and the ellipticity measurement noise $\sigma_{\mathrm{m},V/I}$ of $V-I$ colour selected galaxies in custom CANDELS (Grogin et al., 2011) V (F606W) and I (F814W) band stacks of approximately single-orbit depth[15]. With the complex reduced shear

---

[15] We employ the $\log_{10} S/N_{\mathrm{flux}}$-dependent fits instead of the magnitude-dependent fits provided by S18 in order to account for the slightly higher depth of some of our stacks and the significant dependence of the measurement noise on $\log_{10} S/N_{\mathrm{flux}}$. For comparison, the dependence of $\sigma_{\mathrm{int},V/I}$ on $\log_{10} S/N_{\mathrm{flux}}$ is weak in the regime covered by most of our sources.

Table 7.4 – Number densities of selected source galaxies measured in the cluster fields. We apply the source selection as described in Section 7.6.2 including only sources that pass the lensing selections and have a signal-to-noise ratio $S/N_{\mathrm{flux},606} > 10$, leading to lower numbers compared to Figure 7.9.

Cluster name	n_{gal} [arcmin^{-2}]
SPT-CL J0156$-$5541	14.3
SPT-CL J0205$-$5829	12.7
SPT-CL J0313$-$5334	20.1
SPT-CL J0459$-$4947	10.7
SPT-CL J0607$-$4448	13.3
SPT-CL J0640$-$5113	10.2
SPT-CL J0646$-$6236	14.9
SPT-CL J2040$-$4451	11.2
SPT-CL J2341$-$5724	12.6
average	13.3

estimates $\epsilon_{V/I}$ obtained in the V band and the I band, respectively, and the shape weights

$$w_{V/I} = \left[\sigma_{\epsilon,V/I}\right]^{-2} \tag{7.18}$$

we compute the filter-combined reduced shear estimate as

$$\epsilon_{\mathrm{comb}} = \frac{w_V \epsilon_V + w_I \epsilon_I}{w_V + w_I} \, . \tag{7.19}$$

The measurement noise is independent between the stacks in the different filters, which is why the combined ellipticity measurement variance reads

$$\sigma^2_{\mathrm{m,comb}} = \frac{(w_V \sigma_{\mathrm{m},V})^2 + (w_I \sigma_{\mathrm{m},I})^2}{(w_V + w_I)^2} \, . \tag{7.20}$$

In the relevant S/N or magnitude regime, differences are small between $\sigma_{\mathrm{int},V}$ and $\sigma_{\mathrm{int},I}$ for the colour-selected source samples from S18. In addition, Jarvis & Jain (2008) found that intrinsic shapes are highly correlated between *HST* images of galaxies in different optical filters. Therefore, as an approximation, we simply interpolate the intrinsic ellipticity dispersion between the filters

$$\sigma_{\mathrm{int,comb}} = \frac{w_V \sigma_{\mathrm{int},V} + w_I \sigma_{\mathrm{int},I}}{w_V + w_I} \, , \tag{7.21}$$

allowing us to compute shape weights for the combined shear estimate as

$$w_{\mathrm{comb}} = \left[\sigma^2_{\mathrm{int,comb}} + \sigma^2_{\mathrm{m,comb}}\right]^{-1} \, . \tag{7.22}$$

We reach an average final source density after all photometry and shape cuts of 13.3 arcmin^{-2} (see Table 7.4). Note that this is substantially lower than the values shown in Figure 7.9 because we now include the signal-to-noise ratio and lensing cuts[16].

7.8 Weak lensing results

Our pipeline used to obtain weak lensing constraints largely follows S18 and S21 to which we refer the reader for more detailed descriptions.

7.8.1 Mass reconstructions

The weak lensing convergence κ and shear γ are both second-order derivatives of the lensing potential (e.g. Bartelmann & Schneider, 2001). As a result, it is possible to reconstruct the convergence distribution from the shear field up to a constant, which is also known as the mass-sheet degeneracy (Kaiser & Squires, 1993; Schneider & Seitz, 1995). Here we employ the Wiener-filtered reconstruction algorithm from McInnes et al. (2009) and Simon et al. (2009), where we fix the mass-sheet degeneracy by setting the average convergence inside the observed fields to zero. We compute S/N maps of the reconstruction, where the noise map is computed as the RMS image of the κ field reconstructions of 500 noise shear fields, which were created by randomising the ellipticity phases in the real source catalogue. Given the limited field of view and our choice to set the average convergence to zero, we expect to slightly underestimate the true S/N levels (S21).

The obtained S/N reconstructions are shown as contours in the left/upper panels of Figures 7.10 and 7.18 – 7.20 in Section 7.16. SPT-CL $J0646{-}6236$ and SPT-CL $J2040{-}4451$ show clear peaks in the mass reconstruction signal-to-noise ratio maps with $S/N_{\mathrm{peak}} > 3$ (see Table 7.5 for details). We find tentative counterparts to the clusters with $2 < S/N_{\mathrm{peak}} < 3$ for SPT-CL $J0156{-}5541$, SPT-CL $J0459{-}4947$, SPT-CL $J0640{-}5113$, and SPT-CL $J2341{-}5724$. The other clusters either show no significant peak in their corresponding mass reconstruction S/N maps, or only a peak close to the edge of the field of view, which is less reliable and likely spurious.

7.8.2 Fits to the tangential reduced shear profiles

We compute the tangential component ('t') and the cross component ('×') of the reduced shear (introduced in Section 7.3) in linear bins of width 100 kpc (see the right/lower panels of Figure 7.10 and Figures 7.18 – 7.20 in Section 7.16) around

---

[16] While the number density is affected by a change of the signal-to-noise ratio cut, we find that the average geometric lensing efficiency is not sensitive to it. The change is smaller than ~ 1 per cent comparing the results with or without the cut at $S/N_{\mathrm{flux},606} > 10$.

Table 7.5 – Constraints on the peaks in the mass reconstruction signal-to-noise ratio maps including their locations (α, δ), positional uncertainties $(\Delta\alpha, \Delta\delta)$ as estimated by bootstrapping the galaxy catalogue (note that this is underestimates the true uncertainty as found by Sommer et al., 2022), and their peak signal-to-noise ratios $(S/N)_{\mathrm{peak}}$. We exclude unreliable peaks close to the edge of the field of view (compare Figures 7.10–7.19).

Cluster	α [deg J2000]	δ [deg J2000]	$\Delta\alpha$ [arcsec]	$\Delta\delta$ [arcsec]	$\Delta\alpha$ [kpc]	$\Delta\delta$ [kpc]	$(S/N)_{\mathrm{peak}}$
SPT-CL $J0156-5541$	29.04676	-55.69426	9.1	4.8	76	41	2.0
SPT-CL $J0459-4947$	74.92771	-49.77739	8.1	9.6	69	81	2.2
SPT-CL $J0640-5113$	100.08319	-51.21488	6.4	5.5	53	46	2.6
SPT-CL $J0646-6236$	101.62890	-62.62016	1.1	2.0	9	16	5.3
SPT-CL $J2040-4451$	310.24056	-44.86349	4.6	3.7	39	31	3.4
SPT-CL $J2341-5724$	355.34768	-57.41418	7.7	8.1	64	68	2.2

both the X-ray centroids (when available) and the SZ centres of the targeted clusters. We fit the tangential reduced shear profiles using spherical NFW (Navarro et al., 1997) models following Wright & Brainerd (2000), employing the concentration–mass relation from Diemer & Kravtsov (2015) with updated parameters from Diemer & Joyce (2019). When deriving mass constraints, we exclude the cluster cores ($r < 500\,\mathrm{kpc}$), since the inclusion of smaller scales would both increase the intrinsic scatter and systematic uncertainties related to the mass modelling (see e.g. Sommer et al., 2022; Grandis et al., 2021). We summarise the resulting fit constraints in Tables 7.6 and 7.7. For clusters with both X-ray and SZ centres, we regard the X-ray-centred analysis as our primary result given the smaller expected mass modelling biases (see Section 7.8.3).

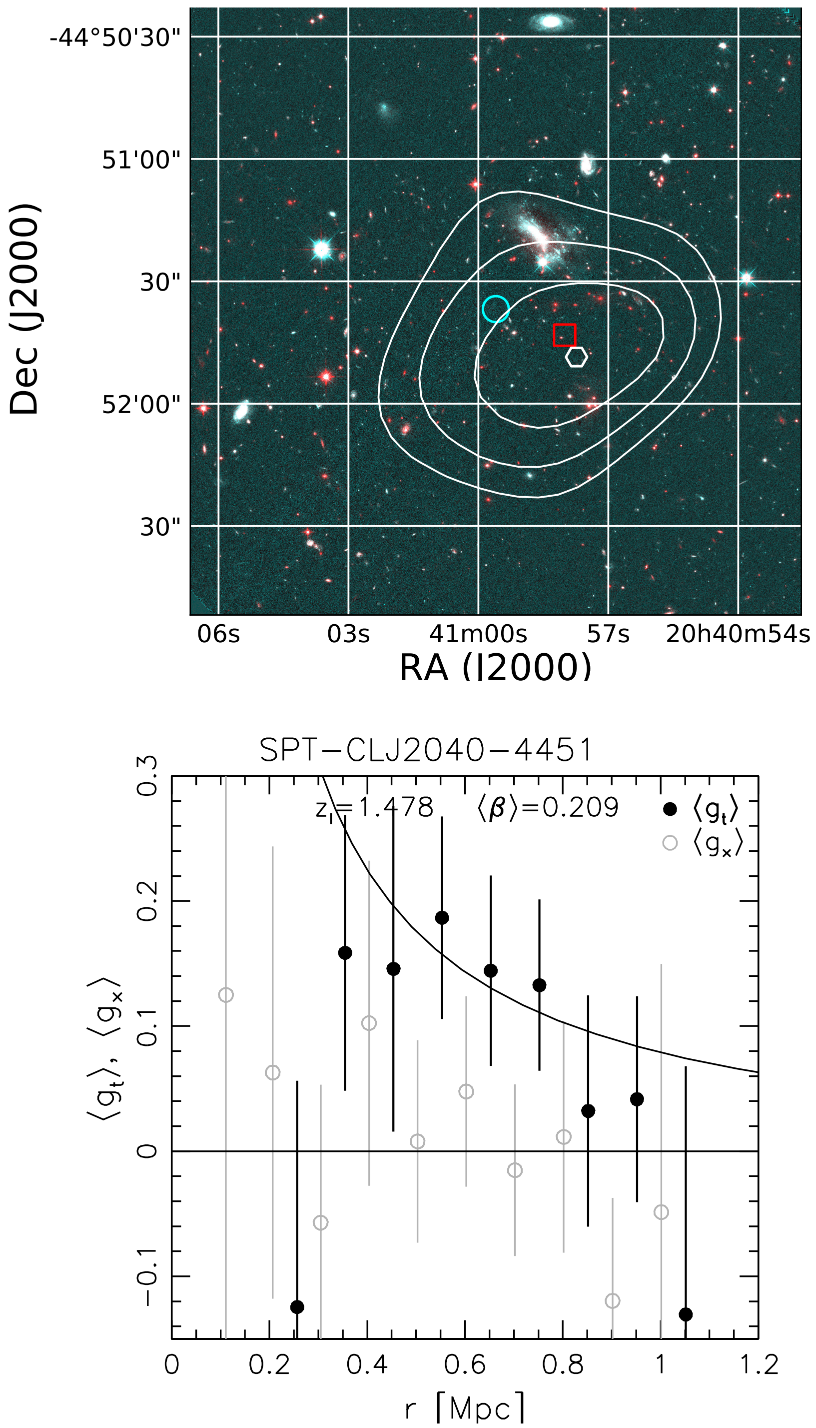

Figure 7.10 – Weak lensing results for SPT-CL *J*2040−4451. *Top:* Signal-to-noise ratio contours of the mass reconstruction, starting at 2σ in steps of 0.5σ, overlaid on a F606W/F814W/F110W colour image ($2\farcm5 \times 2\farcm5$ cutout). The peak in the S/N map is indicated by the hexagon (excluding potential spurious secondary peaks near the edge of the field of view). The cyan circle and the red square show the locations of the SZ peak and the X-ray centroid, respectively. *Bottom:* Reduced shear profile around the X-ray centre, including the tangential component (solid black circles including the best-fitting NFW model) and the cross component (open grey circles), which has been shifted along the x-axis for clarity.

Table 7.6 – Weak lensing mass constraints derived from the fit of the tangential reduced shear profiles around the X-ray centres using spherical NFW models assuming the $c(M)$ relation from Diemer & Kravtsov (2015) with updated parameters from Diemer & Joyce (2019) for two different over-densities $\Delta \in \{200\mathrm{c}, 500\mathrm{c}\}$. The maximum likelihood mass estimates $M_{\Delta}^{\mathrm{biased,ML}}$ are given in $10^{14}\mathrm{M}_{\odot}$, where errors correspond to statistical 68 per cent uncertainties from shape noise (asymmetric errors), followed by uncorrelated large-scale structure projections, the calibration of the U_{HIGH} band, and variations in the redshift distribution between different lines of sight (for systematic uncertainties see Table 7.3). Statistical corrections for mass modelling biases have not yet been applied for $M_{\Delta}^{\mathrm{biased,ML}}$. They are characterised by $\hat{b}_{\Delta,\mathrm{WL}} = \exp\left[\langle \ln b_{\Delta,\mathrm{WL}} \rangle\right]$ and $\sigma(\ln b_{\Delta,\mathrm{WL}})$, which relate to the mean and the width of the estimated mass bias distribution (see Section 7.8.3).

Cluster	$M_{200\mathrm{c}}^{\mathrm{biased,ML}}$ $[10^{14}\mathrm{M}_{\odot}]$	$\hat{b}_{200\mathrm{c,WL}}$	$\sigma(\ln b_{200\mathrm{c,WL}})$	$M_{500\mathrm{c}}^{\mathrm{biased,ML}}$ $[10^{14}\mathrm{M}_{\odot}]$	$\hat{b}_{500\mathrm{c,WL}}$	$\sigma(\ln b_{500\mathrm{c,WL}})$
SPT-CL $J0156{-}5541$	$4.5^{+3.5}_{-2.9} \pm 1.0 \pm 0.5$	0.88 ± 0.02	0.35 ± 0.03	$3.1^{+2.5}_{-2.1} \pm 0.7 \pm 0.3$	0.92 ± 0.03	0.28 ± 0.05
SPT-CL $J0205{-}5829$	$0.1^{+2.8}_{-2.4} \pm 0.5 \pm 0.0$	0.76 ± 0.03	0.41 ± 0.05	$0.1^{+1.9}_{-1.6} \pm 0.3 \pm 0.0$	0.79 ± 0.03	0.41 ± 0.04
SPT-CL $J0313{-}5334$	$2.8^{+3.3}_{-2.4} \pm 1.1 \pm 0.3$	0.86 ± 0.03	0.44 ± 0.04	$1.9^{+2.4}_{-1.7} \pm 0.8 \pm 0.2$	0.83 ± 0.03	0.37 ± 0.05
SPT-CL $J0459{-}4947$	$4.4^{+6.8}_{-4.4} \pm 1.5 \pm 0.5$	0.85 ± 0.05	0.51 ± 0.08	$3.0^{+5.0}_{-3.0} \pm 1.1 \pm 0.4$	0.79 ± 0.05	0.43 ± 0.10
SPT-CL $J0607{-}4448$	$0.6^{+3.4}_{-2.2} \pm 0.7 \pm 0.1$	0.86 ± 0.03	0.46 ± 0.04	$0.4^{+2.4}_{-1.5} \pm 0.4 \pm 0.0$	0.82 ± 0.04	0.45 ± 0.06
SPT-CL $J0640{-}5113$	$6.6^{+5.1}_{-4.5} \pm 1.1 \pm 0.7$	0.93 ± 0.03	0.27 ± 0.08	$4.6^{+3.8}_{-3.2} \pm 0.8 \pm 0.5$	0.85 ± 0.04	0.37 ± 0.05
SPT-CL $J2040{-}4451$	$16.4^{+5.8}_{-5.7} \pm 1.6 \pm 1.9$	0.89 ± 0.04	0.44 ± 0.06	$12.0^{+4.5}_{-4.4} \pm 1.3 \pm 1.4$	0.74 ± 0.04	0.48 ± 0.06
SPT-CL $J2341{-}5724$	$5.7^{+3.9}_{-3.5} \pm 1.1 \pm 0.6$	0.88 ± 0.03	0.35 ± 0.04	$4.0^{+2.9}_{-2.5} \pm 0.8 \pm 0.4$	0.87 ± 0.03	0.25 ± 0.05

Table 7.7 – As Table 7.6, but for the analysis centring the shear profiles around the SZ centres.

Cluster	$M_{200c}^{\mathrm{biased,ML}}$ $[10^{14}\mathrm{M}_{\odot}]$	$\hat{b}_{200c,\mathrm{WL}}$	$\sigma(\ln b_{200c,\mathrm{WL}})$	$M_{500c}^{\mathrm{biased,ML}}$ $[10^{14}\mathrm{M}_{\odot}]$	$\hat{b}_{500c,\mathrm{WL}}$	$\sigma(\ln b_{500c,\mathrm{WL}})$
SPT-CL $J0156-5541$	$3.9^{+3.4}_{-2.8} \pm 1.1 \pm 0.4$	0.74 ± 0.02	0.41 ± 0.04	$2.7^{+2.5}_{-1.9} \pm 0.8 \pm 0.3$	0.73 ± 0.02	0.36 ± 0.04
SPT-CL $J0205-5829$	$0.3^{+3.1}_{-2.3} \pm 0.5 \pm 0.0$	0.76 ± 0.03	0.38 ± 0.05	$0.2^{+2.2}_{-1.6} \pm 0.4 \pm 0.0$	0.72 ± 0.03	0.40 ± 0.05
SPT-CL $J0313-5334$	$4.3^{+3.8}_{-3.1} \pm 1.2 \pm 0.4$	0.80 ± 0.03	0.33 ± 0.06	$3.0^{+2.8}_{-2.2} \pm 0.8 \pm 0.3$	0.76 ± 0.03	0.34 ± 0.05
SPT-CL $J0459-4947$	$6.9^{+7.0}_{-5.7} \pm 1.7 \pm 0.8$	0.83 ± 0.07	0.49 ± 0.12	$4.9^{+5.3}_{-4.1} \pm 1.2 \pm 0.6$	0.67 ± 0.06	0.65 ± 0.09
SPT-CL $J0607-4448$	$2.4^{+4.0}_{-2.5} \pm 1.0 \pm 0.3$	0.76 ± 0.04	0.23 ± 0.11	$1.7^{+2.9}_{-1.7} \pm 0.7 \pm 0.2$	0.72 ± 0.03	0.34 ± 0.07
SPT-CL $J0640-5113$	$3.4^{+5.1}_{-3.4} \pm 1.0 \pm 0.4$	0.66 ± 0.03	0.56 ± 0.05	$2.3^{+3.7}_{-2.3} \pm 0.7 \pm 0.3$	0.70 ± 0.03	0.36 ± 0.07
SPT-CL $J0646-6236$	$10.8^{+4.0}_{-3.9} \pm 1.1 \pm 1.1$	0.78 ± 0.02	0.41 ± 0.03	$7.6^{+2.9}_{-2.8} \pm 0.8 \pm 0.7$	0.78 ± 0.02	0.39 ± 0.03
SPT-CL $J2040-4451$	$15.7^{+5.8}_{-5.8} \pm 1.5 \pm 1.8$	0.77 ± 0.04	0.40 ± 0.07	$11.5^{+4.5}_{-4.4} \pm 1.2 \pm 1.3$	0.71 ± 0.04	0.47 ± 0.07
SPT-CL $J2341-5724$	$3.8^{+3.8}_{-3.0} \pm 1.0 \pm 0.4$	0.71 ± 0.03	0.46 ± 0.04	$2.6^{+2.7}_{-2.1} \pm 0.7 \pm 0.3$	0.70 ± 0.03	0.41 ± 0.05

7.8.3 Estimation of the weak lensing mass modelling bias

Weak lensing mass estimates can suffer from systematic biases caused by deviations of the cluster from an NFW profile, triaxial or complex mass distributions (e.g. due to mergers), both correlated and uncorrelated large scale structure, and miscentering of the fitted shear profile. The measured weak lensing mass $M_{\Delta,\mathrm{WL}}$ at an overdensity Δ is typically smaller than the true mass of the halo $M_{\Delta,\mathrm{halo}}$ by a factor

$$b_{\Delta,\mathrm{WL}} = \frac{M_{\Delta,\mathrm{WL}}}{M_{\Delta,\mathrm{halo}}} \,. \tag{7.23}$$

This bias also depends on the specific properties of the sample like mass and redshift and the measurement setup regarding the employed concentration–mass relation and radial fitting range.

In this study, we obtain an estimate for the weak lensing mass bias distribution following the method described in Sommer et al. (2022). They show that the traditional, simplifying assumption of a log-normal bias distribution according to

$$\ln\left(\frac{M_{\Delta,\mathrm{WL}}}{M_{\Delta,\mathrm{halo}}}\right) \sim \mathcal{N}(\mu,\sigma^2) \tag{7.24}$$

is a suitable choice in absence of miscentering. Here, $\mathcal{N}(\mu,\sigma^2)$ is the log-normal distribution with expectation value $\mu = \langle \ln b_{\Delta,\mathrm{WL}} \rangle$ and variance σ^2. The expectation value μ in log-space translates to a measure of the bias in linear space via the estimator

$$\hat{b}_{\Delta,\mathrm{WL}} = \exp[\langle \ln b_{\Delta,\mathrm{WL}} \rangle] \,. \tag{7.25}$$

Following Sommer et al. (2022), we use snapshots of the Millennium XXL simulations (MXXL, Angulo et al., 2012) at redshift $z = 1$ to estimate the weak lensing mass bias distribution. We obtain an estimate for each cluster individually by incorporating certain cluster properties. Firstly, we use all haloes in the MXXL simulations with a halo mass within 2σ of the SZ-mass (see Table 7.1). Their mass distributions are projected along three mutually orthogonal axes increasing the effective sample size. Note that we do include a line-of-sight integration length of $200\,h^{-1}$ Mpc and not the full line-of-sight. Consequently, this method takes into account only correlated but not uncorrelated large-scale structure. The projected mass distributions of the massive haloes serve to calculate the shear and convergence fields on a grid with four arcsecond resolution. We convert the shear to the reduced shear using the same average lensing efficiency as in the respective cluster observations. This reduced shear field is azimuthally averaged in the same range and bins as in the cluster analysis to obtain a reduced shear profile. As the centre, we use either the 3D halo centre (most bound particle) or an offset centre drawn from an empirical miscentering distribution. We add noise to the reduced shear profile in each radial bin matching the corresponding uncertainties of the actual cluster tangential reduced shear estimates. We then obtain a weak lensing mass estimate by fitting the tangential reduced shear profile with an NFW profile, analogous to the analysis in our actual cluster observations. Subsequently, the comparison of the obtained weak lensing mass with the true halo mass provides the estimate for the weak lensing mass bias distribution for our specific setup. The full probability distribution $P(M_{\Delta,\mathrm{WL}}|M_{\Delta,\mathrm{halo}})$ is modelled with the help of Baysian statistics as described in Sommer et al. (2022), where the SZ-derived mass estimates ($M_{200c,\mathrm{SZ}}$ and $M_{500c,\mathrm{SZ}}$) from B19 serve as a prior for the mass estimation.

We incorporate miscentering into the estimation of the weak lensing mass bias distribution by applying an offset in a random direction before obtaining the reduced shear profile and subsequently fitting the masses. The offset is drawn from a miscentering distribution derived from the Magneticum Pathfinder Simulation (Dolag et al., 2016) measuring the offset between X-ray centroids (or SZ peaks) from the simulation as a proxy for the centre and the position of the most bound particle (see S21, for a detailed description). Note that the log-normal assumption does not hold anymore for the weak lensing mass bias distribution in case of miscentering. However, the deviation is at the 3-5 per cent level. Therefore, we can still obtain meaningful estimates of the mean bias and scatter from a log-normal fit.

We find that the weak lensing mass bias distribution is nearly independent of mass within the 2σ bounds of the given SZ-derived mass of the respective clusters. Thus, we average the bias and scatter over this mass range and report the results in Tables 7.6 and 7.7. We find that the clusters exhibit a weak lensing mass bias $\hat{b}_{\Delta,\mathrm{WL}}$ between 0.74 and 0.92 in the presence of miscentering (using X-ray centres) with a scatter σ between 0.25 and 0.48 regarding the weak lensing masses M_{500c}. On average the masses computed with the X-ray centre are slightly less biased with a slightly smaller scatter when compared to the masses computed with the SZ centre (see Tables 7.6 and 7.7). This suggests that the X-ray centres are a bit more robust.

Note that we have derived these estimates from the MXXL snapshots at $z = 1$. S21 report weak lensing mass bias estimates, which are interpolated between results at $z = 0.25$ and $z = 1$ according to the given cluster redshift. We find that the results using $z = 0.25$ snapshots are very similar to those at $z = 1$. This suggests that there is no strong redshift evolution, and we decide to report the results from the $z = 1$ snapshots, closest to the redshift range of our sample.

As a cross-check for the mass modelling correction, we compare the mass constraints derived for the analyses using the X-ray centres versus SZ centres in Figure 7.11, applying approximate corrections for the expected mass bias. While the X-ray centred analysis yields slightly lower corrected masses on average, the difference is not significant given the large statistical uncertainties.

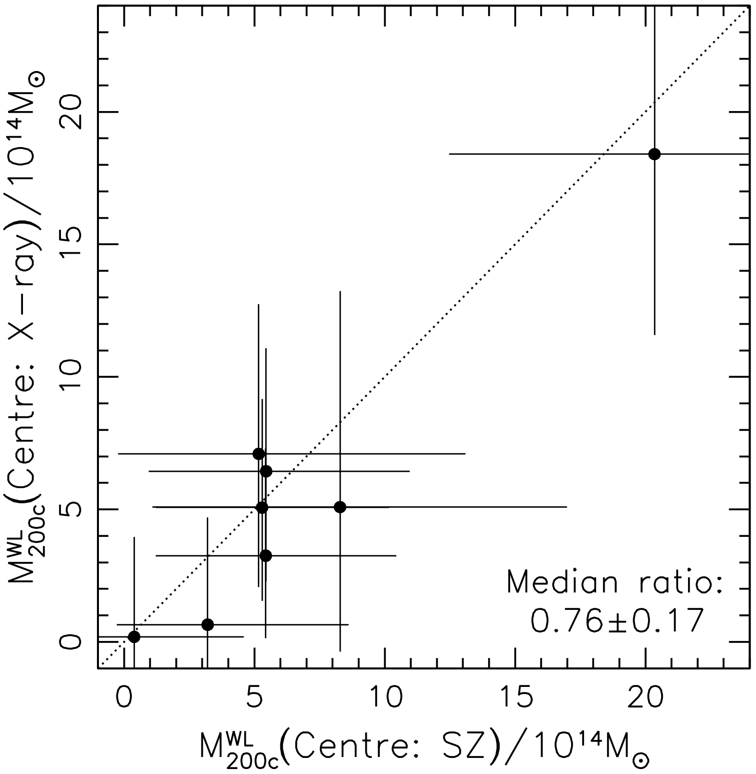

Figure 7.11 – Best-fitting weak lensing mass estimates measured around the X-ray centres versus the SZ centres, applying an approximate correction for statistical mass modelling biases as $M^{\mathrm{WL}}_{200\mathrm{c}} = M^{\mathrm{biased,ML}}_{200\mathrm{c}}/\hat{b}_{200\mathrm{c,WL}}$. The errors indicate the statistical uncertainties given in Tables 7.6 and 7.7. They do not include the additional mass-modelling scatter inferred from the simulations.

7.9 Constraints on the SPT observable-mass scaling relation

In this section, we combine the weak lensing mass measurements of our nine high-redshift SPT clusters (henceforth sample HST-9) with results for clusters at lower redshifts, namely weak lensing mass measurements of 19 SPT clusters with redshifts $0.29 \leq z \leq 0.61$ based on Magellan/Megacam observations (D19, sample Megacam-19) and of 30 SPT clusters with redshifts $0.58 \leq z \leq 1.13$ based on *HST* observations (S21, sample HST-30). We use this sample of in total 58 SPT clusters (we refer to it as HST-39 + Megacam-19) with weak lensing mass measurements to constrain the SPT observable-mass scaling relation. Thereby, we extend the previous studies (S18; D19; B19; S21) out to redshifts of up to $z = 1.7$.

7.9.1 Likelihood formalism for the observable-mass scaling relation

The SPT observable-mass scaling relation is based on the detection significance ξ as a mass proxy. However, during the measurement, ξ is maximised with three free parameters (right ascension, declination, and the core radius θ_{c}). Consequently, the average detection significance $\langle\xi\rangle$ measured across many noise realisations will be higher than the unbiased detection significance ζ (Vanderlinde et al., 2010). Their relation can be quantified from simulations as (Vanderlinde et al., 2010)

$$\langle\xi\rangle \approx \sqrt{\zeta^2+3}\,. \tag{7.26}$$

The scatter in the relation between ζ and ξ is given by a Gaussian of unit width so that we have

$$P(\xi|\zeta) = \mathcal{N}\left(\sqrt{\zeta^2+3}, 1\right)\,. \tag{7.27}$$

Further following Vanderlinde et al. (2010), we define the scaling relation between the unbiased detection significance ζ and the mass M_{500c} as a power-law in mass and the dimensionless Hubble parameter $E(z) \equiv H(z)/H_0$:

$$\langle\ln\zeta\rangle = \ln\left[\gamma_{\mathrm{field}} A_{\mathrm{SZ}} \left(\frac{M_{500c}}{3\times10^{14}\mathrm{M}_\odot/h}\right)^{B_{\mathrm{SZ}}} \left(\frac{E(z)}{E(0.6)}\right)^{C_{\mathrm{SZ}}}\right]\,, \tag{7.28}$$

where A_{SZ}, B_{SZ}, and C_{SZ} parametrise the normalisation, slope, and redshift evolution, respectively, and γ_{field} characterises the effective depth of the individual SPT fields. Since we want to constrain this relation with the help of weak lensing mass measurements, we additionally need to consider the relation between lensing mass and true mass (see Equation 7.23). We set $\Delta = 500c$ and omit this notation in this section for readability, so that the relation reads

$$\ln\langle M_{\mathrm{WL}}\rangle = \ln b_{\mathrm{WL}} + \ln M\,. \tag{7.29}$$

Combining both relations, we therefore obtain the joint relation

$$P\left(\begin{bmatrix}\ln\zeta\\ \ln M_{\mathrm{WL}}\end{bmatrix}|M,z\right) = \mathcal{N}\left(\begin{bmatrix}\langle\ln\zeta\rangle(M,z)\\ \langle\ln M_{\mathrm{WL}}\rangle(M,z)\end{bmatrix}, \Sigma_{\zeta-M_{\mathrm{WL}}}\right)\,, \tag{7.30}$$

where the covariance matrix $\Sigma_{\zeta-M_{\mathrm{WL}}}$ summarises how the logarithms of the observables ζ and M_{WL} scatter. It is given by

$$\Sigma_{\zeta-M_{\mathrm{WL}}} = \begin{pmatrix}\sigma^2_{\ln\zeta} & \rho_{\mathrm{SZ-WL}}\sigma_{\ln\zeta}\sigma_{\ln M_{\mathrm{WL}}}\\ \rho_{\mathrm{SZ-WL}}\sigma_{\ln\zeta}\sigma_{\ln M_{\mathrm{WL}}} & \sigma^2_{\ln M_{\mathrm{WL}}}\end{pmatrix}\,. \tag{7.31}$$

The quantities $\sigma_{\ln\zeta}$ and $\sigma_{\ln M_{\mathrm{WL}}}$ denote the widths of the normal distributions, which characterise the intrinsic scatter in $\ln\zeta$ and $\ln M_{\mathrm{WL}}$, respectively. They are assumed to be independent of redshift and mass. Correlated scatter between the SZ and the weak lensing observable is described by the correlation coefficient $\rho_{\mathrm{SZ-WL}}$.

We note that the weak lensing observable is not the mass M_{WL}, but rather the tangential reduced shear g_{t}. Therefore, we calculate the likelihood for each cluster according to

$$\begin{aligned} P(g_{\mathrm{t}}|\xi, z, \boldsymbol{p}) = \iiint & \mathrm{d}M \, \mathrm{d}\zeta \, \mathrm{d}M_{\mathrm{WL}} \\ & \times \left[P(\xi|\zeta) P(g_{\mathrm{t}}|M_{\mathrm{WL}}, N_{\mathrm{source}}(z), \boldsymbol{p}) \right. \\ & \left. \times \, P(\zeta, M_{\mathrm{WL}}|M, z, \boldsymbol{p}) P(M|z, \boldsymbol{p}) \right] . \end{aligned} \tag{7.32}$$

This equation is analogous to the definitions in D19, B19, and S21, which we refer the reader to for further details. Here, $P(\zeta, M_{\mathrm{WL}}|M, z, \boldsymbol{p})$ is the joint scaling relation introduced in Equation (7.30) and $P(M|z, \boldsymbol{p})$ denotes the halo mass function by Tinker et al. (2008). It represents a weighting required to account for Eddington bias. The vector $\boldsymbol{p}$ summarises the astrophysical and cosmological modelling parameters. Furthermore, the source redshift distribution is given by $N_{\mathrm{source}}(z)$ and the terms $P(\xi|\zeta)$ and $P(g_{\mathrm{t}}|M_{\mathrm{WL}}, N_{\mathrm{source}}(z), \boldsymbol{p})$ contain information about the intrinsic scatter and observational uncertainties in the observables. Finally, the total log-likelihood corresponds to the sum of logarithms of the individual cluster likelihoods

$$\ln \mathcal{L} = \sum_{j=1}^{N_{\mathrm{bin}}} \sum_{i=1}^{N_{\mathrm{cl}}} \ln P(g_{\mathrm{t}}|\xi, z, \boldsymbol{p}) \, , \tag{7.33}$$

where $N_{\mathrm{cl}} = 58$ is the total number of clusters considered to obtain constraints on the SPT observable-mass scaling relation and N_{bin} is the number of radial bins for the reduced shear profiles. Note that we naturally account for the selection function of the sample because we apply the established likelihood formalism only to the clusters from the SPT-SZ survey. Furthermore, the subsamples of clusters with weak lensing measurements were assembled randomly, independent of their lensing signal, so that the likelihood function is complete and does not suffer from biases due to weak lensing selections (D19; B19).

We cannot constrain all parameters in this relation equally well with the given weak lensing mass measurements. In particular, our data set does not allow for meaningful constraints for B_{SZ} and $\sigma_{\ln\zeta}$ (S21). Thus, we introduce the following priors. Regarding the slope parameter, we use a Gaussian prior $B_{\mathrm{SZ}} \sim \mathcal{N}(1.53, 0.1^2)$, which is motivated by the cosmological study in B19. We assume $\sigma_{\ln\zeta} \sim \mathcal{N}(0.13, 0.13^2)$ as used by de Haan et al. (2016) and derived based on mock observations of hydrodynamic simulations from Le Brun et al. (2014). Additionally, we implement the weak lensing mass modelling bias and corresponding scatter obtained in Section 7.8.3 and adopt a flat prior for the correlation coefficient, i.e., $\rho_{\mathrm{SZ-WL}} \in [-1, 1]$.

We conduct the likelihood analysis with an updated version of the pipeline used in B19 and S21, which is embedded in the `COSMOSIS` framework (Zuntz et al., 2015) and where the likelihood is explored with the MULTINEST sampler (Feroz et al., 2009). The full, updated pipeline will be made available in a future publication by Bocquet et al. (in prep.).

We test the likelihood machinery with mock cluster data. We simulate an SPT cluster catalogue with SZ detection significances and redshifts. We chose a number density and shape noise resembling the optical observations and implement an average source redshift distribution to simulate weak lensing cluster observations. These serve as a basis to generate mock shear profiles, which we use as input for the likelihood analysis. Running the analysis on these mock data, we find that the resulting constraints on the scaling relation meet the expectation, thereby providing a valuable consistency check of our pipeline.

7.9.2 Redshift evolution of the ζ-mass relation

We apply the likelihood setup to our full cluster sample of 58 clusters with weak lensing mass measurements to constrain the ζ–mass relation. We present our results in Table 7.8. With our analysis, we constrain the scaling relation parameters as $A_{\mathrm{SZ}} = 1.76 \pm 0.20$ and $C_{\mathrm{SZ}} = 2.13 \pm 1.04$, while the parameter B_{SZ} is dominated by the prior. Figure 7.12 displays the redshift evolution of the scaling relation, now for the first time extending out to redshifts up to $z \sim 1.7$ (red band, result of the fiducial analysis). For comparison, we show the constraints from S21 based on the HST-30 + Megacam-19 samples in blue, demonstrating that our findings in this study are fully consistent with these previous results. This was expected because we added only nine clusters to the previously used sample. In addition, our clusters are at the high-redshift end, which increases statistical uncertainties compared to the clusters at lower and intermediate redshifts. Furthermore, the diagonally hatched region represents the scaling relation constraints from B19, who analysed weak lensing measurements from the Megacam-19 sample and 13 clusters from S18 in combination with X-ray measurements and cluster abundance information. They marginalised over cosmological parameters for a flat $\nu\Lambda$CDM cosmology. For comparison, we also show results computed for a joint analysis of *Planck* primary CMB anisotropies (TT,TE,EE+low-E, Planck Collaboration et al., 2020a) and the SPT cluster abundance as the vertically hatched region. Again, this includes a marginalisation over cosmological parameters assuming a flat $\nu\Lambda$CDM cosmology. This analysis does not incorporate any weak lensing mass measurements.

As also found in S21, we observe an offset between the red and vertically hatched regions implying that the mass scale preferred from our analysis with the weak lensing data sets is lower than the mass scale that would be consistent with the *Planck* $\nu\Lambda$CDM cosmology.

Analogous to S21, we want to check if the simple scaling relation model is applicable over the full, wide redshift range investigated here by performing a binned analysis, where the amplitude A_{SZ} is allowed to vary individually for each bin. There-

Table 7.8 – Fit results for the parameters of the ζ–mass relation, analogously to Table 12 in S21, now including the weak lensing measurements for the nine high-z SPT clusters from this work. SPTcl ($\nu\Lambda$CDM) denotes the results from the B19 study, which combined SPT cluster counts with weak lensing and X-ray mass measurements. The results from the analysis denoted as *Planck* + SPTcl ($\nu\Lambda$CDM) are based on a combination of measurements from the *Planck* CMB anisotropies (TT,TE,EE+low-E, Planck Collaboration et al., 2020a) and SPT cluster counts.

Parameter	Prior	HST-39 + Megacam-19		SPTcl ($\nu\Lambda$CDM)	*Planck* + SPTcl ($\nu\Lambda$CDM)
		fiducial	binned	(B19)	(no WL mass calibration)
$\ln A_{\rm SZ}$	flat	1.76 ± 0.20	–	1.67 ± 0.16	$1.27^{+0.08}_{-0.15}$
$\ln A_{\rm SZ}(0.25 < z < 0.5)$	flat	–	1.72 ± 0.24	–	–
$\ln A_{\rm SZ}(0.5 < z < 0.88)$	flat	–	1.48 ± 0.34	–	–
$\ln A_{\rm SZ}(0.88 < z < 1.2)$	flat	–	2.04 ± 0.52	–	–
$\ln A_{\rm SZ}(1.2 < z < 1.7)$	flat	–	1.98 ± 0.86	–	–
$C_{\rm SZ}$	flat/fixed	2.13 ± 1.04	1.78	$0.63^{+0.48}_{-0.30}$	$0.73^{+0.17}_{-0.19}$
Prior-dominated parameters in our analysis:					
$B_{\rm SZ}$	$\mathcal{N}(1.53, 0.1^2)$	1.56 ± 0.09	1.56 ± 0.09	1.53 ± 0.09	1.68 ± 0.08
$\sigma_{\ln\zeta}$	$\mathcal{N}(0.13, 0.13^2)$	$0.16^{+0.06}_{-0.13}$	$0.15^{+0.04}_{-0.13}$	0.17 ± 0.08	$0.16^{+0.07}_{-0.12}$

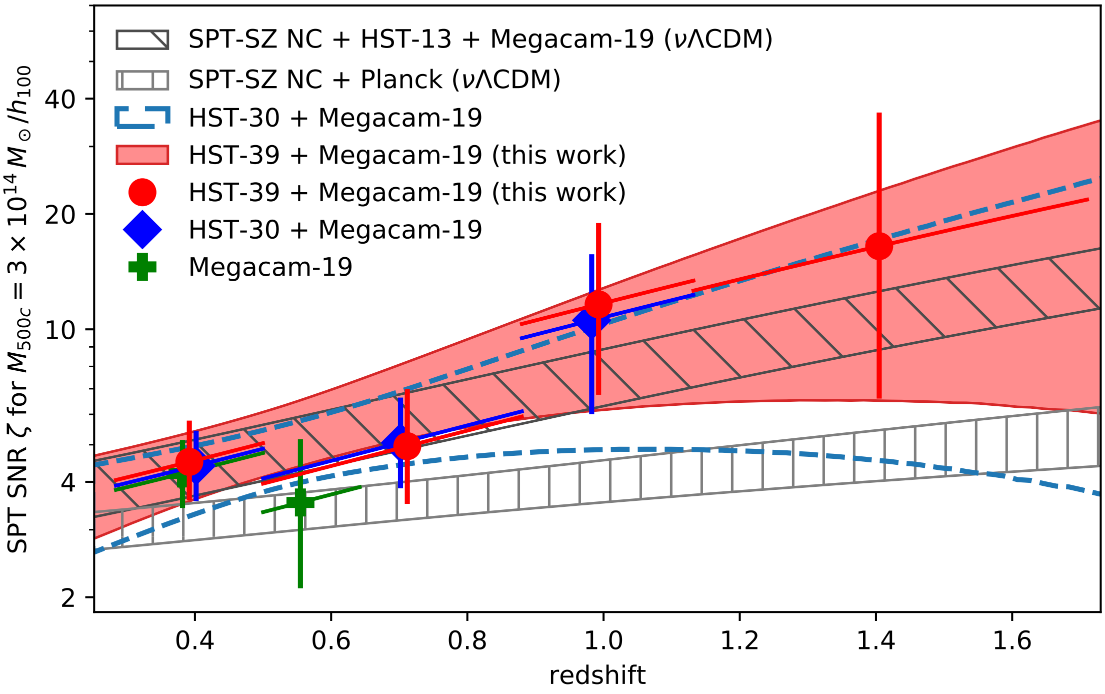

Figure 7.12 – Evolution of the unbiased SPT detection significance ζ at the pivot mass $3 \times 10^{14}\,\mathrm{M}_\odot/h_{100}$ as a function of redshift. The red band indicates the main result of this work. The blue dashed curves show the results using only the weak lensing data from the S21 analysis for comparison. The red and blue data points represent the corresponding binned analysis. They are placed in the centre of the bins. Horizontal error bars represent the bin widths. The redshift evolution parameter is fixed to $C_{\mathrm{SZ}} = 1.78$ for the binned analysis. The diagonally hatched and vertically hatched bands correspond to the relations from the B19 study and the SPT cluster counts in combination with a flat *Planck* $\nu\Lambda$CDM cosmology, respectively. The displayed uncertainties correspond to the 68 per cent credible interval (bands for full relation and error bars for binned analysis).

fore, we add a bin of $1.2 < z < 1.7$ to the bins that were already used before (namely $0.25 < z < 0.5$, $0.5 < z < 0.88$, and $0.88 < z < 1.2$). We keep the redshift evolution parameter fixed to the value from the fiducial analysis in S21 at $C_{\mathrm{SZ}} = 1.78$. From Figure 7.12, we can see that the results in our new high-redshift bin are consistent with the scaling relation results from the full unbinned analysis. Additionally, we find that our results in the lower redshift bins are very similar to the results from the binned analysis in S21. This is also expected because the bins contain the same clusters except for SPT-CL $J0646{-}6236$, which was added to the third redshift bin and only causes a minor shift.

7.10 Discussion

7.10.1 Source selection and scatter in the weak lensing mass constraints

Weak lensing studies of galaxy clusters with ever higher redshifts face the increasingly difficult challenge to identify background galaxies carrying the lensing signal (e.g. Mo et al., 2016; Jee et al., 2017; Finner et al., 2020). In a simplified consideration, the signal-to-noise ratio of a lensing measurement scales with the product of the average geometric lensing efficient $\langle\beta\rangle$ and the square root of the source number density $\sqrt{n}$. For comparison purposes, we define $S/N_{\mathrm{selection}} = \langle\beta\rangle\sqrt{n}$[17]. The average geometric lensing efficiency is tied to the purity of the source sample, that is, the fraction of true background source galaxies. A higher purity is desirable as it also increases the average geometric lensing efficiency. At the same time, cuts to identify true background source galaxies should not be too rigorous as this might reduce the overall source density potentially at the cost of also excluding true background galaxies. Additionally, a lower source density is more subject to shot noise, consequently reducing the lensing signal-to-noise ratio.

Some previous weak lensing studies were conducted with *HST*/WFC3 in infrared bands to measure masses of clusters at redshifts $z \gtrsim 1.5$. They introduced varying techniques to select source galaxies for the lensing measurements. For their weak lensing analysis of cluster SpARCS1049+56 at redshift $z = 1.71$, Finner et al. (2020) select sources via a magnitude cut of $H_{\mathrm{F160W}} > 25.0\,\mathrm{mag}$ and specific shape cuts aiming to remove galaxies with high uncertainty in the ellipticity measurement and objects that are too small or too elongated to be galaxies. Applying this method to their observations, they achieve a source density of $105\,\mathrm{arcmin}^{-2}$ and estimate an average geometric lensing efficiency of $\langle\beta\rangle = 0.107$. This translates into a signal-to-noise ratio of $S/N_{\mathrm{selection}} \sim 1.10$. Alternatively, Jee et al. (2017) perform a weak lensing study of clusters SPT-CL *J*2040−4451 and IDCS J1426+3508 at redshifts $z = 1.48$ and $z = 1.75$, respectively (for a detailed comparison of their results to our results for SPT-CL *J*2040−4451, see Section 7.10.2). They select source galaxies requiring that they are bluer than the cluster red-sequence combined with a bright magnitude and shape measurement uncertainty cut. They obtain a source density of $\sim 240\,\mathrm{arcmin}^{-2}$ with an average lensing efficiency of $\langle\beta\rangle = 0.086$ and $\langle\beta\rangle = 0.120$ for IDCS J1426+3508 and SPT-CL *J*2040−4451, respectively. This corresponds to $S/N_{\mathrm{selection}} \sim 1.33$ and $S/N_{\mathrm{selection}} \sim 1.86$, respectively.

Mo et al. (2016) conducted a weak lensing study of IDCS J1426+3508 prior to Jee et al. (2017) using *HST*/ACS and *HST*/WFC3 data from the bands F606W, F814W, and F160W. They measure galaxy shapes with the F606W imaging select-

---

[17] In principle, the signal-to-noise ratio of a lensing measurement also depends on other parameters such as cluster mass and fit range. We define $S/N_{\mathrm{selection}}$ to represent how the source selection affects the lensing signal-to-noise ratio and compare this quantity for different studies.

ing source galaxies with $24.0 < V_{\mathrm{F606W}} < 28.0$ (the latter is roughly the 10σ depth limit of their observations), $0\farcs27 < \mathrm{FWHM} < 0\farcs9$ (FWHM is measured with `Source Extractor`. Too large/small galaxies are excluded either because they are likely foreground galaxies or to avoid PSF problems, respectively), and $I_{\mathrm{F814W}} - H_{\mathrm{F160W}} < 3.0$ (to exclude cluster red-sequence galaxies). They achieve an average lensing efficiency of $\langle\beta\rangle = 0.086$ at a source density of $89\,\mathrm{arcmin}^{-2}$, resulting in $S/N_{\mathrm{selection}} \sim 0.81$.

In conclusion, both NIR studies (Jee et al., 2017; Finner et al., 2020) achieve higher source densities, but lower average geometric lensing efficiencies than our study, which has an average source density of $13.3\,\mathrm{arcmin}^{-2}$ and an average geometric lensing efficiency of $\langle\beta\rangle = 0.244$, and thus $S/N_{\mathrm{selection}} \sim 0.89$. The studies by Jee et al. (2017) and Finner et al. (2020) owe the high signal-to-noise ratios mainly to very deep observations enabling high source densities. In contrast, our study focuses on a high purity as visible in Figures 7.5 and 7.8, which display that we select almost only high-z sources at $z \gtrsim 2$ with high lensing efficiency, while keeping the contamination of foreground, cluster, and near background galaxies low. This strategy results in an average lensing efficiency, which is more than twice as high, and it helps to keep systematic uncertainties low for several reasons. Firstly, excluding galaxies at the cluster redshift minimises uncertainties related to the correction for cluster member contamination. Secondly, galaxies in the near background are located in a regime where $\beta(z)$ is a steep function of z. Thus, systematic redshift uncertainties lead to larger systematic uncertainties in $\langle\beta\rangle$ than for the distant background galaxies selected in our approach. Finally, the efficient removal of foreground galaxies minimises the impact that catastrophic redshift outliers scattering between low and high redshifts have on the computation of $\langle\beta\rangle$ (see S18; R20). While we find that the uncertainties in the redshift distribution (R20 versus R15_fix comparison and variations between CANDELS/3D-HST fields) dominate the systematic error budget (see Table 7.3), our comparatively low number density introduces high statistical uncertainties, which (together with other statistical uncertainties) outweigh the systematic ones in our current analysis. However, we stress that our approach, which aims to limit systematic uncertainties by using data of moderate depth and applying a stringent background selection, could directly be applied to similar data sets obtained for larger cluster samples.

In combination with the considerable measurement uncertainties and the substantial expected intrinsic scatter (see Section 7.8.3), the best-fitting cluster mass estimates in our study are, therefore, expected to scatter significantly. This likely explains the relatively low mass estimate of SPT-CL $J0205{-}5829$, which is undetected in the weak lensing data despite its high SZ-inferred mass, and the comparably high best-fitting mass estimate for SPT-CL $J2040{-}4451$ (see next section).

7.10.2 Cluster SPT-CL J2040−4451

The very high mass result for cluster SPT-CL J2040−4451 of $M_{200c}^{\mathrm{biased,ML}} = 16.4^{+5.8}_{-5.7} \pm 1.6 \pm 1.9 \times 10^{14}\,\mathrm{M}_{\odot}$ (for comparability the value is not corrected for mass modelling bias, because such a correction is not performed in Jee et al., 2017) presents a contrast to the weak lensing mass constraint reported by Jee et al. (2017) ($M_{200} = 8.6^{+1.7}_{-1.4} \times 10^{14}\,\mathrm{M}_{\odot}$), which is almost a factor of 2 lower. Jee et al. (2017) obtain their weak lensing mass constraint from *HST*/WFC3 imaging in F105W, F140W, and F160W. They fit a spherical NFW profile assuming the mass–concentration relation of Dutton & Macciò (2014) and centred at their measured X-ray peak position (*Chandra* data) excluding sources within a minimum radius $r_{\mathrm{min}} = 25\,\mathrm{arcsec}$, corresponding to 218 kpc at the cluster redshift. Since the WFC3/IR covers an area, which is about 2.4 times smaller than for the ACS/WFC in our analysis, the measurements by Jee et al. (2017), therefore, generally focus on smaller scales of the cluster.

In comparison to that, we measure the weak lensing mass assuming the concentration–mass relation by Diemer & Kravtsov (2015) with updated parameters from Diemer & Joyce (2019), we centre the fit around the X-ray centroid from McDonald et al. (2017) (8.1 arcsec distance to X-ray peak employed by Jee et al., 2017), and we use galaxies outside a minimum radius of $r_{\mathrm{min}} = 500\,\mathrm{kpc}$. We exclude any scales smaller than this to minimize systematic mass modelling uncertainties and the impact of a potential residual cluster member contamination (below the detection limit). Since the X-ray peak and centroid positions are relatively close to each other, it is reasonable to compare the weak lensing mass results without applying the mass modelling correction.

The largest difference between the Jee et al. (2017) study and ours is the source selection strategy. Jee et al. (2017) base their work on imaging, which is significantly deeper (with a limiting magnitude of F140W $\sim 28\,\mathrm{mag}$) than ours but limited to a smaller field of view. Their red-sequence-motivated selection of background galaxies (galaxies at F105W − F140W < 0.5 are selected) results in a source number density of $\sim 240\,\mathrm{arcmin}^{-2}$ with a fraction of non-background sources (with $z \leq z_{\mathrm{cluster}}$) of approximately 45 per cent. Additionally, the inclusion of scales at $218 < r < 500\,\mathrm{kpc}$ likely shrinks statistical uncertainties since the lensing signal is high in the inner regions of the cluster. This allows them, in turn, to achieve small uncertainties of the weak lensing mass constraints (see Section 7.10.1). However, the inclusion of such core regions usually increases the intrinsic scatter and mass modelling uncertainties (see also Section 7.8.3).

Note that the selection strategy is tailored only to remove red cluster members residing on the red-sequence. Faint, blue cluster member contamination could still introduce systematic biases in the lensing measurements (e.g. Broadhurst et al., 2005; Okabe et al., 2010a; Applegate et al., 2014; Melchior et al., 2017; Medezinski et al., 2018). Jee et al. (2017) discuss that the fraction of faint, blue cluster members increases with redshift, which is why they check their selection for cluster member contamination. Examining source density radial profiles and magnitude distributions of the source galaxies as compared to those in control fields, they conclude that it is negligible for their analysis.

Our more strict selection strategy for the background galaxies based on magnitudes/colours from four bands is contaminated by 17 to 20 per cent of non-background galaxies. The shallower data finally result in a source number density of 11.2 arcmin^{-2} for SPT-CL J2040−4451 so that our analysis exhibits substantially larger uncertainties in the weak lensing mass constraints. In the light of these uncertainties, our cluster mass results and the Jee et al. (2017) results differ only by $\sim 1.2\sigma$. However, we find that our weak lensing mass differs from the SZ-based (Table 7.1) and X-ray based masses ($M_{500} = 3.10^{+0.79}_{-0.47} \times 10^{14}\,\mathrm{M}_\odot$, McDonald et al., 2017) by 1.7σ and 1.8σ, respectively. We conclude that our mass constraint for SPT-CL J2040−4451 confirms the generally higher lensing mass by Jee et al. (2017), albeit with a higher statistical uncertainty.

Jee et al. (2017) report the detection of the cluster in their weak lensing mass map at the location $\alpha = 20^{\mathrm{h}}40^{\mathrm{m}}57\overset{\mathrm{s}}{.}85$ and $\delta = -44^\circ 51' 42\overset{''}{.}4$ with 6σ significance. In our mass map, we detect a peak at 3.4σ, with a separation of 6.6 arcsec from the location in Jee et al. (2017). While this offset is slightly larger than our estimate of the positional uncertainty derived using bootstrapping (see Table 7.5), we note that Sommer et al. (2022) found that bootstrapping substantially underestimates the true uncertainty. The peaks from both studies are close to the X-ray centroid position from McDonald et al. (2017) so that they are overall in agreement. We also note that the peak in our weak lensing mass reconstruction for SPT-CL J2040−4451 closely coincides with the X-ray centroid. Accordingly, the shear profile is approximately centered on the position that maximises the lensing signal. This likely scatters the result high, which is further exacerbated by the statistical mass bias correction.

Jee et al. (2017) state that given the mass function by Tinker et al. (2008) and cosmology constraints by Planck Collaboration et al. (2016a) only ~ 1 cluster of mass $M_{200} = 8.6 \times 10^{14}\,\mathrm{M}_\odot$ at this high redshift is expected to be found in the full sky. They argue that the existence of SPT-CL J2040−4451 could, therefore, challenge the ΛCDM cosmological model, even though they also state that an interpretation based on an individual cluster is difficult. Of course, a higher mass as reported here would be even less expected, but we emphasise that our study aims to provide mass constraints that are accurate on average for our sample of nine galaxy clusters. Out of these, SPT-CL J2040−4451 is the one with the highest best-fitting cluster mass estimate, so it appears likely that the mass estimate has scattered high. Together with the large statistical uncertainty, our result thus does not lead us to expect that the cluster poses a significant challenge to the ΛCDM model. On the contrary, based on our weak lensing measurements, the SPT cluster population is less massive than what one would expect in a *Planck* ΛCDM cosmology, also at very high redshifts (see Section 7.9).

7.11 Summary and conclusions

In this work, we studied the gravitational lensing signal of a sample of nine clusters with high redshifts $z \gtrsim 1.0$ in the SPT-SZ Survey. They all exhibit a strong SZ signal with a high SZ detection significance $\xi > 6.0$. We obtained weak lensing mass constraints from shape measurements of galaxies with high-resolution *HST*/ACS imaging in the F606W and F814W bands. With the help of additional *HST* imaging using WFC3/IR in F110W and VLT/FORS2 imaging in U_{HIGH}, we applied a strategy to photometrically select background galaxies, even for clusters at such challenging high redshifts.

Using updated photometric redshift catalogues computed by R20 for the CANDELS/3D-HST fields as a reference, we estimated the source redshift distribution and calculated the average geometric lensing efficiency applying the same selection criteria in the reference photometric redshift catalogues as in the cluster observations. We also added Gaussian noise to the reference catalogues if they were deeper than our cluster observations. We carefully investigated sources of systematic and statistical uncertainties for estimates of the average geometric lensing efficiency. We found consistent results in the HUDF field comparing our photometric measurements employing the algorithm LAMBDAR for adaptive aperture photometry and the S14 photometric measurements based on fixed aperture photometry. A comparison based on photometric and spectroscopic redshifts revealed a ~ 3 per cent difference in calculating the average geometric lensing efficiency, which we accounted for in the weak lensing analysis. Investigating further sources of systematic uncertainties, we identified that differences (e.g. depth, filters) between the CANDELS/3D-HST fields contribute the most to the systematic uncertainty in the source selection, contributing 8.6 per cent. The overall systematic uncertainty of the source redshift selection and calibration amounts to 12.9 per cent for the cluster mass scale.

We reconstructed the projected cluster mass distributions based on the shear measurements of the selected (preferentially background) galaxies. In the resulting mass maps, we detected two of the clusters with a peak at $S/N > 3$, four clusters with $S/N > 2$, and three clusters were not detected. We obtained weak lensing mass constraints by fitting the tangential reduced shear profiles with spherical NFW models, employing a fixed concentration–mass relation by Diemer & Kravtsov (2015) with updated parameters from Diemer & Joyce (2019). We reported statistical uncertainties from shape noise, uncorrelated large-scale structure projections, line-of-sight variations in the source redshift distribution, and uncertainties in the calibration of the U_{HIGH} band. We also estimated mass modelling biases using simulated clusters from the Millennium XXL simulations accounting for miscentering. Masses based on the X-ray centre are less biased and exhibit a slightly smaller scatter of the mass bias than masses obtained using SZ centres. This is consistent with findings in previous studies (e.g. Sommer et al., 2022, S21).

Our weak lensing mass result for SPT-CL $J2040{-}4451$ is notably higher in comparison with measurements from Jee et al. (2017), while for other clusters in the sample, we obtain lower weak lensing mass results than expected from the SZ-based mass. Our goal is to obtain mass constraints for our cluster sample that are accurate on average. In the additional light of large statistical uncertainties in our study, we conclude that our mass result for this cluster has likely scattered high. Thus, we do not expect that the cluster poses a significant challenge to the ΛCDM model.

Finally, we used the obtained weak lensing mass measurements in a joint analysis with measurements for clusters at lower (D19) and intermediate (S21) redshifts to constrain the scaling relation between the debiased SPT cluster detection significance ζ and cluster mass, thereby expanding the previous studies by B19 and S21 to higher redshifts $z > 1.2$. Our binned analysis of the redshift evolution of the ζ–mass scaling relation reveals that the new highest redshift bin at $1.2 < z < 1.7$ is consistent with the scaling relation behaviour predicted from lower redshifts. Our results for the full, unbinned analysis confirm previous findings where the mass scale preferred in an analysis including the weak lensing measurements is lower than the mass scale required for consistency with the *Planck* $\nu\Lambda$CDM cosmology presented in Planck Collaboration et al. (2020a).

In our pilot study, we developed an approach for weak lensing mass measurements of high-z clusters with well-controlled systematics. Our analysis has been limited by statistical uncertainties, but those could be reduced in the future via an application of the approach to a larger sample. Such extended samples have recently started to become available. Several cluster surveys have uncovered massive galaxy clusters at ever higher redshifts with a well-defined selection function, especially with the help of the SZ effect (e.g. Hilton et al., 2021; Bleem et al., 2020; Huang et al., 2020). Currently, eROSITA (Predehl et al., 2014) is conducting an X-ray survey of the sky expected to detect on the order of 100,000 clusters. These cluster samples form an excellent basis for constraints on cosmological parameters and dark energy properties. Upcoming surveys from *Euclid* (Laureijs et al., 2011), the *Nancy Grace Roman Space Telescope* (formerly known as WFIRST, Spergel et al., 2015), and the Vera C. Rubin Observatory (LSST Science Collaboration et al., 2009) will provide improved and critically required constraints on the cluster masses over a wide redshift range, where the exquisite depth of the *Nancy Grace Roman Space Telescope* will be particularly valuable for the very high-redshift regime. At the moment, however, pointed follow-up observations of individual massive, high-redshift clusters with high-resolution *HST* imaging are the best way to constrain cluster masses at high redshifts. Our study pioneers in these efforts with the first weak lensing study of a galaxy cluster sample with a well-defined selection function from the SPT-SZ survey extending to the highest redshifts from $z \sim 1$ up to $z \sim 1.7$. While the small sample size and limited depth of the data imply large statistical uncertainties, there also remain notable systematic uncertainties. The statistical uncertainties can be addressed by adding new weak lensing data of more high-redshift clusters. The statistical uncertainties still dominate over the systematic ones in this study. However, the systematic uncertainties need to be reduced in the future. Our study shows that the largest systematic uncertainty for lensing studies of high-redshift galaxy clusters arises from the calibration of the source redshift distribution. Here, surveys such as the planned *James Webb Space Telescope* Advanced Deep Extragalactic Survey[18] (JADES) will help to calibrate the redshift distributions, especially for high-redshift clusters, which are observed with deep imaging data. This survey will provide imaging and spectroscopy to unprecedented depth and infer photometric and spectroscopic redshifts over an area of 236 arcmin^2 in the GOODS-South and GOODS-North fields. Additionally, direct calibration methods and those utilizing the stacked redshift probability distribution functions of galaxies already show promising results and need to be further explored to help reduce systematic uncertainties in the redshift calibration (e.g. Euclid Collaboration et al., 2021). Furthermore, in-depth analyses of hydrodynamical simulations will help to better understand and reduce systematics due to the concentration–mass relation, the weak lensing mass modelling, and miscentering distribution uncertainties.

7.12 Appendix A: Comparison of S14 and LAMBDAR photometry

While we measure fluxes in our observations with the LAMBDAR software, we only have the S14 photometry available when we estimate the redshift distribution from the CANDELS/3D-HST fields. Therefore, we check how consistent we expect our measurements to be with the S14 photometry. We can perform this check on the region in the HUDF field, which we observed in the VLT FORS2 U_{HIGH} band. In addition to our stack in the U_{HIGH} band, we download the stacks[19] the S14 team used in the bands F606W, F814W, F850LP, and F125W (F606W + F850LP: programme 9425 with PI M. Giavalisco, F814W: programme 12062 with PI S. Faber, F125W: programme 13872 with PI G. Illingworth) and measure the photometry on these stacks with LAMBDAR. We use the PSF models provided on the 3D-HST website. We then match the galaxies in our catalogue with the galaxies in the S14 photometric catalogue with the `associate` function from the `LDAC` tools, requiring a distance of not more than $0\farcs3$ for a match. We interpolate the magnitude J_{110} from our measurements in the filters F850LP and F125W.

In this appendix, we define all offsets of the magnitudes or colours in terms of S14 photometry minus LAMBDAR photometry. In Figure 7.13, we show how our magnitude measurements with LAMBDAR compare to the S14 photometry. We notice a negative shift with a median offset of up to ~ -0.1 mag between S14

---

[18] https://pweb.cfa.harvard.edu/research/james-webb-space-telescope-advanced-deep-extragalactic-survey-jades

[19] https://archive.stsci.edu/prepds/3d-hst/

and LAMBDAR in all of the *HST* bands with a scatter of $\sim 0.3\,\mathrm{mag}$. In part, this negative shift is caused by sources with a `Source Extractor` detection flag of FLAG > 0 (based on our detection in the F606W band). For these sources, `Source Extractor` recognises, for instance, contamination by nearby sources or blending. We notice that the magnitude differences of these sources are predominantly negative in the direct comparison of S14 and LAMBDAR, meaning that S14 measurements are systematically brighter than LAMBDAR measurements. This is consistent with the expectation given the measurement techniques. S14 utilise aperture photometry, where fluxes are measured within apertures of fixed size with a diameter of $0\overset{\prime\prime}{.}7$ for *HST* images. In contrast to that, LAMBDAR actively deblends photometry and thus measures fainter magnitudes for blended sources. But also for sources with FLAG $= 0$, we find a slight asymmetry skewed towards more negative magnitude differences between the S14 and LAMBDAR photometry.

For the U_{HIGH} band, we find a median offset of -0.062 with a scatter of 0.703, which is a considerably larger scatter than for the *HST* bands. This is likely connected to the difference in depth between the U_{VIMOS} stack from S14 (5σ depth $27.4\,\mathrm{mag}$) and our U_{HIGH} stack (5σ depth $26.6\,\mathrm{mag}$) and the difference of the seeing ($0\overset{\prime\prime}{.}8$ for U_{VIMOS} versus $1\overset{\prime\prime}{.}0$ for U_{HIGH}). We find that including a conversion from the U_{VIMOS} band to the U_{HIGH} band based on the respective filter curves does not reduce this scatter.

Regarding the comparisons of colour measurements (see Figure 7.14), we find slightly positive shifts for all colours based on *HST* bands. In particular, these colours typically exhibit small shifts of up to $\sim 0.04\,\mathrm{mag}$ with a scatter of up to $\sim 0.11\,\mathrm{mag}$. The shift for $U_{\mathrm{HIGH}} - V_{606}$ is $-0.005\,\mathrm{mag}$ with a scatter of $0.712\,\mathrm{mag}$. Systematic shifts of this order will only mildly impact the estimates of the average lensing efficiency $\langle\beta\rangle$, as we show in Section 7.14. We additionally reduced a data set in the filter F110W (programme 14043, PI: F. Bauer) located within the GOODS-South field and compared our F110W photometry with the results from the S14 photometric catalogues. We found only mild offsets of $-0.010\,\mathrm{mag}$ and $-0.022\,\mathrm{mag}$ between the S14 and our photometry for the colours $V_{606} - J_{110}$ and $I_{814} - J_{110}$, respectively.

When we calculate the average lensing efficiency for the cluster fields, we could, in principle, apply the scatter, which we measure when comparing the S14 and LAMBDAR photometry to all CANDELS/3D-HST catalogues to account for the different measurement techniques. However, we have to keep in mind that the comparison, which we present here, is limited in some respects: the U bands we compare here have different depths so that we cannot clearly distinguish between effects due to depth and due to the different filter curves of U_{HIGH} and U_{VIMOS}. Additionally, the CANDELS/3D-HST fields employed different U bands, and also each field has different depths in different filters. Therefore, we decide to account for differences in depth in a consistent way for all five CANDELS/3D-HST fields by adding Gaussian noise based on the difference to the depths in our cluster fields (see

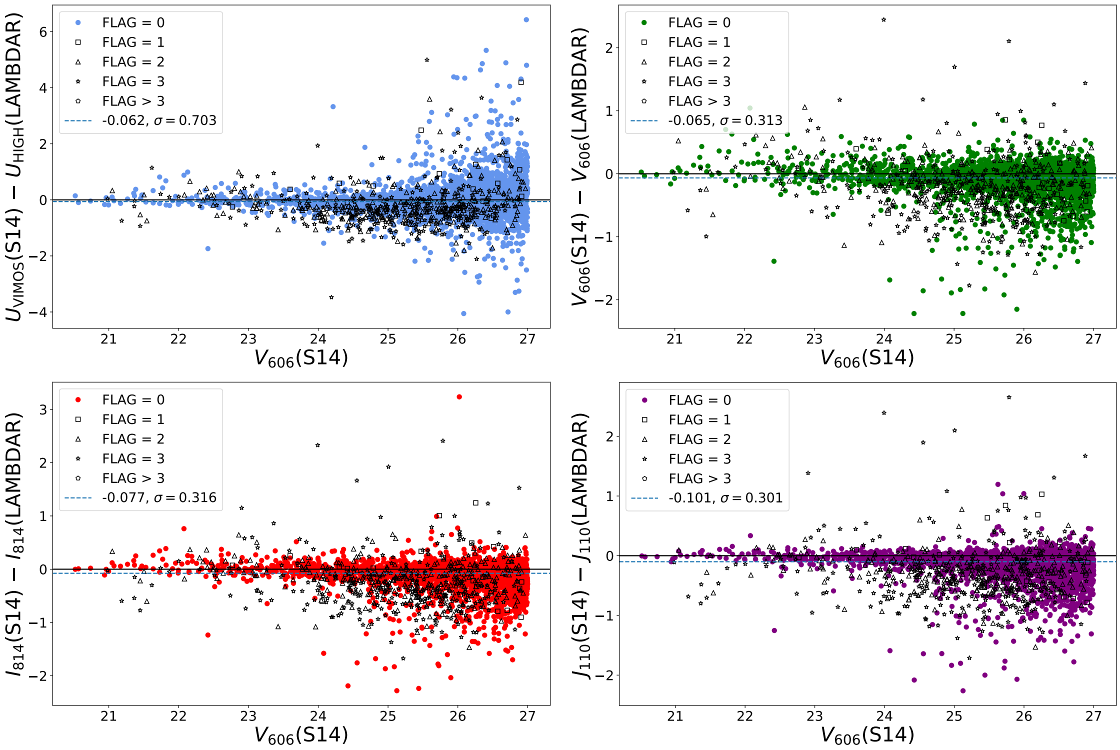

Figure 7.13 – Magnitude differences between S14 and LAMBDAR photometry for the $U_{\rm HIGH}$, V_{606}, I_{814}, and J_{110} magnitudes. The blue dashed lines represent the median, and we indicate the scatter of the respective bands in the legend label. We show all matched galaxies down to $V_{606} < 27.0$ mag. Note the different scales on the y-axis for the U magnitudes and the *HST*-based magnitudes.

Table 7.1). However, we do investigate how shifts in the photometry as presented in this section can affect the average lensing efficiency and add the related uncertainties to our error budget (see Table 7.3 and Section 7.14).

7.13 Appendix B: Robustness of the photometric zeropoint estimation via the galaxy locus method

For our U band calibration purposes, we define the galaxy locus to comprise all galaxies in the magnitude range $24.2 < V_{606} < 27.0$, but excluding galaxies approximately at the cluster redshift ($1.2 \lesssim z \lesssim 1.7$) through a cut in the VIJ colour plane (see Figure 7.1). As described in Section 7.5.3, we correct for small shifts in the U band photometry among the five CANDELS/3D-*HST* fields based on the peak position of highest density in the UVI colour plane. These shifts are listed in Table 7.9.

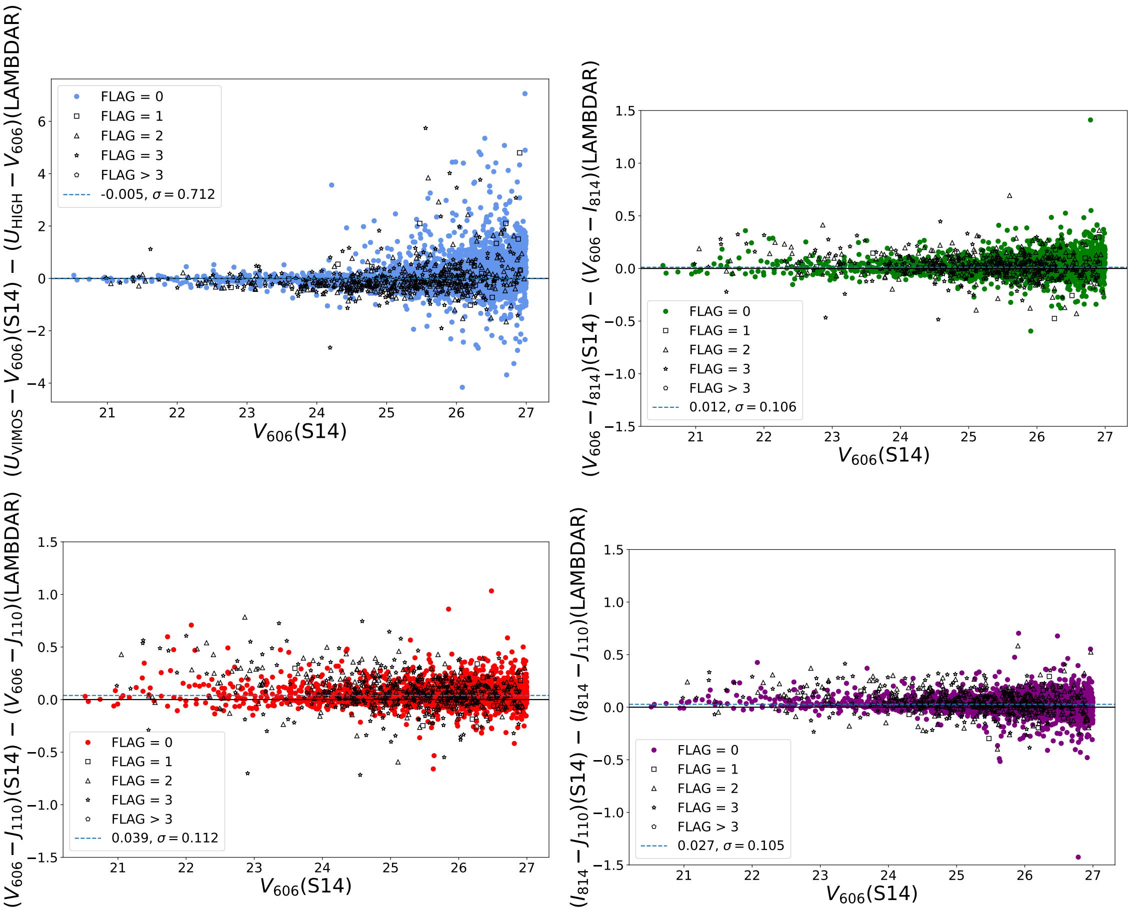

Figure 7.14 – Colour differences between S14 and LAMBDAR photometry for the colours $U_{\rm HIGH} - V_{606}$, $V_{606} - I_{814}$, $V_{606} - J_{110}$, and $I_{814} - J_{110}$. The blue dashed lines represent the median and we indicate the scatter of the respective colours in the legend label. We show all matched galaxies down to $V_{606} < 27.0$ mag. Note the different scales on the y-axis for the $U - V_{606}$ colour and the *HST*-based colours.

In order to estimate how well the zeropoint calibration of the $U_{\rm HIGH}$ band works for the observations of our cluster fields, we test the zeropoint estimation in the CANDELS/3D-HST fields using only subsets of galaxies that approximately match the number of galaxies available in the cluster fields. Our cluster field observations roughly cover a field of view of 11 arcmin^2. We, therefore, only use galaxies from a region of this size from a random position in the respective CANDELS/3D-HST fields. A number of around 400 to 600 galaxies per subsample belongs to our galaxy locus (as defined by the magnitude and colour cuts in Section 7.5.3), which approximately equals the expected number of locus galaxies in our cluster fields. Since we have already applied a shift to the U bands in the CANDELS/3D-HST fields as explained above, this means that we measure the residual zeropoint offset for 100 different (possibly overlapping) subsamples and report the average residual zero-

Table 7.9 – *First column*: Names of the CANDELS/3D-HST fields. *Second column*: Overview about the measured zeropoint offsets in the U band between the galaxy loci from the five CANDELS/3D-HST catalogues from S14 with respect to the locus in the GOODS-South field, which serves as an anchor. *Third column*: Average residual offset computed from 100 subsamples in the CANDELS/3D-HST fields (drawn from areas with a similar field of view as *HST*/ACS) after applying the 'full' correction (second column). The values correspond to the average and scatter.

	Zeropoint offsets	
Field	full [mag]	100 samples [mag]
AEGIS	0.121	$-0.013\,,\sigma = 0.053$
COSMOS	0.121	$-0.021\,,\sigma = 0.062$
UDS	0.121	$-0.037\,,\sigma = 0.076$
GOODS-North	-0.040	$-0.020\,,\sigma = 0.080$
GOODS-South	0.0	$-0.027\,,\sigma = 0.055$

point offset and scatter in Table 7.9. Overall, we find that the offsets do not exceed a value of ~ -0.04 mag with a scatter of 0.08 mag. The impact of such offsets is studied in Section 7.14.

7.14 Appendix C: Effect of systematic offsets in the photometry on $\langle\beta\rangle$

In order to estimate how systematic shifts in the photometry affect the average lensing efficiency, we apply different systematic shifts to the colours $U - V_{606}$, $V_{606} - I_{814}$, $V_{606} - J_{110}$, and $I_{814} - J_{110}$ from the S14 photometry. We then calculate $\langle\beta\rangle$ based on the photometric redshifts for the colour-selected galaxies. Since we apply a Gaussian noise to the U band from the GOODS-South field, we evaluate five noise realisations. We present the effect of systematic offsets in the photometry in Figure 7.15. Here, we distinguish between two cases: in the left panels, we show how the shifts of the photometry affect the average lensing efficiency for the matched galaxies in the HUDF region, considering the five available redshift catalogues by R15, R15_fix, R20, S14 and Oe18; in the right panels, we show the results for the five full R20 CANDELS/3D-HST redshift catalogues. A summary of the uncertainty level of the photometric shifts (based on our results presented in Sections 7.12 and 7.13) and the consequential uncertainties of the average lensing efficiency are presented in Table 7.10.

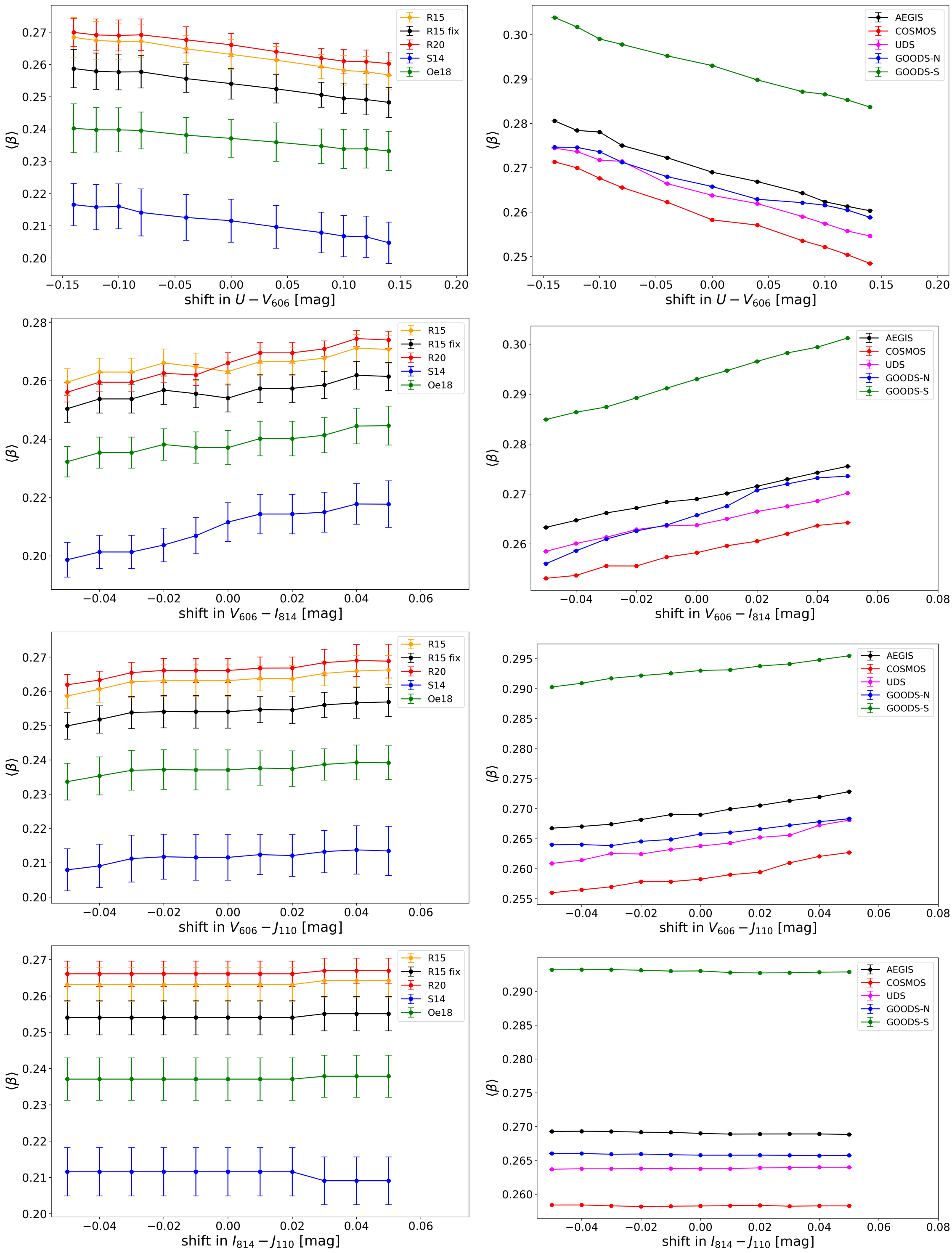

Figure 7.15 – Changes of the average lensing efficiency $\langle\beta\rangle$ when a systematic shift is applied to the colours $U - V_{606}$, $V_{606} - I_{814}$, $V_{606} - J_{110}$, and $I_{814} - J_{110}$ (based on the S14 photometry). *Left:* Impact of systematic shifts for the matched galaxies in the HUDF region, based on photometric redshifts from five reference catalogues. *Right:* Impact of systematic shifts for the galaxies in the five CANDELS/3D-HST fields with photometric redshifts from R20.

Table 7.10 – We list how the expected photometric uncertainties of relevant colours affect the average lensing efficiency. We quantify this by calculating the difference $\Delta\beta$ between the results for $\langle\beta\rangle$ based on the S14 photometry shifted by the expected uncertainty in a positive and negative direction. We divide this by the average lensing efficiency $\langle\beta\rangle$ without shift of the photometry. We use a lens redshift of $z_l = 1.4$ as reference. *Column 3:* Impact on the average lensing efficiency for matched galaxies in the HUDF region. We report the value based on the R20 photometric redshifts. *Column 4:* Average impact on the average lensing efficiency for galaxies in the five CANDELS/3D-HST fields using the R20 photometric redshifts.

Colour	expected uncert.	$\left(\frac{\Delta\langle\beta\rangle}{\langle\beta\rangle}\right)_{\mathrm{HUDF,R20}}$	$\left(\frac{\Delta\langle\beta\rangle}{\langle\beta\rangle}\right)_{\mathrm{CANDELS}}$
$U - V_{606}$	±0.08 mag	2.7 %	4.1 %
$V_{606} - I_{814}$	±0.02 mag	2.9 %	2.2 %
$V_{606} - J_{110}$	±0.05 mag	2.7 %	2.2 %
$I_{814} - J_{110}$	±0.05 mag	0.3 %	0.1 %

7.15 Appendix D: Benefits of including the U band for the colour selection of background galaxies

In Section 7.6.2, we have established and tested a strategy for the selection of background source galaxies behind galaxy clusters at redshifts $1.2 \lesssim z \lesssim 1.7$. We applied cuts in the colour spaces $V_{606} - J_{110}$ versus $U - V_{606}$ and $I_{814} - J_{110}$ versus $V_{606} - I_{814}$ based on the bands F606W and F814W from *HST*/ACS, F110W from *HST*/WFC3, and U_{HIGH} from VLT FORS2. The calibration of the U_{HIGH} band is challenging due to the lack of an adequate reference catalogue with well-calibrated magnitudes for the cluster fields. We introduced a calibration technique with a galaxy locus for which we estimate a statistical uncertainty of 0.08 mag.

In this appendix, we demonstrate that the additional use of the U_{HIGH} band is still beneficial for an efficient background source selection. For comparison, we perform a selection without using the U_{HIGH} band, thus only using the bands F606W, F814W, and F110W. In Figure 7.16, we show how only galaxies with $V_{606} - I_{814} < 0.4$ and $I_{814} - J_{110} < 0.2$ are selected, which are preferentially at redshifts $z \gtrsim 1.8$. As before, we apply a bright and faint cut at $V_{606} > 24.2$ and $V_{606} < 27.0$, respectively. Analogously to Section 7.6.2 (also Figure 7.3), this figure is based on the photometric catalogue computed for the GOODS-South field by Skelton et al. (2014). The resulting redshift distribution is shown in the top panel of Figure 7.17. The distributions are based on a selection from the same matched galaxies in the HUDF region as described in Section 7.6.2 with photometric redshift information from the five catalogues R15, R15_fix, R20, S14, and Oe18. Additionally, we apply a signal-to-noise ratio cut of $S/N_{\mathrm{flux}} > 10.0$ as done in Section 7.6.2. The bottom panel of this figure displays the redshift distribution from the selection introduced in Sec-

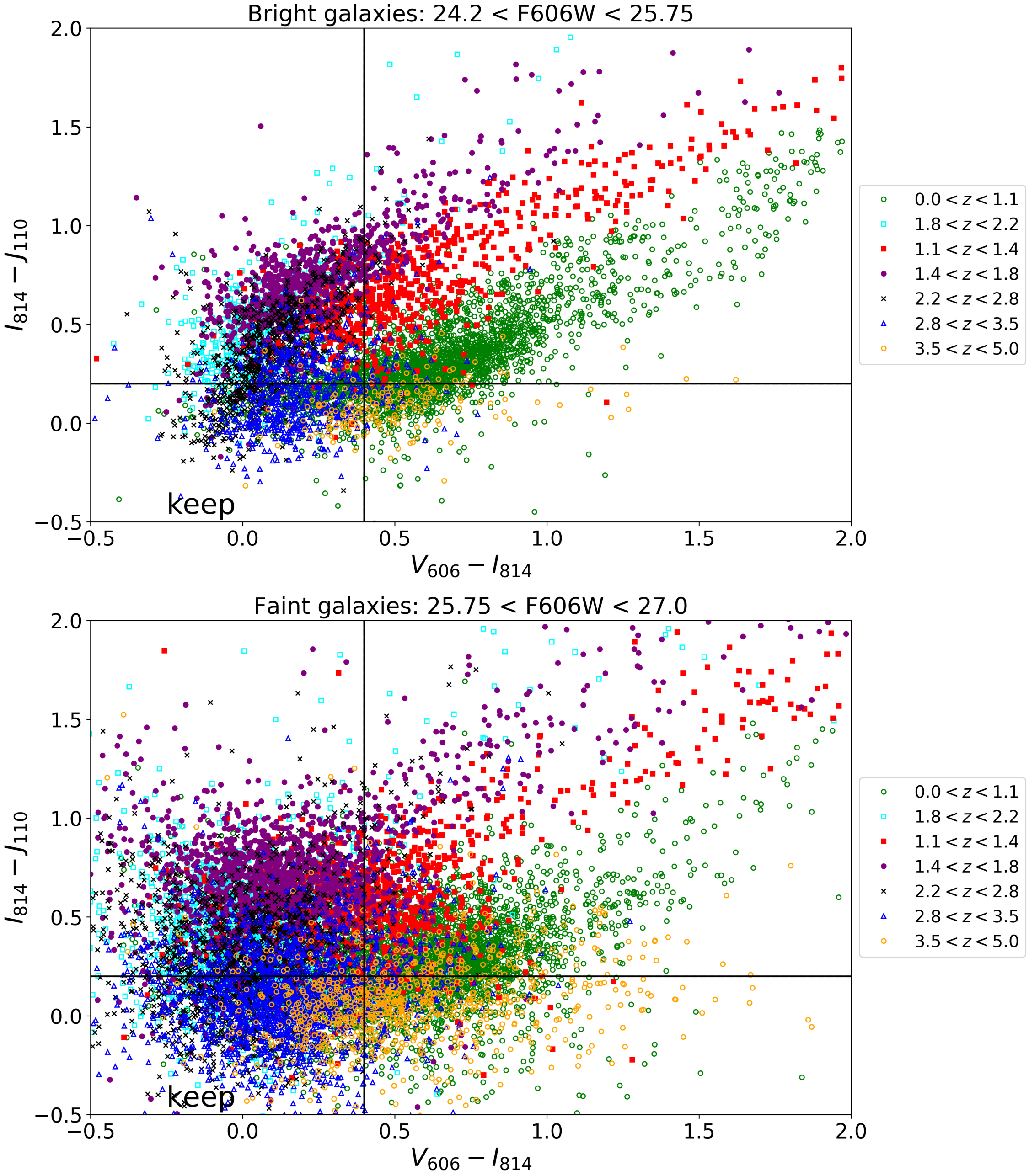

Figure 7.16 – We show the selection of background source galaxies solely based on the bands F606W, F814W, and F110W for a cluster at redshift $1.2 \lesssim z \lesssim 1.7$. Analogously to Figure 7.3 in Section 7.6.2, we show the selection for bright (*top*) and faint (*bottom*) galaxies. As opposed to the selection including the U_{HIGH} band, the cuts do not differ for the bright and faint regime. We just show both plots for better comparability with the selection in Section 7.6.2. Galaxies with $V_{606} - I_{814} < 0.4$ and $I_{814} - J_{110} < 0.2$ are selected (lower left corner, ‘keep’).

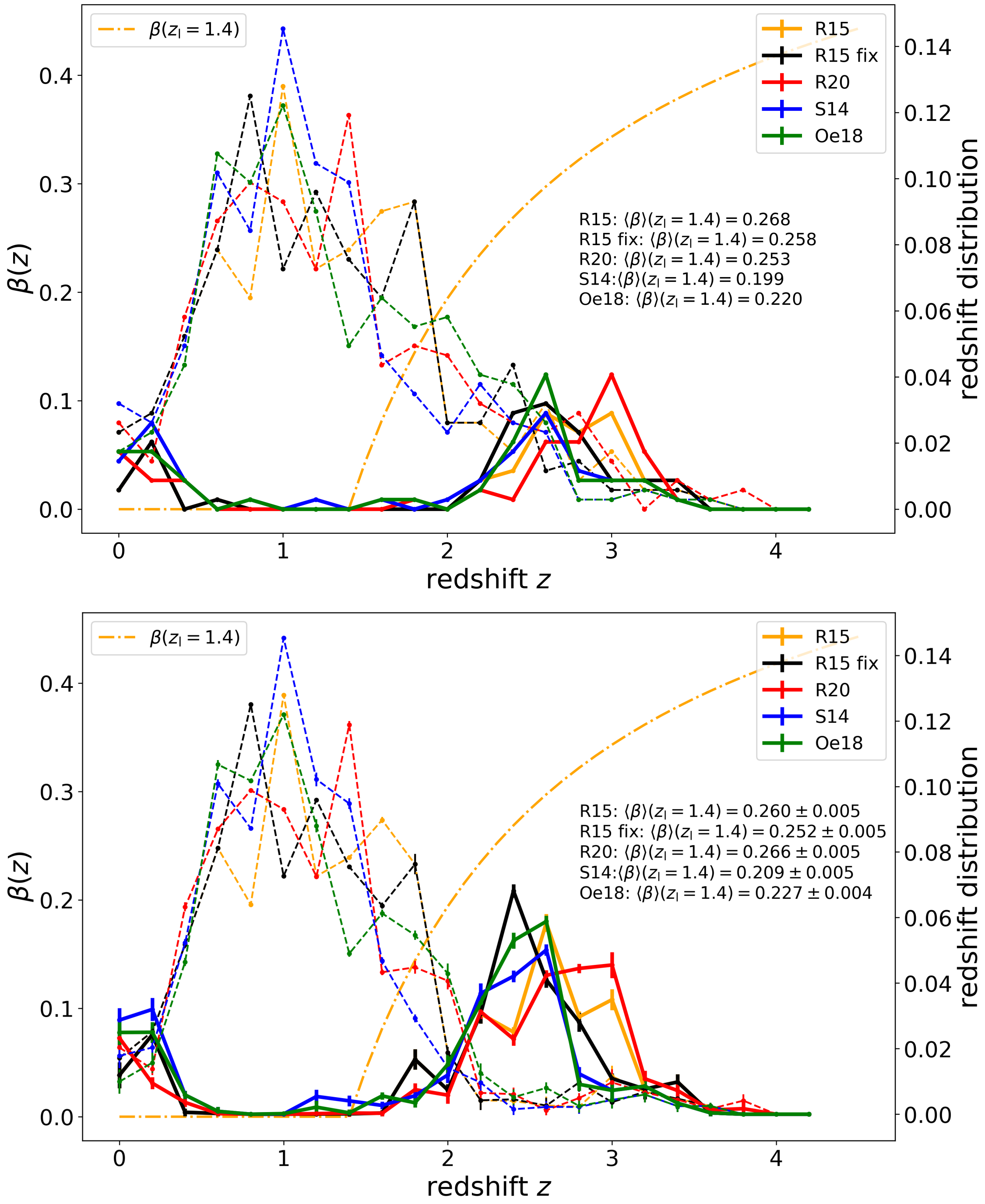

Figure 7.17 – We show the redshift distribution of colour selected galaxies for a selection with (*bottom*) and without (*top*) using the U_HIGH band (solid line; the dashed line corresponds to the removed galaxies). The average geometric lensing efficiency is calculated at a reference redshift of $z = 1.4$. The distributions only show galaxies matched between the five reference redshift catalogues (R15, R15_fix, R20, S14, and Oe18). The selection is performed based on the S14 photometry in both panels.

tion 7.6.2 (see Figure 7.5). Comparing the selection with and without the $U_{\rm HIGH}$ band, we find that the average lensing efficiency is very similar. In both cases, galaxies at the cluster redshift are properly removed and a small contamination by foreground galaxies remains. However, including the $U_{\rm HIGH}$ band allows for the selection of a larger number of galaxies. Therefore, the resulting signal-to-noise ratio $S/N_{\rm selection} = \langle\beta\rangle\sqrt{n}$ characterised by the product of the average lensing efficiency $\langle\beta\rangle$ and the square root of the number density $\sqrt{n}$ is about 1.4 times higher than for a selection without the $U_{\rm HIGH}$ band (taking the results based on the R20 catalogue as reference). The number density for the selection without the $U_{\rm HIGH}$ band can only be increased at the cost of a higher contamination by foreground galaxies and especially by galaxies at the cluster redshift.

Thus, while a background source selection without the $U_{\rm HIGH}$ band is possible, it is still recommended to include it to achieve a notably higher signal-to-noise ratio for the weak lensing analysis. We achieved this improvement despite the differences in the instruments and filters used for the observations of the different CANDELS/3D-HST fields and our cluster fields (see Section 7.5.3). Thus, we expect that the improvement is likely insensitive to the exact U band bandpass shape. While the statistical uncertainty of the U band calibration of 0.08 mag is comparably large, it is subdominant in comparison with the other contributions of statistical uncertainty (see Tables 7.3, 7.6, and 7.7).

7.16 Appendix E: Weak lensing results: mass maps and tangential reduced shear profiles

We show the weak lensing results, including the mass maps and tangential reduced shear profiles for the studied cluster sample.

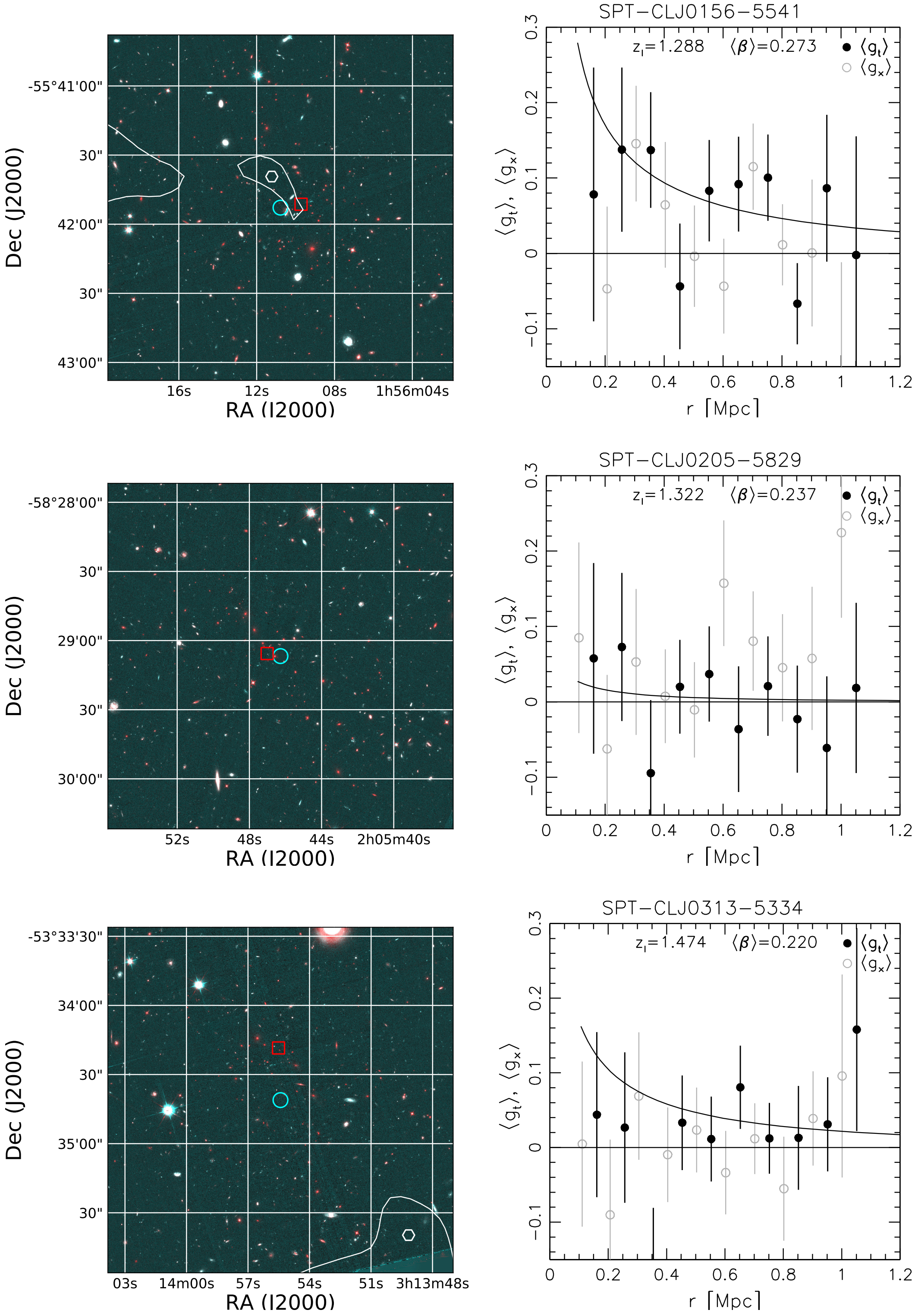

Figure 7.18 – Weak lensing results for the clusters in our sample (see the caption of Figure 7.10 for details).

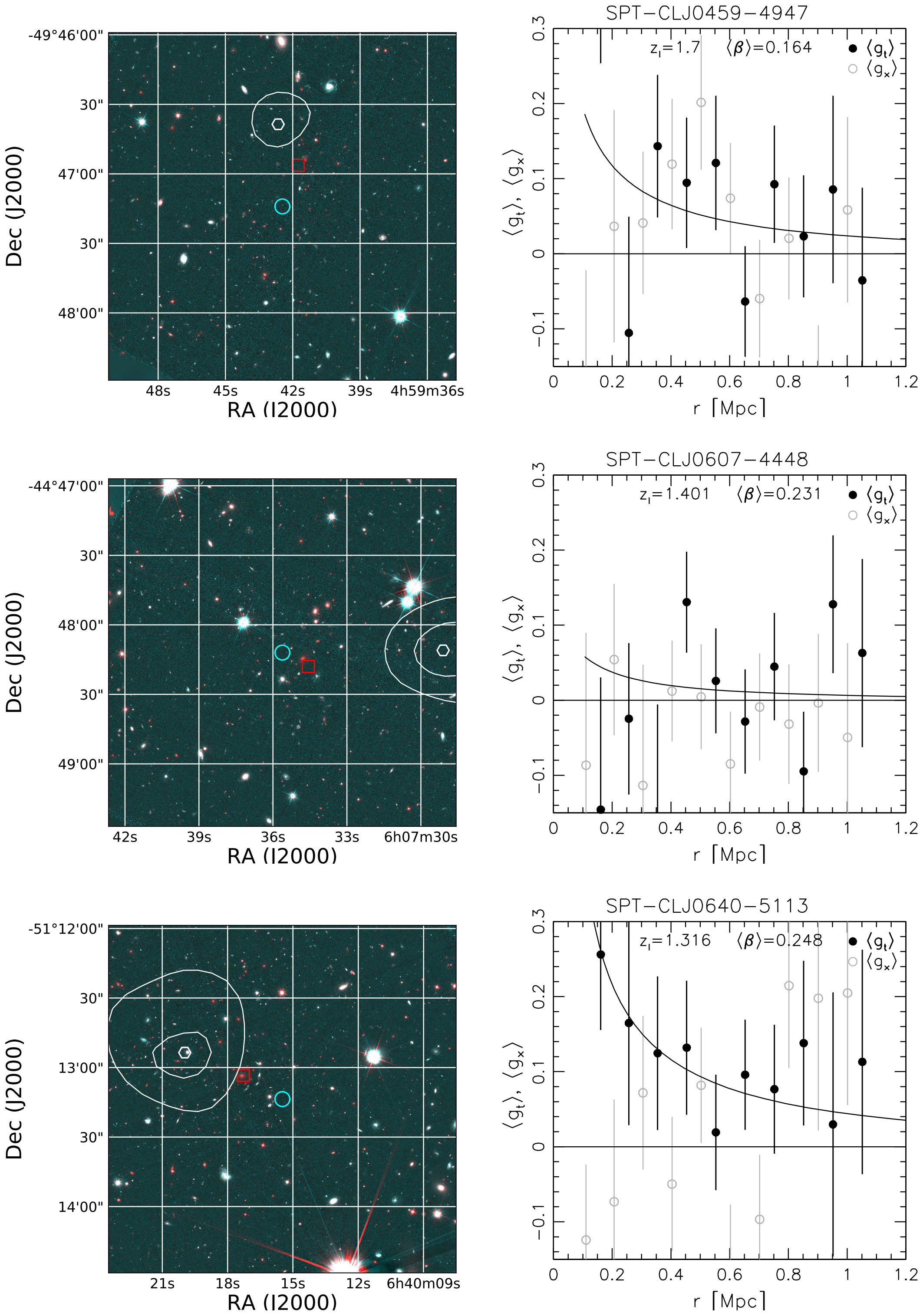

Figure 7.19 – Weak lensing results for the clusters in our sample (continued, see the caption of Figure 7.10 for details).

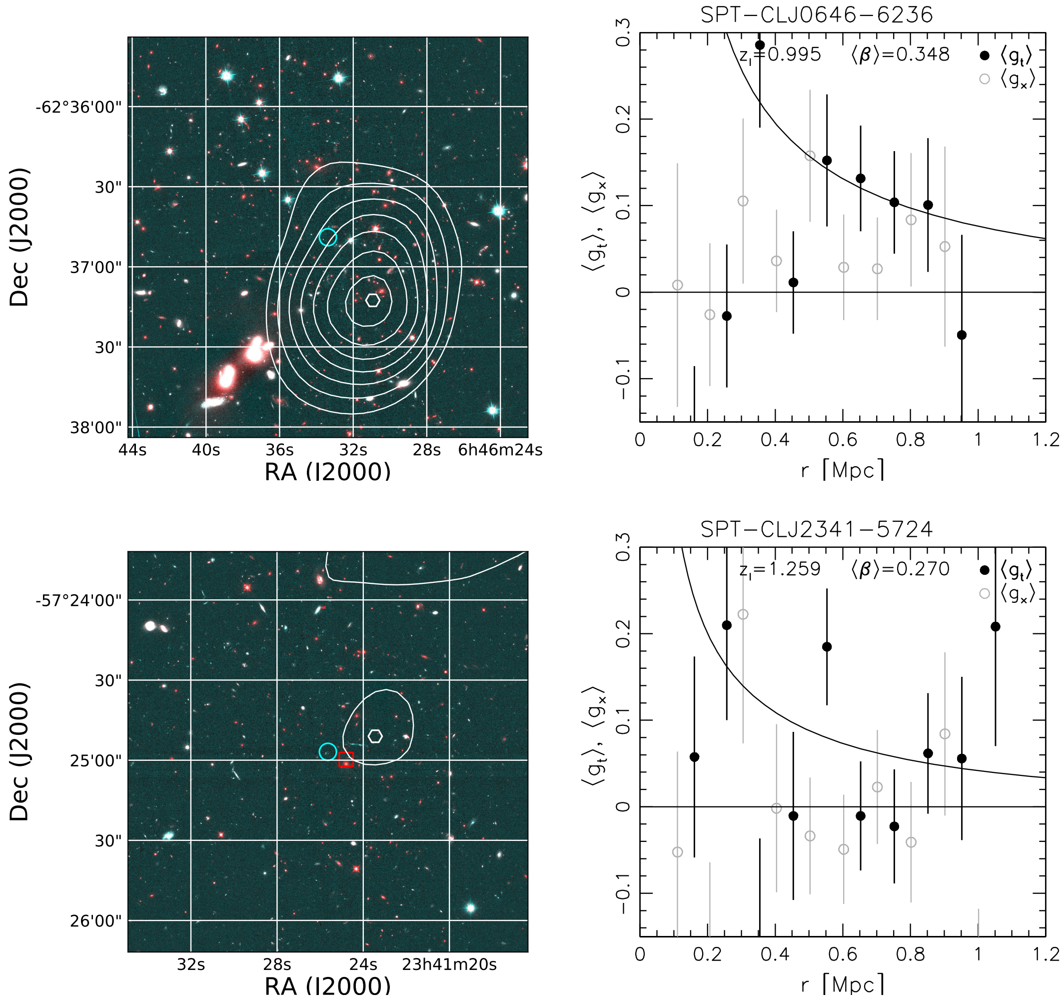

Figure 7.20 – Weak lensing results for the clusters in our sample (continued, see the caption of Figure 7.10 for details). For SPT-CL *J*0646−6236 the reduced shear profile was computed with respect to the SZ centre.

CHAPTER 8

Conclusions

The research presented in this thesis is concerned with the selection function and weak lensing mass scale of SZ-selected galaxy cluster samples at high redshifts. In the previous chapters, I presented an optical follow-up study of galaxy cluster candidates from PSZ2 and an *HST* weak lensing analysis of massive, distant galaxy clusters from the SPT-SZ survey. In the following, I summarise the most important results of these research projects and comment on their relevance in a larger scientific context. Finally, I finish with an outlook on optical follow-up and weak lensing studies of galaxy clusters.

Optical follow-up of 32 *Planck* cluster candidates

In Chapter 6, we confirmed 18 (7) out of 32 *Planck* SZ-detected cluster candidates at redshifts $z > 0.5$ ($z > 0.8$) as massive clusters through an optical follow-up study. We used optical data in the r, i, and z bands from ACAM at the William Herschel Telescope for a red-sequence analysis to obtain photometric redshift and optical richness estimates. Additionally, we analysed long-slit observations for a subset of nine cluster candidates to measure spectroscopic redshifts.

Comparing the optical richness with the expected SZ-mass according to the scaling relation by Rozo et al. (2015), we found that the majority of clusters is less rich than predicted by the relation. Such a discrepancy is expected due to projection effects, noise-induced detections, and in particular, the Eddington bias, which becomes increasingly important at low SZ-detection significance like in our cluster candidate sample. We quantified a strict (loose) confirmation criterion, where the cluster is rich/massive enough to be the dominant source of the SZ signal. This is the case when the candidate is at least 50 (25) per cent as rich as the expectation value from the richness-mass scaling relation by Rozo et al. (2015). The fraction of confirmed cluster candidates from PSZ2 in our sample is compatible with the expectation for the sample purity when compared to studies by Planck Collaboration et al. (2016c) and van der Burg et al. (2016).

Additionally, we found that eight out of nine cluster candidates with very low SZ detection significance $3.0 \lesssim S/N < 4.5$ fulfil the loose confirmation criterion. This demonstrates that optical preselection of cluster candidates is a useful method to uncover massive clusters at low S/N from a huge number of low S/N detections, which cannot be completely and systematically followed up with pointed observations. At the same time, auxiliary observations are indispensable as an independent verification method with the power to uncover selection biases such as the Eddington effect.

While the preselection implies a complex selection function of our sample, which prohibits its use for cosmological studies, the validated massive, high-redshift clusters in our study can well be studied further in an astrophysical context. Furthermore, our newly obtained photometric and spectroscopic redshifts in particular of the 23 PSZ2 candidates (this equals approximately five per cent of the candidates without follow-up at the time when the PSZ2 catalogue was published, Planck Collaboration et al., 2016c) enable computations of their SZ-masses, which are required for studies with the complete PSZ2 sample. With this, we provide a notable contribution to a complete follow-up of PSZ2 cluster candidates, especially at high redshifts.

HST weak lensing analysis of nine massive galaxy clusters at $z \gtrsim 1.0$ in the SPT-SZ Survey

Chapter 7 presents an *HST* weak lensing analysis of nine high-redshift galaxy clusters at $z \gtrsim 1.0$ with high SZ detection significances ($\xi > 6.0$) in the SPT-SZ survey. We conducted weak lensing galaxy shape measurements in the ACS bands F606W and F814W. We used the observations in these bands in combination with observations in band F110W from WFC3 on board the *HST* and in band U_{HIGH} from the FORS2 imager at the VLT for a robust photometric selection preferentially of background source galaxies via suitable cuts in colour-colour space. We estimated the source redshift distribution and the average geometric lensing efficiency by applying these photometric selection cuts to revised CANDELS/3D-HST photometric redshift catalogues by Raihan et al. (2020), matching their depth to the one of our observations by adding Gaussian noise. We obtained weak lensing mass estimates by fitting the tangential reduced shear profiles with spherical NFW models assuming a fixed concentration–mass relation by Diemer & Kravtsov (2015) with updated parameters from Diemer & Joyce (2019). Uncertainties in the mass modelling, for example, due to triaxiality, deviations from an NFW profile, or miscentering introduce a mass bias, which we quantified from Millennium XXL simulations following Sommer et al. (2022). We carefully accounted for systematic uncertainties in the weak lensing mass measurements, finding that variations between the CANDELS/3D-HST fields contribute the most, unless when SZ centres are used instead of X-ray centres. Statistical uncertainties with the largest contribution from shape noise outweigh the systematic uncertainties.

We used the weak lensing mass measurements in conjunction with results at lower and intermediate redshifts from Dietrich et al. (2019) and Schrabback et al. (2021), respectively, to constrain the redshift evolution of the scaling relation between the unbiased SZ detection significance ζ and the cluster mass. In agreement with previous results, we found that the constraints including the weak lensing mass calibration suggest a lower mass scale than constraints informed by a flat *Planck* $\nu\Lambda$CDM cosmology combined with the SPT-SZ cluster counts. While our measurements of the high-redshift clusters are subject to large uncertainties, a binned analysis revealed that the highest redshift bin is consistent with constraints from lower redshifts.

With our study, we took a first step to understanding the redshift evolution of SZ-mass scaling relations out to very high redshifts $z \gtrsim 1.2$. We provide the first constraints on the weak lensing mass scale of clusters at these redshifts for a sample from the SPT-SZ survey, which benefits from a well-defined selection function. Additionally, our study provides an efficient background source selection strategy with close to no contamination by cluster members for clusters at $z \gtrsim 1.2$ based on four photometric bands.

Outlook

The multi-component and multi-wavelength nature of galaxy clusters provides an excellent basis for an independent verification method of detected galaxy cluster candidates. Our study in Chapter 6 uses the well-established method of optical follow-up to help quantify the selection function of the PSZ2 catalogue of SZ-detected cluster candidates. This technique will continue to be used for future cluster samples reaching ever higher redshifts and lower mass thresholds. Currently, synergies of large optical and SZ surveys are already being exploited for a coherent follow-up within large overlapping sky areas, including for example, DES + SPT (SPT-pol Extended Cluster Survey, Bleem et al., 2020), SDSS/RedMaPPer/AllWISE mid-infrared source catalogue + *Planck* (Planck Collaboration et al., 2016c), and DES/HSC/KiDS + ACT (Hilton et al., 2021). First optical follow-up studies have also been conducted for eROSITA (Klein et al., 2021). A complete follow-up of all detected cluster candidates is crucial for a proper understanding of the survey selection function. Here, one needs to ensure that the confirmation criteria are carefully chosen to be as consistent as possible across the entire sample of detected candidates, which can be achieved more easily with optical or NIR surveys covering large sky areas. Future surveys conducted by the *Euclid* satellite (Laureijs et al., 2011), the Vera C. Rubin Observatory (LSST Science Collaboration et al., 2009), and the

Nancy Grace Roman Space Telescope (formerly known as WFIRST, Spergel et al., 2015) will provide suitable deep optical and/or NIR follow-up imaging over large sky areas.

Additionally, these surveys will help to calibrate the weak lensing cluster mass scale and related observable-mass scaling relations over a broad redshift range with unprecedented precision. For clusters at high redshifts, presently the most sensitive route to obtain such measurements is provided by pointed high-resolution follow-up observations with *HST*. In Chapter 7, we presented such an *HST* weak lensing study, extending earlier results to higher redshifts. For future constraints, systematics will need to be well-understood and minimised, especially with the high precision in mind that *Euclid*, the Vera C. Rubin Observatory (LSST), and the *Nancy Grace Roman Space Telescope* will provide. Our pilot study for high-redshift clusters showed that uncertainties in the calibration of the source redshift distribution contribute the most to the systematic error budget with around 13 per cent (for the cluster mass scale). It will be crucial to reduce these uncertainties for future studies aiming to constrain the cluster mass scale at the high-redshift end with better statistical precision. This redshift regime is accessible for lensing studies through deep observations. However, these studies require sufficiently deep photometric redshift catalogues and sufficient spectroscopic completeness for a robust calibration of the redshift distribution. Both will become available, for instance, with the planned *James Webb Space Telescope* Advanced Deep Extragalactic Survey[1] (JADES). This survey will obtain imaging and spectroscopy over 236 arcmin^2 in the GOODS-South and GOODS-North fields, reaching unprecedented depths (5σ depth of 30.6/29.6 mag in band F115W in the deep/medium subsurvey, Williams et al., 2018). This will form an excellent basis for photometric and spectroscopic redshift measurements, thereby helping to reduce systematic uncertainties. Furthermore, weak lensing surveys such as *Euclid* are currently developing strategies to calibrate the source distribution in tomographic redshift bins with very high accuracy. For example, this includes direct calibration methods using spectroscopic training samples and the combination of the photometric redshift probability distribution functions (zPDFs) of individual galaxies (Euclid Collaboration et al., 2021). The direct methods can reliably recover the mean redshift without requiring deep photometry, but they need a low fraction of spectroscopic failures. The methods using zPDFs also provide robust estimates of the mean redshift, especially when deep photometry is used to account for biases. Another promising technique for redshift calibration is via so called cross-correlation redshifts, which exploit the fact that galaxies in a common volume are highly correlated due to the gravitational clustering of matter in the Universe (e.g. Newman, 2008; van den Busch et al., 2020). Here, measuring the angular cross-correlation between a target sample of galaxies with unknown redshifts and a reference sample of galaxies with well-known (spectroscopic) redshifts allows to constrain the redshift

---

[1] `https://pweb.cfa.harvard.edu/research/james-webb-space-telescope-advanced-deep-extragalactic-survey-jades`

distribution of the target sample. In addition to these considerations regarding the calibration of the source redshift distribution, systematic uncertainties related to weak lensing mass modelling, the concentration–mass relation, and the miscentering distribution need to be reduced, e.g., with the help of more in-depth analyses of hydrodynamical simulations (e.g. Grandis et al., 2021).

Bibliography

Abell G. O., 1958, ApJS, 3, 211

Addison G. E., Hinshaw G., Halpern M., 2013, MNRAS, 436, 1674

Aghanim N., et al., 2015, A&A, 580, A138

Ahmad Q. R., et al., 2001, Phys. Rev. Lett., 87, 071301

Aihara H., et al., 2011, ApJS, 193, 29

Aker M., et al., 2019, Phys. Rev. Lett., 123, 221802

Alam S., et al., 2017, MNRAS, 470, 2617

Alcock C., et al., 2000, ApJ, 542, 281

Allen S. W., Rapetti D. A., Schmidt R. W., Ebeling H., Morris R. G., Fabian A. C., 2008, MNRAS, 383, 879

Allen S. W., Evrard A. E., Mantz A. B., 2011, ARA&A, 49, 409

Amodeo S., et al., 2018, ApJ, 853, 36

Andreon S., Congdon P., 2014, A&A, 568, A23

Angulo R. E., Springel V., White S. D. M., Jenkins A., Baugh C. M., Frenk C. S., 2012, MNRAS, 426, 2046

Applegate D. E., et al., 2014, MNRAS, 439, 48

Applegate D. E., et al., 2016, MNRAS, 457, 1522

Aprile E., et al., 2017, Phys. Rev. Lett., 119, 181301

Armengaud E., et al., 2019, Phys. Rev. D, 99, 082003

Arnaud M., Pratt G. W., Piffaretti R., Böhringer H., Croston J. H., Pointecouteau E., 2010, A&A, 517, A92

Astropy Collaboration et al., 2018, AJ, 156, 123

Austermann J. E., et al., 2012, in Holland W. S., Zmuidzinas J., eds, Society of Photo-Optical Instrumentation Engineers (SPIE) Conference Series Vol. 8452, Millimeter, Submillimeter, and Far-Infrared Detectors and Instrumentation for Astronomy VI. p. 84521E (`arXiv:1210.4970`), doi:10.1117/12.927286

Bacon R., et al., 2015, A&A, 575, A75

Baggett S., et al., 2002, HST WFPC2 Data Handbook, v. 4.0, ed. B. Mobasher, Baltimore, STScI

Barrena R., et al., 2018, A&A, 616, A42

Bartelmann M., 1996, A&A, 313, 697

Bartelmann M., Maturi M., 2017, Scholarpedia, 12, 32440

Bartelmann M., Schneider P., 2001, Phys. Rep., 340, 291

Bayliss M. B., et al., 2014, ApJ, 794, 12

Beckwith S. V. W., et al., 2006, AJ, 132, 1729

Benítez N., 2000, ApJ, 536, 571

Benn C., Dee K., Agócs T., 2008, in Ground-based and Airborne Instrumentation for Astronomy II. p. 70146X, doi:10.1117/12.788694

Bertin E., 2011, in Evans I. N., Accomazzi A., Mink D. J., Rots A. H., eds, Astronomical Society of the Pacific Conference Series Vol. 442, Astronomical Data Analysis Software and Systems XX. p. 435

Bertin E., Arnouts S., 1996, A&AS, 117, 393

Betoule M., et al., 2014, A&A, 568, A22

Biffi V., et al., 2016, ApJ, 827, 112

Bîrzan L., Rafferty D. A., Brüggen M., Intema H. T., 2017, MNRAS, 471, 1766

Bleem L. E., et al., 2015, ApJS, 216, 27

Bleem L. E., et al., 2020, ApJS, 247, 25

Boada S., Hughes J. P., Menanteau F., Doze P., Barrientos L. F., Infante L., 2018, ArXiv e-prints accepted for publication in ApJ, p. arXiv:1809.06378

Bocquet S., et al., 2019, ApJ, 878, 55

Böhringer H., et al., 2000, ApJS, 129, 435

Böhringer H., et al., 2001, A&A, 369, 826

Böhringer H., Chon G., Collins C. A., Guzzo L., Nowak N., Bobrovskyi S., 2013, A&A, 555, A30

Böhringer H., Chon G., Retzlaff J., Trümper J., Meisenheimer K., Schartel N., 2017, AJ, 153, 220

Bouwens R. J., et al., 2011, ApJ, 737, 90

Bower R. G., Lucey J. R., Ellis R. S., 1992, MNRAS, 254, 601

Brammer G. B., van Dokkum P. G., Coppi P., 2008, ApJ, 686, 1503

Brammer G. B., et al., 2012, ApJS, 200, 13

Brinchmann J., et al., 2017, A&A, 608, A3

Bringmann T., Weniger C., 2012, Physics of the Dark Universe, 1, 194

Broadhurst T., Takada M., Umetsu K., Kong X., Arimoto N., Chiba M., Futamase T., 2005, ApJ, 619, L143

Brunetti G., Jones T. W., 2014, International Journal of Modern Physics D, 23, 1430007

Buddendiek A., et al., 2015, MNRAS, 450, 4248

Bulbul E., et al., 2019, ApJ, 871, 50

Burenin R. A., et al., 2018, Astronomy Letters, 44, 297

Capasso R., et al., 2019, MNRAS, 482, 1043

Carlberg R. G., 1984, ApJ, 286, 403

Carlberg R. G., Yee H. K. C., Ellingson E., 1997, ApJ, 478, 462

Carlstrom J. E., Holder G. P., Reese E. D., 2002, ARA&A, 40, 643

Carvalho P., Rocha G., Hobson M. P., 2009, MNRAS, 393, 681

Carvalho P., Rocha G., Hobson M. P., Lasenby A., 2012, MNRAS, 427, 1384

Cavaliere A., Fusco-Femiano R., 1976, A&A, 500, 95

Chambers K. C., et al., 2016, preprint, (`arXiv:1612.05560`)

Chiu I., et al., 2016, MNRAS, 455, 258

Chiu I., et al., 2018, MNRAS, 478, 3072

Chiu I.-N., et al., 2021, arXiv e-prints submitted to A&A, p. arXiv:2107.05652

Chromey F. R., 2010, To Measure the Sky. Cambridge University Press

Chu A., Durret F., Márquez I., 2021, A&A, 649, A42

Clowe D., Bradač M., Gonzalez A. H., Markevitch M., Randall S. W., Jones C., Zaritsky D., 2006, ApJ, 648, L109

Colless M., et al., 2001, MNRAS, 328, 1039

Costanzi M., et al., 2021, Phys. Rev. D, 103, 043522

Dawson K. S., et al., 2016, AJ, 151, 44

DeMaio T., et al., 2020, MNRAS, 491, 3751

Diemer B., Joyce M., 2019, ApJ, 871, 168

Diemer B., Kravtsov A. V., 2015, ApJ, 799, 108

Dietrich J. P., Böhnert A., Lombardi M., Hilbert S., Hartlap J., 2012, MNRAS, 419, 3547

Dietrich J. P., et al., 2019, MNRAS, 483, 2871

Dodelson S., 2003, Modern cosmology. Academic Press

Dolag K., Komatsu E., Sunyaev R., 2016, MNRAS, 463, 1797

Douspis M., Salvati L., Aghanim N., 2019, arXiv e-prints, p. arXiv:1901.05289

Dutton A. A., Macciò A. V., 2014, MNRAS, 441, 3359

Eddington A. S., 1913, MNRAS, 73, 359

Ellis R. S., et al., 2013, ApJ, 763, L7

Erben T., Van Waerbeke L., Bertin E., Mellier Y., Schneider P., 2001, A&A, 366, 717

Erben T., et al., 2005, Astronomische Nachrichten, 326, 432

Euclid Collaboration et al., 2021, A&A, 647, A117

Feroz F., Hobson M. P., Bridges M., 2009, MNRAS, 398, 1601

Finner K., James Jee M., Webb T., Wilson G., Perlmutter S., Muzzin A., Hlavacek-Larrondo J., 2020, ApJ, 893, 10

Fixsen D. J., 2009, ApJ, 707, 916

Fukuda Y., et al., 1998, Phys. Rev. Lett., 81, 1562

Fukugita M., Peebles P. J. E., 2004, ApJ, 616, 643

Fukugita M., Hogan C. J., Peebles P. J. E., 1998, ApJ, 503, 518

Funk S., 2015, Proceedings of the National Academy of Science, 112, 12264

Gaia Collaboration et al., 2016a, A&A, 595, A1

Gaia Collaboration et al., 2016b, A&A, 595, A2

Gerbino M., Lattanzi M., 2018, Frontiers in Physics, 5, 70

Ghirardini V., et al., 2021, ApJ, 910, 14

Giodini S., Lovisari L., Pointecouteau E., Ettori S., Reiprich T. H., Hoekstra H., 2013, Space Sci. Rev., 177, 247

Gladders M. D., Yee H. K. C., 2005, ApJS, 157, 1

Gladders M. D., López-Cruz O., Yee H. K. C., Kodama T., 1998, ApJ, 501, 571

Grandis S., Bocquet S., Mohr J. J., Klein M., Dolag K., 2021, arXiv e-prints, p. arXiv:2103.16212

Grogin N. A., et al., 2011, ApJS, 197, 35

Haiman Z., Mohr J. J., Holder G. P., 2001, ApJ, 553, 545

Hamana T., Sakurai J., Koike M., Miller L., 2015, PASJ, 67, 34

Hansen S. M., McKay T. A., Wechsler R. H., Annis J., Sheldon E. S., Kimball A., 2005, ApJ, 633, 122

Hernández-Martín B., et al., 2020, A&A, 640, A117

Heymans C., et al., 2006, MNRAS, 368, 1323

Heymans C., et al., 2021, A&A, 646, A140

High F. W., Stubbs C. W., Rest A., Stalder B., Challis P., 2009, AJ, 138, 110

Hilton M., et al., 2018, ApJS, 235, 20

Hilton M., et al., 2021, ApJS, 253, 3

Hinshaw G., et al., 2013, ApJS, 208, 19

Hlavacek-Larrondo J., et al., 2015, ApJ, 805, 35

Hoekstra H., Franx M., Kuijken K., Squires G., 1998, ApJ, 504, 636

Hoekstra H., Franx M., Kuijken K., 2000, ApJ, 532, 88

Hoekstra H., Bartelmann M., Dahle H., Israel H., Limousin M., Meneghetti M., 2013, Space Sci. Rev., 177, 75

Hogg D. W., 1999, arXiv e-prints, pp astro–ph/9905116

Horne K., 1986, PASP, 98, 609

Howell S. B., 2006, Handbook of CCD Astronomy, 2 edn. Cambridge University Press

Huang N., et al., 2020, AJ, 159, 110

Hubble E. P., 1926, ApJ, 64, 321

Hubble E., 1929, Proceedings of the National Academy of Science, 15, 168

Hurier G., Aghanim N., Douspis M., 2017, arXiv e-prints submitted to A&A, p. arXiv:1702.00075

Huterer D., Shafer D. L., 2018, Reports on Progress in Physics, 81, 016901

Ilbert O., et al., 2013, A&A, 556, A55

Inami H., et al., 2017, A&A, 608, A2

Israel H., Erben T., Reiprich T. H., Vikhlinin A., Sarazin C. L., Schneider P., 2012, A&A, 546, A79

Jarvis M., Jain B., 2008, J. Cosmology Astropart. Phys., 2008, 003

Jee M. J., Ko J., Perlmutter S., Gonzalez A., Brodwin M., Linder E., Eisenhardt P., 2017, ApJ, 847, 117

Jeltema T. E., Kehayias J., Profumo S., 2009, Phys. Rev. D, 80, 023005

Kaiser N., 2000, ApJ, 537, 555

Kaiser N., Squires G., 1993, ApJ, 404, 441

Kaiser N., Squires G., Broadhurst T., 1995, ApJ, 449, 460

Kettula K., et al., 2015, MNRAS, 451, 1460

Khullar G., et al., 2019, ApJ, 870, 7

Klein M., et al., 2018, MNRAS, 474, 3324

Klein M., et al., 2019, MNRAS, 488, 739

Klein M., et al., 2021, arXiv e-prints accepted for special issue in A&A, p. arXiv:2106.14519

Koekemoer A. M., et al., 2011, ApJS, 197, 36

Koekemoer A. M., et al., 2013, ApJS, 209, 3

Koester B. P., et al., 2007, ApJ, 660, 239

Krist J. E., Hook R. N., Stoehr F., 2011, in Kahan M. A., ed., Society of Photo-Optical Instrumentation Engineers (SPIE) Conference Series Vol. 8127, Optical Modeling and Performance Predictions V. p. 81270J, doi:10.1117/12.892762

Kron R. G., 1980, ApJS, 43, 305

Kuijken K., et al., 2015, MNRAS, 454, 3500

LSST Science Collaboration et al., 2009, arXiv e-prints, p. arXiv:0912.0201

Laureijs R., et al., 2011, arXiv e-prints, p. arXiv:1110.3193

Le Brun A. M. C., McCarthy I. G., Schaye J., Ponman T. J., 2014, MNRAS, 441, 1270

Le Brun A. M. C., McCarthy I. G., Schaye J., Ponman T. J., 2017, MNRAS, 466, 4442

Le Fèvre O., et al., 2005, A&A, 439, 845

Lesci G. F., et al., 2020, arXiv e-prints submitted to A&A, p. arXiv:2012.12273

Lesgourgues J., Pastor S., 2006, Phys. Rep., 429, 307

Lin Y.-T., Mohr J. J., Stanford S. A., 2004, ApJ, 610, 745

Lin Y.-T., Mohr J. J., Gonzalez A. H., Stanford S. A., 2006, ApJ, 650, L99

Liu J., et al., 2015, MNRAS, 449, 3370

Liu A., et al., 2021, arXiv e-prints submitted to A&A, p. arXiv:2106.14518

Luppino G. A., Kaiser N., 1997, ApJ, 475, 20

Mahdavi A., Hoekstra H., Babul A., Bildfell C., Jeltema T., Henry J. P., 2013, ApJ, 767, 116

Malmquist K. G., 1925, Meddelanden fran Lunds Astronomiska Observatorium Serie I, 106, 1

Mandelbaum R., 2018, ARA&A, 56, 393

Mantz A. B., Allen S. W., Morris R. G., Rapetti D. A., Applegate D. E., Kelly P. L., von der Linden A., Schmidt R. W., 2014, MNRAS, 440, 2077

Mantz A. B., et al., 2015, MNRAS, 446, 2205

Mantz A. B., Allen S. W., Morris R. G., Simionescu A., Urban O., Werner N., Zhuravleva I., 2017, MNRAS, 472, 2877

Mantz A. B., Allen S. W., Morris R. G., Canning R. E. A., Bayliss M., Bleem L. E., Floyd B. T., McDonald M., 2020, MNRAS, 496, 1554

Marinacci F., et al., 2018, MNRAS, 480, 5113

Massey R., et al., 2014, MNRAS, 439, 887

McDonald M., et al., 2013, ApJ, 774, 23

McDonald M., et al., 2016, ApJ, 817, 86

McDonald M., et al., 2017, ApJ, 843, 28

McInnes R. N., Menanteau F., Heavens A. F., Hughes J. P., Jimenez R., Massey R., Simon P., Taylor A., 2009, MNRAS, 399, L84

Medezinski E., et al., 2018, PASJ, 70, 30

Melchior P., et al., 2017, MNRAS, 469, 4899

Melin J.-B., Bartlett J. G., Delabrouille J., 2006, A&A, 459, 341

Melin J.-B., et al., 2012, A&A, 548, A51

Miyatake H., et al., 2019, ApJ, 875, 63

Miyazaki S., et al., 2012, in McLean I. S., Ramsay S. K., Takami H., eds, Society of Photo-Optical Instrumentation Engineers (SPIE) Conference Series Vol. 8446, Ground-based and Airborne Instrumentation for Astronomy IV. p. 84460Z, doi:10.1117/12.926844

Miyazaki S., et al., 2018, PASJ, 70, S27

Mo W., et al., 2016, ApJ, 818, L25

Moffat A. F. J., 1969, A&A, 3, 455

Momcheva I. G., et al., 2016, ApJS, 225, 27

More S., Miyatake H., Mandelbaum R., Takada M., Spergel D. N., Brownstein J. R., Schneider D. P., 2015, ApJ, 806, 2

Mroczkowski T., et al., 2019, Space Sci. Rev., 215, 17

Muzzin A., et al., 2013a, ApJS, 206, 8

Muzzin A., et al., 2013b, ApJ, 777, 18

NASA/LAMBDA Archive Team 2021, Optical Depth to Reionization, τ, `https://lambda.gsfc.nasa.gov/education/graphic_history/taureionzation.cfm`, Last updated: 2021-03-19; Accessed: 2021-08-14

Nagai D., Kravtsov A. V., Vikhlinin A., 2007, ApJ, 668, 1

Naiman J. P., et al., 2018, MNRAS, 477, 1206

Navarro J. F., Frenk C. S., White S. D. M., 1996, ApJ, 462, 563

Navarro J. F., Frenk C. S., White S. D. M., 1997, ApJ, 490, 493

Nelson K., Lau E. T., Nagai D., Rudd D. H., Yu L., 2014a, ApJ, 782, 107

Nelson K., Lau E. T., Nagai D., 2014b, ApJ, 792, 25

Nelson D., et al., 2018, MNRAS, 475, 624

Newman J. A., 2008, ApJ, 684, 88

Nicastro F., et al., 2018, Nature, 558, 406

Niikura H., et al., 2019, Nature Astronomy, 3, 524

Oesch P. A., et al., 2010a, ApJ, 709, L21

Oesch P. A., et al., 2010b, ApJ, 725, L150

Oesch P. A., et al., 2018, ApJS, 237, 12

Okabe N., Takada M., Umetsu K., Futamase T., Smith G. P., 2010a, PASJ, 62, 811

Okabe N., Zhang Y. Y., Finoguenov A., Takada M., Smith G. P., Umetsu K., Futamase T., 2010b, ApJ, 721, 875

Oke J. B., Gunn J. E., 1983, ApJ, 266, 713

Pacaud F., et al., 2016, A&A, 592, A2

Pacaud F., et al., 2018, A&A, 620, A10

Palanque-Delabrouille N., et al., 2015, J. Cosmology Astropart. Phys., 2015, 011

Peacock J. A., 1999, Cosmological Physics. Cambridge University Press

Pen U.-L., 1997, New A, 2, 309

Perlmutter S., et al., 1999, ApJ, 517, 565

Piffaretti R., Arnaud M., Pratt G. W., Pointecouteau E., Melin J. B., 2011, A&A, 534, A109

Pillepich A., et al., 2018, MNRAS, 475, 648

Planck Collaboration et al., 2014a, A&A, 571, A20

Planck Collaboration et al., 2014b, A&A, 571, A29

Planck Collaboration et al., 2016a, A&A, 594, A13

Planck Collaboration et al., 2016b, A&A, 594, A24

Planck Collaboration et al., 2016c, A&A, 594, A27

Planck Collaboration et al., 2020a, A&A, 641, A5

Planck Collaboration et al., 2020b, A&A, 641, A6

Pratt G. W., Arnaud M., Biviano A., Eckert D., Ettori S., Nagai D., Okabe N., Reiprich T. H., 2019, Space Sci. Rev., 215, 25

Predehl P., et al., 2014, in Takahashi T., den Herder J.-W. A., Bautz M., eds, Society of Photo-Optical Instrumentation Engineers (SPIE) Conference Series Vol. 9144, Space Telescopes and Instrumentation 2014: Ultraviolet to Gamma Ray. p. 91441T, doi:10.1117/12.2055426

Press W. H., Schechter P., 1974, ApJ, 187, 425

Rafelski M., et al., 2015, AJ, 150, 31

Raihan S. F., Schrabback T., Hildebrandt H., Applegate D., Mahler G., 2020, MNRAS, 497, 1404

Reiprich T. H., Böhringer H., 2002, ApJ, 567, 716

Renzini A., 1997, ApJ, 488, 35

Rettura A., Chary R., Krick J., Ettori S., 2018, ApJ, 867, 12

Riess A. G., et al., 1998, AJ, 116, 1009

Robertson H. P., 1935, ApJ, 82, 284

Rowe B. T. P., et al., 2015, Astronomy and Computing, 10, 121

Rozo E., et al., 2009a, ApJ, 699, 768

Rozo E., et al., 2009b, ApJ, 703, 601

Rozo E., Rykoff E. S., Bartlett J. G., Melin J.-B., 2015, MNRAS, 450, 592

Ruel J., et al., 2014, ApJ, 792, 45

Rykoff E. S., et al., 2012, ApJ, 746, 178

Rykoff E. S., et al., 2014, ApJ, 785, 104

Rykoff E. S., et al., 2016, ApJS, 224, 1

Salvato M., Ilbert O., Hoyle B., 2019, Nature Astronomy, 3, 212

Sanders J. S., Fabian A. C., Russell H. R., Walker S. A., 2018, MNRAS, 474, 1065

Saro A., et al., 2015, MNRAS, 454, 2305

Sasaki S., 1996, PASJ, 48, L119

Schechter P., 1976, ApJ, 203, 297

Schellenberger G., Reiprich T. H., 2017, MNRAS, 471, 1370

Schirmer M., 2013, ApJS, 209, 21

Schlafly E. F., Finkbeiner D. P., 2011, ApJ, 737, 103

Schneider P., 2015, Extragalactic Astronomy and Cosmology: An Introduction. Springer Verlag, doi:10.1007/978-3-642-54083-7

Schneider P., Seitz C., 1995, A&A, 294, 411

Schrabback T., et al., 2007, A&A, 468, 823

Schrabback T., et al., 2010, A&A, 516, A63

Schrabback T., et al., 2018, MNRAS, 474, 2635

Schrabback T., et al., 2021, MNRAS, 505, 3923

Schumann M., 2019, Journal of Physics G Nuclear Physics, 46, 103003

Seitz C., Schneider P., 1997, A&A, 318, 687

Shi X., Komatsu E., Nelson K., Nagai D., 2015, MNRAS, 448, 1020

Shi X., Komatsu E., Nagai D., Lau E. T., 2016, MNRAS, 455, 2936

Shull J. M., Smith B. D., Danforth C. W., 2012, ApJ, 759, 23

Simon P., Taylor A. N., Hartlap J., 2009, MNRAS, 399, 48

Skelton R. E., et al., 2014, ApJS, 214, 24

Slipher V. M., 1917, The Observatory, 40, 304

Smith G. P., et al., 2016, MNRAS, 456, L74

Sommer M. W., Schrabback T., Applegate D. E., Hilbert S., Ansarinejad B., Floyd B., Grandis S., 2022, MNRAS, 509, 1127

Spergel D., et al., 2015, arXiv e-prints, p. arXiv:1503.03757

Springel V., et al., 2005, Nature, 435, 629

Springel V., et al., 2018, MNRAS, 475, 676

Stalder B., et al., 2013, ApJ, 763, 93

Stott J. P., Pimbblet K. A., Edge A. C., Smith G. P., Wardlow J. L., 2009, MNRAS, 394, 2098

Strazzullo V., et al., 2019, A&A, 622, A117

Streblyanska A., Barrena R., Rubiño-Martín J. A., van der Burg R. F. J., Aghanim N., Aguado-Barahona A., Ferragamo A., Lietzen H., 2018, A&A, 617, A71

Streblyanska A., Aguado-Barahona A., Ferragamo A., Barrena R., Rubiño-Martín J. A., Tramonte D., Genova-Santos R. T., Lietzen H., 2019, A&A, 628, A13

Sunyaev R. A., Zeldovich Y. B., 1972, Comments on Astrophysics and Space Physics, 4, 173

Tanabashi M., et al., 2018, Phys. Rev. D, 98, 030001

Tanimura H., et al., 2019, MNRAS, 483, 223

Teplitz H. I., et al., 2013, AJ, 146, 159

The Dark Energy Survey Collaboration 2005, arXiv e-prints, pp astro–ph/0510346

Tinker J., Kravtsov A. V., Klypin A., Abazajian K., Warren M., Yepes G., Gottlöber S., Holz D. E., 2008, ApJ, 688, 709

Tisserand P., et al., 2007, A&A, 469, 387

Tonry J. L., et al., 2012, ApJ, 750, 99

Truong N., et al., 2018, MNRAS, 474, 4089

Umetsu K., 2010, arXiv e-prints, p. arXiv:1002.3952

Umetsu K., 2020, A&A Rev., 28, 7

Vanderlinde K., et al., 2010, ApJ, 722, 1180

Vikhlinin A., et al., 2009, ApJ, 692, 1060

Villaescusa-Navarro F., et al., 2020, ApJS, 250, 2

Voges W., et al., 1999, A&A, 349, 389

Walker A. G., 1937, Proceedings of the London Mathematical Society, 42, 90

Williams C. C., et al., 2018, ApJS, 236, 33

Wise J. H., 2019, Contemporary Physics, 60, 145

Wright C. O., Brainerd T. G., 2000, ApJ, 534, 34

Wright E. L., et al., 2010, AJ, 140, 1868

Wright A. H., et al., 2016, MNRAS, 460, 765

Zhang Y., et al., 2019, MNRAS, 487, 2578

Zohren H., Schrabback T., van der Burg R. F. J., Arnaud M., Melin J.-B., van den Busch J. L., Hoekstra H., Klein M., 2019, MNRAS, 488, 2523

Zuntz J., et al., 2015, Astronomy and Computing, 12, 45

de Haan T., et al., 2016, ApJ, 832, 95

van Dokkum P. G., 2001, PASP, 113, 1420

van Uitert E., Gilbank D. G., Hoekstra H., Semboloni E., Gladders M. D., Yee H. K. C., 2016, A&A, 586, A43

van Weeren R. J., de Gasperin F., Akamatsu H., Brüggen M., Feretti L., Kang H., Stroe A., Zandanel F., 2019, Space Sci. Rev., 215, 16

van den Busch J. L., et al., 2020, A&A, 642, A200

van der Burg R. F. J., et al., 2016, A&A, 587, A23

List of Figures

List of Tables

Acknowledgements

Writing a Ph.D. thesis surely is no easy endeavour and so I want to take the time to thank all the people, who helped me on my journey, be it in an academic context or for my mental well-being.

First of all, my gratitude goes to Tim Schrabback for being an outstanding supervisor. His advice, encouragement, patience, and countless hours of joint discussions have helped me grow to become a better scientist. I could always count on him when I needed help and I highly value our work together.

I would like to thank my official supervisor Peter Schneider for the opportunity to become a Ph.D. student in his research group. I am thankful for his encouragement and trust in me. I also want to thank Thomas Reiprich, the secondary supervisor for this thesis, for his support.

Furthermore, the members of my thesis advisory committee, Peter Schneider, Tim Schrabback, Thomas Reiprich, and Rainer Mauersberger, deserve my gratitude for helping me to keep my Ph.D. thesis on track and to prioritise when necessary.

I was fortunate to be a member of the International Max Planck Research School (IMPRS) during my Ph.D. studies. This not only provided me with numerous opportunities such as workshops and conferences, but it was where I had the chance to meet fantastic fellow Ph.D. students from all over the world.

On many occasions, Sabine Derdau, Ellen Fuhrmann, Elisabeth Kramer, and Christina Stein-Schmitz helped me navigate the more bureaucratic jungle one can sometimes face as a Ph.D. student. I appreciate that they always had kind words and an open ear for me.

During the course of my Ph.D. studies, I had the pleasure to work with many scientists, who contribute to a kind and helpful scientific environment, which I and surely many other students benefited from. I would like to thank Remco van der Burg, who supported me greatly in my first thesis project and helped me take it to the next level. I am grateful to Monique Arnaud, who invited me to visit and work with her research group in Paris. I would like to thank Jean-Baptiste Melin and Matthias Klein for useful discussions and their eye for details, and Angus Wright for his light-hearted and patient way to answer all my questions about LAMBDAR. I would like to thank Sebastian Bocquet for helping to finalise the results for my second thesis project and taking the time to answer a lot of my questions on likelihood analyses. My further gratitude is dedicated to Matt Bayliss, Lindsey Bleem, Esra Bulbul, Mike Gladders, Guillaume Mahler, Keren Sharon, and Alfredo Zenteno.

My work as a doctoral student at the Argelander Institute for Astronomy was coined in the best way by the many versatile people I got to meet, work and connect with. I want to thank Beatriz Hernández-Martín and Fatimah Raihan for their support, the fun chatter, and for establishing our joint motto: ‘just keep swimming’. I would not want to have missed them on the Ph.D. roller coaster. Furthermore, without Jan Luca van den Busch, Beatriz Hernández-Martín, Diana Scognamiglio, Béibhinn Wheelan, Luis Suelves, and Jonah Wagenveld tutoring the lab course and late nights at the telescope would not have been nearly as enjoyable. My special thanks go to Sandra Unruh, Sven Heydenreich, and Jens Erler, who proofread large sections of my thesis and without who it would not be what it is today. I want to thank Beatriz Hernández-Martín, Florian Kleinebreil, Fatimah Raihan, Tim Schrabback, Diana Scognamiglio, Martin Sommer, and Nils Weissgerber for patiently listening to my sometimes seemingly endless reports, questions, and problem discussions about my research projects during our weekly meetings. On Thursday mornings the prospect of the ‘Young Journal Club’ cheered me up on a regular basis thanks to Pierre Burger, Maude Charmetant, Ankur Dev, Sven Heydenreich, Laila Linke, Fatimah Raihan, Dominik Rhiem, Luis Suelves, Sandra Unruh, and Rongchuan Zhao. I want to thank Ole Marggraf for supporting me in the reduction of HST data. Further thanks goes to Davit (Dato) Alkhanishvili, Marcus Keil, David Ohse, Christoph Schürmann, and Benedetta Spina, and Malte Tewes.

My life would also not be complete without my friends Julia Buchner, Robin Buchner, Michelle Spangehl, Michael Hartmann, Andreas Hartmann, and Chris Ulferts. They are simply a wonderful bunch. Additionally, Katharina Rauthmann and Vera Christmann enrich my life with their colourful imagination and cunning wits.

An dieser Stelle möchte ich auch ganz herzlich meinen Eltern Uta und Klaus Zohren, sowie meinem Bruder Hendrik danken, die mir immer den Rücken stärken und mit Rat und Tat zur Seite stehen. Auch bin ich unendlich dankbar, dass in all dieser Zeit immer mein wundervoller Freund Eike Icking an meiner Seite war. Seine Liebe, Geduld und Humor sind ein Geschenk, das noch so viel mehr vermag als mir als Doktorandin zu helfen, nicht den Mut zu verlieren. Ein großer Dank geht auch an Moritz Icking, Christina Fischer und Lisa Icking, mit denen ich mich einfach zu Hause fühle.

Meine Gedanken zum Schluss möchte ich den Mitgliedern meiner Familie widmen, die während meiner Studienzeit als Doktorandin verstorben sind und deren Verlust mich tief berührt hat: meine Großmutter Käthe Zohren, mein Onkel Willibert Zohren und mein Onkel Bernd Zohren.